

UNIVERSITY OF LJUBLJANA  
FACULTY OF MATHEMATICS AND PHYSICS  
DEPARTMENT OF PHYSICS

Anton Potočnik

**MAGNETIC RESONANCE OF MOLECULAR  
SUPERCONDUCTORS BORDERING THE  
ANTIFERROMAGNETIC MOTT-INSULATING  
STATE**

Doctoral thesis

ADVISER: prof. dr. Denis Arčon

Ljubljana, 2013



UNIVERZA V LJUBLJANI  
FAKULTETA ZA MATEMATIKO IN FIZIKO  
ODDELEK ZA FIZIKO

Anton Potočnik

**MAGNETNA RESONANCA MOLEKULARNIH  
SUPERPREVODNIKOV NA MEJI Z  
ANTIFEROMAGNETNIM MOTT-IZOLATORSKIM  
STANJEM**

Doktorska disertacija

MENTOR: izred. prof. dr. Denis Arčon

Ljubljana, 2013



# Acknowledgements

I would first like to acknowledge the financial support of the Slovenian Ministry for Higher Education, Science, and Technology through the Young Researcher educational program.

Second, I would like to thank my advisor, Denis Arčon for his continuous support, countless stimulating discussions, and the opportunity to work in his group. I would also like to thank my co-workers, Andrej Zorko and Matej Pregelj for valuable hints and fruitful discussions. I am grateful to Pavel Cevc for everything he taught me about construction of experiments related to high pressure and microwave technology. A special thanks goes to Peter Jeglič for introducing me to the nuclear magnetic resonance technique and for countless discussions about alkali-doped fullerenes. I would also like to thank Martin Klanjšek for intriguing discussions about strongly correlated materials and superconductivity. A very special thanks go to Andraž Krajnc for all the help with the high-pressure NMR experiments and for writing a wonderful analysis program.

I would like to express my sincere gratitude to Kosmas Prassides, Ruth Zadik, and Ross Colman, as well as, Matthew J. Rosseinsky and Alexey Y. Ganin for providing and characterizing all the samples used in this study and for valuable discussions about the chemistry and physics of the alkali-doped fullerenes.

I am also grateful to Matej Komelj and Nicola Manini from Università degli Studi di Milano for the introduction to the density functional theory and countless suggestions and pointers for interpretation of the DFT results.

I would like to express my sincere gratitude to Massimo Capone and Erio Tosatti from Scuola Internazionale Superiore di Studi Avanzati (SISSA) in Trieste for insightful discussions from the theoretical perspective of alkali-doped fullerenes and for introducing me to the dynamical mean field theory.

Last but not least, I would like to thank Denis Golež and Rok Žitko for interesting theoretical discussions about physics of strongly correlated materials.



# Abstract

This thesis presents a comprehensive study of alkali-doped fullerene materials that are at the border of metal-to-insulator transition (MIT) where they show the highest superconducting transition temperature ( $T_c = 38$  K) of all molecular superconductors. In order to scan the entire phase diagram of these materials we developed a high-pressure nuclear magnetic resonance (NMR) and an electron paramagnetic resonance (EPR) probes that allow us to perform low-temperature experiments under high hydrostatic pressures up to 2 GPa. By focusing on the face-centred cubic (*fcc*)  $\text{Cs}_3\text{C}_{60}$ , *fcc*  $\text{Rb}_x\text{Cs}_{3-x}\text{C}_{60}$  ( $0 < x \leq 3$ ), and the face-centred orthorhombic (*fco*)  $\text{MAK}_3\text{C}_{60}$  (MA = methylamine), we addressed several important questions: Are these materials conventional Bardeen-Cooper-Schrieffer (BCS) or unconventional superconductors? What is the role of strong electron correlations? Is Jahn-Teller (JT) effect present and important for normal and superconducting state?

The magnetic, electronic, and superconducting properties of alkali-doped fullerenes are controlled by the unit-cell volume, which can be varied either by applying external physical pressure or by intercalating different alkali metals into the interstitial sites. At small volumes these materials show metallic behaviour, whereas at larger volumes they go through the MIT into the insulating phase. Our results show that superconductivity deep in the metallic phase resembles BCS superconductivity. However, while approaching MIT, superconducting properties start to deviate away from the BCS predictions around the maximum of the superconducting dome. In this region we observe the onset of non-monotonic behaviour of  $T_c$ , the vanishing of the Hebel-Slichter coherence peak, and the enhancement of the superconducting ratio  $2\Delta/k_B T_c$ . These observations reveal that strong electron correlations are present in the superconducting state close to MIT and thus cannot be correctly described by the BCS formalism. The central conclusion of this thesis, therefore, is that  $A_3\text{C}_{60}$  are unconventional superconductors and not conventional BCS superconductors as believed until now.

High-resolution NMR at cryogenic temperatures allowed us to observe for the first time the JT effect in the insulating phase, as well as, in the metallic phase close to MIT. This is another very important observation that implies that the metallic phase close to MIT is in a non-Fermi liquid state where residual spin carries an orbital angular momentum. Furthermore, in the same region NMR spin-lattice relaxation rate shows pseudogap-like behaviour which is also associated with the non-Fermi liquid description.

Study of non-cubic compound *fco*  $\text{MAK}_3\text{C}_{60}$  by high-pressure EPR and *ab initio* calculations shows that alkali-doped fullerenes have, due to strong electron correlation, strongly renormalized conduction bandwidth which causes an immediate electron localization after the cubic symmetry is broken. The metallic state cannot be restored even under applied pressure of 7 kbar. We show that the large intercalated methylamine molecule sterically deforms  $\text{C}_{60}$  molecule and prevails over the JT effect. Having no JT effect, this material becomes an important model system for testing whether JT effect is indeed involved in the superconductivity of  $A_3\text{C}_{60}$ .

**Keywords:** Alkali-doped fullerenes, unconventional superconductivity, BCS theory, Jahn-Teller effect, metal-to-insulator transition, molecular superconductors, high-pressure physics.

**PACS:** 81.05.ub, 74.70.Wz, 74.25.nj, 76.60.-k, 31.15.E-, 71.20.Tx, 71.30.+h, 07.35.+k



# Povzetek

Ta disertacija predstavlja obširno raziskavo na področju fizike fulerenov z dopiranimi alkalnimi kovinami, ki so blizu prehoda kovina-izolator (PKI) in kjer kažejo najvišjo temperaturo prehoda v superprevodno stanje ( $T_c = 38$  K) med vsemi molekularnimi superprevodniki. Da bi preiskali celotni fazni diagram teh materialov, smo razvili visokotlačne celice za potrebe jedrske magnetne resonance (JMR) in elektronske paramagnetne resonance (EPR) s katerimi lahko dosežemo tlake do 2 GPa. S fokusom na ploskovno-centrirane kubične (*pck*)  $\text{Cs}_3\text{C}_{60}$ , *pck*  $\text{Rb}_x\text{Cs}_{3-x}\text{C}_{60}$  ( $0 < x \leq 3$ ) in ploskovno-centrirane ortorombske (*pcO*)  $\text{MAK}_3\text{C}_{60}$  (MA = metilamin) materiale, smo iskali odgovore na več pomembnih vprašanj povezanih s to družino superprevodnikov: Ali so ti materiali običajni BCS ali pa so neobičajni superprevodniki? Kakšna je vloga močnih korelacij? Ali je Jahn-Tellerjev (JT) pojav prisoten in pomemben v kovinski in superprevodni fazi?

Za fulerene, ki so dopirani z alkalnimi kovinami, je značilno, da so njihove magnetne, elektronske in superprevodne lastnosti določene z velikostjo osnovne celice, ki jo lahko spreminjamo bodisi z zunanjim visokim tlakom bodisi s substitucijo drugih alkalijskih kovin. Materiali z majhnimi osnovnimi celicami so kovinski, tisti z večjimi celicami pa preidejo PKI in postanejo izolatorji pri velikih volumnih. Naši rezultati kažejo, da je globoko v kovinski fazi superprevodnost podobna BCS superprevodnosti, med približevanju k PKI pa se superprevodne lastnosti začenjajo odklanjati od BCS napovedi, približno okoli maksimalnega  $T_c$ . Na tem območju opazimo začetek nemonotonega obnašanja  $T_c$ , izginjanje Hebel-Slichterjevega vrha in ojačitev superprevodnega razmerja  $2\Delta/k_B T_c$ . To nakazuje na prisotnost močnih elektronskih korelacij tudi v superprevodni fazi blizu PKI in zato BCS formalizem, ki upošteva elektronske korelacije le približno, naših rezultatov ne more pravilno napovedati. Glavna ugotovitev te disertacije torej je, da so  $A_3\text{C}_{60}$  neobičajni superprevodniki in ne standardni BCS superprevodniki, kot je bilo mišljeno do sedaj.

JMR eksperimenti z visoko ločljivostjo pri nizkih temperaturah so omogočili, da smo lahko prvič zaznali JT pojav tako v izolatorski, kot tudi v kovinski fazi v bližini PKI. To je še eno zelo pomembno opažanje, ki namiguje na to, da kovinska faza v bližini PKI ni v stanju Fermijeve tekočine, kjer preostali elektronski spin nosi tudi orbitalno vrtilno količino. Še več, v tem istem območju JMR meritve spinsko-mrežnega relaksacijskega časa kažejo na pseudogap obnašanje, ki pa je prav tako pogosto povezano z opisom kovin onkraj modela Fermijeve tekočine.

Študija *pcO*  $\text{MAK}_3\text{C}_{60}$  z EPR pod visokimi tlaki in z računom elektronskih lastnosti je pokazala, da imajo vsi ti materiali, zaradi močnih elektronskih korelacij, močno renormalizirano širino prevodniškega pasu, kar ob zlomitvi kubične simetrije privede do takojšnje lokalizacije elektronov. Povrnitev kovinske faze v  $\text{MAK}_3\text{C}_{60}$  nismo dosegli niti pod tlakom 7 kbar pri nizkih temperaturah. Med drugim smo pokazali, da velika molekula metilamina v kristalni strukturi povzroči močne sterične deformacije molekule  $\text{C}_{60}$ , ki so močnejši od JT. Dejstvo da  $\text{MAK}_3\text{C}_{60}$  nima JT pojava postavlja ta material na izredno pomembno mesto, saj omogoča testiranje vloge JT pojava v superprevodnosti fulerenov, dopiranih z alkalnimi kovinami.

**Ključne besede:** Fulereni z alkalnimi kovinami, neobičajna superprevodnost, teorija BCS, Jahn-Teller pojav, prehod kovina-izolator, fizika visokih tlakov.

**PACS:** 81.05.ub, 74.70.Wz, 74.25.nj,, 76.60.-k, 31.15.E-, 71.20.Tx, 71.30.+h, 07.35.+k



# Contents

<b>Acknowledgements</b>	<b>V</b>
<b>Abstract</b>	<b>VI</b>
<b>Povzetek</b>	<b>VIII</b>
<b>1 Introduction</b>	<b>1</b>
1.1 Fullerenes . . . . .	3
1.2 $A_3C_{60}$ . . . . .	5
1.2.1 Structural Properties . . . . .	5
1.2.2 Electronic properties . . . . .	7
1.2.3 Electron-phonon coupling and Jahn-Teller effect . . . . .	8
1.2.4 Electron correlations . . . . .	9
1.2.5 Superconductivity . . . . .	10
1.2.6 General open questions . . . . .	12
<b>2 Theoretical models for <math>A_3C_{60}</math></b>	<b>15</b>
2.1 Density Functional Theory . . . . .	15
2.2 BCS and Migdal-Eliashberg Theory . . . . .	17
2.3 Dynamical Mean Field Theory . . . . .	20
<b>3 Experimental methods</b>	<b>23</b>
3.1 General Theory of Magnetic Resonance Absorption . . . . .	23
3.2 Electron Paramagnetic Resonance . . . . .	26
3.2.1 Spin Hamiltonian . . . . .	26
3.2.2 Moment Analysis and EPR Linewidth . . . . .	27
3.3 Nuclear Magnetic Resonance . . . . .	29
3.3.1 The nuclear spin Hamiltonian and NMR lineshifts . . . . .	29
3.3.2 Nuclear Relaxation and the Linewidth . . . . .	32
3.3.3 NMR in Paramagnetic Insulators . . . . .	36
3.3.4 NMR in Metals . . . . .	37
3.3.5 NMR in Superconductors . . . . .	41
3.3.6 Magic Angle Spinning NMR . . . . .	44
3.4 High Pressure Experiments . . . . .	45
3.4.1 High-Pressure EPR . . . . .	46
3.4.2 High-Pressure NMR . . . . .	48

<b>4</b>	<b>Importance of <math>t_{1u}</math> degeneracy</b>	<b>51</b>
4.1	Cubic vs. Non-Cubic Crystal Symmetry . . . . .	51
4.2	MAK <sub>3</sub> C <sub>60</sub> under High Pressure . . . . .	52
4.3	DFT study of MAK <sub>3</sub> C <sub>60</sub> . . . . .	54
4.4	Conclusions . . . . .	56
<b>5</b>	<b>Importance of C<sub>60</sub> distortions</b>	<b>57</b>
5.1	Jahn-Teller effect . . . . .	57
5.1.1	Low spin state, $S = 1/2$ . . . . .	59
5.1.2	MAS NMR on Cs <sub>3</sub> C <sub>60</sub> and Rb <sub>0.5</sub> Cs <sub>2.5</sub> C <sub>60</sub> . . . . .	60
5.2	Steric effects . . . . .	63
5.2.1	High-pressure EPR study . . . . .	63
5.2.2	DFT study . . . . .	65
5.3	Conclusions . . . . .	67
<b>6</b>	<b>Importance of structural disorder</b>	<b>69</b>
6.1	Merohedral disorder . . . . .	69
6.2	Substitutional disorder in Rb <sub>x</sub> Cs <sub>3-x</sub> C <sub>60</sub> . . . . .	74
6.3	<i>fcc</i> and A15 crystal symmetries . . . . .	75
6.4	Conclusions . . . . .	77
<b>7</b>	<b>Importance of electron correlations</b>	<b>79</b>
7.1	Bandwidth vs. on-site correlations . . . . .	79
7.1.1	Bandwidth . . . . .	79
7.1.2	Coulomb repulsion . . . . .	80
7.2	MIT transition . . . . .	81
7.2.1	$(U/W)_c$ for <i>fcc</i> A <sub>3</sub> C <sub>60</sub> . . . . .	82
7.2.2	NMR measurements on Cs <sub>3</sub> C <sub>60</sub> and Rb <sub>x</sub> Cs <sub>3-x</sub> C <sub>60</sub> . . . . .	83
7.2.3	MIT border on the Phase diagram . . . . .	101
7.3	$N(E_F)$ in normal state . . . . .	104
7.4	Conclusions . . . . .	106
<b>8</b>	<b>Superconductivity</b>	<b>109</b>
8.1	Superconducting dome . . . . .	109
8.1.1	Chemical vs. hydrostatic pressure . . . . .	111
8.2	Hebel-Slichter coherence peak . . . . .	112
8.3	Superconducting ratio, $2\Delta/k_B T_c$ . . . . .	115
8.4	Conclusions . . . . .	118
<b>9</b>	<b>Discussion</b>	<b>121</b>
9.1	Comparison to other unconventional superconductors . . . . .	122
9.1.1	Unconventional superconductivity . . . . .	126
9.2	Comparison to other light-elements superconductors . . . . .	127
<b>10</b>	<b>Concluding remarks</b>	<b>129</b>
<b>A</b>	<b>High Pressure Cells</b>	<b>133</b>
A.1	High Pressure EPR cell . . . . .	133
A.1.1	Construction details . . . . .	133
A.1.2	Microwave Cavity and Coupling . . . . .	138

A.2	High Pressure NMR cell . . . . .	139
A.2.1	Construction details . . . . .	140
A.2.2	Spectrometer for Ruby fluorescence . . . . .	141
<b>B</b>	<b>Materials</b>	<b>145</b>
B.1	<i>fcc</i> Cs <sub>3</sub> C <sub>60</sub> . . . . .	145
B.2	<i>fcc</i> Rb <sub><i>x</i></sub> Cs <sub>3-<i>x</i></sub> C <sub>60</sub> . . . . .	149
B.2.1	Structural characterisation . . . . .	149
B.2.2	SQUID magnetization measurements . . . . .	152
B.3	<i>fcc</i> CH <sub>3</sub> NH <sub>2</sub> K <sub>3</sub> C <sub>60</sub> (MAK <sub>3</sub> C <sub>60</sub> ) . . . . .	152
B.3.1	Crystal structure . . . . .	152
B.3.2	Compressibility . . . . .	153
B.3.3	Low temperature structure . . . . .	154
B.3.4	DFT calculation parameters . . . . .	154
<b>C</b>	<b>NMR spin-lattice relaxation rate analysis</b>	<b>157</b>
C.1	High Pressure NMR 1/ <sup>13</sup> T <sub>1</sub> analysis . . . . .	158
C.2	<sup>133</sup> Cs NMR spectra decomposition . . . . .	160
	<b>(Extended Abstract in Slovene)</b>	
	<b>Razširjeni povzetek v slovenščini</b>	<b>160</b>
	Uvod . . . . .	161
	<i>t</i> <sub>1u</sub> degeneracija . . . . .	165
	Molekulske deformacije . . . . .	166
	Strukturni nered . . . . .	168
	Elektronske korelacije . . . . .	169
	Superprevodnost . . . . .	171
	Zaključki . . . . .	173
	<b>List of publications</b>	<b>175</b>
	<b>Bibliography</b>	<b>176</b>



*If you do not expect the unexpected  
you will never find it.*

Heraclitus of Ephesus



# 1 Introduction

The discovery of highly symmetrical – soccer-ball shaped –  $C_{60}$  molecule in 1985 by H. Kroto, *et al.* [1] opened an exciting new field of carbon-based fullerene materials that are today widely used in chemistry [2], solar cell technology [3], lubricant technology [4], and condense-matter physics [5]. In the physics community fullerenes initially attracted a lot of attention due to their high icosahedral molecular symmetry from the theoretical perspective [6]. The discovery of high- $T_c$  superconductivity at surprisingly high critical temperatures ( $T_c$ ) [7] and ferromagnetism [8] shifted the interest more to their electronic properties. The first synthesised superconducting fulleride was  $K_3C_{60}$  with  $T_c = 18$  K [9] a value close to the the upper limit set by the standard theory of superconductivity developed by Bardeen, Cooper and Shrieffer (BCS) [10], as thought at that time. It was soon realized that the critical temperature of fullerene superconductors can be even higher when larger alkali metals are intercalated and the unit-cell volume is increased. The maximal  $T_c$  was then quickly raised to  $T_c = 28$  K in  $Rb_3C_{60}$  [11] and  $T_c = 33$  K in  $RbCs_2C_{60}$  [12]. At the time of their discovery only high- $T_c$  cuprates had higher superconducting transition temperatures. Today, the fullerene superconductors hold the record of the highest superconducting transition temperature ( $T_c = 38$  K) among all molecular superconductors [13, 14].

Such a high  $T_c$  cast serious doubts that fullerides are simply standard BCS-type superconductors as thought for many years. This is further supported by a large value of the Coulomb repulsion energy between two electrons on the same  $C_{60}$  molecule in comparison to their electronic kinetic energy, which implies that electron correlations must be very important for this family of materials [5]. Nevertheless, the rich phonon spectra with high energy intramolecular modes provided a satisfactory description of the observed high  $T_c$  and screened Coulomb repulsion within the standard BCS theory until 2008 [5]. Many experimental results supported BCS theory description, e.g., the presence of Hebel-Slichter (H-S) coherence peak in nuclear magnetic resonance (NMR) experiments, isotropic superconducting gap function, superconducting ratio close to the BCS value of  $2\Delta/k_B T_c = 3.53$ , and the isotope effect [5, 7].

In the last two decades more experimental data were gathered on fulleride compounds with distorted, non-cubic crystal structures or compounds with different stoichiometric ratios,  $A_xC_{60}$  ( $A =$  alkali metal). It has been shown that any deviation from the half-filled case of  $x = 3$  or the high cubic crystal structure almost immediately leads to the electron localization and the Mott-insulating state, despite having partially filled conducting band [5]. Such behaviour can be obtained only when strong on-site electron correlations are present. In addition, magnetic measurements show that the low-spin-state is preferred at lower temperatures by the spin singlet-triplet transition in  $Na_2C_{60}$  or  $K_4C_{60}$  [15] or the low-spin state ( $S = 1/2$ ) in case of non-cubic  $A_3C_{60}$  systems [16–18]. Low-spin state arises from the orbital band splitting, which can be either due to the crystal field or the Jahn-Teller effect. In alkali-doped fullerenes the crystal field effect is expected to be

negligible compared to the Jahn-Teller effect [15].

The role of strong electron correlations have finally been revealed when a breakthrough in synthetic route yielded the largest member of fullerene superconducting family, the  $\text{Cs}_3\text{C}_{60}$ . We have shown that at ambient pressure,  $\text{Cs}_3\text{C}_{60}$  is a low-spin state paramagnetic insulator that orders antiferromagnetically at low temperatures [13, 14]. Large size of Cs ion causes three different stable polymorphs: body-centred orthorhombic (*bco*), body-centred cubic (*bcc* or A15), and face-centred cubic (*fcc*). It is worth noting that A15 polymorph has completely disorder-free crystal structure and that *fcc* polymorph show strong frustration effects due to the frustrated geometry of *fcc* lattice. Under moderate pressure of cca. 3 kbar the superconductivity at low temperatures is restored for *fcc* and A15 polymorphs and shows a non-monotonic behaviour of  $T_c$  with varying pressure or volume that continues the trend set by previous compounds at lower volumes. The maximum is now even higher than the previous record, being 38 K and 35 K for A15 and *fcc* polymorphs, respectively. Today, fullerene superconductors are in the fourth place among high- $T_c$  superconductors. The only superconductors with higher  $T_c$  are  $\text{MgB}_2$  ( $T_c = 39$  K [19]), iron-pnictide ( $T_c = 56$  K [20]), and cuprate ( $T_c = 133$  K [21]) superconductors.

The presence of strong correlations that lead to an insulating state is not correctly treated by the standard BCS theory. BCS theory also fails to explain a non-monotonic behaviour of  $T_c$  as a function of the unit-cell volume [5]. The main questions are thus (a) whether extensions to the BCS theory can still explain the experimental observations, (b) are Jahn-Teller effect and magnetism present also in the metallic state close to metal-to-insulator transition (MIT), (c) if they are, are they involved in the peculiar superconducting state close to MIT, and (d) is the fullerene superconductivity similar to the unconventional superconductivity observed in cuprates or iron pnictides.

Throughout the research of alkali-doped fullerenes magnetic resonance techniques, e.g., nuclear magnetic resonance and electron paramagnetic resonance (EPR), played an important role and gave various crucial insights and local properties of normal and superconducting state of  $A_3\text{C}_{60}$  compounds [7]. To address the above questions we, therefore, developed high pressure measuring cells for NMR and EPR experiments and perform NMR and EPR measurements under ambient pressure, high physical pressure and, so-called, chemical pressure on the  $A_3\text{C}_{60}$  compounds. This allowed us to measure local electronic and magnetic properties over a large range of volumes and scan the phase diagram in the vicinity of the MIT. To study the effects of non-cubic symmetry and molecular distortions related to the Jahn-Teller effect we measured high-pressure EPR and performed electronic structure computations on  $\text{MAK}_3\text{C}_{60}$ .

Following the introduction to alkali-doped fullerenes, the modern theoretical models of strongly correlated superconductivity in fullerenes are given in Chapter 2. The magnetic resonance technique covering a nuclear magnetic resonance and electron paramagnetic resonance in different phases is together with the developed high pressure cells presented in Chapter 3. The effect of characteristic electronic band structure on the normal state properties is presented in Chapter 4. Deformations of  $\text{C}_{60}$  molecules either due to intercalated molecules or Jahn-Teller effect are presented and discussed how they impact the normal properties of alkali-doped fullerenes in Chapter 5. In Chapter 6 disorder effects caused either by random molecular merohedral orientation or the substitutional disorder between different intercalated alkali metals are discussed. The effects of electron correlations near MIT observed by NMR is presented and discussed in Chapter 7. Superconductivity as observed by NMR experiments is presented in Chapter 8. Finally, the discussion of the normal and superconducting properties in comparison to other unconventional superconductors is given in Chapter 9 and concluding remarks in Chapter 10.

Several details concerning high-pressure technique development and measurement details, various crystal structures and their temperature and pressure dependences as well as the details related to the electron structure calculations and NMR data analysis are all given in Appendix.

## 1.1 Fullerenes

The  $C_{60}$  molecule was discovered by H. Kroto, *et al.* when trying to synthesise the interstellar pure carbon-based particles in the laboratory [1]. They have shown that  $C_{60}$  molecules are a new allotrope of carbon that has a spherical soccer-ball-like shape. In  $C_{60}$  molecule 60 carbon atoms are placed at the corners of truncated icosahedron (Fig. 1.1a). The name buckminsterfullere, bukyball or just fullerene is derived from the name of a noted futurist and inventor Buckminster Fuller, who designed numerous geodesic domes (most famous is the one in Montreal, Canada) that closely resemble the shape of fullerene molecule [22]. The carbon atoms on a fullerene molecule form 12 pentagon and 20 hexagon rings. The edges between two hexagons are double carbon-carbon bonds with a length of 1.391 Å and the edges between pentagon and hexagon rings are single bonds with slightly longer length of 1.455 Å [5]. Single and double bonds are shown by light amber and amber colour in Fig. 1.1a. The values of double and single bond lengths and the molecular geometry lead to  $C_{60}$  diameter of 7.1 Å [5]. High icosahedral symmetry ( $I_h$ ) of  $C_{60}$  molecule constitutes of 15 two-fold rotational symmetry operations, 20 three-fold rotational symmetry operations, 24 five-fold rotational symmetry operations, identity operation, and inversion operation through the centre of molecule [6]. Altogether 120 symmetry elements represent the full icosahedral group. The nature of alternating double and single bonds was initially claimed to be of aromatic type and that  $C_{60}$  molecules are "superaromatic" molecules [23]. However, recent findings point towards non-aromaticity or even anti-aromatic character [23].

The  $I_h$  point group is the largest among 32 point groups. High degree of symmetry means that fullerene molecules will be highly degenerate in their electronic and phononic states. The electronic structure of isolated  $C_{60}$  molecule is shown in Fig. 1.1b. Being similar to spherical geometry the energy states are in the first approximation comparable to the spherical harmonics where the number of degeneracy goes as  $d(n) = 2n + 1$  where  $n$  represents  $n$ -th level. In  $C_{60}$  molecules the icosahedral symmetry is lower than the spherical symmetry and therefore the energy states transform according to the irreducible representations of  $I_h$  as can be evident from Fig. 1.1b. After adding  $4 \times 60 = 240$  electrons, 180 of them will form C–C  $\sigma$  single and double bonds that hold together  $C_{60}$  molecules and are far below the Fermi level. The remaining 60 electrons will occupy mostly outer  $p_z$ -like orbitals that point perpendicular to the  $C_{60}$  surface, similar to the  $\pi$  orbitals in graphite. However, due to a curved surface these orbitals have a small admixture of  $s$  orbitals in them [7, 25]. After all electrons fill to available electronic states the five-fold degenerate ( $h_u$ ) highest occupied molecular orbitals (HOMO) is completely full and the three-fold degenerate ( $t_{1u}$ ) lowest unoccupied molecular orbital (LUMO) is completely empty (Fig. 1.1b). The energy gap between HOMO and LUMO is  $E_g \simeq 2$  eV. Similar to electronic states, the intramolecular phonon modes can also be grouped by the irreducible representations of  $I_h$  symmetry.

Initial experiments by Kroto, *et al.* were done on small amount of  $C_{60}$  molecules obtained by a laser induced evaporation of graphite substrate in an inert Ar atmosphere [1]. A major breakthrough was made in  $C_{60}$  synthesis by W. Krätschmer *et al.* which

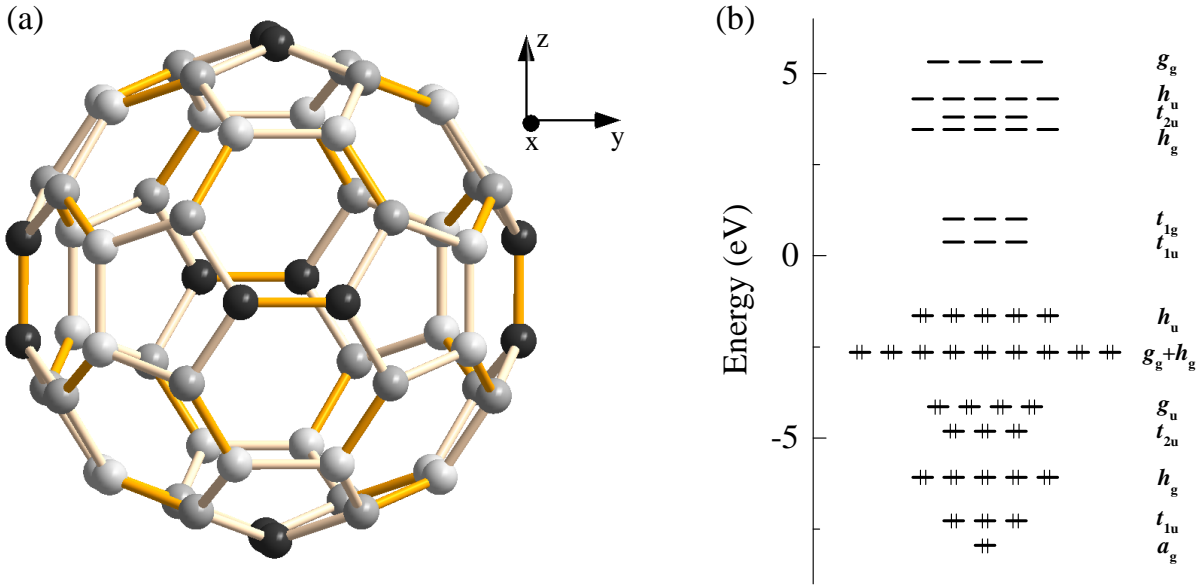


Figure 1.1: (a) Atomic positions of the C<sub>60</sub> molecule in standard orientation. Three non-equivalent carbon atoms are depicted in black, gray and light gray colours. Single bonds forming a pentagon are distinguished from double bonds by lighter colour. (b) Hückel energy levels of an isolated C<sub>60</sub> molecule, adapted from [24]. The corresponding irreducible representations of I<sub>h</sub> symmetry are added to energy levels.

boosted the fullerene production and consequently the fullerene research. They used high-purity graphite electrodes, ignited an arc discharge between them, and obtained large quantities of solid C<sub>60</sub> crystals [26]. XRD study confirmed the icosahedral geometry of C<sub>60</sub> and showed that C<sub>60</sub> form a face-centred cubic (*fcc*) crystal structure with the unit-cell size of  $a = 14.16 \text{ \AA}$  [7] (Fig. 1.2). The *fcc* crystal structure has two types of interstitial cavities, a larger octahedral cavity (Fig. 1.2a) with a radius of 2.1 Å and a smaller tetrahedral cavity (Fig. 1.2b) with a radius of 1.1 Å, taking  $a = 14.2 \text{ \AA}$  [7].

C<sub>60</sub> molecules reorient almost freely at room temperatures and below 260 K they become orientationally ordered in the space group  $Pa\bar{3}$  [27]. Depending on a temperature range there are three types of C<sub>60</sub> reorientational dynamics as observed by <sup>13</sup>C NMR [28]. A completely isotropic reorientation at high temperatures becomes limited below  $\sim 280 \text{ K}$  to fast uniaxial reorientations with a slow axis flipping. Next transition occurs at  $\sim 150 \text{ K}$  where slow axis flipping freezes and C<sub>60</sub> reorient only uniaxially. And finally, below  $\sim 80 \text{ K}$  also uniaxial dynamics freezes and C<sub>60</sub> molecules become static.

The electronic properties of solid C<sub>60</sub> crystal are consistent with a band insulating state. This is due to large energy gap between HOMO and LUMO derived-bands, which is not removed by electron dispersion. Rather narrow bandwidth of  $W \simeq 0.6 \text{ eV}$  comes from relatively large distance between the closest carbons of neighbouring molecules (3.1 Å). This value is comparable to the interlayer distance in graphite (3.35 Å) [7].

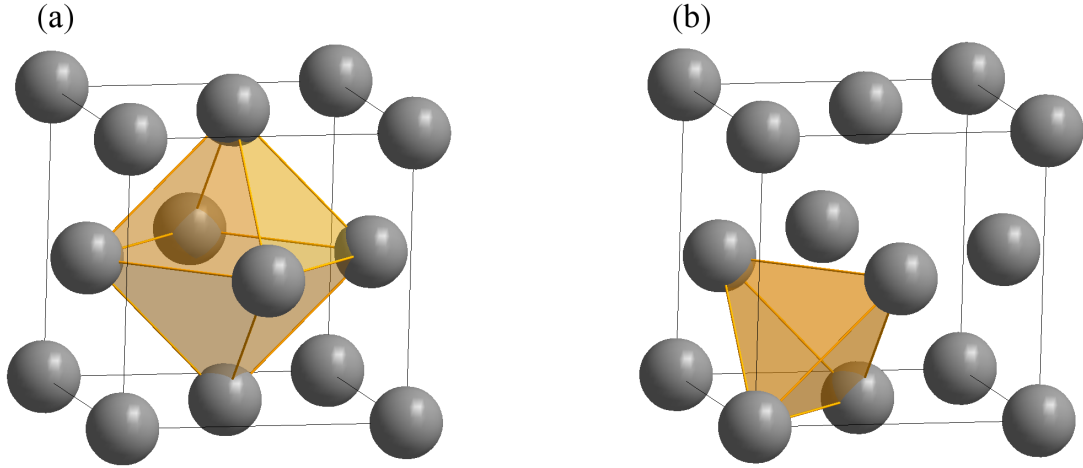


Figure 1.2: *fcc* crystal structure of solid  $C_{60}$ .  $C_{60}$  molecules are presented with gray balls. In  $C_{60}$  crystal structure there are two types of interstitial cavities (a) one octahedral and (b) two tetrahedral ones per unit-cell.

It was soon realized that octahedral and tetrahedral cavities in  $C_{60}$  crystals can be filled with different electron donors or acceptors which leads to doping of conducting  $t_{1u}$  band. Widely used electron donors are the alkali metals. In order to add electrons to three-fold degenerate  $t_{1u}$  LUMO derived band up to 6 alkali metals can be intercalated to the  $C_{60}$  crystal yielding  $A_xC_{60}$ ,  $0 \leq x \leq 6$  compounds. Interestingly, only  $x = 3$  system is metallic. Compounds with  $x = 1$  have polymerized  $C_{60}$  molecule with structure depending on the alkali metals [25, 29, 30]. Compounds with  $x = 2$  are unstable and decompose in  $AC_{60}$  and  $A_3C_{60}$  with only exception of  $Na_2C_{60}$  [31, 32]. All  $A_4C_{60}$  compounds are stable and grow in *bco* structures. They are, just like  $Na_2C_{60}$  all insulating despite having only partially filled conducting band [15, 25, 31, 32].  $x = 5$  compounds are also unstable, yielding a mixture of  $A_4C_{60}$  and  $A_6C_{60}$  [33], and finally  $A_6C_{60}$  compounds are normal band insulators like  $C_{60}$ . The metallic and superconducting properties seem to be limited to the half filling case. It has been shown that superconducting transition temperature decrease very steeply when stoichiometry deviates from  $x = 3$  [30].

## 1.2 $A_3C_{60}$

### 1.2.1 Structural Properties

The intercalation of three alkali metals per  $C_{60}$  molecule in principle does not change the *fcc* crystal structure [34]. An exception is  $Cs_3C_{60}$  where besides *fcc* other stable polymorphs are possible. The alkali metal atoms are positioned in the octahedral and tetrahedral interstitial sites as shown in Fig. 1.3a. In case of ternary compounds, e.g.,  $CsRb_2C_{60}$ , the larger alkali atom goes into the octahedral and the smaller to the tetrahedral site. Alkali metal atoms with an exception of sodium have larger ionic radii compared to the size of tetrahedral site. This causes an expansion of the unit-cell after intercalation. As a consequence larger intercalated alkali metals yield larger unit-cell volumes. In addition, to avoid close contact between  $C_{60}$  and  $A^+$  ions  $C_{60}$  molecules reorient in such a way that they face alkali ions in the tetrahedral site with the hexagon rings. This changes the space group of  $A_3C_{60}$  to  $Fm\bar{3}m$ . Such description is valid only for alkali metals larger than Na. When Na atoms are intercalated the crystal structure changes to simple cubic [30]. On the other hand, Cs metal is so enormous that it does not only

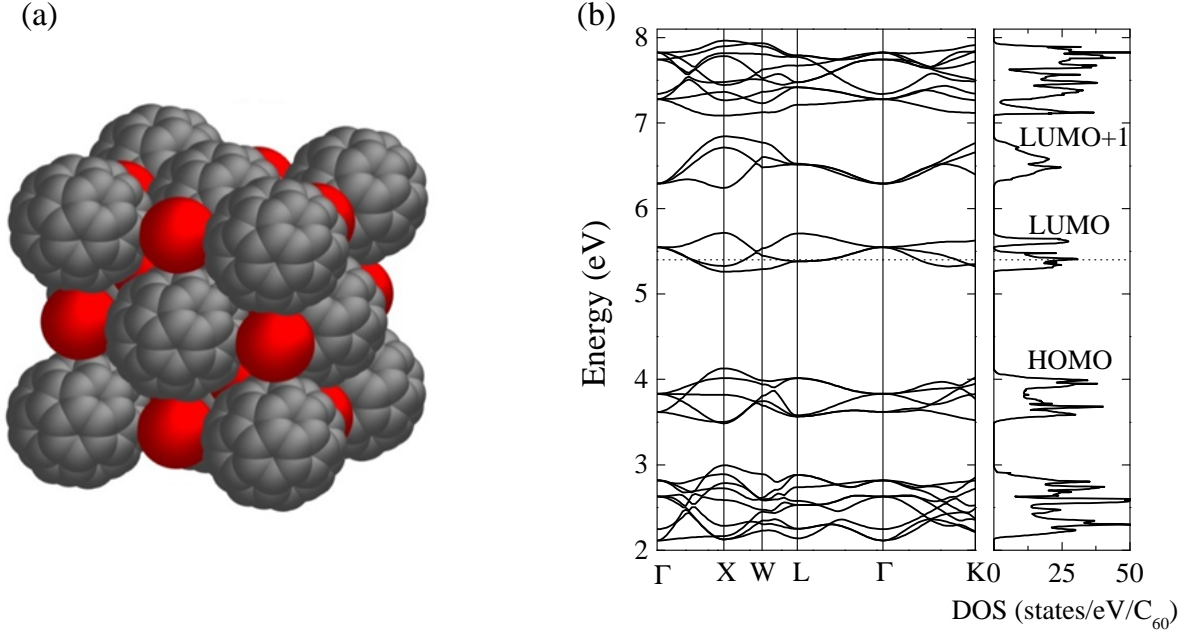


Figure 1.3: (a)  $A_3C_{60}$  crystal structure. (b) Electronic band structure and density of states calculated for  $K_3C_{60}$  with Quantum Espresso.

expand the unit cell, but it yields more than one stable crystal structure.  $Cs_3C_{60}$  has three polymorphs: *bco*, A15 (*bcc*), and *fcc*, among which only *fcc* and A15 polymorphs show superconductivity. A special case is also Li metal. Its highly electropositive nature cause a strong hybridization of Li *s*-orbitals with  $t_{1u}$  molecular orbitals which results in a destruction of superconductivity at low temperatures [30].

In the *fcc*  $A_3C_{60}$  crystal structure with  $Fm\bar{3}m$  space group each  $C_{60}$  molecule has three inequivalent carbon atoms. They are at the crystallographic positions C1: (0, 0.0491, 0.2407), C2: (0.2051, 0.0767, 0.0987) and C3: (0.1764, 0.1533, 0.0503) with the multiplicity of 12, 24, and 24, respectively [14]. Three inequivalent carbons are shown by black, gray, and light gray colour in Fig. 1.1.

The space group  $Fm\bar{3}m$  exhibit two non-equivalent orientations of  $C_{60}$  molecule in the unit cell. This means that  $C_{60}$  in  $A_3C_{60}$  are orientationally disordered between two, so-called merohedral orientations, that differ by a two-fold rotation around any crystal axis. Two merohedral orientations are called *x*-oriented, where the double bond through *z*-axis is parallel to *x*-axis (Fig. 1.1a), and *y*-oriented with analogous definition.

## Disorder

The reorientational dynamics of  $C_{60}$  in  $A_3C_{60}$  is by intercalating larger alkali metals reduced. This is mostly due to a small size of tetrahedral interstitial sites where alkali ions are practically bedded down into the center of the hexagon. The freezing temperature of rotational dynamics is increasing with the size of alkali metals. For example, in  $C_{60}$ ,  $K_3C_{60}$ , and  $Rb_2CsC_{60}$ , the uniaxial rotational dynamics completely freezes on the NMR time scale (100 MHz) at  $\sim 100$ ,  $\sim 200$ , and  $\sim 300$  K, respectively [7]. Highly expanded  $A_3C_{60}$  compounds ( $Rb_xCs_{3-x}C_{60}$ ) that will be studied in this thesis have all very high freezing temperatures ( $T_{\text{freez}} > 300$  K). Their  $C_{60}$  molecules will be frozen in one of two possible merohedral orientations without site-to-site correlations. This is called the

merohedral orientational disorder.

In ternary compounds ( $A_x A'_{3-x} C_{60}$ ) there is yet another type of disorder. For a certain values of  $x$  two different alkali ions will both occupy either tetrahedral or octahedral sites. This introduces, so-called, substitutional disorder. We shall study the effects of the two types of disorder in Chap. 6.

At the end we note that A15 polymorph of  $Cs_3 C_{60}$  that has *bcc* crystal structure contains no merohedral or substitutional disorder. This compound is completely disorder-free material which is a rare example among superconductors with high  $T_c$  [13].

## 1.2.2 Electronic properties

With the intercalation of three alkali metal atoms their valence electrons transfer completely to  $C_{60}$  molecule. The three transferred electrons occupy triply degenerate LUMO  $t_{1u}$ -derived bands. In  $A_3 C_{60}$  transferred electrons become delocalized due to overlapping  $t_{1u}$  orbitals with neighbouring molecules. The overlap is non-negligible since  $t_{1u}$  orbitals have mostly  $p_z$  character which radiate out from the  $C_{60}$  surface. The non-interacting electronic band-structure is shown in Fig. 1.3b. The structure is similar to the  $C_{60}$  solid compound but with half-filled  $t_{1u}$  molecular orbitals derived bands. The  $t_{1u}$  band is well isolated from HOMO and LUMO+1 bands with band gaps of  $\sim 1.1$  and  $\sim 0.3$  eV, respectively (for  $K_3 C_{60}$ ). The  $t_{1u}$  derived bandwidth is  $W \sim 0.5$  eV. A narrow bandwidth is characteristic for molecular solids and comes from a relatively small overlap between neighbouring molecular orbitals. It is interesting to note that with intercalation of larger alkali metal atoms the unit-cell volume is expanded. This thus provides an efficient method for tuning the nearest neighbour  $C_{60}$ - $C_{60}$  distance and consequently the overlap between  $t_{1u}$  orbitals. Reduction of overlap is reflected in reduction of the  $t_{1u}$  bandwidth and consequently in the increase of the density of states at the Fermi level [ $N(E_F)$ ]. Intercalation of larger alkali metals would, therefore, give narrower bandwidths, which will be of central importance to this thesis.

### Crystal symmetry

Cubic crystal symmetry maintains the triple degeneracy of  $t_{1u}$ -derived bands. In the electronic band structure (Fig. 1.3b) degeneracy is reflected in the triply-degenerate state at the  $\Gamma$  point. As we shall see this degeneracy is crucial for the metallic and superconducting state of  $A_3 C_{60}$ . Compounds with distorted crystal symmetry, either face-centred tetragonal or orthorhombic symmetry, have all removed orbital degeneracy which is in the electronic band structure reflected as a non-degenerate states at the  $\Gamma$  point. Interestingly, all these materials are not metallic but rather insulating and antiferromagnetic at low temperatures [17, 35–37]. Non-cubic crystal structures and corresponding insulating ground states were observed in compounds that have in addition to small alkali metals intercalated also neutral anisotropic molecules like  $NH_3$  or  $CH_3NH_2$  (MA). The resulting compounds are  $NH_3 Rb_x K_{3-x} C_{60}$  [17, 35] and  $MAK_3 C_{60}$  [36]. The crystal anisotropy comes from the anisotropic intercalated molecules. In case of  $NH_3 K_3 C_{60}$  the cell parameter anisotropy is  $c/a = 0.915$  and  $b/a = 0.996$  and for  $MAK_3 C_{60}$  anisotropy is  $c/a = 0.888$  and  $b/a = 0.9985$ . The intercalated molecules serve primary as anisotropic spacers that expand the crystal structure. However, their presence seems to influence also the electronic structure. Either by doubling the unit-cell as is the case in  $NH_3 K_3 C_{60}$  [38] or by influencing the electronic states measured by EPR linewidth or  $g$ -factor [18], when rotational dynamics of MA becomes frozen in  $MAK_3 C_{60}$ . The extend of this influence is

yet to be determined.

It is peculiar that rather small discrepancy away from the cubic symmetry leads to completely different – insulating – ground state. This is in odds with the density functional theory (DFT-LDA) which gives metallic ground state of non-cubic  $\text{NH}_3\text{K}_3\text{C}_{60}$  [39]. This indicates (i) that the additional crystal field due to  $\text{NH}_3$  molecules does not split the tree  $t_{1u}$  orbitals to such extend that material will become band insulator and (2) strong electron correlations must be present which results in the Mott-insulating ground state [5]. Another peculiarity is associated with the anomalous antiferromagnetic transition temperature, Néel temperature ( $T_N$ ), of  $\text{MAK}_3\text{C}_{60}$  compared to other orthorhombic  $\text{NH}_3\text{Rb}_x\text{K}_{3-x}\text{C}_{60}$  compounds. In later  $T_N = 40 - 80$  K [17], whereas in  $\text{MAK}_3\text{C}_{60}$   $T_N = 11$  K despite having similar unit-cell volumes [37]. Whether this is an effect of slightly larger anisotropy or the proposed hydrogen-bond between MA protons and  $\text{C}_{60}$  molecules [36] remains to be seen.

### 1.2.3 Electron-phonon coupling and Jahn-Teller effect

There are several phonon modes in the  $A_3\text{C}_{60}$  crystals as can be seen in Fig. 1.4. In the low-energy site there are librations of  $\text{C}_{60}$  molecules ( $\sim 3$  meV), intermolecular vibrations ( $\sim 5$  meV), and optical phonons where alkali cations vibrate relative to  $\text{C}_{60}^{3-}$  anions (7–12 meV). On the high-energy site there are intramolecular vibrations with radial ( $\sim 0.06$  eV) and tangential character (0.12–0.19 eV). The tangential intramolecular modes have very large energy that is comparable to the electron bandwidth. Such a large intramolecular phonon energies come from the fact that carbon atoms are light elements that are connected by strong single and double covalent bonds, which according to  $\omega = \sqrt{k/m}$  gives large vibrational frequencies. Another interesting feature of  $A_3\text{C}_{60}$  phonon modes is that they are rather well separated in energy. Given a phonon energy value one can easily determine the associated phonon mode. It has been shown that the electron-phonon coupling strength varies for different phonon modes. For example, low-energy phonons are only weakly coupled to the  $t_{1u}$  electronic states, compared to much stronger coupling with intramolecular phonons [5].

For molecular systems with degenerate electronic states there is another type of electron-phonon interaction, namely the Jahn-Teller effect. H. Jahn and E. Teller proved the Jahn-Teller theorem which states that for any molecular systems with degenerate ground state associated with molecule configuration there exists a symmetry-breaking interaction that causes a molecular deformation associated with the removal of electronic degeneracy [6]. The importance of JT effect in fullerenes has been initially recognized by theoreticians [41, 42] and only later indirect proof was found by experimentalists. Namely, NMR experiments on  $\text{Na}_2\text{C}_{60}$  and  $\text{Cs}_4\text{C}_{60}$  show an energy gap that was assigned to JT effect [15], optical measurements on the same compounds see deformations that can also be associated with the JT effect [43], measured low-spin state of the non-cubic or hyper-expanded alkali-doped fullerenes, or NMR measurements on TDAE- $\text{C}_{60}$  [8].

Strong electron-phonon coupling between  $\text{C}_{60}$  intramolecular phonons and  $t_{1u}$  electrons is according to the group theory possible only for two phonon mode symmetries, the isotropic  $A_g$  and anisotropic five-fold degenerate  $H_g$  phonon modes [5, 6]. The Jahn-Teller effect removes the orbital degeneracy by changing the energy levels relative to each other. The centre of gravity of electronic levels is unaffected by JT interaction. Now, since the isotropic phonon modes ( $A_g$ ) do not change energy level with respect to each other and only affect the energy level centre of mass these are not JT-active modes. On the other hand,  $H_g$  phonon modes have compatible properties with the JT effect and

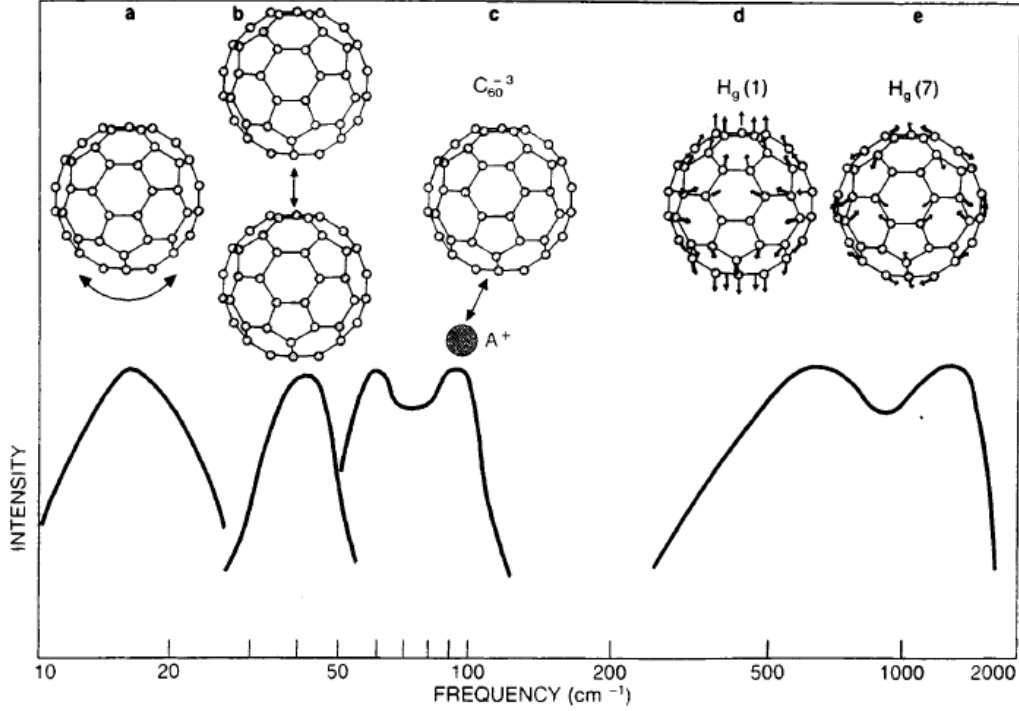


Figure 1.4: Phonon modes of alkali-doped fullerenes: (a) librations, (b) intermolecular modes, (c) optical modes, (d) intramolecular modes with radial character and (e) intramolecular modes with tangential character. Adapted from [40].

are thus JT-active modes [5, 6]. JT distorted  $C_{60}$  molecule can have three symmetries,  $D_{2h}$ , when deformation is along the two-fold rotational axis,  $D_{5d}$  when the molecule is deformed along five-fold rotational axis, and  $D_{3d}$  when deformation is along three-fold rotational axis or hexagons. When a single electron is added to the neutral  $C_{60}$  molecule the deformation is analogous to the elongation or flattening along a given symmetry axis. In case of three electrons added on  $C_{60}$  the deformation are bimodal [41]. An example obtained by DFT-LDA calculations are shown in Fig. 1.5 [44].

### 1.2.4 Electron correlations

We already noted that having two or more electrons on the same  $C_{60}$  molecule they become repelled by the Coulomb repulsion interaction. A simple estimate of this on-site repulsion energy,  $U$ , on the isolated molecule and in the classical picture where two point charge electrons maintain the maximal possible interelectron distance of  $C_{60}$  diameter (7.1 Å) yields  $U \approx 2$  eV. A more rigorous quantum mechanical description of Coulomb interaction gives smaller value of  $U$ , which is even further reduced when  $C_{60}$  is put into a solid where electron screening effects are present. The real value of  $U$  is believed to be  $U = 0.8\text{--}1.5$  eV [5]. The Coulomb repulsion energy,  $U$ , that needs to be paid when two electrons are simultaneously on a single  $C_{60}$ , should be compared to kinetic energy gained by electron hopping to that site. Such behaviour is best described by the Hubbard model that is in second quantisation written as

$$\mathcal{H} = - \sum_{\langle i,j \rangle \sigma} \left( t_{ij} c_{j\sigma}^\dagger c_{i\sigma} + \text{h.c.} \right) + U \sum_{i=1}^N n_{i\uparrow}^\dagger n_{i\downarrow}, \quad (1.1)$$

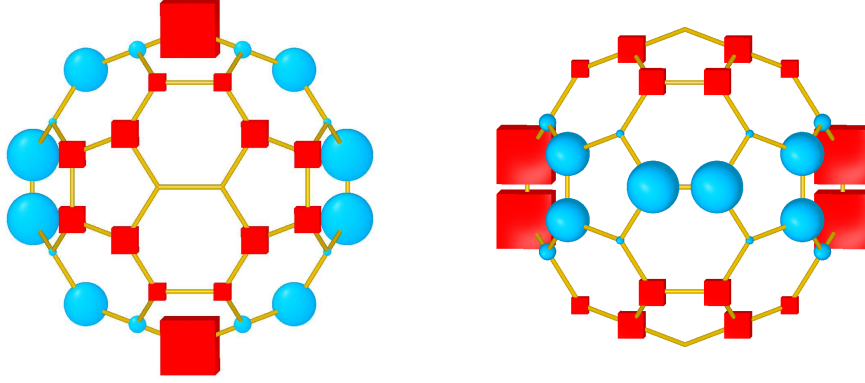


Figure 1.5: Example of two different JT deformations expected for  $C_{60}^{3-}$  ions with  $D_{2h}$  symmetry. The actual deformations are too small to be directly observed ( $\Delta r \simeq 0.02 \text{ \AA}$ ). Instead inwards and outwards radial distortions away from icosahedral geometry are depicted with blue spheres and red cubes, respectively.

where  $\langle \rangle$  denotes nearest neighbours,  $\sigma$  is spin number,  $c_i^\dagger$  is creation,  $c_i$  is annihilation, and  $n_i$  is number operator on the site  $i$ . Since MIT is successfully described by the Hubbard model, the Coulomb repulsion energy is often called also Hubbard parameter  $U$ . Since the kinetic energy is related to the bandwidth,  $W$ , the ratio  $U/W$  becomes a very important indicator of the strength of electron correlations. For  $U/W < 1$  this ratio gives a metallic state and for  $U/W > 1$  the Mott-insulating state<sup>1</sup>. As we have also noted earlier the bandwidth is decreasing with increasing unit-cell volume which makes the ratio  $U/W$  a monotonically increasing function of the unit-cell volume. Here we considered that  $U$  is a molecular property and volume independent or slightly increasing due to the weakening of screening effects in the vicinity of MIT at  $U/W = 1$ . It is peculiar that in metallic  $A_3C_{60}$  compounds this ratio is  $U/W = 1.6\text{--}3$  for  $K_3C_{60}$  or  $Rb_3C_{60}$ . Such a high ratio was explained by the triple-orbital degeneracy of  $t_{1u}$ -derived band [5].

That  $A_3C_{60}$  are close to MIT was suggested by measurements on several non-cubic compounds,  $A_4C_{60}$ ,  $NH_3K_3C_{60}$  or  $MAK_3C_{60}$ , that shown antiferromagnetic insulating ground state, even-though their unit-cell volume is comparable to the volume of metallic  $K_3C_{60}$  or  $Rb_3C_{60}$  compounds. A more direct evidence of the importance of strong electron correlations came with hyper-expanded *fcc* compound  $Li_3(NH_3)_6C_{60}$  that also exhibits antiferromagnetic insulating ground state [45]. The ultimate proof that strong electron correlations are indeed present in  $A_3C_{60}$  came with the discovery of the largest member,  $Cs_3C_{60}$ , which is antiferromagnetic insulating at ambient pressure conditions and becomes metallic at moderate pressure of  $\sim 2$  kbar [13, 14].

### 1.2.5 Superconductivity

The superconducting state of  $A_3C_{60}$  received a lot of attention in the past mostly due to its relatively high  $T_c$  [40]. At the time of discovery only high- $T_c$  cuprates were known to be higher. Soon after the discovery it was found that  $T_c$  can be further increased by increasing the unit-cell volume or by intercalating larger alkali metals (Fig. 1.6). Fullerene superconductivity was from the beginning explained by the standard BCS theory. Rich phonon spectra supported the BCS theory in fullerenes. Furthermore, the phase diagram

<sup>1</sup>Mott-insulating state is an insulating state caused by strong electron correlations in partially filled conducting band. This is different from the band insulators.

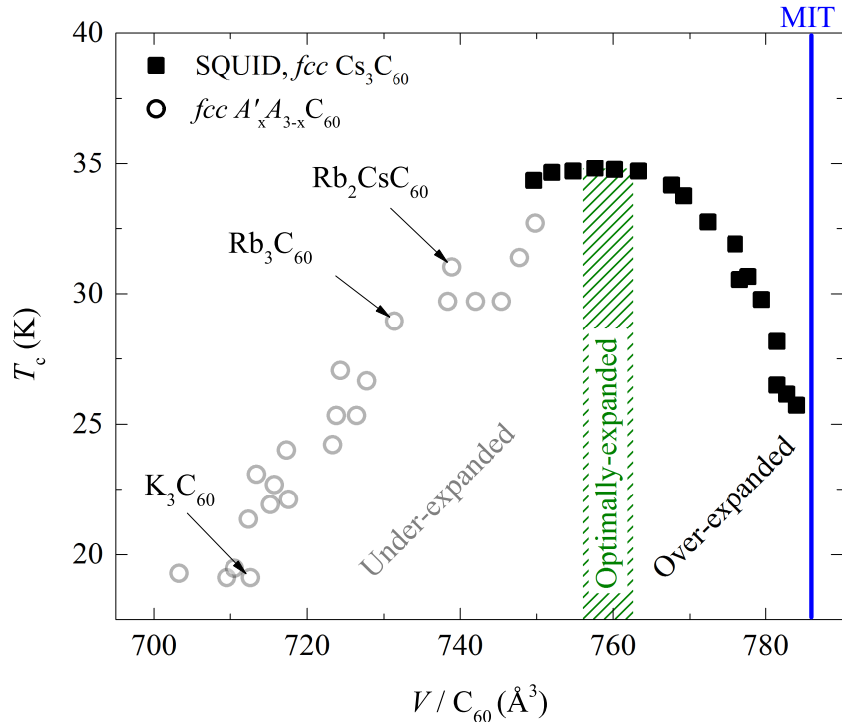


Figure 1.6: Superconducting transition temperature ( $T_c$ ) as a function of unit-cell volume which also represents the low temperature phase diagram of  $fcc A_3C_{60}$ . Previous measurements on  $A'_x A_{3-x} C_{60}$  (adapted from [30]) compounds are shown with gray empty circles and recent SQUID measurements [13] with black squares  $fcc Cs_3C_{60}$ . According to the shape of superconducting dome we define three regions: the under-expanded region at low volume, the optimally-expanded region at  $\sim 760 \text{ \AA}^3$  and over-expanded region at higher volumes. The MIT is denoted by blue vertical line.

known at that time show that  $T_c$  was monotonically increasing function of the unit-cell volume, which is also in agreement with standard BCS theory, where  $T_c$  is expressed to be a function of coupling constant  $\lambda$  [46]

$$k_B T_c = 1.14 \hbar \omega_D \exp(-1/\lambda), \quad (1.2)$$

where  $\lambda = N(E_F) \tilde{V}$  and  $\tilde{V}$  is the electron-phonon coupling. The monotonic increase of  $T_c$  in  $A_3C_{60}$  compounds comes from a monotonic increase of the density of states at the Fermi level [ $N(E_F)$ ]. BCS theory in fullerenes was supported also by other experimental observations like Hebel-Slichter coherence peak in NMR relaxation rate [47], BCS value of superconducting ratio  $2\Delta/k_B T_c = 3.53$  [7, 25], isotope effects [25], etc.

Although BCS theory was widely accepted for  $A_3C_{60}$ , there was growing number of arguments that spoke against it. For example, the H-S peak, clearly observed in standard superconductors, is in  $A_3C_{60}$  strongly suppressed, the superconducting ratio  $2\Delta/k_B T_c$  is approximately of the BCS value, however, different experiments gave different results, even as high as  $2\Delta/k_B T_c = 5.3$  by scanning tunnelling microscopy [48]. At the same time there were many theoretical studies suggesting that BCS theory does not take correctly into account all the effects found in  $A_3C_{60}$  systems, for example, narrow conduction band, clearly distinguished phonon modes in a rich structured phonon spectra, structured electronic density of states, Jahn-Teller effect, and finally the strong Coulomb repulsion energy.

Some of the above effects were implemented in the extended BCS theory, the Migdal-

Eliashberg theory, which was afterwards used to explain the fullerene superconductivity. Assuming the Migdal theorem, which states that vertex corrections can be neglected when phonon modes are much lower in energy than the relevant electronic states [25], the Migdal-Eliashberg theory correctly considers the whole phonon spectra and accounts for the Coulomb repulsion energy in a perturbative manner. Even-though more properties could be explained in this way the validity of Migdal-Eliashberg theory is still questionable for  $A_3C_{60}$ . One problem of Migdal-Eliashberg theory is the Migdal's theorem which assumes low phonon energies, whereas for  $A_3C_{60}$  intramolecular phonons are expected to be relevant with energies that are comparable to the electronic ones. Another problem of Migdal-Eliashberg theory becomes evident when high  $T_c$  of  $A_3C_{60}$  is estimated. In order to obtain such a high values strong Coulomb repulsion,  $U$ , must be strongly renormalized. This is, however, possible only with strong retardation effects that can arise only from the low-energy optical phonon modes. The involvement, of optical phonons in the superconducting pairing mechanism is less likely than intramolecular phonons [5, 7].

The synthesis of the largest member,  $Cs_3C_{60}$ , gives a valuable insight also in the superconductivity close to the MIT. The recovery of the superconducting state at moderate pressure of  $\sim 2$  kbar shows a non-monotonic behaviour where  $T_c$  first increases with increasing pressure and after it reaches a maximum  $T_c$  decreases with increasing pressure or decreasing volume. At small volumes  $T_c$  follows the same trend that was established by previous measurements on  $A_3C_{60}$  (Fig. 1.6). Based on the complete phase diagram of  $A_3C_{60}$  we will designate three regions that will be used through this thesis. The *under-expanded region* spans up to the  $V_{\max} = 760 \text{ \AA}^3$ , the *optimally-expanded region* is around  $V_{\max}$  where  $T_c$  is maximal, and the *over-expanded region* is for volumes larger than  $V_{\max}$  (Fig. 1.6). A non-monotonic behaviour of  $T_c$  and the proximity to the antiferromagnetic insulating phase is reminiscent to the unconventional superconductivity, found in cuprates, iron-pnictides, heavy fermions, and others [49].

If we want to discuss the superconductivity of  $A_3C_{60}$  in terms of unconventional superconductivity we need to generalized the term *unconventional superconductivity*. Until now, this term was used for systems where phonon mediated pairing could not explain the superconducting properties or where the superconducting gap function was different than the isotropic  $s$ -wave type. We explicitly define the unconventional superconductivity as a phenomenon that cannot be correctly explained by the BCS framework containing, either the weak-coupling standard BCS theory, extension for the strong coupling case, Migdal-Eliashberg extension, etc.

### 1.2.6 General open questions

In this thesis we will try to answer the following open questions which span from specialized to general questions related to the alkali-doped fullerene systems:

- How can crystal structure effect the electronic states?
- What is the origin of mysterious T' line in alkali metal NMR spectrum?
- What is the effect of structural disorder?
- What happens to the Jahn-Teller effect in the vicinity of metal-to-insulator transition?
- What is the effect of strong electron correlations?

- What is the order of metal-insulator phase transition or is there a phase coexistence of insulating and metallic state?
- Are the antiferromagnetic fluctuations present?
- Are  $A_3C_{60}$  conventional BCS or unconventional superconductors?



## 2 Theoretical models for $A_3C_{60}$

Metallic and superconducting state of  $A_3C_{60}$  compounds is after two decades of intense research still controversial. In the beginning it was believed that the metallic and superconducting states were not different from the simple metals described by non-interacting Fermi liquid theory and standard BCS theory of superconductivity. However, there were peculiar details that were not in quantitative agreement with these simple theories [5]. At the same time arguments appeared that  $A_3C_{60}$  materials might have correlated electrons and that the Jahn-Teller-type electron-phonon interaction could also be important. Because of this  $A_3C_{60}$  compounds became interpreted within weakly interacting Fermi-liquid theories. The discovery of Mott-insulating  $Cs_3C_{60}$  compound again changed the view and opened doors for new theories that would correctly treat strong electron correlations.

In this chapter we will present widely used theories that described  $A_3C_{60}$  compounds, namely the density functional theory, the BCS theory and dynamical mean field theory.

### 2.1 Density Functional Theory

The conducting ground state of molecular solid  $A_3C_{60}$  has been in the past described by an *ab-initio* technique in the uncorrelated limit [24, 25, 50, 51]. Presently the best approach to compute the non-interacting many-body problems is the density functional theory (DFT) [52, 53]. Its main concept is that the quantum many-body system can be equally well described by the electron density. In this way most of the electronic ground state properties could be computed with an adequate accuracy. DFT has been used to compute electronic structures, molecular and crystal structures, vibrational frequencies and related IR and Raman spectra, atomization energies, ionization energies, magnetic properties, *etc.* [52]. In alkali-doped fullerenes this technique has been widely used for the calculation of the electron band-structure and the density of states [24, 51, 54].

DFT solves the many-body Schrödinger equation by mapping it to the single particle problem in a potential that takes into account many-body interactions. The obtained non-linear equation is then solved self-consistently by an iterative method. DFT is based on the Born-Oppenheimer approximation where nuclei are assumed to be static in their potential minimum. In this approximation electronic Hamiltonian consists of the kinetic term, potential term due to the Coulomb interaction with nuclei  $[V(\vec{r}_i)]$  and electron-electron Coulomb interaction term

$$\mathcal{H}_e = -\frac{\hbar^2}{2m} \sum_i \nabla_i^2 + \sum_i V(\vec{r}_i) + \frac{e^2}{4\pi\epsilon_0} \sum_i \sum_{j>i}^N \frac{1}{|\vec{r}_i - \vec{r}_j|}. \quad (2.1)$$

The ground state energy of the above Hamiltonian is calculated by the variational principle

$$E = \min_{\Psi} \langle \Psi | \mathcal{H}_e | \Psi \rangle \quad (2.2)$$

which states, that the ground state energy will be obtained for such wavefunction  $\Psi$  that the expectation value of the Hamiltonian will be minimal. The ground state energy is uniquely defined by the external potential  $V(\vec{r}_i)$ , originating for example from positively charged nuclei, which is the only free input parameter. This can be written more explicitly as

$$E[V] = \min_{\Psi} \left[ \langle \Psi | K + W | \Psi \rangle + \int \rho(\vec{r}) V(\vec{r}) d^3\vec{r} \right], \quad (2.3)$$

where  $K$  is kinetic term,  $W$  is electron-electron interaction term of the Eq. 2.1, and  $\rho(\vec{r}) = e \langle \Psi(\vec{r}) | \Psi(\vec{r}) \rangle$ . One can see, that the partial derivative of the above equation is  $\rho(\vec{r}) = \partial E / \partial V(\vec{r})$ . Such derivative relation is encountered in the thermodynamics between the two conjugate variables, e.g., pressure and volume. The thermodynamic system can be uniquely determined by either of the two conjugate variables by means of the Legendre transform of the state functions. In the same way external potential  $[V(\vec{r}_i)]$  and the electron density  $[\rho(\vec{r}_i)]$  are interchangeable – conjugate variables – where each uniquely describes the many-body quantum system. This is known as the first Hohenberg-Kohn theorem [55]. Furthermore, Legendre transformation of the ground state energy can be written as a functional  $F[\rho] = E - \int V(\vec{r})\rho(\vec{r})d^3\vec{r}$  with electron density as the extensive variable. Another Legendre transform of  $F[\rho]$  is again the ground state energy written in variational form as

$$E[V] = \min_{\rho} \left[ F[\rho] + \int V(\vec{r})\rho(\vec{r})d^3\vec{r} \right], \quad (2.4)$$

which means that by finding the electron density that would minimize the right-hand side of Eq. 2.4 one would obtain the ground state energy of the system defined by  $V(\vec{r})$ . This is known as the second Hohenberg-Kohn theorem [53].

If the functional  $F[\rho]$  would be known, the problem could be solved exactly. Unfortunately, this is not the case. However, Kohn and Sham were still able to solve this problem by splitting  $F[\rho]$  into the known part, containing the non-interacting term  $T_0[\rho]$  and the classic electron-electron interaction term, and the unknown part denoted by the exchange-correlation functional  $E_{xc}[\rho]$  [53]

$$F[\rho] = T_0[\rho] + \frac{e^2}{4\pi\epsilon_0} \frac{1}{2} \int \frac{\rho(\vec{r})\rho(\vec{r}')}{|\vec{r} - \vec{r}'|} d^3\vec{r}d^3\vec{r}' + E_{xc}[\rho]. \quad (2.5)$$

To solve variational equation (Eq. 2.4) one would proceed by equating the derivative of the right-hand side of Eq. 2.4 with respect to  $\rho$  to chemical potential,  $\mu$ , a Lagrange multiplier to constrain the electron density by the number of electrons in the system

$$\frac{\delta T_0}{\delta \rho(\vec{r})} + \left[ \frac{e^2}{4\pi\epsilon_0} \int \frac{\rho(\vec{r}')}{|\vec{r} - \vec{r}'|} d^3\vec{r}' + \frac{\delta E_{xc}}{\delta \rho(\vec{r})} + V(\vec{r}) \right] = \mu. \quad (2.6)$$

For the non-interacting electron system the solution would be written by similar Eq. 2.6 where the square brackets contain only  $V(\vec{r})$ . However, in the case of interacting electrons the potential is generalized as it is written in the square brackets of Eq. 2.6 where all terms are a function of  $\vec{r}$ . This generalized potential can be expressed as  $v_{KS}[\rho](\vec{r})$ . Now, the interacting many-body system can be mapped to a number of single-electron systems with the same generalized potential  $[v_{KS}[\rho](\vec{r})]$ , which can be solved by single-electron Schrödinger equations [56]

$$\left( -\frac{\hbar^2}{2m} \nabla^2 + v_{KS}[\rho](\vec{r}) \right) \psi_u(\vec{r}) = \varepsilon_u \psi_u(\vec{r}), \quad \rho(\vec{r}) = \sum_u |\psi_u(\vec{r})|^2 \theta(\varepsilon_u - \mu). \quad (2.7)$$

Here  $\theta(\varepsilon)$  is a step function and  $\psi_u(\vec{r})$  are the so-called Kohn-Sham single-electron orbitals. Their number is equal to the number of electrons. Within the Hartree-Fock approximation for the many-body wavefunction these orbitals must fulfil the orthonormal condition  $\langle \psi_u | \psi_v \rangle = \delta_{u,v}$ . The Eqs. 2.7 are non-linear equations and are solved self-consistently by an iterative procedure.

The unknown exchange-correlation term can be calculated only approximately. The two most popular approximations are the *local density approximation* (LDA) and the *generalized gradient approximation* (GGA) [52]. LDA is based on the concept of the uniform electron gas where electrons move in a positively charged background distribution such that the total ensemble is held neutral. This approximation usually predicts exchange, ionization, and dissociation energies with an error of 10–20%. However, the bond lengths of molecules or solids are calculated well, i.e. within  $\sim 2\%$  accuracy [52]. This approximation usually fails in weakly correlated systems since their ground state is far from being similar to the uniform free electron gas system. The GGA additionally considers the gradient of the electron density to account for the non-homogeneity of the true electron-system. In this way the accuracy of the atomized energies is improved for small molecules by a factor of 3–5 compared to LDA [52]. However, low-order gradient expansion is also not sufficient to correctly describe correlated materials which have strongly varying electronic density.

It is surprising that DFT calculations have been relatively successful in describing  $A_3C_{60}$  systems. Having a narrow bandwidth and strong on-site Coulomb repulsion interaction these systems are expected to be correlated [5]. The bare electronic structure calculations obtained by DFT largely failed to describe the highly-expanded  $Cs_3C_{60}$  compounds that shows insulating behaviour despite having partially filled conduction band as shown by DFT calculations [13, 14, 54]. In the vicinity of MIT other theories taking into account strong electron-correlations have to be considered.

## 2.2 BCS and Migdal-Eliashberg Theory

Superconductivity is another many-body effect that cannot be explained by DFT. It was discovered in 1911 by H. K. Onnes and explained in 1956 by Bardeen, Cooper and Schrieffer who developed the first microscopic theory of superconductivity [10]. The BCS theory was for many years after the discovery one of the most successful and detailed quantum theory that was capable of explaining numerous experiments. Most of today known superconductors belong to this clan. Its limitations were first exposed with the discovery of the high-temperature cuprate superconductors in 1984 [57]. In standard BCS superconductors the superconductivity is driven by the phonon-mediating mechanism. The discovery of superconductivity in  $A_3C_{60}$  systems [9] was immediately followed by BCS theory explanation due to rich phonon spectra of  $C_{60}$  molecules. Until the discovery of  $Cs_3C_{60}$  BCS theory was able to explain some important properties, for instance an increase of  $T_c$  with increasing unit-cell volume or the superconducting ratio  $2\Delta/k_B T_c = 3.53$  [7]. However, indications of strong electron-electron correlations, which are found in all non-conventional high-temperature superconductors, cast some doubts about such a simple explanation. Therefore, the BCS theory of  $A_3C_{60}$  was extended to include also the electron correlations under the Migdal-Eliashberg theory. These two theories are presented next.

The central concept of the BCS theory is that at low enough temperatures the free electrons become attracted and form Cooper pairs. The pairs' bosonic nature allows them

to condensate, which yields the known superconducting properties. In the BCS theory the attraction between the electrons is mediated by the phonons. This attraction can be imagined in the following way. Locally, the electron's negative charge is compensated by the displacement of the positive ions towards the electron. Since the ionic dynamics is much slower than the electronic the ions will still be in a more dense arrangement after electron is long gone which creates an excess of positive charge. This charge attracts another electron and is responsible for the indirect electron attraction. In the other words, the electron initially in the state  $\vec{k}_1$  forms a phonon with momentum  $\vec{q}$  and ends up in state  $\vec{k}'_1$ . The created phonon interacts with another electron which goes from the initial state  $\vec{k}_2$  to the final state  $\vec{k}'_2$ . Since the phonon energy in a crystal cannot exceed Debye energy ( $\hbar\omega_D$ ) and the initial and final electron states has to be occupied and empty, respectively, the Cooper pairs will form only within a narrow belt of the width of  $\vec{q}_D = c/\omega_D$  ( $c$  is speed of sound in solid) near the Fermi surface. The maximal number of Cooper pairs is obtained for  $\vec{q} \rightarrow 0$  resulting in the Cooper pair state ( $\vec{k} \uparrow, -\vec{k} \downarrow$ ).

By adding an additional electron in the state  $\vec{k}$  the energy will increase to [58]  $E_{\vec{k}} = \sqrt{\varepsilon_{\vec{k}}^2 + \Delta_0^2}$ , where  $\varepsilon_{\vec{k}}$  is a non-interacting  $\vec{k}$ -state electron energy and  $\Delta_0$  is a measure of the attraction interaction. We can see that even for  $\varepsilon_{\vec{k}} = 0$  the added electron will be in a state separated from the ground state by the energy gap of  $\Delta_0$  [59]. The presence of the superconducting gap is central to the theory of superconductivity and it has been proposed by J. Bardeen even before the BCS theory. The superconducting gap has been extensively measured and observed in different materials including the unconventional superconductors [60]. The above relation of the elementary excitation energies of the quasiparticles provides another important BCS property – the BCS density of states. Density of state can be for BCS superconductors written as

$$\rho(E) = \frac{d\nu}{dE} = \frac{d\nu}{d\varepsilon} \frac{d\varepsilon}{dE} = N(0) \frac{E}{\sqrt{E^2 - \Delta_0^2}}, \quad (2.8)$$

where  $d\nu/dE$  is number of levels per energy interval and  $d\nu/d\varepsilon$  gives the density of states near the Fermi level for the non-interacting metal. The logarithmic divergence of the density of state at  $E = \Delta_0$  is characteristic for the BCS theory and it is responsible for one of the first experimental confirmation of the BCS theory, the observation of the H-S peak in NMR experiment. We shall come back to H-S peak in Sec. 3.3.5.

At elevated temperatures thermal fluctuations start to break the Cooper pairs. The reduced number of pairs that contribute to the energy of the collective ground state reduce the value of the superconducting gap which vanishes completely at the critical temperature  $T_c$ . Above this temperature the material behaves as a normal metal. The temperature dependent gap value is in the weak-coupling limit given by the gap function [58]

$$\frac{1}{N(0)\tilde{V}} = \int_0^{\hbar\omega_D} \frac{d\varepsilon}{\sqrt{\varepsilon^2 + \Delta^2(T)}} \tanh \frac{\sqrt{\varepsilon^2 + \Delta^2(T)}}{2k_B T}, \quad (2.9)$$

where  $\tilde{V}$  is indirect electron-electron interaction energy and  $k_B$  is Boltzmann constant. Using Eq. 2.9 we can express zero temperature gap function ( $\Delta_0$ ) and the critical temperature (defined as  $T$  where  $\Delta \rightarrow 0$ ) in the weak-coupling limit ( $\lambda = N(0)\tilde{V} < 0.3$ )

as

$$\Delta_0 = 2\hbar\omega_D \exp\left(-\frac{1}{\lambda}\right), \quad (2.10)$$

$$k_B T_c = 1.14\hbar\omega_D \exp\left(-\frac{1}{\lambda}\right). \quad (2.11)$$

One can see that the critical temperature and the zero temperature gap function are directly proportional. Eliminating the unknown  $\lambda$  we can write the superconducting ratio

$$\frac{2\Delta_0}{k_B T_c} = 3.53, \quad (2.12)$$

a value that is in good agreement with numerous experiments performed on the standard superconductors.

In the BCS theory the electron-electron Coulomb repulsion is neglected. This is a good approximation for normal metals where electron charge is screened due to strong delocalization. BCS theory is, therefore, derived in the limit of strong retardation effects where phonon energy is much lower than electron kinetic energy,  $\hbar\omega_D/E_F \ll 1$ . Furthermore, the assumption that only electrons in the narrow band around Fermi level form Cooper pairs with the width of  $\sim\Delta_0$  inherently treats the electron-phonon interaction in the weak-coupling limit, which can be expressed as  $\lambda \ll 1$  or  $k_B T_c/\hbar\omega_{\text{ln}} \ll 1$  [58], where  $\omega_{\text{ln}}$  is the logarithmic average of phonon spectrum or roughly the frequency of phonons participating in the Cooper pair formation.

In the intermediate and strong coupling regimes the electrons forming Cooper pairs are not any more limited to the narrow band, but rather come from a much broader region. The extended BCS theory that takes this into an account and additionally include the electron-electron Coulomb interaction and the full frequency-dependent electron-phonon coupling is called the *Migdal-Eliashberg theory* (ME) [61]. The main assumptions that are incorporated in the ME theory are the Migdal's theorem, which states that the if  $\hbar\omega_D/E_F \ll 1$ , then the electron-phonon interaction can be expressed by the simplest diagram in the diagrammatic expansion, and that the Coulomb repulsion can be described by a phenomenological parameter  $\mu^*$ . Within this theory the critical temperature is given by McMillan formula [5],

$$k_B T_c = \frac{\hbar\omega_{\text{ln}}}{1.2} \exp\left[\frac{-1.04(1+\lambda)}{\lambda - \mu^*(1+0.62\lambda)}\right], \quad (2.13)$$

where  $\mu^*$  is renormalized Coulomb parameter  $\mu = N(0)U$  with  $U$  being the Coulomb repulsion energy. Renormalization of  $\mu$  comes from the fact that the electronic energy scale, is much larger than the phonon energy scale which allows to project out the states that are much further away from the Fermi level than the phonon energy. The renormalization is expressed as

$$\mu^* = \frac{\mu}{1 + \mu \log(B/\hbar\omega_{\text{ph}})}. \quad (2.14)$$

Here  $B$  is a typical maximal electronic energy (e.g. half the bandwidth) above which the screening of the Coulomb repulsion is not effective and  $\omega_{\text{ph}}$  is typical phonon frequency. For large values of  $B$  the above expression becomes  $\mu^* \approx 1/\log(B/\hbar\omega_{\text{ph}})$  which is independent of  $\mu$ . This can be found in standard superconductors where  $B/\hbar\omega_{\text{ph}} = 1000$  yielding a small  $\mu^*$  of the order of  $\mu^* = 0.1$  [5]. In general, the parameter  $\mu^*$  works against phonon pairing and therefore always reduces  $T_c$ .

Another important result of the ME theory is the approximate analytical formula for the superconducting ratio in the intermediate and strong coupling regimes where a single parameter,  $T_c/\omega_{\text{ln}}$ , measures the coupling strength [61]

$$\frac{2\Delta_0}{k_{\text{B}}T_c} = 3.53 \left[ 1 + 12.5 \left( \frac{k_{\text{B}}T_c}{\hbar\omega_{\text{ln}}} \right)^2 \ln \left( \frac{\hbar\omega_{\text{ln}}}{2k_{\text{B}}T_c} \right) \right] \quad (2.15)$$

The numerical factors 12.5 and 2 could not be correctly obtained from the theory. For this reason a collection of experimental superconducting ratios from various standard BCS superconductors have been used to determine the parameters by least square fitting method [61].

The BCS and the Migdal-Eliashberg theories have been extensively used to explain superconductivity of the under-expanded fullerene superconductors [5, 25]. The explanations were relatively successful despite several oversimplifications not justified for fullerenes: (i) the Migdal's theorem works only for negligible phonon energies compared to the electron energies. In fullerenes the intramolecular phonon energies, which are believed to be participating in the superconducting mechanism are ( $\sim 0.1$  eV) of the same order of magnitude as the typical electron hopping energy (0.5 eV). (ii) Strong retardation effects, required for the BCS theory, and necessary to reduce effective Coulomb parameter in ME theory are in fullerene superconductors most probably not present. On the other hand, the Coulomb repulsion energy for the two electrons on the same  $\text{C}_{60}$  molecule is  $\sim 1$  eV. Without retardation effects critical temperature is according to Eq. 2.13 reduced to practically zero, which is not in agreement with experimental observations [5, 25]. Such arguments have been to some extent met with the possibility of other low laying phonon modes participating in the pairing mechanism and that the electron's kinetic energy scale should be much higher, as is found inside  $\text{C}_{60}$  molecule. Other arguments being against BCS and ME theories are that highly structured density of states due to narrow electronic bands, strong electron correlations, and the Jahn-Teller effect are not treated correctly [5]. Such considerations have cast doubts on the ME theory and inspired researcher to search for a new theories.

## 2.3 Dynamical Mean Field Theory

Strong electron correlations and comparable phonon energy scale to that of the bandwidth and the Coulomb repulsion require in  $A_3\text{C}_{60}$  a different approach. The model that considers these elements is based on a three-band Hubbard model with half-filling case [62]. Such model correspond to  $\text{C}_{60}$  molecules with  $t_{1u}$  threefold-degenerate lower unoccupied orbitals (LUMO) filled with  $n = 3$  electrons. On each site, electrons repel each other due to Coulomb interaction  $U \sim 1$  eV. The term describing on-site Coulomb interaction is written as [62]

$$\mathcal{H}_U = \frac{U}{2}(n - 3)^2, \quad (2.16)$$

where  $n = c^\dagger c$  is the number operator, which corresponds to the number of  $t_{1u}$  electrons on a  $\text{C}_{60}$  molecule. This term is the Hubbard term written in alternative form [62]. In addition to the Coulomb repulsion interaction electrons on each molecular site experience a weaker interorbital Hund's rule exchange coupling,  $J_{\text{H}}$ . Due to the full rotational orbital symmetry this term is written as [62]

$$\mathcal{H}_J = J \left( 2\vec{S} \cdot \vec{S} + \frac{1}{2}\vec{L} \cdot \vec{L} \right) + \frac{5}{6}J(n - 3)^2, \quad (2.17)$$

where  $J = -J_H < 0$ , and  $\vec{S}$  and  $\vec{L}$  are spin and orbital angular momentum operators. We note, that Hund's rule exchange favours high spin and high orbital momentum state. In this theory the electron-phonon interaction is treated with the JT coupling of the electrons in the  $t_{1u}$  orbitals to the  $C_{60} H_g$  intramolecular vibrations. The JT effect splits the  $t_{1u}$  orbital degeneracy and thus favours the low-spin state. The JT effect opposes the Hund's rule exchange. To rigorously treat JT coupling one has to consider the full carbon dynamics in  $C_{60}$  molecules. However, due to strong electron correlations close to the Mott transition the renormalized coherent bandwidth ( $W \rightarrow ZW$ ,  $Z \ll 1$ ) can become smaller than the phonon energies. In this antiadiabatic limit the carbon dynamics can be integrated out yielding an unretarded effective JT interaction with the same form as the Hunds' rule exchange, but with an opposite sign of  $J$ . In this limit the JT effect and the Hund's rule exchange can both be written by Eq. 2.17 with  $J = -J_H + J_{JT}$ .

Such a model with many-body on-site interactions and weak intermolecular coupling is ideally suited to be solved with the *dynamical mean field theory* (DMFT) [63]. DMFT is quantum mechanical equivalent to the classical mean field theory where on the expense of the spatial fluctuations the local dynamics can be obtained exactly. The mean field approximation is obtained by mapping the lattice model to the Anderson impurity model (AIM) embedded into a free-electron Fermi bath [63]. The bath is then determined self-consistently. The AIM for the fullerene system has the following form

$$\mathcal{H} = \mathcal{H}_U + \mathcal{H}_J + \sum_{kl} \varepsilon_{kl} a_{kl}^\dagger a_{kl} + \sum_{kl} V_{kl} (c^\dagger a_{kl} + \text{h.c.}), \quad (2.18)$$

where  $\varepsilon_{kl}$  are the bath fermion energy levels labelled by index  $k$  and an orbital index  $l = x, y, z$  and  $V_{kl}$  are the coupling parameters between the bath fermions ( $a_{kl}^\dagger$ ) and impurity fermions ( $c^\dagger$ ). In the above equation  $a_{kl}^\dagger$  and  $c^\dagger$  are creation and  $a_{kl}$  and  $c$  are annihilation operators.

The single particle properties, like energy eigenvalues, can be calculated either by solving Hamiltonian or with a single particle correlation function (Green's function). The later approach is used in DMFT in order to self-consistently determine the unknown bath energies ( $\varepsilon_{kl}$ ) and coupling constants ( $V_{kl}$ ). First the Hamiltonian (Eq. 2.18) is solved using initial guessed values for  $\varepsilon_{kl}$  and  $V_{kl}$ . Authors of the DMFT for fullerene superconductors used exact diagonalization technique for solving AIM [62]. After the Hamiltonian is solved the obtained solution is used to compute the interacting local Green's function,  $G_a(i\omega_n) = -\langle c^\dagger(i\omega_n)c(i\omega_n) \rangle$ , where  $i\omega_n$  are discrete Matsubara frequencies [64].

To obtain the unknown parameters one needs to consider a representation of the local Green's function corresponding to AIM. Such a representation can be obtained by minimizing the effective action of the impurity orbitals [64]. The obtained representation has the following form [63]

$$\mathcal{G}_{0a}^{-1}(i\omega_n) = (i\omega_n + \mu) - \sum_k \frac{V_{ka}^2}{i\omega_n - \varepsilon_{ka}}, \quad (2.19)$$

where  $\mu$  is the chemical potential. This AIM representation of the Green's function can also be considered as a generalization of the Weiss field of the classical mean field approximation (MFA) theory. Similar to the classical MFA theory,  $\mathcal{G}_{0a}(i\omega_n)$  and  $G_a(i\omega_n)$ , the later plays the role of observable magnetization, are related by the self consistency condition. Since the isolated  $t_{1u}$ -derived band can be effectively approximated by a semicircular density of states [62], the self-consistency condition can be simplified to the form

$$\mathcal{G}_{0a}^{-1}(i\omega_n) = (i\omega_n + \mu) - t^2 G_a(i\omega_n). \quad (2.20)$$

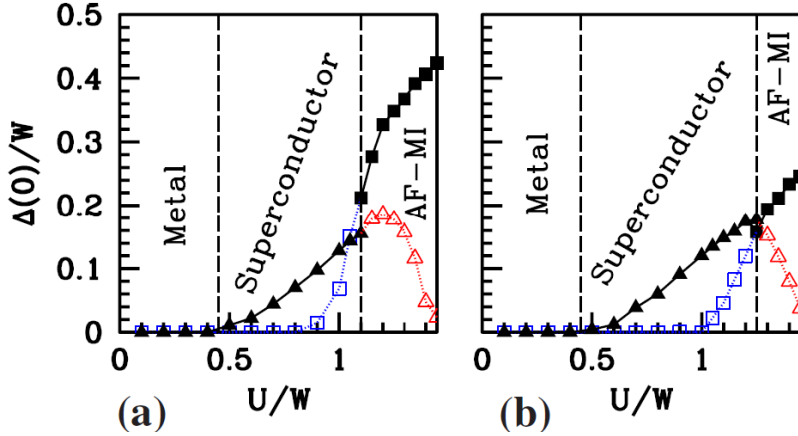


Figure 2.1: Phase diagram of  $A_3C_{60}$  computed by DMFT. The superconducting (triangles) and the antiferromagnetic order parameter (squares) as a function of  $U/W$ . DMFT gives the first order phase transition at the MIT. In (a) no frustration has been introduced and in (b) a moderate frustration was introduced in the model. The superconducting phase in the vicinity of MIT is called strongly correlated superconductivity and cannot be obtained by standard BCS theory. Adapted from [62].

In the above expression  $t = W/4$  is a quarter of the bandwidth. The new Weiss field  $[\mathcal{G}_{0a}(i\omega_n)]$ , obtained by Eq. 2.20, is then approximated with AIM representation (Eq. 2.19) by the least square fitting method. The resulting fitting parameters  $\varepsilon_{ka}$  and  $V_{ka}$  are used in the next iteration when solving Hamiltonian (Eq. 2.18). DMFT self-consistency iteration is repeated until the the old and new Weiss fields become acceptably similar.

The above description of the DMFT theory is suitable for the paramagnetic case where no symmetry is broken. To obtain superconducting or antiferromagnetic solutions the authors implicitly broke the symmetry by using Nambu-Gor'kov spinor representation for the superconducting case and spinor representation of a bipartite lattice for antiferromagnetic state [62]. In this way they were able to obtain the superconducting and the antiferromagnetic order parameters separately as a function of temperature and  $U/W$  (Fig. 2.1). In case of phase coexistence the stable phase was subsequently determined by calculation of the total energy. They found that for small effective  $J$  (comparable to the experimental values  $J \sim 100$  meV) besides a small BCS-like superconducting region near  $U/W = 0$  a dome-shaped superconducting region appears near the Mott transition ( $U/W \sim 1.5$  in DMFT). In addition, they also found a coexistence of the superconducting and the antiferromagnetic phases and first order phase transition between the two at the MIT. Interestingly, the superconducting ratio  $2\Delta/k_B T_c$  was found to have BCS value over a large  $U/W$  interval, signalling weak-coupling case, however, close to the Mott transition the ratio increases and reaches up to cca. 5, indicating a crossover to the strong coupling regime as will be presented in Sec. 8.3. Despite having strong limitations concerning the spatial degrees of freedom, DMFT theory currently provides the best description of the  $A_3C_{60}$  experimental results.

# 3 Experimental methods

In this section we describe all the experimental techniques used in the study of the triply-doped fullerenes. Since we will be concerned with the magnetic, structural, electronic, and superconducting local properties our central techniques will be the magnetic resonance techniques, namely the nuclear magnetic resonance (NMR) and the electron paramagnetic resonance (EPR). This chapter will begin with a description of the general theory of the magnetic resonance and followed by a discussion of each technique in more details. In the end we will present high-pressure NMR and EPR cells developed during the thesis.

## 3.1 General Theory of Magnetic Resonance Absorption

Magnetic resonance techniques are based on an interaction between the applied electromagnetic waves and the magnetic moments of a material in an external magnetic field. In the classical picture one can explain magnetic resonance as the precession of the magnetic moments in the external magnetic field. The moment's dynamics is expressed by the precession equation written as

$$\frac{d\vec{\mu}}{dt} = \vec{\omega}_L \times \vec{\mu}, \quad \omega_L = \gamma B_0. \quad (3.1)$$

In this equation  $\vec{\mu}$  is magnetic moment,  $\gamma$  is gyromagnetic ratio,  $B_0$  is the external magnetic field, and  $\omega_L$  is the Larmor precession frequency. The gyromagnetic ratio is proportional to the magnetic moment ( $\hbar\gamma_\alpha = g_\alpha\mu_\alpha$ ) coming either from electron, almost any type of nucleus, or even the muon.

In quantum picture the magnetic field splits the energy levels of magnetic moments, the so-called Zeeman splitting, and when the energy of applied electromagnetic waves equal the splitting between the two levels electromagnetic waves can get absorbed by causing a transition between these levels. In other words, an applied electromagnetic wave would trigger a resonant response if its frequency would match the Larmor frequency. In an ideal case when nuclear moments are isolated from the environment the electromagnetic wave energy absorption would be expressed as a Dirac delta function at  $\omega_L$  on a frequency axis. However, in the real systems the local interactions affect the resonant frequency and broaden the resonance lines. By measuring the absorption spectra a detailed information about the electronic and magnetic environment of magnetic moments can be obtained.

The complete quantum mechanical description of the magnetic resonance absorption was paved by R. Kubo and K. Tomita in 1954 [65]. Their general theory of magnetic

resonance absorption is in principle a linear response theory of a magnetic moment,  $\vec{M} = \hbar\gamma \sum_i \vec{S}_i$ , perturbed by the linearly polarized harmonic magnetic field  $\vec{B}_1(t) = B_1 \cos(\omega t)$ . A starting point of their theory is a spin Hamiltonian,  $\mathcal{H} = \mathcal{H}_0 + \mathcal{H}'$ , where the terms commuting with the spin operator,  $\mathcal{H}_0$ , and the non-commuting terms,  $\mathcal{H}'$ , containing magnetically anisotropic terms like dipolar interaction are separated. The later term is normally much smaller and is thus treated as a perturbation.

Magnetic resonance experiments measure the energy absorption of electromagnetic waves in the sample. In magnetic experiments the sample is placed where the standing electromagnetic wave has a maximum magnetic field component. In order to derive the absorption of energy we assume that spin susceptibility [ $\chi(\omega) = \chi'(\omega) + i\chi''(\omega)$ ] is uniform across the sample and that the sample is perturbed by harmonically oscillating applied magnetic field ( $\vec{B}(t) = \vec{B}e^{i\omega t}$ ). The real part of the response of the magnetization in such field is expressed as

$$\vec{M}(t) = \frac{\vec{B}}{\mu_0} [\chi'(\omega) \cos \omega t - \chi''(\omega) \sin \omega t]. \quad (3.2)$$

The dissipated energy of the magnetic system is the averaged change of energy ( $dE = V \vec{B} \cdot d\vec{M}$ ) per unit time.  $V$  is the sample volume. Taking only the real part we arrive at

$$P = \frac{\overline{dE}}{dt} = V \frac{\overline{\vec{B} \cdot d\vec{M}}}{dt} = -\omega V \frac{B^2}{\mu_0} [\overline{\chi'(\omega) \sin \omega t \cos \omega t} + \overline{\chi''(\omega) \cos^2 \omega t}]. \quad (3.3)$$

The average over one time period will cancel the first term. Using  $\overline{\cos^2 \omega t} = 1/2$  the dissipated power is equal to

$$P(\omega) = -\frac{1}{2} \omega V \frac{B^2}{\mu_0} \chi''(\omega). \quad (3.4)$$

The measured magnetic resonance spectrum is, therefore, proportional to the dynamic spin susceptibility of the sample.

Next, we will show how the dynamic spin susceptibility and the measured spectrum can be calculated. In the limit where thermal fluctuation energy is much larger than the magnetic moment's level splitting, the energy absorption spectrum given by the imaginary part of dynamic magnetic susceptibility [ $\chi''(\omega)$ ] can be expressed as

$$\chi''(\omega) = \frac{\omega V}{2k_B T} \int_{-\infty}^{\infty} \langle M^x(t) M^x(0) \rangle e^{-i\omega t} dt. \quad (3.5)$$

Here  $V$  is the sample volume,  $k_B$  is the Boltzmann constant,  $T$  is temperature, and  $\langle \rangle$  represent ensemble averaging. Assuming that the external static field is along the  $z$ -axis the energy absorption spectrum is given by the thermally averaged fluctuations of the transverse magnetic moment. This is a direct result of the fluctuation-dissipation theorem [66]. Eq. 3.5 could be rewritten by going into the interaction picture where components of the magnetic moment operator transform as  $\widetilde{M}(t) = e^{-i\mathcal{H}_0 t} M(t) e^{i\mathcal{H}_0 t}$ . Using raising and lowering operators,  $M^\pm = M^x \pm iM^y$ , and taking into account  $\langle M^\pm(t) M^\pm \rangle = 0$ , the absorption spectrum is then written as

$$\chi''(\omega) = \frac{\omega V}{8k_B T} \int_{-\infty}^{\infty} \left( \langle \widetilde{M}^+(t) M^-(0) \rangle e^{-i(\omega - \omega_L)t} + \langle \widetilde{M}^-(t) M^+(0) \rangle e^{-i(\omega + \omega_L)t} \right) dt. \quad (3.6)$$

We can see that the absorption spectrum is peaked at  $\omega = \pm \omega_L$ . In case there is no magnetic anisotropy ( $\mathcal{H}' = 0$ ) all the terms in Hamiltonian commute with the spin operator. This leads to a time-independent correlation function (angle brackets in Eq. 3.6)

and finally in the spectrum consisting of two Dirac delta functions at  $\pm\omega_L$ . The resonance linewidth and the lineshape in general are related to the time dependence of the correlation function  $\langle \widetilde{M}^+(t)M^-(0) \rangle$ . In practice, linewidths are much smaller than the Larmor frequency, and therefore the negative frequency term can be omitted. In this approximation the normalized magnetic resonance lineshape is expressed as a Fourier transform of the magnetization relaxation function  $\phi(t)$  obtained from Eq. 3.6

$$I(\omega) = \int_{-\infty}^{\infty} \phi(t) e^{-i(\omega - \omega_L)t} dt, \quad \phi(t) = \frac{\langle \widetilde{M}^+(t)M^-(0) \rangle}{\langle M^+M^- \rangle}. \quad (3.7)$$

In the case of random Gaussian processes the magnetic moment relaxation function can be approximated by [65]

$$\phi(t) = \exp \left( - \int_0^t (t - \tau) \psi(\tau) d\tau \right), \quad (3.8)$$

where spin correlation function is given by

$$\psi(\tau) = \frac{\langle [\widetilde{H}'(\tau), M^+(0)][M^-(0), \widetilde{H}'(0)] \rangle}{\hbar^2 \langle M^+M^- \rangle}. \quad (3.9)$$

In this expression square brackets  $[A, B]$  denote commutator of the operators  $A$  and  $B$ . The correlation function can be further approximated with a Gaussian function,  $\psi(\tau) = \psi(0) \exp(-\tau^2/2\tau_c^2)$ , where  $\tau_c$  is the spin correlation time. The lineshape, therefore, strongly depends on the spin correlation time. In the limit of large correlation times ( $\tau_c \gg t$ ), which is commonly the case in NMR, the correlation function decays so slowly that it can be approximated by a constant. The relaxation function thus becomes a Gaussian function

$$\phi(t) \approx \exp \left( -\psi(0) \int_0^t (t - \tau) d\tau \right) = \exp \left( -\frac{\psi(0)}{2} t^2 \right). \quad (3.10)$$

and the lineshape is also a Gaussian function with the linewidth or the second moment equal to

$$M_2 = \hbar^2 \psi(0) = \frac{\langle [H', M^+][M^-, H'] \rangle}{\langle M^+M^- \rangle}. \quad (3.11)$$

In other limiting case where correlation times are small ( $\tau_c \ll t$ ), for example due to large exchange coupling constant with respect to the linewidth usually encountered in the EPR, the integral in Eq. 3.8 is evaluated at very long times where the relaxation function has an exponential behaviour,

$$\phi(t) \approx \exp \left( -\psi(0) \int_0^\infty (t - \tau) e^{-\frac{\tau^2}{2\tau_c^2}} d\tau \right) = \exp \left( -\sqrt{\frac{\pi}{2}} \psi(0) \tau_c t \right). \quad (3.12)$$

The spectral profile in this limit is a Lorentzian function with a linewidth,  $\Delta\omega \propto M_2/J$ , where  $J = h/\tau_c$  is an exchange coupling constant. The linewidth of the spectral function decreases with increasing exchange constant, which is known as the *exchange narrowing* of the resonant lines [67].

## 3.2 Electron Paramagnetic Resonance

In the unpaired electron spin resonance the magnetic moments originate from the localized or itinerant electrons. This technique can be applied to study the paramagnetic compounds containing atoms with incomplete electronic shells, e.g. the transition metal compounds, ordinary metals, magnetically ordered systems, insulating materials with paramagnetic imperfections, or in organic salts where electrons are transferred to the organic molecule where they stay unpaired, e.g. poly-aromatic hydrocarbons or fullerenes [67]. Besides the resonance of the individual moments the magnetic absorption is possible also on the collective states in the antiferromagnetic or ferromagnetic ordered phases, the so-called antiferromagnetic and ferromagnetic resonance (AFMR and FMR). When the collective resonances are not present the spin resonance absorption is limited to the paramagnetic species and it is thus called the *electron paramagnetic resonance* (EPR).

### 3.2.1 Spin Hamiltonian

The interaction of the electron spin with its environment is described by an electron spin Hamiltonian. Apart from the rare-earth elements in majority of other elements the unfilled orbitals are in the outer shells. For this reason the electrons in the solid state materials interact relatively strongly with the crystal field due to surrounding electrostatic potential or covalent bonds. This causes a splitting of the degenerate orbital degrees of freedom and consequently "quench" the electron's orbital angular momentum,  $\langle L_z \rangle = 0$ , leaving the spin angular momentum as the only origin of the electronic magnetic moment [68]. In addition, the electron spin and the orbital momentum interact by a spin-orbit or LS-coupling, written as  $\mathcal{H}_{LS} = \lambda \vec{L} \cdot \vec{S}$ . Although, in amplitude the LS-coupling is smaller than the crystal-field effects it still perturbs the total Hamiltonian which results in a small amount of previously quenched orbital angular momentum mixed to the total electron's angular momentum. The total magnetic moment, which is proportional to the total angular momentum, interacts with an external magnetic field through a Zeeman interaction written as  $\mathcal{H}_Z = \mu_B (g_0 \vec{S} + \vec{L}) \cdot \vec{B}$ , where  $\mu_B$  is Bohr magneton and  $g_0$  is the free electron  $g$ -factor,  $g_0 = 2.0023$ . Considering both the LS-coupling and the Zeeman interaction as a perturbation to the ground state determined by the crystal field, one can write an *effective spin Hamiltonian* as [68]

$$\mathcal{H}_s = \sum_{\mu,\nu} g_0 \mu_B B_\mu (\delta_{\mu,\nu} - \lambda \Lambda_{\mu,\nu}) S_\nu - \lambda^2 S_\mu \Lambda_{\mu,\nu} S_\nu, \quad (3.13)$$

where we have omitted a spin-independent diamagnetic term. In this expression  $\mu$  and  $\nu$  are Cartesian components and the tensor  $\Lambda_{\mu,\nu}$  is defined as

$$\Lambda_{\mu,\nu} = \sum_n \frac{\langle 0 | L_\mu | n \rangle \langle n | L_\nu | 0 \rangle}{E_n - E_0}. \quad (3.14)$$

Here the sum runs over all the excited states corresponding to a given shell. We note that the orbital angular momentum degrees of freedom are integrated out of the wavefunction and thus only spin operator  $\vec{S}$  remains in Eq. 3.13. The first term in the effective spin Hamiltonian (Eq. 3.13) is the Zeeman term with an anisotropic  $g$ -factor tensor,  $g_{\mu,\nu} = g_0 (\delta_{\mu,\nu} - \lambda \Lambda_{\mu,\nu})$ . In a compact form it can be written as

$$\mathcal{H}_Z = \mu_B \vec{S} \cdot \overleftrightarrow{g} \cdot \vec{B}. \quad (3.15)$$

The second term is the single-ion anisotropy term which represents energy anisotropy of a spin direction. In the local frame, where it has a diagonal form, this term can be written as

$$\mathcal{H}_{\text{cf}} = D_{\text{cf}}S_z^2 + E_{\text{cf}}(S_x^2 - S_y^2), \quad (3.16)$$

where parameters  $D_{\text{cf}}$  and  $E_{\text{cf}}$  are related to the principal values of  $\Lambda$  tensor [68]. We note that for a spin system with  $S = 1/2$  single ion anisotropy has no effect as both states ( $S_z = \pm 1/2$ ) have the same energy.

Besides the Zeeman term another dominant interaction, present in the magnetic solids, is the *exchange interaction* between the spin magnetic moments,

$$\mathcal{H}_{\text{ex}} = \sum_{(i,j)} J_{ij}^{\alpha\beta} S_i^\alpha S_j^\beta, \quad (3.17)$$

where the summation runs over all spin pairs  $(i, j)$  and  $\alpha$  and  $\beta$  represent  $x$ ,  $y$ , and  $z$ . Several magnetic mechanism can be expressed with this expression: (1) the direct exchange interaction coming from the quantum exchange term of the Coulomb interaction favouring the parallel spin or the ferromagnetic alignment; (2) the kinetic exchange interaction found in the Mott-insulators and comes from the second order perturbation of the Hubbard model, favouring antiferromagnetic spin alignment [69], and (3) the indirect or super-exchange interaction, that is mediated by the bridging anion's electrons. This interaction varies not only with the distance, but also with their relative position. When exchange is mediated by itinerant electrons the phenomenon is called RKKY exchange interaction [70]. In solid state materials studied by EPR the isotropic exchange interaction is very common and is together with the Zeeman term a part of  $\mathcal{H}_0$  since both commute with the spin operator. This means that isotropic exchange interaction (Eq. 3.17) does not broaden the spectrum linewidth. Nevertheless, it sets the spin correlation time ( $1/\tau_c \propto \omega_e \propto J$ ) of the spin correlation function (Eq. 3.9) and accordingly causes the exchange narrowing of the spectral lines. For this reason most of the EPR spectra have Lorentzian shape.

An anisotropic interaction commonly observed in the solid state materials is the dipolar interaction between the magnetic moments. It is written as

$$\mathcal{H}_{\text{dd}} = \sum_{i \neq j} \frac{\mu_0}{4\pi} \gamma_e^2 \hbar^2 \left[ 3 \frac{(\vec{S}_i \cdot \vec{r})(\vec{S}_j \cdot \vec{r})}{r^5} - \frac{\vec{S}_i \cdot \vec{S}_j}{r^3} \right], \quad (3.18)$$

where  $\gamma_e$  is the electron gyromagnetic ratio and  $\vec{r}$  is the spatial vector connecting the two spins. As we have shown before the anisotropic terms do not change the absorption line position, but rather contribute to the spectral linewidth. In general, there are more anisotropic interaction that can be considered in the electron spin Hamiltonian e.g. anisotropic exchange interaction or Dzyaloshinsky-Moriya interaction [71], however, since these are not encountered in the fullerene superconductors we will not discuss them further.

The hyperfine interaction between the electron spins and the nuclear magnetic moments is usually negligible in magnetically dense systems and will thus not be further examined.

### 3.2.2 Moment Analysis and EPR Linewidth

The origin of the linewidth is the anisotropic part of the spin Hamiltonian, which does not commute with the spin operator. We have shown before that due to short spin

correlation time the EPR lineshape is best approximated by a Lorentzian function with the linewidth proportional to  $M_2/J$ . A more accurate estimation of the linewidth could be obtained by the moment analysis [72]. Doing an inverse Fourier transform of Eq. 3.7 and taking the even  $2k$ -th derivative one obtains the expression for  $2k$ -th moment of the spectral function [68]

$$\langle \omega^{2k} \rangle = \frac{\int \omega^{2k} I(\omega) d\omega}{\int I(\omega) d\omega} = (-1)^k \frac{\langle [[\mathcal{H}, [\mathcal{H}, \dots [\mathcal{H}, S^+] \dots]]^2 \rangle}{\langle S^+ S^- \rangle}, \quad (3.19)$$

where  $\mathcal{H}$  is the total spin Hamiltonian and  $S^\pm = \sum_i S_i^\pm$  and "... " denotes  $k$ -th repetition of the commutator.

We note that the zero-th order or the integral over the spectral shape is proportional to the static electron spin susceptibility,  $\chi_s$ . This can be shown by the Kramers-Kronig relation where  $\chi'_s(0) = \int \chi''_s(\omega)/\omega d\omega$ . In the case of narrow bandwidth compared to  $\omega_L$ , a condition fulfilled in all practical examples, the static spin susceptibility is proportional to the integral of the absorption spectrum  $\chi'_s(0) = 1/\omega_L \int \chi''_s(\omega)/d\omega$ .

In order to obtain second moment of the spectral line relative to the resonant frequency, it is useful to subtract the isotropic Zeeman term from  $\mathcal{H}$ . Due to a symmetric shape of the resonant absorption lines all odd spectral moment are equal to zero. Much better estimation of the linewidth can be obtained by considering up to the fourth spectral moment. The linewidth defined as the with full width at half maximum (fwhm) can be obtained by [72]

$$\Delta\omega_{\text{fwhm}} = C \sqrt{\frac{M_2^3}{M_4}}, \quad (3.20)$$

where a numerical constant  $C$  is not strictly determined as  $M_2$  and  $M_4$  both diverge in case of Lorentzian lines. For this reason it is necessary to artificially suppress the spectral tails. This is to some extent reasonable since the strong exchange coupling limit is valid only up to  $\sim\omega_e$ . One possibility to avoid this problem is to examine the cut-off Lorentzian function at arbitrary cut-off value. The calculated constant  $C = \pi/3$  is in this case independent of the exact cut-off value. Other possibilities are to use Gaussian or exponential window functions with a characteristic width of  $\omega_e$ . In these two cases the constants are  $C = 2\sqrt{\pi/6}$  and  $C = 2\pi/\sqrt{6}$  for Gaussian and exponential functions, respectively [72]. For systems where localized spins are coupled by dipolar and strong isotropic exchange interaction (e.g. Mott-insulating alkali-doped fullerenes) the second and the fourth moments are expressed as [73]

$$M_2 = \frac{1}{3} S(S+1) \sum_k B_{jk}^2 = \frac{1}{4} \sum_k B_{jk}^2, \quad (3.21)$$

$$M_4 = \frac{2}{N} \sum_{k,l;k \neq l \neq j} J_{jk}^2 (B_{jl} - B_{kl})^2 + J_{jk} J_{kl} (B_{jl} - B_{jk})(B_{jl} - B_{kl}), \quad (3.22)$$

where  $N$  is number of sites and term  $B_{jk}$  is written as

$$B_{jk} = \frac{3g^2\mu_B^2}{r_{jk}^3} \left( \frac{3\cos^2\theta_{jk} - 1}{2} \right). \quad (3.23)$$

Here  $r_{jk}$  correspond to the distance between  $j$ -th and  $k$ -th spin and  $\theta_{jk}$  is angle between external magnetic field and the line connecting  $j$ -th and  $k$ -th spin. In the special case of equivalent exchange coupling constants between different pairs the linewidth becomes

$$\Delta\omega \propto \frac{M_2}{J}. \quad (3.24)$$

We note that in the EPR experiments presented in this thesis the irradiated microwave frequency was fixed and the external magnetic field was swept. This does not change the above discussion and results. To transform expressions from the frequency to the magnetic field axis the relation  $\hbar\Delta\omega = g\mu_B\Delta B_0$  has to be applied.

### 3.3 Nuclear Magnetic Resonance

Nuclear magnetic resonance (NMR) is another local probe technique, which has been widely used to study structural, magnetic and electronic properties of the materials. The versatile and non-invasive attributes have made NMR widely spread and popular technique also outside physics community, especially in the field of chemistry, biology, and medicine [74]. From the physics point of view NMR is particularly useful since it can measure almost any material at different local sites in the unit-cell corresponding to different nuclei. The technique measures the response of the material in the external magnetic field after the irradiation with the radio-frequency (RF) electromagnetic waves. Radio frequencies (of the order of 100 MHz) and relatively slow nuclear spin dynamics<sup>1</sup> allow the use of the RF pulse techniques which can provide more information of the studied material. For example, pulsed sequences allow to measure directly the spin-lattice and spin-spin relaxation times and various correlation effects [67]. As in all magnetic resonance techniques, the Larmor precession frequency ( $\nu_L$ ) is proportional to the Zeeman splitting of the magnetic moment states written as

$$\Delta E = h\nu_L = \hbar\gamma_n B_0, \quad (3.25)$$

where  $\gamma_n$  is the nuclear gyromagnetic ratio and  $B_0$  is the external magnetic field. The evolution of nuclear dynamics is dominated by the Zeeman interaction with the external magnetic field. The information about the local physical properties come from a weaker interaction with the nuclear environment, e.g., dipolar, hyperfine, or quadrupole interaction.

#### 3.3.1 The nuclear spin Hamiltonian and NMR lineshifts

The absorption of the RF pulses and the response of the system is described by the nuclear spin Hamiltonian. In the external magnetic field the full Hamiltonian of the individual nuclear spin ( $I$ ) in solid is written as sum of Zeeman, dipolar, hyperfine, and quadrupole interaction terms [67]

$$\mathcal{H} = \mathcal{H}_{\text{Zeeman}} + \mathcal{H}_{\text{dipolar}} + \mathcal{H}_{\text{hf}} + \mathcal{H}_{\text{Q}}. \quad (3.26)$$

The dominating term is the Zeeman interaction between the nuclear spin ( $I$ ) and the external magnetic field ( $B_0$ )

$$\mathcal{H}_{\text{Zeeman}} = -\gamma_n \hbar \vec{I} \cdot \vec{B}_0. \quad (3.27)$$

The strong static external field will be in what follows aligned along  $z$ -axis (quantisation axis). The Zeeman energy for a nucleus in  $|I, m\rangle$  state, where  $m$  is a spin projection on the quantisation axis, is thus  $E_m = -\gamma_n \hbar B_0 m$ . Transitions between different nuclear states come from the interaction with the RF alternating magnetic field ( $\vec{B}_1$ ) perpendicular

---

<sup>1</sup>Nuclear spin dynamics is relatively slow due to weak interaction between the nuclear spin and the magnetic and electronic system.

to the external static magnetic field produced in the coil surrounding the sample. The perturbation term is written as

$$\mathcal{H}_{\text{pert}} \propto \gamma_n \vec{B}_1 \cdot \vec{I}_x \cos(\omega_c t), \quad (3.28)$$

where  $\omega_c$  is the frequency of the RF pulse. The probability for the transition between nuclear states is written as

$$W_{m,m'} \propto |\langle m | I_x | m' \rangle|^2 = \frac{1}{2} |\langle m | I_+ + I_- | m' \rangle|^2. \quad (3.29)$$

The NMR transitions are possible only for  $\Delta m = \pm 1$ , which is a selection rule for magnetic dipolar transitions. In the NMR experiment the absorption and consequently a spectral line will appear at Larmor frequency that will produce transitions between two consecutive nuclear spin states

$$\nu_L = \frac{E_m - E_{m-1}}{h} = \gamma_n B_0. \quad (3.30)$$

In reality the measured spectra is shifted from the Larmor frequency due to atomic or molecular diamagnetic or paramagnetic response produced by atomic core electrons or molecular valence electrons in the presence of external magnetic field. Such shift is normally an atomic or a molecular property and is called *chemical shift* and denoted by  $\sigma$  [67]. It is very difficult to calculate chemical shift from the first principles and for this reason the position of the spectral lines are always given as a shift from the line position of the reference sample. In metallic samples additional shift is found due to the hyperfine interaction with the itinerant electrons which is called the *Knight shift* and will be discussed in the following sections. Both shifts can be included in the general Zeeman term in a tensor form.

$$\mathcal{H}_{\text{Zeeman}} = -\gamma_n \hbar \vec{I} (\overset{\leftrightarrow}{1} - \overset{\leftrightarrow}{\sigma} + \overset{\leftrightarrow}{K}) \vec{B}_0. \quad (3.31)$$

The local magnetic field at the nucleus produced by the electron spin moments can have two origins. For the non-magnetic atoms the magnetic field originates from the dipolar interaction of the electron spin moments of neighbouring magnetic atoms

$$\mathcal{H}_{\text{dipolar}} = \frac{\mu_0}{4\pi} \gamma_e \gamma_n \hbar^2 \sum_j \left[ 3 \frac{(\vec{I} \cdot \vec{r}_j)(\vec{S}_j \cdot \vec{r}_j)}{r_j^5} - \frac{\vec{I} \cdot \vec{S}_j}{r_j^3} \right] = \vec{I}_i \cdot \sum_{j \neq i} \overset{\leftrightarrow}{D}_{ij} \cdot \vec{S}_j, \quad (3.32)$$

where  $\gamma_e$  is electron gyromagnetic ratio,  $\vec{S}_j$  is the electron spin operator at the  $j$ -th atomic site and  $\vec{r}_j$  is vector from the nucleus to the  $j$ -th electron spin. The dipolar interaction tensor in Eq. 3.32 has zero trace ( $\text{Tr}(\overset{\leftrightarrow}{D}) = 0$ ) and is thus entirely anisotropic. This also means that in the case of powder samples the NMR spectrum will not be shifted, but instead, the line will be broadened. Broadening of the spectra due to dipolar interaction will be discussed in section 3.2.2.

For magnetic atoms or molecules with on-site spin polarized electrons they interact with the nucleus by a much stronger hyperfine interaction written as

$$\mathcal{H}_{\text{hf}} = \vec{I}_i \cdot \overset{\leftrightarrow}{A}_{ii} \cdot \vec{S}_i, \quad (3.33)$$

for the nucleus at the site  $i$ . In the single-electron theory the hyperfine interaction can be expressed in two ways. For the  $s$ -wave electrons the hyperfine term is written as

$$\mathcal{H}_{\text{hf,contact}} = \frac{\mu_0}{4\pi} \frac{8\pi}{3} \gamma_e \gamma_n \hbar^2 \vec{I}_i \cdot \vec{S}_i \delta(\vec{r}), \quad (3.34)$$

where  $\delta(\vec{r})$  is a Dirac delta function and  $\vec{r}$  is vector between the nucleus and the on-site electrons. This is the isotropic Fermi contact interaction term, which is non-zero only for isotropic  $s$ -wave electrons. Higher anisotropic wavefunctions, for example,  $p$ -,  $d$ -,  $f$ -wavefunctions have vanishing probability at the nucleus site and thus have no contact term contributions. In the metallic samples this term is responsible for the Knight shift, which would be discussed later.

For  $p$ -,  $d$ -,  $f$ -wave or higher spin-polarized electrons, whose density is further away from the nucleus, the hyperfine interaction can be expressed as an anisotropic dipolar interaction

$$\mathcal{H}_{\text{hf,dipolar}} = \frac{\mu_0}{4\pi} \gamma_e \gamma_n \hbar^2 \left[ 3 \frac{(\vec{I}_i \cdot \vec{r})(\vec{S}_i \cdot \vec{r})}{r^5} - \frac{\vec{I}_i \cdot \vec{S}_i}{r^3} \right]. \quad (3.35)$$

The limits of the single-electron theory were revealed when strong contact interaction was found in materials that have unpaired electrons only in higher non-isotropic orbitals (such as  $p$ ,  $d$ , or  $f$ ). Such effects were later explained by the many-body theory where the contact hyperfine coupling come from the polarization of the core electrons in the  $s$ -wave state. The exact calculation of the hyperfine coupling constants is far from trivial and the coupling constant is, therefore, usually taken as a phenomenological anisotropic tensor.

In cases when non-magnetic atom is strongly bounded with a magnetic atom or when its atomic  $s$ -orbitals are mixed with molecular orbital containing spin-polarized electrons the polarization can be transferred to that non-magnetic atom. The interaction between nucleus and the indirectly polarized on-site electrons is called the transferred hyperfine interaction and is expressed as

$$\mathcal{H}_{\text{thf}} = \vec{I}_i \cdot \sum_j \overset{\leftrightarrow}{A}_{ij} \cdot \vec{S}_j. \quad (3.36)$$

Finally, we consider a different kind of interaction based on electrostatic interaction. The nuclei with  $I > 1/2$  have nuclear quadrupole moment  $Q$  that interacts with the local electric field gradient (EFG)  $V_{ij}$  produced by the distribution of surrounding electrons and nuclei. The Hamiltonian for the nuclear quadrupole interaction is written as [75]

$$\mathcal{H}_Q = \frac{e^2 q Q}{4I(2I-1)} \left[ 3I_z^2 - I(I+1) + \frac{1}{2} \eta (I_+^2 + I_-^2) \right], \quad (3.37)$$

where  $e$  is the electron charge,  $eq = |V_{ZZ}|$  is the principal value of the EFG tensor,  $\eta$  is the asymmetry parameter  $\eta = (V_{XX} - V_{YY})/V_{ZZ}$ , and  $I_{\pm} = I_x \pm iI_y$  are the spin lowering and rising operators, respectively. This Hamiltonian is written in the principal frame of the EFG tensor, where  $|V_{ZZ}| \geq |V_{YY}| \geq |V_{XX}|$  and consequently  $0 \leq \eta \leq 1$ .

In a large external magnetic field the quadrupole interaction is calculated as a perturbation to the Zeeman term and in the first order the expectation energy for a nuclear spin wavefunction  $|I, m\rangle$  is written as

$$E_m^{(1)} = \frac{h\nu_Q}{2} \left( \frac{3 \cos^2 \theta - 1}{2} + \frac{1}{2} \eta \sin^2 \theta \cos 2\phi \right) [m^2 - I(I+1)/3], \quad (3.38)$$

where  $\nu_Q = 3e^2 q Q / [2I(2I-1)]$ , and  $\theta, \phi$  are polar and azimuthal angles of the magnetic field in the EFG principal frame. The frequency shift of the resonance line corresponding to the transition between  $(m \leftrightarrow m-1)$  nuclear states is expressed as

$$\nu_m^{(1)} = \frac{E_m^{(1)} - E_{m-1}^{(1)}}{h} = -\nu_Q \left( \frac{3 \cos^2 \theta - 1}{2} + \frac{1}{2} \eta \sin^2 \theta \cos 2\phi \right) \left( m - \frac{1}{2} \right). \quad (3.39)$$

The central transition between ( $1/2 \leftrightarrow -1/2$ ) is un-shifted with respect to the Larmor frequency  $\nu_L$ , whereas transitions between higher magnetic numbers appear as a satellite lines symmetrically shifted from the central line at  $\nu_L$ . In the second order perturbation also the central line becomes shifted away from  $\nu_L$ , however the shift is much smaller, of the order of  $\nu_Q^2/\nu_L$ . The shift of the central transition ( $1/2 \leftrightarrow -1/2$ ) is in the second order perturbation given by [76]

$$\begin{aligned} \nu_{1/2}^{(2)} = & -\frac{1}{6} \frac{\nu_Q^2}{\nu_L} \left\{ I(I+1) - \frac{3}{4} \right\} \left[ \left( -\frac{27}{8} + \frac{9}{4} \eta \cos 2\phi - \frac{3}{8} (\eta \cos 2\phi)^2 \right) \cos^4 \theta \right. \\ & + \left( \frac{30}{8} - \frac{1}{2} \eta^2 - 2\eta \cos 2\phi + \frac{3}{4} (\eta \cos 2\phi)^2 \right) \cos^2 \theta \\ & \left. + \left( -\frac{3}{8} + \frac{1}{3} \eta^2 - \frac{1}{4} \eta \cos 2\phi - \frac{3}{8} (\eta \cos 2\phi)^2 \right) \right]. \end{aligned} \quad (3.40)$$

When computing the NMR spectrum different probabilities for different nuclear state transitions have to be considered. The probability for a transition between two consecutive states is written as

$$W_{m,m-1} \propto |\langle m | I_x | m-1 \rangle|^2 = I(I+1) - m(m-1) \quad (3.41)$$

being smaller for transition with higher  $m$  numbers. Satellite lines have smaller probability amplitudes and in case of the powder samples these lines are also broadened due to distribution over  $\theta$  and  $\phi$  angles. Satellites further away from the central line are, therefore, harder to observed.

### 3.3.2 Nuclear Relaxation and the Linewidth

In an ideal system where nuclear spins feel only external magnetic field the transition between two energy states would be represented as a delta function in the absorption spectrum. In the real systems the nuclei are coupled also to neighbouring magnetic moments or the electrostatic field via interactions described in the previous subsection that can be treated as the perturbation to the Zeeman term. In what follows we will limit the discussion only to the magnetic interactions. The relaxation function (Eq. 3.8) and consequently the line broadening depend on the perturbation terms in the nuclear spin Hamiltonian (Eq. 3.26). In case of NMR a simplified derivation of the relaxation rates can be obtained by realizing that the local interaction terms, e.g. hyperfine or dipolar interaction, can be effectively seen as sources of fluctuating local magnetic fields at the nucleus site coupled to them with an effective interaction term

$$\mathcal{H}_1(t) = -\gamma_n \hbar \sum_q b_q(t) I_q, \quad (3.42)$$

where  $\vec{b}(t) = \vec{B}_{\text{loc}}(t) - \langle \vec{B}_{\text{loc}} \rangle$ ,  $\langle \vec{B}_{\text{loc}} \rangle$  being static local field and  $q = x, y, z$  are three vector components. Calculation of time derivative of the nuclear spin expectation values considering the perturbation term (Eq. 3.42) to the Zeeman term (Eq. 3.31) gives the Bloch equations [67]

$$\frac{d\langle I_z \rangle}{dt} = \gamma_n \left( \langle \vec{I} \rangle \times \vec{B}_0 \right)_z - \frac{\langle I_z \rangle - I_0^z}{T_1}, \quad (3.43)$$

$$\frac{d\langle I_{x,y} \rangle}{dt} = \gamma_n \left( \langle \vec{I} \rangle \times \vec{B}_0 \right)_{x,y} - \frac{\langle I_{x,y} \rangle}{T_2}. \quad (3.44)$$

In the above equations the first term is the precession term, describing the torque that external magnetic field  $\vec{B}_0$  along  $z$ -axis is exerting on the nuclear spin component perpendicular to its direction. The second terms describe damping and are responsible for the nuclear spin relaxation back to the equilibrium state ( $\vec{I}_0 = I_0^z$ ). The relaxation time for the spin component along  $\vec{B}_0$  is the spin-lattice relaxation time ( $T_1$ ), whereas the perpendicular spin component relaxes with the spin-spin relaxation time ( $T_2$ ). The spin-lattice relaxation time is associated with the energy loss. Within the calculations outlined above the two relaxation times have the following form

$$\frac{1}{T_1} = \gamma_n^2 [k_{xx}(\omega_0) + k_{yy}(\omega_0)], \quad (3.45)$$

$$\frac{1}{T_2} = \frac{\gamma_n^2}{2} [k_{xx}(\omega_0) + k_{yy}(\omega_0) + 2k_{zz}(0)], \quad (3.46)$$

where  $k_{qq'}$  are the spectral densities of the  $q$ -component fluctuating field

$$k_{qq'}(\omega) = \frac{1}{2} \int_{-\infty}^{\infty} \langle b_q(t)b_{q'}(t+\tau) \rangle e^{-i\omega\tau} d\tau. \quad (3.47)$$

Here  $\langle \rangle$  denotes ensemble average. The relation for the spin-spin relaxation rate ( $1/T_2$ ) is valid only when  $1/T_2$  is smaller than the Larmor precession frequency  $\omega_0$ , else  $1/T_2$  has to be specified separately for  $x$  and  $y$  directions [67]. The spin-lattice ( $1/T_1$ ) relaxation rate (Eq. 3.45) is a function of the fluctuating local fields perpendicular to the quantization axis ( $z$ -direction). Only these fields can change the nuclear moment's  $z$ -component and consequently the nuclear spin Zeeman energy. The transition between these states is possible only by the EM fields with the Larmor frequency which is the reason why  $1/T_1$  depends on the spectral density of the fluctuating fields at the Larmor frequency. On the other hand, the spin-spin relaxation rate  $1/T_2$  (Eq. 3.46), which is directly related to the NMR spectral linewidth, consists of two parts. The first part is exactly one half of the spin-lattice relaxation rate and corresponds to the finite spin lifetime contribution to the linewidth. The second part comes from the fluctuating field spectral density along  $z$ -axis at zero frequency. The static component comes from the fact that, in contrast to spin-lattice relaxation rate, the reorientation of the nuclear spin perpendicular to the quantisation axis does not require energy change. In principle there is another contribution to the  $1/T_2$  relaxation rate which was in the above discussion avoided by taking the ensemble average in Eq. 3.47. The so-called homogeneous broadening comes from the spatial distribution of the local magnetic fields and it is normally much larger than the bare  $T_2$  effect. However, its contribution to the spin-spin relaxation rate could be experimentally removed by using a NMR pulse technique called the "spin-echo" pulse sequence.

Since the calculation of the  $T_2$  relaxation rate is not so relevant for this work, we focus on the  $T_1$  relaxation rate. To derive the spin-lattice relaxation rate further, where we would be able to include the origin of local magnetic fluctuations more easily, we proceed by inserting Eq. 3.47 into Eq. 3.45 and using  $b_{\pm} = b_x \pm ib_y$ . The expression for the spin-lattice rate becomes

$$\frac{1}{T_1} = \frac{\gamma_n^2}{2} \int_{-\infty}^{\infty} \langle \{b_+(0)b_-(\tau)\} \rangle e^{-i\omega_0\tau} d\tau, \quad (3.48)$$

where we used a symmetrized product,  $\{AB\} = (AB + BA)/2$ , to get the real part of the quantum correlation function. In materials with unpaired electron spin moments

the magnetic field fluctuations at the nucleus' site are correlated to the electron spin fluctuations through the hyperfine interaction (Eq. 3.34–3.36). The hyperfine magnetic field is written as  $\vec{b}(t) = \sum_j \overset{\leftrightarrow}{A}_j \cdot \vec{s}_j(t)$ , where  $\overset{\leftrightarrow}{A}_j$  is rank-two general hyperfine tensor and  $s_j(i)$  is the fluctuating part of the electron spin number  $\vec{s}_j(t) = \vec{S}_j(t) - \langle \vec{S} \rangle$ . Adding this to Eq. 3.48 and using Fourier transformations  $s_j^\mu(t) = 1/\sqrt{N} \sum_{\vec{q}} e^{-i\vec{q}\cdot\vec{r}_j} s_{\vec{q}}^\mu(t)$  and  $A_{\vec{q}}^{\mu\nu} = \sum_i e^{i\vec{q}\cdot\vec{r}_i} A_i^{\mu\nu}$  one arrives at [77]

$$\frac{1}{T_1} = \frac{\gamma_n^2}{2N} \sum_{\vec{q}\mu\nu} \left( A_{\vec{q}}^{x\mu} A_{-\vec{q}}^{x\nu} + A_{\vec{q}}^{y\mu} A_{-\vec{q}}^{y\nu} \right) \int_{-\infty}^{\infty} \langle \{s_{\vec{q}}^\mu(0) s_{-\vec{q}}^\nu(\tau)\} \rangle e^{-i\omega_0\tau} d\tau, \quad (3.49)$$

where  $\mu, \nu = \{x, y, z\}$  and  $N$  is number of  $\vec{q}$  vectors due to transferred hyperfine interaction. Due to the symmetrized product the integral of the above equation can be written as a sum of two terms,  $[J_1(\vec{q}, \omega_0) + J_2(\vec{q}, \omega_0)]/2$ , also known as the spectral densities. It can be shown [66] that these two densities are related as  $J_1 = \exp(-\beta\hbar\omega) J_2$ . In the high-temperature limit,  $\hbar\omega \ll k_B T$ , they are the same,  $J_1 \approx J_2$ , and the integral factor of Eq. 3.49 can be replaced by  $J_1(\vec{q}, \omega_0)$ . On the other hand, spectral density can be related to the dynamic spin susceptibility using fluctuation-dissipation theorem [66]

$$\chi''_{\mu\nu}(\vec{q}, \omega) = \frac{1}{2\hbar} (1 - e^{-\beta\hbar\omega}) J_1(\vec{q}, \omega) \approx \frac{\omega}{2} \frac{1}{k_B T} \int_{-\infty}^{\infty} \langle s_{\vec{q}}^\mu(0), s_{-\vec{q}}^\nu(\tau) \rangle e^{-i\omega\tau} d\tau. \quad (3.50)$$

Dynamic spin susceptibility, as defined here, is in units of inverse energy ( $J^{-1}$ ). By joining Eq. 3.49 and Eq. 3.50 the relaxation rate can be for an arbitrary hyperfine tensor written as

$$\frac{1}{T_1} = \frac{\gamma_n^2}{N} k_B T \sum_{\vec{q}\mu\nu} \left( A_{\vec{q}}^{x\mu} A_{-\vec{q}}^{x\nu} + A_{\vec{q}}^{y\mu} A_{-\vec{q}}^{y\nu} \right) \frac{\chi''_{\mu\nu}(\vec{q}, \omega_0)}{\omega_0}. \quad (3.51)$$

If we now restrict the hyperfine tensor to the diagonal form ( $A_{\mu\nu} = A_{\mu\mu} \delta_{\mu\nu}$ ), as is the case with the contact interaction, the spin-lattice relaxation can be simplified to

$$\frac{1}{T_1} = \frac{\gamma_n^2}{2N} \sum_{\vec{q}, \alpha=xx,yy} |A_\alpha(\vec{q})|^2 \int_{-\infty}^{\infty} \langle \{s_{\vec{q}}^+(0) s_{-\vec{q}}^-(\tau)\} \rangle e^{-i\omega_0\tau} d\tau = \quad (3.52)$$

$$= \frac{\gamma_n^2}{N} k_B T \sum_{\vec{q}, \alpha=xx,yy} |A_\alpha(\vec{q})|^2 \frac{\chi''_{\perp}(\vec{q}, \omega_0)}{\omega_0}. \quad (3.53)$$

In the last expression  $\chi''_{\perp}(\vec{q}, \omega_0)$  corresponds to the electron spin susceptibility perpendicular to the external magnetic field. Eq. 3.53 is also known as *Moriya expression* for the spin-lattice relaxation rate [78]. This expression is the most general expression for  $T_1$  and as we will show later, the relaxation rates in different phases can all be derived from Eq. 3.53. Since the Larmor frequency is typically much smaller than typical electronic energies Moriya expression is often evaluated in the limit when  $\omega_0 \rightarrow 0$ .

The  $\vec{q}$  dependent hyperfine coupling constant is very important when studying materials that exhibit magnetic fluctuations. In such case the dynamic spin susceptibility would contain a peak at a certain  $\vec{q}$  vector which might get filtered out for some nuclei depending on their site symmetry. For example, in case of antiferromagnetic fluctuations a nucleus at the octahedral site will not experience any transferred hyperfine magnetic field from the neighbouring antiferromagnetically aligned spins. The hyperfine magnetic field from one neighbour having a certain spin direction will be cancelled out by the

transferred field from the neighbour on the opposite site with an opposite spin direction. Such cancellation is much smaller in case of tetrahedral symmetry since it does not contain an inversion symmetry operation. Assuming that the transferred hyperfine coupling constant is equal for all the neighbouring sites we can put  $\vec{q}$  dependence of the hyperfine constant into a *form factor*,  $|A(\vec{q})|^2 = A^2 \mathcal{F}(\vec{q})$ . To calculate the form factor for different site symmetries we follow the definition of the  $\vec{q}$  dependent hyperfine constant  $A_{\vec{q}} = \sum_i e^{i\vec{q}\cdot\vec{r}_i} A_i$ , which leads to

$$|A(\vec{q})|^2 = A^2 \mathcal{F}(\vec{q}) = A^2 \left| \sum_i e^{i\vec{q}\cdot\vec{r}_i} \right|^2, \quad (3.54)$$

where  $\vec{r}_i$  runs over all the neighbouring magnetic sites. For a nuclei with an on-site electronic spin moment, as is the case of  $^{13}\text{C}$ , the transferred hyperfine coupling constant is negligible and the form factor is therefore independent of  $\vec{q}$ . For such nuclei the spin-lattice relaxation rate will be an unfiltered sum of the dynamic spin susceptibility over all  $\vec{q}$ . In case of octahedral site symmetry the form factor is expressed as

$${}^{\text{O}}\mathcal{F}(\vec{q}) = 4 \left[ \cos\left(\frac{q_x a}{2}\right) + \cos\left(\frac{q_y a}{2}\right) + \cos\left(\frac{q_z a}{2}\right) \right]^2, \quad (3.55)$$

where neighbouring magnetic moments are positioned at  $\vec{r}_i = \frac{a}{2}(\pm 1, \pm 1, 0)$ ,  $\frac{a}{2}(\pm 1, 0, \pm 1)$ , and  $\frac{a}{2}(0, \pm 1, \pm 1)$ . In case of tetrahedral site the form factor has the form

$${}^{\text{T}}\mathcal{F}(\vec{q}) = 16 \left[ \cos\left(\frac{q_x a}{4}\right)^2 \cos\left(\frac{q_y a}{4}\right)^2 \cos\left(\frac{q_z a}{4}\right)^2 + \sin\left(\frac{q_x a}{4}\right)^2 \sin\left(\frac{q_y a}{4}\right)^2 \sin\left(\frac{q_z a}{4}\right)^2 \right], \quad (3.56)$$

obtained by neighbouring magnetic moments being positioned at  $\vec{r}_i = \frac{a}{4}(\pm 1, 1, 1)$ ,  $\frac{a}{4}(1, \pm 1, 1)$ , and  $\frac{a}{4}(1, 1, \pm 1)$ . The form factors for octahedral and tetrahedral sites are as a function of  $\vec{q}$  in two dimensions depicted in Fig. 3.1. In the third dimension we fixed  $q_z a = \pi$  in order to visualize how form factor affects antiferromagnetic spin arrangement at  $\vec{q}a = (\pi, \pi, \pi)$ . In case of octahedral site (Fig. 3.1a) the form factor is zero for this  $\vec{q}$  and, therefore, the antiferromagnetic fluctuations are filtered out completely. In case of tetrahedral site (Fig. 3.1b) the antiferromagnetic fluctuations will be only partially filtered out and will still contribute to the spin-lattice relaxation rate as was illustrated above.

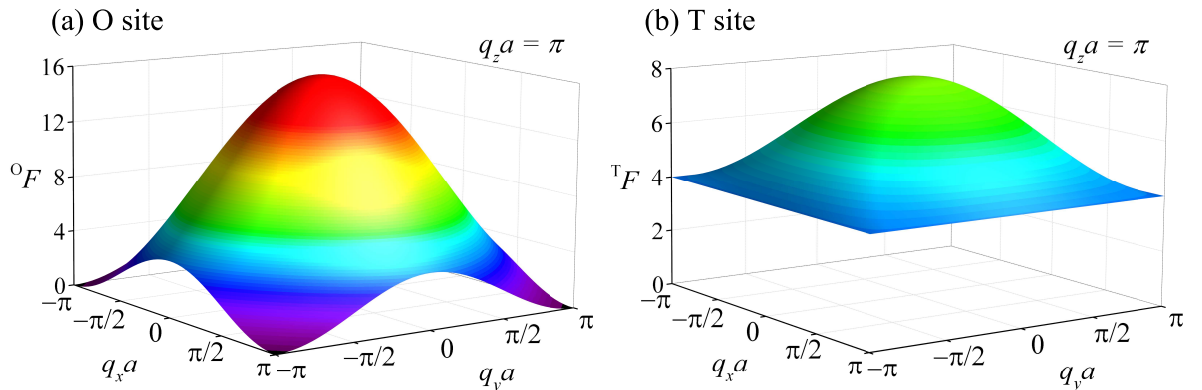


Figure 3.1: Form factors for (a) octahedral site symmetry and (b) tetrahedral site symmetry shown as a function of two dimensions. The third dimension was fixed to  $q_z a = \pi$  in order to visualize its effect on the antiferromagnetic fluctuations which appear at  $\vec{q}a = (\pi, \pi, \pi)$ .

Let us briefly describe the influence of the non-magnetic contributions to the relaxation rate due to quadrupole interaction. The effect of the static EFG tensor to the line-shape has been discussed above, however additional broadening can be observed if the EFG tensor is time dependent and with large fluctuating spectrum close to the Larmor frequency. This is most notably observed in liquids where EFG tensor fluctuates due to the motion of molecules or atoms and consequently due to a rapid change of nuclear environment. Similar contribution to the nuclear relaxation rates can be observed also in magnetic solids where EFG tensor is modulated by the lattice vibrations. In this respect a linear temperature dependence of the spin-lattice relaxation rate is commonly observed when direct phonon processes are dominated, which is accounted for a single phonon creation and annihilation processes. On the other hand, phonons can also be scattered inelastically similarly to the Raman processes. In such cases the temperature dependence of the  $T_1$  parameter has a power law dependence with  $T^2$  or  $T^7$  dependence depending on the temperature with respect to the Debye temperature [75].

In the next three subsections we will focus on the Knight shift and the spin-lattice relaxation rate in the insulating, metallic and superconducting phases.

### 3.3.3 NMR in Paramagnetic Insulators

#### Isotropic lineshift

Magnetic moments in magnetic insulators are localised either by a large band gap between valence and conducting band or due to strong electron correlations, found in Mott insulators. Most of magnetic insulators have unpaired electrons in partially occupied  $d$ -atomic orbitals of the transition metal ions (e.g.  $\text{K}_3\text{Cu}_3\text{Fe}_2\text{F}_{15}$  [79]) or in  $f$ -atomic orbitals of the rare-earth element compounds (e.g.  $\text{Nd}_3\text{Ga}_5\text{SiO}_{14}$  [80]). There are fewer examples of  $p$ -orbital magnetism (e.g. TDAE- $\text{C}_{60}$  [8],  $\text{AO}_2$  or  $\text{A}_4\text{O}_6$  [81]), however, their number has in recent years strongly increased [82]. Since unpaired electrons are not in the  $s$ -orbitals they do not produce an isotropic hyperfine magnetic field at the nucleus site and, therefore, the NMR spectral position in such powder materials is shifted only by chemical shift. However, in some of the magnetic insulators additional isotropic lineshift comes from the transferred hyperfine interaction. Taking this into account we derive the isotropic NMR lineshift of insulators with nonzero isotropic hyperfine interaction (Eq. 3.36) together with the Zeeman interaction term for nucleus and electrons as

$$\mathcal{H} = \hbar\gamma_e S_z B_0 - \hbar\gamma_n I_z B_0 + A I_z S_z. \quad (3.57)$$

The part of energy that depend on the nuclear spin is written as

$$\mathcal{H}_n = -\hbar\gamma_n I_z (B_0 + B_{\text{hf}}), \quad B_{\text{hf}} = -\frac{A S_z}{\hbar\gamma_n}. \quad (3.58)$$

where  $B_{\text{hf}}$  represents a hyperfine magnetic field due to polarized electrons. The hyperfine fields can be quite large, even of the order of the external magnetic field [83], which would strongly effect the NMR line. However, in reality this is not observed. The electron spin relaxation is much faster than the nuclear spin dynamics and, therefore, the nucleus sees a time averaged hyperfine field proportional to the mean value of the electron spin component  $\langle S_z \rangle$  [83]. The averaged spin component is proportional to the bulk magnetization,  $M_z = N\hbar\gamma_e \langle S_z \rangle$  which can be in external magnetic field expressed as  $M_z = \chi_s B_0 / \mu_0$ .  $\chi_s$  is the uniform static electron spin susceptibility. The isotropic

hyperfine shift is then

$$K_{\text{hf}} = \frac{\Delta B_{\text{hf}}}{B_0} = \frac{A}{N\mu_0\hbar^2\gamma_n\gamma_e}\chi_s. \quad (3.59)$$

In the above expression the hyperfine coupling constant is given in units of [ $J$ ], Knight shift in units of [ppm], and spin susceptibility is without units. In practice spin susceptibility is often given in cgs units of [emu/mol]. In this system it is convenient to express hyperfine coupling constant in the units of [ $\text{Oe}/\mu_B$ ] =  $10^{-7}\mu_B N_A$  [ppm/(emu/mol)] =  $5.5848 \cdot 10^{-3}$  [ppm/(emu/mol)].

### Spin-Lattice Relaxation

In solid state magnetic insulators the magnetic field fluctuations at the nucleus site originate either from interaction with lattice due to thermal movement of ions or from the neighbouring electron spin dynamics. The later is in magnetic insulators much faster than thermal fluctuations due to exchange interaction between electrons. In such cases the material's Curie or Néel temperature is smaller than the Debye temperature [84]. Since the thermal contribution has been discussed above we focus now on the spin-lattice relaxation rate caused by the fluctuating hyperfine magnetic fields due to electrons-electron exchange coupling ( $J$ ). The theory of the nuclear relaxation in the exchange-coupled antiferromagnets has been derived by Moriya [84] who showed that the electron spin-spin correlation function in the presence of exchange coupled electrons has in the high temperature limit the Gaussian form [29, 84]

$$\langle S_\alpha(0)S_{\alpha'}(t) \rangle = \delta_{\alpha,\alpha'} \frac{1}{3} S(S+1) \exp\left(-\frac{1}{2}\omega_{\text{ex}}^2 t^2\right). \quad (3.60)$$

Here  $\omega_{\text{ex}}$  denotes the exchange frequency which is expressed as

$$\omega_{\text{ex}} = \frac{2}{3} J^2 / \hbar^2 z S(S+1). \quad (3.61)$$

In this expression  $z$  is the number of nearest neighbours and  $J$  is the electron exchange coupling constant. For isotropic hyperfine tensor  $A$  (Eq. 3.36) the Moriya expression using Gaussian correlation function (Eq. 3.60) gives the following relation for the spin-lattice relaxation rate for the magnetic insulators

$$\frac{1}{T_1} = \sqrt{2\pi} A^2 \frac{S(S+1)}{3\omega_{\text{ex}}} \quad (3.62)$$

In the above relation hyperfine constant is expressed in units of Hz. In case of dipolar anisotropic hyperfine tensor similar relation is obtain with an addition of factor 1/2 [84]. The general spin-lattice relaxation rate in magnetic insulators is then written as [14]

$$\frac{1}{T_1} = \sqrt{2\pi} \left( A_{\text{iso}}^2 + \frac{1}{2} A_{\text{dip}}^2 \right) \frac{S(S+1)}{3\omega_{\text{ex}}}, \quad (3.63)$$

where  $A$  again has units of Hz.

### 3.3.4 NMR in Metals

#### Knight shift

The Knight shift has been first observed in metals where a much larger shift than the previously determined chemical shift has been observed. The origin of an additional shift

has been found to be a local magnetic field produced by the spin polarized conduction electrons in an external magnetic field. In this case the hyperfine magnetic field is produced by the contact interaction (Eq. 3.34) between nuclei and the conducting electrons. The derivation of the Knight shift is similar to that of the hyperfine shift in the magnetic insulators (Eqs. 3.57–3.59).

Since in metals it is somewhat easier to determine the hyperfine constant  $A$  we will next derive the complete expression for the Knight shift. We start with the contact interaction term between nuclei and conducting electrons (Eq. 3.34) and integrate out the electronic degrees of freedom [67]

$$\mathcal{H}' = \frac{\mu_0}{4\pi} \frac{8\pi}{3} \gamma_e \gamma_n \hbar^2 \vec{I}_j \cdot \int \psi_e^* \sum_l \vec{S}_l \delta(\vec{r}_l) \psi_e d\tau_e, \quad (3.64)$$

where we use properly antisymmetrized Bloch wavefunctions ( $\psi_{\vec{k}}(\vec{r}) = u_{\vec{k}}(\vec{r}) e^{i\vec{k}\cdot\vec{r}}$ ) to account for Pauli exclusion principle. Assuming quantization of electron spins along  $z$  direction, the above expression can be for the  $j$ -th nucleus written as [67]

$$\mathcal{H}' = \frac{\mu_0}{4\pi} \frac{8\pi}{3} \gamma_e \gamma_n \hbar^2 I_{zj} \sum_{\vec{k}, S_z} |u_{\vec{k}, S_z}(0)|^2 S_z f(\vec{k}, S_z), \quad (3.65)$$

where  $f(\vec{k}, S_z)$  is the Fermi function. The summation over  $S_z$  together with the Fermi function gives the average conduction electron magnetic moment, which is proportional to the electron spin susceptibility

$$\gamma_e \hbar \left( \frac{1}{2} \right) f \left( \vec{k}, \frac{1}{2} \right) + \gamma_e \hbar \left( -\frac{1}{2} \right) f \left( \vec{k}, -\frac{1}{2} \right) = \langle \mu_{z, \vec{k}} \rangle = \chi_{\vec{k}}^s H_0. \quad (3.66)$$

The nuclear part of the contact interaction term is then written as

$$\frac{\mu_0}{4\pi} \frac{8\pi}{3} \gamma_n \hbar I_{zj} \sum_{\vec{k}} |u_{\vec{k}}(0)|^2 \chi_{\vec{k}}^s H_0. \quad (3.67)$$

The summation over  $\vec{k}$  can be next rewritten as the energy integral using density of states  $[N(E)]$ . At this point we note that the spin susceptibility is a peak function close to the Fermi energy as electronic states above or below the Fermi energy are either fully occupied or fully empty and thus do not contribute to the spin susceptibility. Taking this into account and assuming that  $|u_{\vec{k}}(0)|^2$  varies sufficiently slowly near the Fermi surface, the final form of the interaction term with the  $j$ -th spin is written as

$$\gamma_n \hbar I_{zj} \left[ \frac{1}{4\pi} \frac{8\pi}{3} \langle |u_{\vec{k}}(0)|^2 \rangle_{E_F} \chi_s B_0 \right]. \quad (3.68)$$

In the above expression  $\langle \rangle_{E_F}$  is the average over the Fermi surface and  $\chi_s = \int \chi^s(E) N(E) dE$  is the uniform static spin susceptibility in metals or the Pauli spin susceptibility [69]. The expression (Eq. 3.68) is equivalent to the nuclear spin interaction term with an additional hyperfine magnetic field  $\Delta B$  (in the square brackets) that gives the Knight shift [67]

$$\frac{\Delta B}{B_0} = K = \frac{1}{4\pi} \frac{8\pi}{3} \langle |u_{\vec{k}}(0)|^2 \rangle_{E_F} \chi_s. \quad (3.69)$$

## Spin-Lattice Relaxation

The spin-lattice relaxation rate ( $1/T_1$ ) in metals can be obtained by deriving the dynamic spin susceptibility in the free electron limit and then use the Moriya expression (Eq. 3.53).

We have already shown that in the magnetic resonance experiments the measured energy absorption is proportional to the dynamic spin susceptibility (Eq. 3.4)

$$P(\omega) = -\frac{1}{2}\omega V \frac{B^2}{\mu_0} \chi''(\omega). \quad (3.70)$$

Absorption of energy can be, on the other hand, calculated also considering transition probabilities between different energy states. The term that induces the electron transitions due to the harmonic external perturbation is the Zeeman form. Considering harmonic magnetic field ( $B(t) = B\cos\omega t$ ) this term has the form in the second quantization [85]

$$\mathcal{H}_1(t) = -\hbar\gamma_e \sum_{k,l=1}^n \frac{1}{2} \left( c_{k\uparrow}^\dagger c_{l\uparrow} - c_{k\downarrow}^\dagger c_{l\downarrow} \right) \langle \psi_k | B | \psi_l \rangle \frac{1}{2} (e^{i\omega t} + e^{-i\omega t}), \quad (3.71)$$

$$= \mathcal{H}_{1,0} \frac{1}{2} (e^{i\omega t} + e^{-i\omega t}), \quad (3.72)$$

where the last line defines operator  $\mathcal{H}_{1,0}$ . Using Fermi golden rule we can calculate the transition probability per unit time  $W_{0e}$  between the ground state ( $\Psi_0$ ) and the excited state ( $\Psi_e$ ) under the influence of this perturbation term as

$$W_{0e}(\omega) = \frac{2\pi}{\hbar} |\langle \Psi_0 | \mathcal{H}_{1,0} | \Psi_e \rangle|^2 \delta(E_e - E_0 + \hbar\omega). \quad (3.73)$$

To make the connection between quantum mechanical result and thermodynamics we need to consider how likely it is for an electron to be in an initial state and how likely it is that the excited state is empty. The expression for all transitions from the ground state to all possible excited states giving the absorption rate is written as

$$W_{0\rightarrow}(\omega) = \sum_e W_{0e}(\omega) \quad (3.74)$$

$$= \hbar^2 \gamma_e^2 \frac{\pi}{2\hbar} \sum_{i,j=1}^n f(E_i) [1 - f(E_j)] |\langle \psi_i | B | \psi_j \rangle|^2 \delta(E_i - E_j + \hbar\omega). \quad (3.75)$$

In the above expression  $E_i < E_j$ . Similar expression can be obtained for the stimulated emission ( $W_{0\leftarrow}$ ) where indices  $i$  and  $j$  are interchanged whereas  $E_i < E_j$  must still hold. The net absorbed power is

$$P(\omega) = \hbar\omega [W_{0\rightarrow}(\omega) - W_{0\leftarrow}(\omega)] \quad (3.76)$$

$$= \omega \hbar^2 \gamma_e^2 \frac{\pi}{2} \sum_{i,j=1}^n [f(E_i) - f(E_j)] |\langle \psi_i | B | \psi_j \rangle|^2 \delta(E_i - E_j + \hbar\omega). \quad (3.77)$$

In the limit  $\hbar\omega \rightarrow 0$  the expression  $[f(E_i) - f(E_j)]\delta(E_i - E_j + \hbar\omega)$  can be written as the Fermi function derivative  $-\hbar\omega f'(E_i)\delta(E_i - E_j + \hbar\omega)$ . If we additionally assume that external magnetic field is uniform over the sample volume, in case when harmonic fields'

wavelength is much larger than the sample size, the expression for the absorbed power can be simplified to

$$P(\omega) = -\omega^2 \hbar^3 \gamma_e^2 B^2 \frac{\pi}{2} \sum_{i,j=1}^n f'(E_i) \delta(E_i - E_j + \hbar\omega), \quad (3.78)$$

where we used the normalization of the wavefunctions, ( $|\langle \psi_i \psi_j \rangle|^2 = \langle \psi_i \psi_i \rangle \langle \psi_j \psi_j \rangle = 1$ ). In metals at practical temperatures and in the limit  $\hbar\omega \rightarrow 0$  the derivative of the Fermi function is equal to the negative Dirac delta function,  $-f'(E_i) \delta(E_i - E_j + \hbar\omega) = f'(E_i) f'(E_j)$ . If we also relate the dissipated power with the imaginary dynamic spin susceptibility (Eq. 3.4) we arrive at

$$\chi''(\omega) = \pi \frac{\mu_0}{V} \omega \hbar^3 \gamma_e^2 \left| \sum_{i=1}^n f'(E_i) \right|^2. \quad (3.79)$$

In the limit of small magnetic fields the Fermi function derivative can be written as  $f'(E_i) = [f(E_{i\uparrow}) - f(E_{i\downarrow})]/\hbar\gamma_e B$ . Similarly to the derivation used for the Knight shift (Sec. 3.3.4) the difference between Fermi function for spin up and spin down can be expressed as an averaged conduction electron magnetic moment  $\langle \mu_{z,i} \rangle$  that is proportional to the static spin susceptibility. The dynamic spin susceptibility is then expressed as

$$\chi''(\omega) = \frac{4\pi V \hbar \omega}{\mu_0 \hbar^2 \gamma_e^2} \chi_s^2. \quad (3.80)$$

where we used  $\sum_i \chi_i^s = \chi_s$  for the static spin susceptibility. We see that the imaginary dynamic spin susceptibility in metals is proportional to frequency and the static spin susceptibility squared. Being odd function of frequency satisfy the necessary condition for the imaginary susceptibility  $\chi''(0) = 0$ , which means that in the static case there is no dissipation of energy. This result is of prime importance and it will be used to explain the measured spin-lattice relaxation times in the highly expanded alkali-doped fullerenes.

Next, we use Moriya's expression (Eq. 3.53) with isotropic hyperfine constant ( $\vec{q} = 0$ ) adapted<sup>2</sup> for dynamic spin susceptibility from Eq. 3.80.

$$\frac{1}{T_1} = \gamma_n^2 k_B T |A|^2 \frac{V}{\mu_0 \hbar^2 \gamma_e^2} \frac{\chi''(\omega_0)}{\omega_0}. \quad (3.81)$$

As we have shown before, in metals the hyperfine field comes from the contact interaction between nuclei and the conducting electron spins. To get the hyperfine constant  $A$ , we use Eq. 3.65 without the electron spin number since  $\vec{b} = \sum_j \overleftrightarrow{A_j} \cdot \vec{s}_j$ . Applying  $\sum_{\vec{k}} |u_{\vec{k}}(0)|^2 f(\vec{k}) = \langle |u_{\vec{k}}(0)| \rangle_{E_F}$ , contact hyperfine interaction can be expressed with the Knight shift (Eq. 3.69)

$$A = \frac{2}{3} \mu_0 \gamma_e \hbar \langle |u_{\vec{k}}(0)| \rangle_{E_F}^2 = \mu_0 \gamma_e \hbar \frac{K}{V \chi_s}, \quad (3.82)$$

where  $\chi_s$  is without units. Finally, we join Moriya's expression (Eq. 3.81), dynamic spin susceptibility (Eq. 3.80) and hyperfine field (Eq. 3.82) which leads us to the well known Korringa relation for metals [67]

$$(T_1 T) K^2 = \frac{\hbar}{4\pi k_B} \frac{\gamma_e^2}{\gamma_n^2} [\beta]. \quad (3.83)$$

<sup>2</sup>The expression has been multiplied with coefficients so that SI dynamic spin susceptibility without units can be used.

On the right hand side there are only fundamental constants, which should be universal for all conducting materials. However, the above derivation has been done assuming non-interacting electrons. In more general case, where such interactions are considered, the Korringa relation has the same form with an additional quantity  $\beta$  called the Korringa factor. We have shown that for the non-interacting case  $\beta = 1$ . For antiferromagnetic electron spin correlations  $\beta < 1$  and for ferromagnetic correlations  $\beta > 1$  [78].

### 3.3.5 NMR in Superconductors

NMR technique was one of the first techniques that help established the BCS theory [86], even-though the magnetic field is expelled from the superconductor due to the Meissner effect. At that time, when only type-I superconductors were known, special trick was invented to overcome this problem [86]. However, with the discovery of type-II superconductors, where above certain critical field ( $H_{c1}$ ) normal phase penetrates the superconducting phase in the form of normal state vortexes, the direct NMR measurement became possible. This is also the case of fullerene superconductors that are studied in this thesis. In this subsection we will describe how the Knight shift and the nuclear spin-lattice relaxation rate behave in the superconducting state and what information can be extracted from NMR experiments.

#### Knight shift and Yosida function

When material goes into the superconducting state the conduction electrons condensate and form Cooper pairs. Their total spin can be either a spin singlet ( $S = 0$ ) or spin triplet ( $S = 1$ ) which depends on the pairing mechanism. The most common case is the spin singlet state found in all standard BCS superconductors, HTc superconductors, cuprates or iron pnictides, and also in fulleride superconductors. As the sample is cooled the number of spin-polarized non-paired electrons or the quasiparticles is diminishing. This is reflected by the exponential reduction of the Pauli susceptibility and the Knight shift.

The amount of remaining Knight shift in the superconducting state as a function of temperature is described by Yosida function [87]. The Yosida function can be derived from the normal state spin susceptibility. An expression for normal state spin susceptibility,  $\chi_n$ , can be obtained considering difference between spin up and spin down conduction electrons in the presence of external magnetic field

$$\langle \mu \rangle = \frac{g\mu_B}{2}(n_\uparrow - n_\downarrow) \quad (3.84)$$

$$= \frac{g\mu_B}{2} \sum_{\vec{k}} [f(E_{\vec{k}} - g\mu_B B/2) - f(E_{\vec{k}} + g\mu_B B/2)] \quad (3.85)$$

$$\approx -\frac{g^2\mu_B^2}{2} B \sum_{\vec{k}} \frac{\partial f(E_{\vec{k}})}{\partial E_{\vec{k}}}. \quad (3.86)$$

The spin susceptibility in the normal state is then written as

$$\chi_n = \frac{\langle \mu \rangle}{VB/\mu_0} = -\mu_0 \frac{g^2\mu_B^2}{2V} \sum_{\vec{k}} \frac{\partial f(E_{\vec{k}})}{\partial E_{\vec{k}}}. \quad (3.87)$$

The sum in this equation can be replaced by an integral and the density of states

$$\chi_n = -\mu_0 \frac{g^2\mu_B^2}{2V} \int_{-\infty}^{\infty} N(E) \frac{\partial f(E)}{\partial E} dE. \quad (3.88)$$

One can see from above equation that only excited electrons close to the Fermi energy contribute to the spin susceptibility. For this reason at practical temperatures the derivative of the Fermi function can be written as Dirac delta function and the normal state spin susceptibility becomes proportional to the density of states at the Fermi energy [69].

In the superconducting state a gap opens at the Fermi level which reduces the amount of available excited states. This can be taken into account by using the superconducting density of states. For standard superconductors one can use BCS density of states [10] (Eq. 2.8)

$$N_{\text{BCS}}(E, T) = N(0) \frac{|E|}{\sqrt{E^2 - \Delta(T)^2}}, \quad (3.89)$$

where  $N(0)$  is the normal-state density of states at the Fermi level and  $\Delta(T)$  is temperature dependent superconducting gap function. The gap function for standard superconductors can be obtained by numerically solving the BCS gap equation in the weak-coupling limit ( $\lambda \rightarrow 0$ ) [10] (Eq. 2.9)

$$1 = \lambda \int_0^{\hbar\omega_D} \frac{1}{\sqrt{\varepsilon^2 + \Delta^2}} \tanh\left(\frac{\sqrt{\varepsilon^2 + \Delta^2}}{2k_B T}\right) d\varepsilon, \quad (3.90)$$

where  $\omega_D$  is a Debye frequency and  $\lambda$  is a dimensionless electron-phonon coupling parameter. The ratio between the Knight shift in the superconducting state to the Knight in the normal state is given by the Yosida function as [87, 88]

$$\frac{K_s(T)}{K_n(T_c)} = 2 \int_{\Delta}^{\infty} \frac{E}{\sqrt{E^2 - \Delta(T)^2}} \frac{\partial f(E, T)}{\partial E} dE. \quad (3.91)$$

In an approximation one can renormalize the gap function and obtain the Yosida function for intermediate and strong-coupling limits ( $2\Delta/k_B T_c > 3.53$ ). By comparing experimental Knight shift to the calculated one, it is then possible to obtain the superconducting coupling strength.

To correctly interpret the NMR lineshift ( $\sigma$ ) in the superconducting state it is important to note that it contains not only of the chemical and the Knight shift but also of demagnetization effect due to the Meissner screening currents. For type-II superconductors and assuming small demagnetization effect this contribution could be phenomenologically added to the total shift as

$$\sigma = \sigma_C + K + \frac{\Delta B}{B}. \quad (3.92)$$

The temperature dependent Knight shift could be obtained only if more than one nucleus in the unit cell could be measured. The shift is then obtained with the subtraction of lineshifts of the two nuclei

$$\Delta\sigma(T) = \sigma_1(T) - \sigma_2(T) = \sigma_{C1} - \sigma_{C2} + (A_1 - A_2)\chi(T). \quad (3.93)$$

The remaining unknown is the temperature independent difference between the two chemical shifts. This can be further determined only if data are measured at low enough temperatures where the Knight shift vanishes.

### Spin-lattice relaxation time ( $T_1$ )

In metals the nuclear spin-lattice relaxation rate comes from the hyperfine contact interaction between the spin polarized nuclei and the conducting electrons. Nuclear relaxation

is caused by the scattering of the thermally excited electrons near Fermi energy on the polarized nuclei. Similarly as in the case of the Knight shift, the opening of the superconducting gap effectively reduces the number of excited quasiparticles and thus reduces the probability for the scattering event. The spin-lattice relaxation rate is below the superconducting transition temperature exponentially decreasing with decreasing temperature and becomes zero at 0 K. We can discuss the exponential decay of the relaxation rate in more details by first deriving the Korringa relation for metals in an alternative way as has been done in Sec. 3.3.4.

First we realize that in case of scattering of electrons on the nuclei the transition probabilities for nuclei and for electrons must be equal. This means that the nuclear spin-lattice relaxation rate must be equal to the transition probability between initial and final states of the electrons. In quantum mechanics the transition probability per unit time is given by the Fermi golden rule (Eq. 3.73) and if we consider only conduction electrons we have to sum all electron transitions from the occupied initial state (i) to the non-occupied final states (f)

$$W = \frac{2\pi}{\hbar} \sum_{i,f} f(E_i) [1 - f(E_f)] |\langle \psi_i | \mathcal{H} | \psi_f \rangle|^2 \delta(E_i - E_f + \Delta E), \quad (3.94)$$

where  $|\langle \psi_i | \mathcal{H} | \psi_f \rangle|^2$  is transition matrix element and  $\Delta E$  is the difference between initial and final state Zeeman energy. Changing the summation to the integration we arrive at

$$\frac{1}{T_1} = W = \frac{2\pi}{\hbar} \int |\langle \psi_i | \mathcal{H} | \psi_f \rangle|^2 f(E_i) [1 - f(E_f)] N(E_i) N(E_f) dE_i, \quad (3.95)$$

where  $E_f = E_i + \Delta E$ . From this relation we can easily obtain the Korringa relation (Eq. 3.83) by assuming that Zeeman energy is negligible ( $\Delta E \rightarrow 0$ ) and that the matrix element and the density of states do not change over the temperature interval  $k_B T$  and can be expressed by the Knight shift squared.

To obtain spin-lattice relaxation rate in superconductors we consider the opening of the gap by taking the superconducting density of states and an appropriate matrix element. For the standard BCS superconductors we use BCS density of state (Eq. 3.89) and the matrix element appropriate for the NMR experiment [46, 89],  $|\langle \psi_i | \mathcal{H} | \psi_f \rangle|^2 = M^2 [1 + \Delta^2 / (E_i E_f)]$ . The spin lattice relaxation rate is then written as [90, 91]

$$\frac{1}{T_1} = \frac{2\pi}{\hbar} M^2 \int_0^\infty \text{Re} \left\{ N(E_i) \sqrt{\frac{E_i E_f + \Delta^2}{E_i^2 - \Delta^2}} \right\} \text{Re} \left\{ N(E_f) \sqrt{\frac{E_i E_f + \Delta^2}{E_f^2 - \Delta^2}} \right\} f(E_i) [1 - f(E_f)] dE, \quad (3.96)$$

where  $\Delta E = E_f - E_i = \hbar(\gamma_e + \gamma_n) B_0$  the Zeeman energy, and Re denotes the real part. In principle  $\Delta$  can be generalized to  $\Delta = \Delta(T, E) = \Delta_1 + i\Delta_2$ .

In the BCS limit of real isotropic gap function and small magnetic fields ( $\Delta E \rightarrow 0$ ) the above equation can be simplified to

$$\frac{1}{T_1} = \frac{2\pi}{\hbar} M^2 N(E_F)^2 k_B T \int_\Delta^\infty \frac{E^2 + \Delta(T)^2}{E^2 - \Delta(T)^2} \frac{\partial f(E, T)}{\partial E} dE, \quad (3.97)$$

where  $N(E_F)$  is normal state density of states at the Fermi energy. Here we used relation  $f(E_i) [1 - f(E_f)] = k_B T \partial f(E) / \partial E$  when  $\Delta E \rightarrow 0$ . Due to logarithmic singularity at  $E = \Delta$  in the BCS density of states, the relaxation rate just below the transition temperature does not decrease, as is expected due to opening of the gap, but it increases, reaches a

maximum, and then starts to exponentially decrease with decreasing temperature. This, so-called *Hebel-Slichter* coherence peak, was one of the first experimental confirmations of the BCS theory and is, therefore, a hallmark of conventional BCS superconductivity. In the limit of small temperatures ( $T \ll T_c$ ), where thermally excited quasiparticles come only from the narrow region close to the singularity, the logarithmic singularity could be replaced with a Dirac delta function,  $\delta(E - \Delta(0))$ . In the limit of low temperatures the spin-lattice relaxation rate behaves as an Arrhenius law

$$\frac{1}{T_1} \propto \exp\left(-\frac{\Delta(0)}{k_B T}\right). \quad (3.98)$$

The Hebel-Slichter coherence peak can be suppressed by several factors like the presence of impurities, disorder, magnetic field, strong electron-phonon interaction, strong electron-electron interaction of the anisotropic gap function. All these effects can be modelled by generalized Eq. 3.96 [90, 91] as will be discussed in Sec. 8.2.

### 3.3.6 Magic Angle Spinning NMR

Nuclear magnetic resonance technique has in the recent few decades strongly established in the areas of chemistry and structural biology, mostly due to new techniques like high-resolution NMR spectroscopy which allow scientists to gain information about the molecular structure and configuration dynamics of very large molecules like proteins and DNA [92]. Normally, in powdered samples such detailed information are hidden within broad spectral lines due to various anisotropic interaction, for example, anisotropic chemical shift, dipolar interaction, and the first order quadrupole interaction.

One of the earlier techniques used was dissolving samples in a liquid. Fast reorientations, in a time scale ( $\tau \approx 10^{-11}$ s) much faster than NMR time scale, cause narrowing of anisotropically broadened lines. The factor  $3 \cos^2\theta - 1$ , known as the second order Legendre polynomial, can be found in the first order quadrupole frequency shift (Eq. 3.39), secular part of the Hamiltonian of the dipolar interaction

$$\mathcal{H}_{d,sec} = \frac{\mu_0 \gamma_e \gamma_n \hbar^2}{4\pi r^3} \sum_j \left[ I_z S_z - \frac{1}{2}(I_x S_x + I_y S_y) \right] (1 - 3 \cos^2\theta_j), \quad (3.99)$$

or the anisotropic chemical or Knight shift expressed in axially symmetric second order tensor [67]

$$\sigma(\theta) = \sigma_{iso} + (\sigma_{||} - \sigma_{iso}) \left( \frac{3 \cos^2\theta - 1}{2} \right), \quad (3.100)$$

where  $\theta$  is angle from the principal axis and  $\sigma_{||}$  is the longitudinal shift component perpendicular to the principal axis. The fast isotropic reorientation of molecules reduces the effects of the mentioned terms because the integral

$$\int (3 \cos^2\theta - 1) d\Omega \quad (3.101)$$

over the sphere vanishes. Here  $d\Omega$  is the element of the spherical angle.

Dissolving material in a liquid solvent is not always appropriate, especially when studying solid state materials with interesting molecular or electronic interactions. Similar line narrowing as in the liquid case can be obtained also for this materials when they are physically rotated by the "magic" angle with respect to the external magnetic field.

This technique is thus called the magic angle spinning (MAS) NMR. By rotating the sample around an axis tilted by  $\theta_M$  from the external magnetic field, the angle  $\theta$  in the  $(3 \cos^2\theta - 1)$  expressions oscillates around  $\theta_M$  value and if this rotation is fast enough (larger than the linewidth) the angle can be replaced by the average value,  $\theta_M$ . The same conclusion can be obtained by the transformation of the second order Legendre polynomial into the rotating reference frame with the means of addition theorem of spherical harmonics [67]. Setting  $\theta_M$  to the magic angle value for which

$$3 \cos^2\theta_M - 1 = 0, \quad \theta_M = 54.7^\circ, \quad (3.102)$$

the solid state NMR lines become narrowed in a similar fashion as in the liquid state.

The limit of fast rotation is in practical cases not always met. The highest spinning frequencies with the modern MAS rotor heads can reach up to  $\nu_r = 70$  kHz [74], however, the linewidths, especially at low temperatures can be still larger. In such case the side bands, theoretically Dirac delta functions, can be observed in the spectrum separated by  $\pm N \nu_r$ , where  $N$  is an integer number. By increasing the rotation frequency the side bands move further away having less intensity and finally vanish when rotation frequency exceeds the resonance linewidth.

### 3.4 High Pressure Experiments

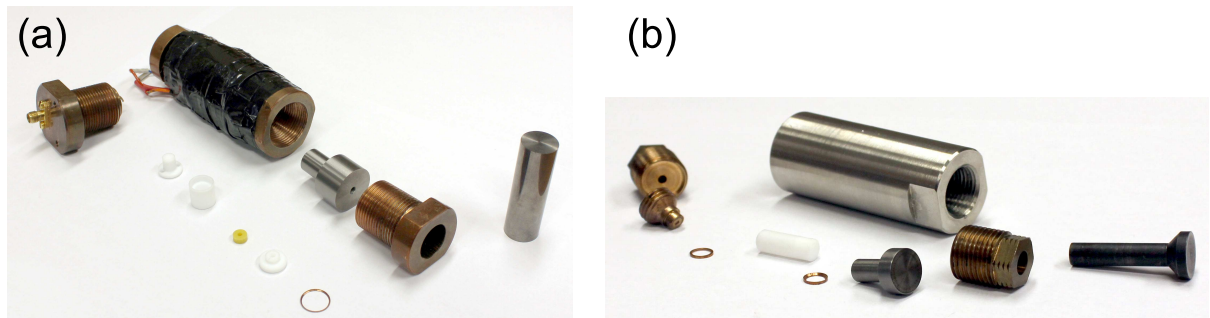


Figure 3.2: Photography of (a) high-pressure EPR cell and (b) high-pressure NMR cell.

One of the aims of this thesis was to develop extensions to the EPR and NMR spectrometers that would enable one to vary an additional degree of freedom – the hydrostatic pressure. In this subsection two newly built piston cylinder clamp-type cells are presented (Fig. 3.2). Each cell is adapted to the spectrometer configuration and cryostat's size, as well as the electromagnetic wave-length used to probe the sample's magnetic moments during the magnetic resonance measurement.

The high hydrostatic pressure in the clamp-type cells is produced by sealing the bottom part of the cylindrical cell. Then after loading the central chamber with Teflon holder a coil or a dielectric resonator and sample, this chamber is filled with the pressure transmitting medium that ensures hydrostatic conditions. The chamber is then sealed with anti-extrusion sealing ring and a piston. Piston is slightly pressed and locked by the locknut (Fig. 3.3). High pressure (HP) is achieved by pressing directly on the piston by strong metallic rod, so-called, plunger using a large industry press. By pushing the piston inwards the locknut becomes loose, which allows one to easily screw it further inwards to piston. After the industrial press is released the force is transferred to the locknut

which maintains the high pressure in the chamber. Loaded cell is then prepared for the measurements.

Main challenges in developing such HP probes are:

- achieve high hydrostatic pressures,
- *in-situ* measurement of the pressure,
- reduce leakage possibility while cells are used over a large temperature and pressure ranges,
- in case of EPR probe, achieve optimal coupling between the waveguide and the inner microwave resonator,
- design non-magnetic and small enough cell to fit the cryostat inserted in magnets with high magnetic field.

In the following sections solution to the above challenges are described in details.

### 3.4.1 High-Pressure EPR

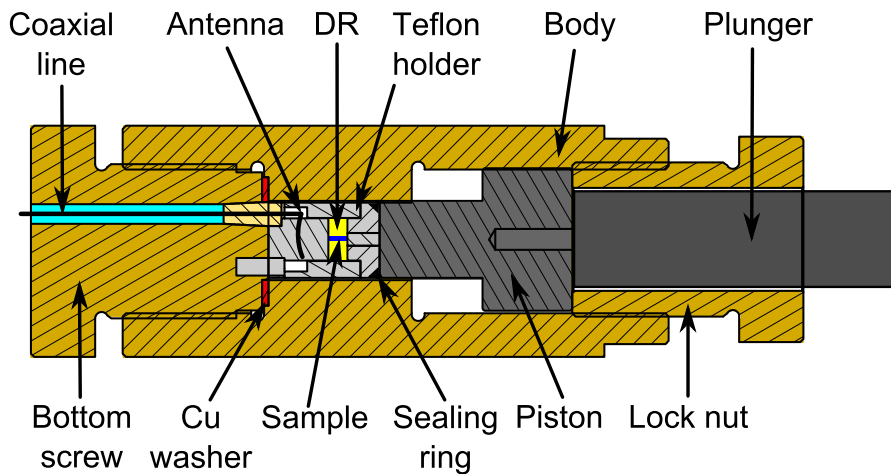


Figure 3.3: Drawing of the assembled high-pressure EPR cell.

The assembly of the main parts of high-pressure EPR cell is illustrated in Fig. 3.3. For this experiment the clamp-type cell was adapted by making the pressurised chamber a microwave resonator. In addition, a special care was taken to achieve good coupling between the waveguide and the resonator surrounded by thick metallic walls. The cell was designed to fit into the Oxford cryostat CF935 in vertical orientation. Its length is 120 mm and diameter cca. 36 mm (see App. A.1.1). Most of the cell was made by hardened non-magnetic BeCu alloy, only the piston and the plunger were made by non-magnetic WC with higher tensile strength.

To establish a high-quality microwave resonator inside the pressure cell we used a commercial ceramics dielectric resonator (DR) with unloaded  $Q$ -factor of  $\sim 10000$ . Its large dielectric constant ( $\epsilon \approx 30$ ) effectively confines the electromagnetic waves to the resonator. In principle, the confinement is not complete; the electromagnetic field decays exponentially outside the resonator, which is determined by the difference of the dielectric

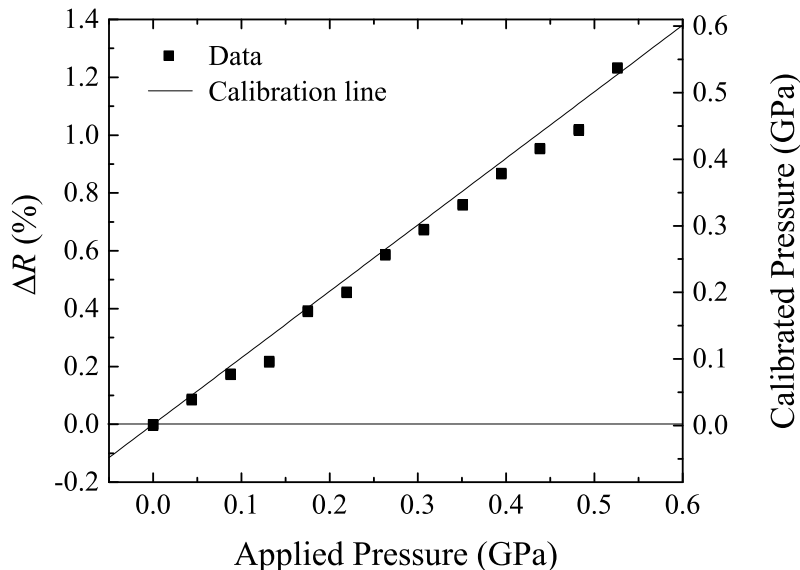


Figure 3.4: Change of resistance of cca. 30 cm long manganine wire in high-pressure EPR cell as a function of calculated applied pressure at room temperature. Tilted line corresponds the resistance change calculated from the calibration data found in literature [97].

constant between DR and surrounding medium ( $\epsilon \approx 2$ ). The boundary conditions set by the conducting walls of the pressure chamber, therefore, only slightly influence the resonator frequency. DR have been used before for the EPR experiments [93–95] and even for high-pressure experiments [96], but were never used inside a clamped-type cell. Such configuration for the first time allows large sample volumes, better resonant quality factors and better optimal microwave coupling. A detailed description with all technical details of the EPR high-pressure cell can be found in App. A.1.1.

A successful coupling between the waveguide and the resonator was achieved using an electric coupling system with  $\lambda/4$  L-shaped antenna. The microwaves are brought to the central chamber surrounded by thick metallic walls through a coaxial line made in the bottom screw. At the end of this cable a conducting wire was shaped in the L-shaped antenna pointing along the eigenmode’s electric field (See App. A.1.2). In this way a quality factor of  $Q \approx 3000 - 6000$  was achieved at frequencies of approx. 9.4 GHz. The coupling strength strongly depends on the precise DR position and on the amount and type of sample. Empirically, a precise positioning of both is required to obtain high  $Q$ -factor and optimal coupling strength. Due to static geometry of the coupling system no direct coupling optimization is possible during the measurements. To some extent the coupling can be optimized by using external slight-screw tuner.

Relatively large coaxial line window is often a source of pressure transmitting medium leakage. For this reason a conical ceramics cork was manufactured to avoid the leakage (Fig 3.3). Leakage is further reduced with the copper wisher at the bottom screw side and the anti-extrusion ring at the piston side.

The pressure in the EPR high-pressure cell as a function of applied force was calibrated at room temperature with the manganine wire. The manganine is known to have linear pressure dependent resistivity with a slope of 2.3%/GPa [97]. The manganine resistivity change and the corresponding calculated values using the above coefficient is shown in Fig. 3.4. The datapoints were obtained by calculating the applied pressure from

the applied force and the pistons incident surface. The agreement between measured and calculated resistance change (shown by the calibration line) is excellent. At low temperatures a drop of cca. 0.3 GPa is expected when cooling from room temperature to the liquid nitrogen temperatures [98] and is nearly independent at even lower temperatures.

### 3.4.2 High-Pressure NMR

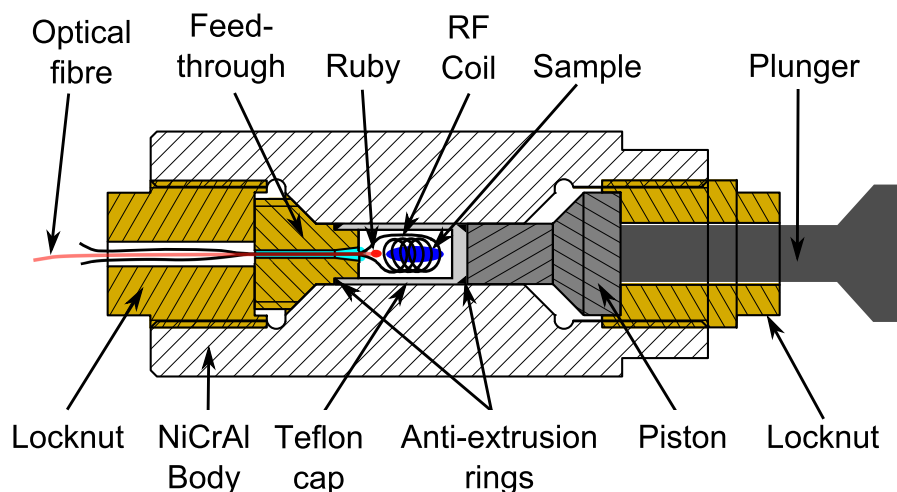


Figure 3.5: Drawing of the assembled high-pressure NMR cell.

Piston cylinder clamped-type cell made for high-pressure NMR experiments is shown in Fig. 3.5. This cell was constructed to fit in the NMR cryostat in the horizontal orientation, perpendicular to the external magnetic field. Its length is thus cca. 53 mm and diameter is 20 mm. In the NMR experiment it is sufficient to pressurize the RF coil containing the sample and not the whole resonator setup as is the case with the EPR experiment. This simplifies the construction of the cell and allows even higher pressures. To achieve the highest pressures a special and rare non-magnetic NiCrAl material [99] was used for the construction of the cell's body. The geometry and the use of NiCrAl allows maximal pressures of 2 GPa for large sample quantities of several mg. Detailed drawings are given in App. A.2.

The high-pressure experiment is prepared first by constructing a feed-through with RF coil and an optical fibre with ruby powder attached at the end of the fibre (see App. A.2.1). Next, the sample is mounted inside the coil, usually wrapped in the Teflon tape, and together with the feed-through and the anti-extrusion ring covered by the Teflon cap that was previously filled with pressure transmitting medium. Assembled feed-through was inserted into the body and locked by the locknut. From the other end the second anti-extrusion ring was inserted together with the piston and pressed with the second locknut. High pressures were achieved using the plunger and external press as discussed above.

The pressure transmitting medium is selected depending on the type of NMR measurements. For  $^{13}\text{C}$  NMR measurements a silicon oil is used since it does not contain carbon atoms. For other measurements e.g.  $^{133}\text{Cs}$  or  $^{87}\text{Rb}$  a mixture of 1:1 Fluorinert FC70 and FC770 is normally used. In the pressure range used in our experiments (up to 2 GPa) all these pressure media maintain acceptable hydrostatic conditions in the pressure range of our experiments [100, 101].

## Pressure Calibration

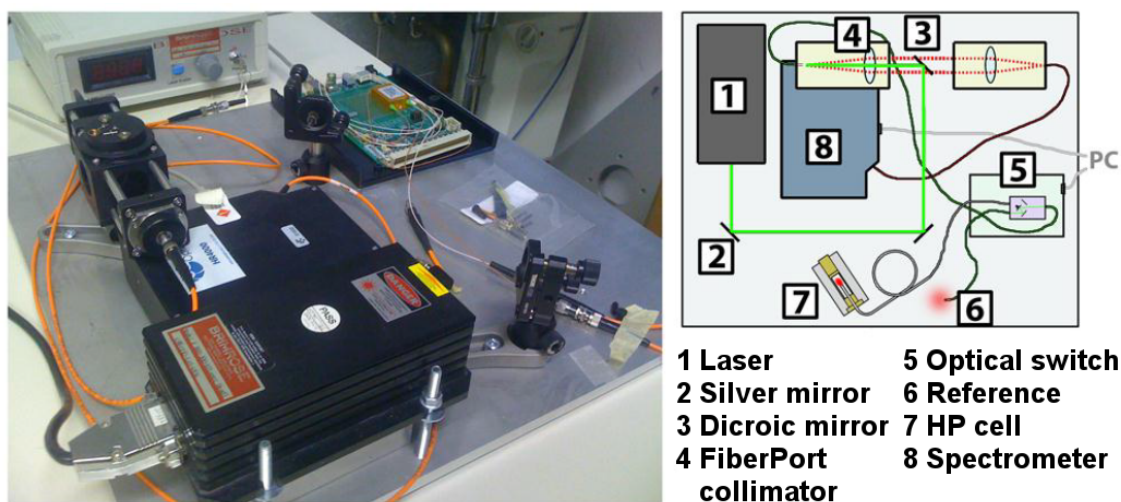


Figure 3.6: Optical spectrometer for measuring the ruby fluorescence shift induced by applied hydrostatic pressure inside the cell. The spectrometer was designed for measuring two ruby samples.

For the high-pressure NMR experiments presented in this thesis the precise *in situ* pressure determination at various temperatures is crucial. To be able to measure the pressure we use ruby fluorescent lineshift as a function of pressure, a technique that is well documented in the literature [102–104]. Besides the shift due to pressure, the fluorescence lines also strongly shift with temperature. To accurately measure the pressure independently of temperature we constructed a two channel optical spectrometer for measuring ruby fluorescence (Fig. 3.6). Spectrometer details can be found in App. A.2.2. An optical switch was introduced to switch by demand between the ruby sample inside the high-pressure cell and the reference sample that was mounted outside touching the cell’s exterior. In this way the two ruby samples are both at the same temperature in the cryostat during the measurement. In reality the temperature inside and outside the high-pressure cell is not exactly the same. Above cca. 50 K this difference is less than 1 K, but at low temperatures the difference can be up to 4 K. Fortunately, the ruby’s lineshift as a function of temperature is temperature independent below cca. 75 K [105] and, therefore, the pressure error due to temperature effects is negligible over the whole temperature range. The pressure is thus determined from the ruby fluorescence lineshift difference between the ruby inside the cell and the reference ruby. The difference between the two samples line position is, thus, solely due to the pressure difference.

Ruby ( $\text{Al}_3\text{O}_4:\text{Cr}^{3+}$ ), the corundum crystal with  $\text{Cr}^{3+}$  impurities substituted for Al atoms, has a fluorescence spectrum that consists of several lines (Fig. 3.7), two strong ones ( $R_1$  and  $R_2$  at 692.9 and 694.4 nm, respectively) correspond to transitions between the first excited and the ground state of the chromium  $d^3$  electrons. The splitting between the lines is due to combined trigonal crystal distortion and the spin-orbit coupling. There are also two notable weaker lines at larger wavelengths that correspond to the exchange coupled  $\text{Cr}^{3+}$  neighbours,  $N_1$  line at 704.9 nm and  $N_2$  line at 701.7 nm [103]. In Fig. 3.7 an optical spectrum is shown for ambient and 1.4 GPa pressures at 28 K and in the 9.34 T magnetic field of the NMR magnet. It can be seen that all four lines shift under pressure and that  $R_1$  and  $R_2$  lines have Zeeman splitting due to the four-fold multiplicity of the  $\text{Cr}^{3+}$  ground state. Due to this splitting the precise determination of the pressure from  $R_1$

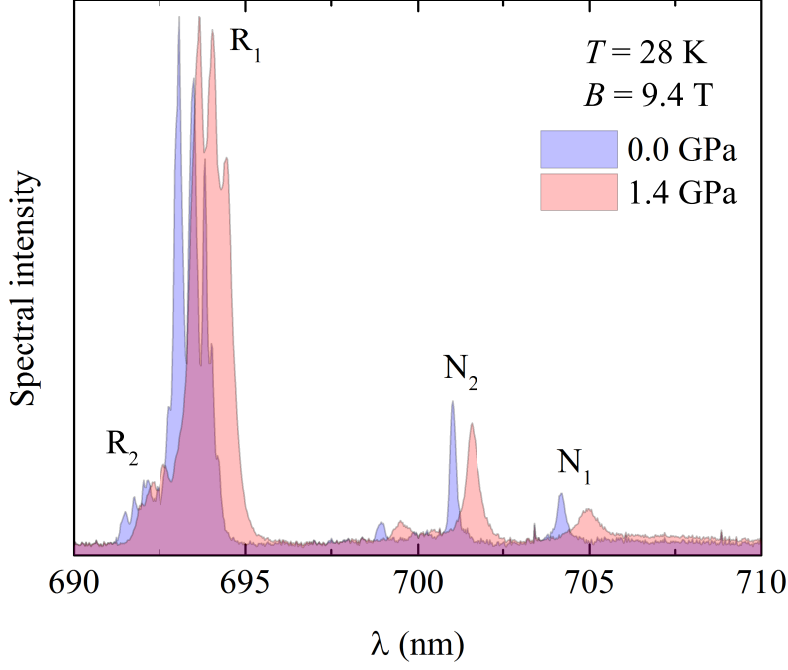


Figure 3.7: Optical spectrometer for measuring the ruby fluorescence in the NMR high-pressure cell as well as the reference ruby powder.

or  $R_2$  lines is rather difficult in the magnetic field. For this reason we chose  $N_2$  line for the pressure measurements, even-though, its intensity is very weak at room-temperature. The pressure determination at high-temperatures has, therefore, large errorbars, however, at lower temperatures the pressure determination gets more accurate. For pressure range up to 2.0 GPa all ruby lineshifts are linear functions of the pressure. The linear coefficient ( $dp/d\lambda$ ) for the  $N_2$  line was obtain by fitting the data reported in Ref. [102]. After  $N_2$  coefficient was obtained it was used to determine pressure for all experiments. The pressure coefficients for  $R_1$ ,  $N_2$ , and  $N_1$  lines are for comparison summarized in Tab. 3.1. The precise position of the  $N_2$  line was obtained by fitting Lorentzian function to the  $N_2$  line.

	$R_1$	$N_2$	$N_1$
$dp/d\lambda$ [GPa/nm]	2.740 [104]	<b>1.88(4)</b> [102]	2.43(4) [102]

Table 3.1: Linear coefficients of the three calibrated fluorescence lines.  $N_2$  and  $N_1$  values were obtained by fitting data in Ref. [102].

## 4 Importance of $t_{1u}$ degeneracy

Electronic and magnetic properties are in metallic and superconducting alkali-doped fullerenes believed to be controlled by a single parameter, the unit-cell volume. For example, by changing the unit-cell volume the entire phase diagram of  $A_3C_{60}$  can be obtained [14]. The metallic and superconducting properties were also found to be very sensitive to the crystal symmetry where even a small discrepancy away from cubic symmetry results in the Mott-insulating ground state, despite having similar unit-cell volume compared to the metallic compounds. This is for example the case for  $NH_3Rb_xK_{3-x}C_{60}$  [17, 35] and  $MAK_3C_{60}$  [36, 37]. There are two important questions: why these compounds lose their metallic character and whether metallic and superconducting properties can be restored in non-cubic materials.

In this chapter we will try to answer these questions by presenting the high-pressure EPR measurements and electronic band structure calculations on orthorhombic compound  $MAK_3C_{60}$ .

### 4.1 Cubic vs. Non-Cubic Crystal Symmetry

Isolated  $C_{60}$  molecule has triply-degenerate  $t_{1u}$  lowest unoccupied orbitals. They can be viewed as three  $p$ -like orbitals pointing in all three dimensions ( $x$ ,  $y$ , and  $z$ ). When  $C_{60}$  molecules form a crystal,  $fcc$  crystal structure maintains (Wannier)  $t_{1u}$  orbital degeneracy which is reflected by the triply-degenerate  $\Gamma$  point in the electronic band structure [24, 51]. Since the intercalation of three alkali metals do not remove the cubic crystal symmetry either, the degeneracy of the  $\Gamma$  point remains even after the intercalation and charging of  $C_{60}$  molecule. On the other hand, in compounds with removed cubic crystal symmetry due to intercalation of anisotropic molecules as in  $NH_3Rb_xK_{3-x}C_{60}$  and  $MAK_3C_{60}$  the three (Wannier)  $t_{1u}$  orbitals are no longer equivalent and the degeneracy in the  $\Gamma$  is lost [39]. If the intercalated molecules act only as spacers and not directly influence the electronic structure, the observed different ground states can be attributed to the  $t_{1u}$  degeneracy in the  $\Gamma$  point and the presence of strong electron correlations.

The role of orbital degeneracy on the ground state was studied by O. Gunnarsson *et al.* [106]. They found out that the critical ratio  $(U/W)_c$  at which the system goes through MIT depends on the degeneracy relevant orbitals, roughly as  $(U/W)_c = \sqrt{N_d}$ , where  $N_d$  is the number of degenerate orbitals.<sup>1</sup> In addition, the crystal lattice and possible frustration effects can further increase the critical ratio up to  $(U/W)_c = 2.5$  [5]. A detailed study gave in case of  $fcc$   $A_3C_{60}$  systems a critical ratio is  $(U/W)_c = 2.3$  [5]. This analysis is in agreement with the experimentally determined metallic ground state, although the estimated bandwidth,  $W$ , is by a factor of  $\sim 2$  smaller than the Coulomb

---

<sup>1</sup>Derivation of this expression is given in Sec. 7.2.1

repulsion energy,  $U$  [7].

Now, the question remains is what would happens if the degeneracy is gradually removed. N. Manini *et al.* [39] studied this problem with DMFT using two-orbital Hubbard model with a variable orbital splitting ( $\Delta$ ) and searched for MIT. They constructed Manini, Santoro, Dal Corso, Tosatti (MSDT) phase diagram where DMFT two-band critical ratio  $(U/W)_c = 1.7$  for  $\Delta/W = 0$  steeply decreases as a function  $\Delta/W$  down to a one-band critical ratio  $(U/W)_c \approx 1.3$  which is independent of  $\Delta/W$ . Adapted MSDT phase diagram is shown in Fig. 4.4. The difference between the two-orbital and single-orbital critical ratios is by a factor of  $1.8/1.3 = 1.4$ , which is close to the Gunnarsson's prediction of  $\sqrt{2} = 1.41$ . A steep nearly linear dependence of the critical ratio can be understood as follows: the effect of the strong electron correlations can be within the Fermi liquid theory modelled as a renormalization of the charge carrier particles' mass. The renormalization factor, the quasiparticle weight,  $z$ , consequently renormalizes the conduction bandwidth,  $zW$  [39]. The transition to the insulating state will occur when the orbital splitting ( $\Delta$ ) exceeds the renormalized quasiparticle bandwidth ( $\Delta \sim zW$ ). The amount of orbital splitting that is required to push the system over MIT is thus inversely proportional to the strength of electron correlations ( $1/z$ ).

This analysis suggests that  $A_3C_{60}$  are all strongly correlated. Next interesting question is how close to MIT are  $NH_3K_3C_{60}$  and  $MAK_3C_{60}$  compounds..

## 4.2 $MAK_3C_{60}$ under High Pressure

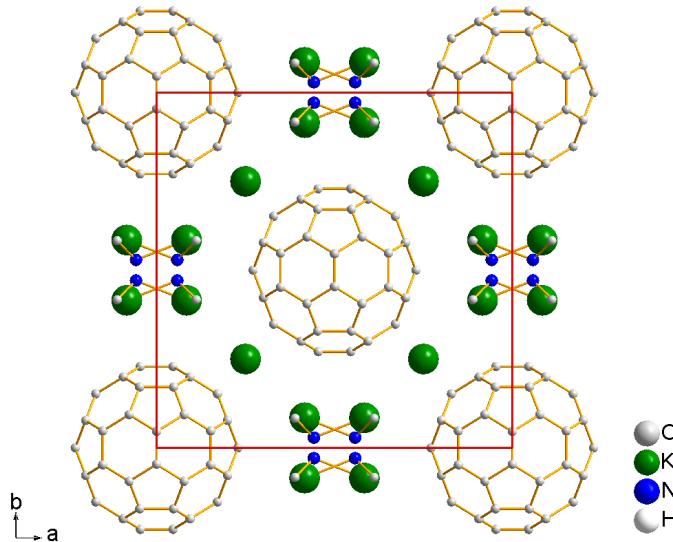


Figure 4.1: The unit-cell atom arrangement of the  $MAK_3C_{60}$  compound.  $MA^-K^+$  groups are disordered between four equivalent positions in the octahedral interstitial sites. All four possible configurations are shown. In addition,  $C_{60}$  molecules are merohedrally disordered, not shown.

To explore the effects of crystal anisotropy on the ground state we decided to study  $MAK_3C_{60}$ , where relatively large anisotropic  $CH_3NH_2$  molecules stabilize the face centred orthorhombic unit cell [36]. Methyl-amine molecules reside in the large octahedral interstitial sites where they are coordinated with potassium anion. The other two potassium anions are positioned in the smaller tetrahedral interstitial sites. The presence of MAK groups distorts the cubic symmetry with yielding a cell parameter ratios  $b/a = 0.9985$

and  $c/a = 0.8882$ . Crystal structure is shown in Fig. 4.1 and further details can be found in App. B.3.1. Its large unit-cell volume ( $V = 779.1(1)\text{\AA}^3$ ) is still smaller than the critical volume for face-centred cubic compounds ( $V_c = 799.7(3)\text{\AA}^3$  at RT) [14] and by neglecting 11% distortion of the  $c$ -axis one would expect a metallic ground state. However, it has been experimentally shown that the  $\text{MAK}_3\text{C}_{60}$  is an insulator at ambient pressure with an antiferromagnetic long range order at surprisingly low Néel temperature of  $T_N = 11\text{ K}$  [18, 37, 107, 108].

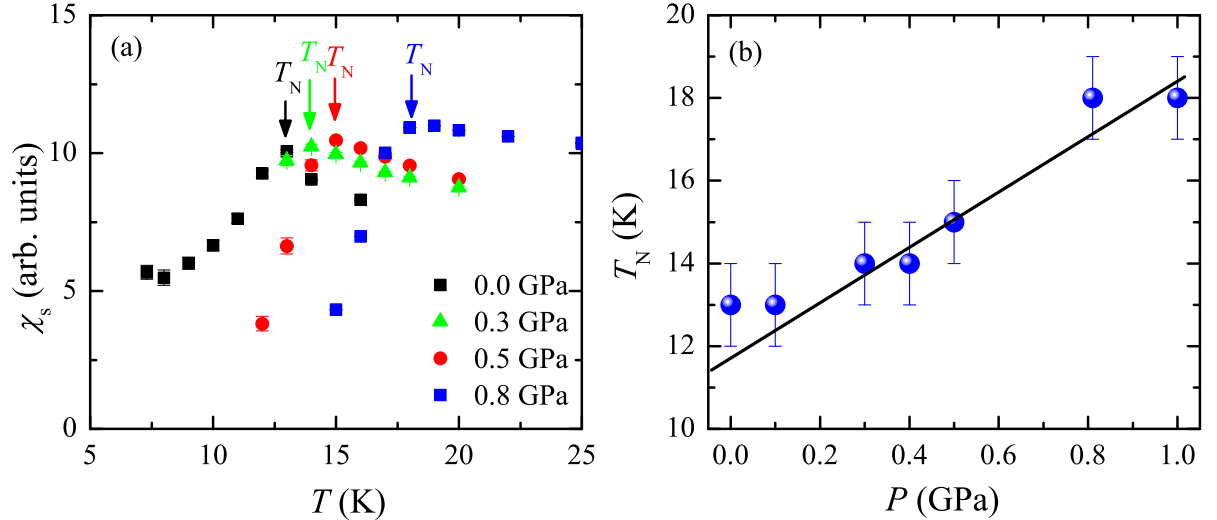


Figure 4.2: EPR signal intensity as a function of temperature and nominal pressure. Only the transition to the antiferromagnetic state could be observed at low temperatures.

Drastic change in the ground state could be explained by a strong response on lifting of the  $t_{1u}$  orbital degeneracy by the orthorhombic crystal field. To test how sensitive the ground state is on the crystal field anisotropy we performed high-pressure EPR experiments reaching 7 kbar at low temperatures ( $\sim 10\text{ K}$ ). We measured the electron spin susceptibility<sup>2</sup>,  $\chi_s$ , as a function of temperature and pressure. Without applied pressure we observe at 13(1) K a sudden drop of spin susceptibility. A similar drop has been previously observed at 11 K and recognized as the onset of the AFM order [18], thus we relate the measured  $\chi_s$  drop to the AFM transition. With increasing pressures we observed an increase of Néel temperature going from 11 K at ambient pressure to 18 K at the maximal applied nominal pressure of 10 kbar (Fig. 4.2). Taking into account that the pressure drops for about 3 kbar on cooling from room-temperature to liquid nitrogen temperatures  $\sim 77\text{ K}$ , the slope of the Néel temperature increase as a function of pressure is 1.0(3) K/kbar. Such increase of Néel temperature is expected as the exchange interaction constants between neighbouring  $\text{C}_{60}$  molecules depend on the overlap of their electronic orbitals, which increase as the unit-cell volume decreases or the applied pressure increases.

We note that no transition to a metallic or a superconducting state could be found up to 7 kbar at low temperatures. The smallest obtained volume at 7 kbar and  $\sim 30\text{ K}$  is  $V_{\min} = 730(2)\text{\AA}^3$  which is estimated from compressibility and thermal contraction data (App. B.3.1).  $V_{\min}$  is considerably lower (7.1%) than the critical volume at which *fcc* compounds go through MIT ( $V_c^{\text{LT}} = 786.0\text{\AA}^3$ ) [14]. We ascribe the stability of the insulating state to the breaking of the cubic symmetry.  $V_{\min} = 730(2)\text{\AA}^3$  now represents the upper limit of the critical volume for orthorhombic alkali fullerenes.

<sup>2</sup>Electrons spin susceptibility is proportional to the EPR signal intensity as discussed in Sec. 3.2.2.

### 4.3 DFT study of $\text{MAK}_3\text{C}_{60}$

We have shown that the ground state sensitively depends on deviation from the cubic symmetry. To quantify this dependence and explore the MSDT phase diagram [39], we performed DFT calculation on face-centred orthorhombic  $\text{MAK}_3\text{C}_{60}$  crystal structure within the LDA approximation. Technical details of these DFT computations are given in App. B.3.4.

The three metallic  $t_{1u}$  bands are well isolated from other molecular orbital-derived bands as is the case with every fullerene compound [5]. The band gap between “ $\text{C}_{60}$  HOMO” ( $h_u$ -derived bands) and “ $\text{C}_{60}$  LUMO” ( $t_{1u}$ -derived bands) is 0.96 eV, while the separation between “ $\text{C}_{60}$  LUMO” and “ $\text{C}_{60}$  LUMO+1” ( $t_{1g}$ -derived bands) is 0.59 eV. For comparison we refer here to the corresponding gaps of 1.16 eV and 0.38 eV computed for cubic  $\text{K}_3\text{C}_{60}$  [50], and to the experimental values, roughly 1.8 eV and 1 eV respectively [109]. The underestimation of the band gaps, standard for LDA calculations, is fortunately of little consequence in our case. The neat separation of the different band groups allows us to focus entirely on  $t_{1u}$ -derived bands close to the Fermi energy (Fig. 4.3). Not surprisingly, bare DFT-LDA nonmagnetic calculations yield for  $\text{MAK}_3\text{C}_{60}$  a metallic ground state with a half-filled  $t_{1u}$  band. However, as we have already pointed out several experiments proofs that  $\text{MAK}_3\text{C}_{60}$  is an insulator which clearly suggests that the mean-field DFT metallic state is driven to Mott-Hubbard insulating state by electron correlations.

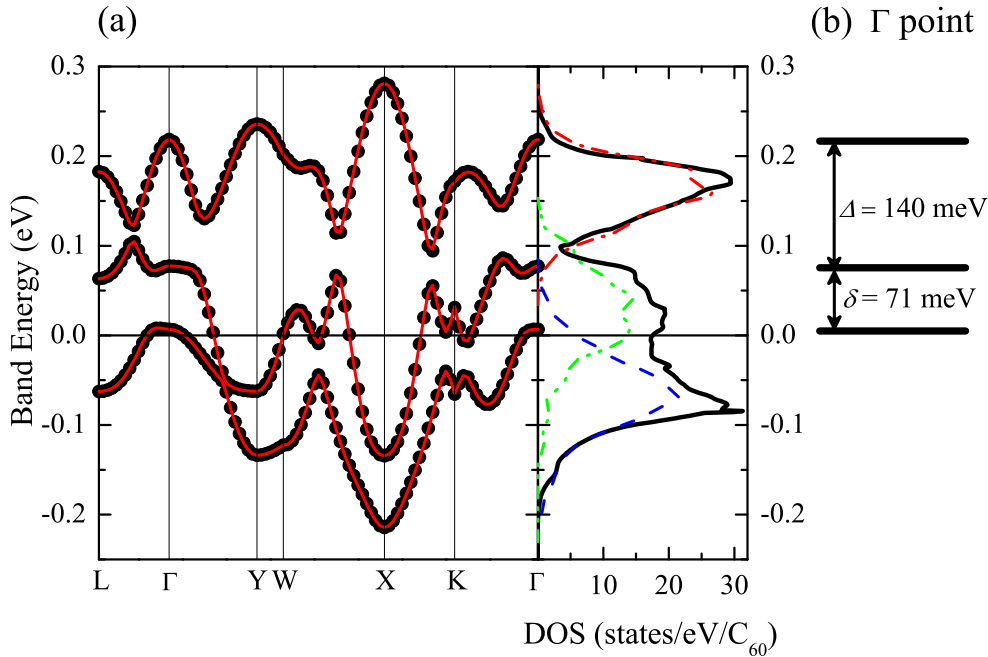


Figure 4.3: (a) Band-structure and DOS for the room temperature  $\text{MAK}_3\text{C}_{60}$  crystal structure. Red solid line is the interpolated band-structure using the maximally localized Wannier orbitals - see text for details. Black solid line: the total DOS; the red dot-dashed line, green dash-dot-dotted line, and blue dashed line represent the projected DOS on the first, second and the third Wannier orbital, respectively. (b) The splitting of  $t_{1u}$  bands at the  $\Gamma$  point, defining the orthorhombic crystal-field anisotropy.

Orthorhombic crystal symmetry is reflected in the band-structure [Fig. 4.3(a)] by (i) the removal of the threefold degeneracy at the  $\Gamma$  point [Fig. 4.3(b)]; and (ii) the inequivalence of Y and X points. At the  $\Gamma$  point we compute an energy splitting between

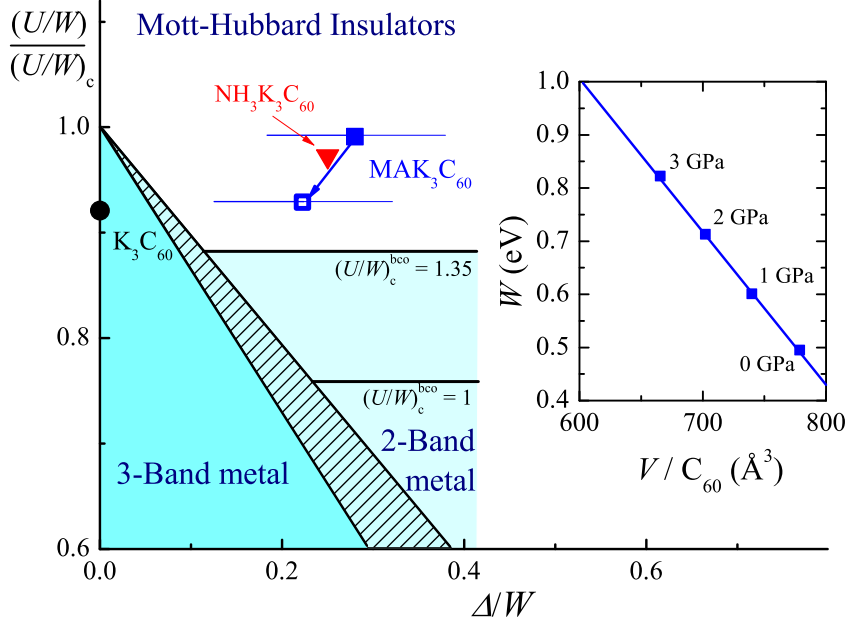


Figure 4.4: MSDT phase diagram for fullerides adapted from Ref. 39 including  $\text{MAK}_3\text{C}_{60}$  (blue full square for ambient conditions and blue empty square for low temperature, high pressure condition),  $\text{NH}_3\text{K}_3\text{C}_{60}$  (red triangle), and  $\text{K}_3\text{C}_{60}$  (black circle). Two black vertical lines indicate expected MIT transitions for non-degenerate case assuming  $(U/W)_c = 1.35$  and  $1.0$ . Inset: Volume dependence of the bandwidth computed by means of DFT-LDA for the room-temperature  $\text{MAK}_3\text{C}_{60}$  structure.

the first and the second and between the second and the third  $t_{1u}$  energy levels of  $\delta = 71$  meV and  $\Delta = 140$  meV, respectively. For comparison, the corresponding energy splittings for  $\text{NH}_3\text{K}_3\text{C}_{60}$  are  $\delta \approx 30$  meV and  $\Delta \approx 150$  eV [39]. In general,  $\Delta$  reflects the main orthorhombic crystal-field anisotropy and  $\delta$  tracks the smaller anisotropy in the  $ab$  plane. Surprisingly, band-structure anisotropies of the two systems are very much comparable despite some obvious crystallographic differences, like for instance the ratio  $c/a$ , which is 0.89 and 0.91 for  $\text{MAK}_3\text{C}_{60}$  and  $\text{NH}_3\text{K}_3\text{C}_{60}$ , respectively. The resulting total  $t_{1u}$  density of states (DOS), roughly shaped in three peaks, and shown in Fig. 4.3(a) resembles that of  $\text{NH}_3\text{K}_3\text{C}_{60}$  [39]. We obtain a quite large DOS at the Fermi energy,  $N(E_F) = 17$  states/eV/ $C_{60}$ , which is a result of expanded lattice structure and the resulting smaller bandwidth  $W = 0.50$  eV. For comparison, we refer here to the  $W \approx 0.6$  eV reported for  $\text{NH}_3\text{K}_3\text{C}_{60}$  and  $\text{K}_3\text{C}_{60}$ , which are characterized by smaller unit cells [39].

The above results allow us to place  $\text{MAK}_3\text{C}_{60}$  on the MSDT phase diagram. Manini *et. al.* [39] used  $\Delta/W$  as a measure of the anisotropy, which also defines the distance to the MIT boundary in non-cubic fullerides. For  $\text{MAK}_3\text{C}_{60}$  the anisotropy ratio is  $\Delta/W = 0.29$ , which is slightly larger than the value for  $\text{NH}_3\text{K}_3\text{C}_{60}$  ( $\Delta/W = 0.25$ ) and thus deeper in the Mott-insulating phase and further away from the 3-band metallic phase. Since critical value  $(U/W)_c$  depends on the crystal geometry we cannot compare experimental value for  $fcc$  structure to the DMFT result computed in the Bethe lattice. We instead plot the normalized ratio  $(U/W)/(U/W)_c$  as a function of  $\Delta/W$ . Normalized  $U/W$  can be expressed also as  $(U/W)/(U/W)_c \sim W_c/W \sim V/V_c$  in the limit where bandwidth is a linear function of pressure. In Fig. 4.4 we show the resulting phase diagram together with  $\text{K}_3\text{C}_{60}$  and  $\text{NH}_3\text{K}_3\text{C}_{60}$  positions. The boundaries between different phases are at this level given only schematically from the DMFT results for two-band system. For this reason

we draw a shaded area that represents the uncertainty of the line where the anisotropy is large enough to reduce the number of effectively degenerate bands and two horizontal lines which indicate the MIT in the reduced band region for two hypothetical *bco* critical ratios, 1.35 from DMFT results and 1 as one would expect for a non-degenerate case. For obtaining this values we used  $U = 1$  eV.

Application of the hydrostatic pressure increases the bandwidth and consequently reduces  $U/W$  and  $\Delta/W$  ratios. With our experimental results we can set experimental limits in the MSDT phase diagram. To add  $\text{MAK}_3\text{C}_{60}$  under hydrostatic pressure of 0.7 kbar and low temperature ( $T \approx 10$  K) on the MSDT phase diagram we compute the bandwidth as a function of decreasing unit-cell volume, mimicking the effect of an external pressure. The pressure dependence of the unit-cell parameters was taken from the high-resolution X-ray data measured under hydrostatic conditions (App. B.3.1). To prevent unphysical contact between  $\text{C}_{60}$  and MA groups we carried out a structural optimization for each volume. The bandwidth increases monotonically with decreasing unit-cell volume, or increasing pressure, with the slope of  $dW/dP = 100$  meV/GPa (inset to Fig. 4.4). In the limit of large  $U$  ( $U \gg t$ , where  $t \propto W$  is the hopping integral) the Hubbard model can be mapped on to the antiferromagnetic Heisenberg model with  $J \propto -t^2/U$  [69]. Since the Néel temperature is proportional to the antiferromagnetic exchange coupling between the spins, we estimate  $T_N(1 \text{ GPa})/T_N(0) \sim (W/W_0)^2 = 1.44$ , which gives  $T_N(1 \text{ GPa}) = 16$  K. This is comparable to our experimental value of  $T_N(0.7 \text{ GPa}) = 18(1)$  K.

The position of  $\text{MAK}_3\text{C}_{60}$  at high-pressure and low temperature is also depicted in Fig. 4.4. This point ( $\Delta/W \simeq 0.2(1)$  and  $(U/W)/(U/W)_c = 0.93$ ) now represents the upper limit for the insulating state in the MSDT phase diagram. By using relation obtained by MSDT [39],  $\Delta \sim zW$ , the Fermi-theory renormalization parameter can be estimated as  $z < 0.2$  at  $(U/W)/(U/W)_c = 0.93$ . We note that the band splitting  $\Delta$  notably changes with the structural difference caused by the optimization of high-pressure structures. To account for this effects we included  $x$ -axis error bar of 15% denoted by blue vertical lines attached to the  $\text{MAK}_3\text{C}_{60}$  points.

At the end we note that the orbital splitting used in the above study might not be best described by the splitting in the  $\Gamma$  point. Energy in the  $\Gamma$  is within tight-binding approximation calculated as  $\varepsilon_i(k=0) = a_i + \sum_n t_{in}$ , where  $n$  counts the nearest neighbours and  $a_i$  is the energy of  $i$ -th Wannier orbital. Since the hopping integrals become strongly reduced near MIT, due to strong renormalization, level splitting should be calculated as a difference between Wannier orbital energies,  $a_i$ .

## 4.4 Conclusions

The effects of  $t_{1u}$  degeneracy have been studied with a face-centred orthorhombic  $\text{MAK}_3\text{C}_{60}$  compound were studied by high-pressure EPR technique and electronic structure calculations. We have shown that orthorhombic compounds immediately become insulating due to strongly renormalized (reduced)  $t_{1u}$  bandwidth caused by strong electron correlations. We were unable to obtain a metallic phase even under the maximal pressure of 7 kbar. Instead we estimated the position of  $\text{MAK}_3\text{C}_{60}$  on the MSDT phase diagram, from where we conclude that  $\text{MAK}_3\text{C}_{60}$  is deeper in the insulating phase than  $\text{NH}_3\text{K}_3\text{C}_{60}$  and that the application of the hydrostatic pressure reduces the sample's anisotropy to  $\Delta/W = 0.2(1)$  at  $(U/W)/(U/W)_c = 0.93$ , where the system is still insulating.

# 5 Importance of $C_{60}$ distortions

The unique properties of fullerene systems can be to a large extent attributed to the high icosahedral symmetry of  $C_{60}$  molecule. High stability and stiffness of  $C_{60}$  molecules preserve its high symmetry even when small crystal fields are present, e.g., in solid state. For this reason effects due to removal of high molecular symmetry were studied less extensively. Nevertheless, these effects are believed to be important for electronic and magnetic properties. In this chapter we will study effects of molecular distortions in two different cases: the distortion due to Jahn-Teller effect and distortions due to steric effects.

## 5.1 Jahn-Teller effect

A three-fold degeneracy of  $t_{1u}$ -derived electronic band and rich phonon spectrum led many scientists to suspect that Jahn-Teller (JT) effects might be important in  $A_3C_{60}$  compounds [6]. JT effect can be observed in systems where degeneracy of electronic ground state is a result of the structural symmetry. After odd number of electrons are added to such degenerate ground state, JT effect causes a spontaneous structural deformation which removes the structural symmetry and breaks the energy level degeneracy. In this way the energy of the system is lower for, so-called, JT energy.

JT effect is a consequence of electron-phonon coupling. Since the dynamics of nuclei is much slower than dynamics of electrons JT effect is discussed in the adiabatic limit. A simple example of JT effect is a two dimensional system ( $\epsilon \otimes E$ ) where electron doublet ( $|\alpha\rangle, |\beta\rangle$ ) is coupled to two orthogonal phonon degrees of freedom ( $Q_\vartheta, Q_\epsilon$ ). The Hamiltonian of the electron-phonon coupling describing JT effect is in the space of electron doublet written as [6]

$$H = -\frac{1}{2} \left( \frac{\partial^2}{\partial Q_\vartheta^2} + \frac{\partial^2}{\partial Q_\epsilon^2} + Q_\vartheta^2 + Q_\epsilon^2 \right) + k^E \begin{bmatrix} -Q_\vartheta & Q_\epsilon \\ Q_\epsilon & Q_\vartheta \end{bmatrix}, \quad (5.1)$$

where we used  $\hbar\omega = 1$ . The left part describes two harmonic oscillators corresponding to the two phonon modes and the right part describes the electron-phonon coupling. The electron-phonon interaction matrix depends on the symmetry representations of electronic orbitals and phonon modes. At the same time symmetry considerations also define which irreducible representations are JT active, namely the phonon mode irreducible representation must be a part of a outer product of the electronic irreducible symmetry representation with its self ( $\epsilon \otimes \epsilon$ ). The JT effect is best illustrated by plotting the potential of the above equation (Eq. 5.1). Two potential surfaces (adiabatic potential energy surfaces - APES) corresponding to the two electronic states are shown in Fig. 5.1. The lowest APES has a characteristic "Mexican hat" shape with a minimum at finite  $Q$  value.

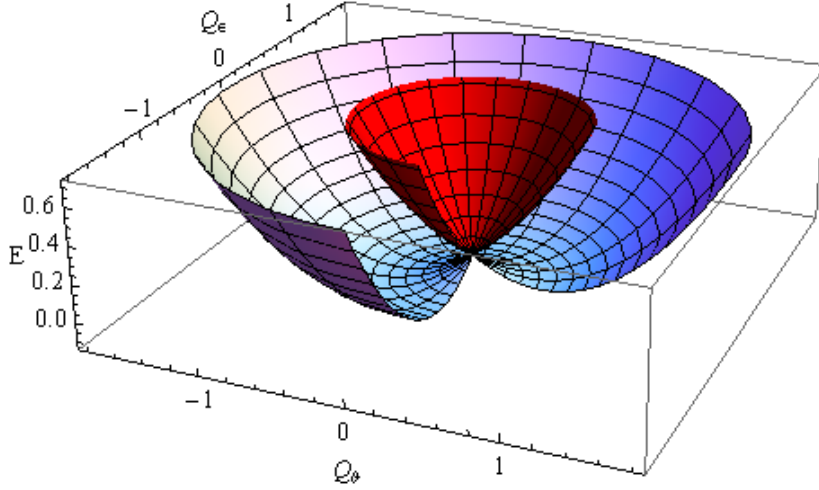


Figure 5.1: Upper (red) and lower (rainbow) adiabatic potential energy surfaces for  $E \otimes \varepsilon$  example.

This means that the system has lower energy at a certain distortion away from the equilibrium position. In addition, one can see that there is not a single minimum, but rather a continuum with  $SO(2)$  symmetry. In such case JT distortion is continuously changing, which is called *dynamic Jahn-Teller effect*. Adding potential terms to the above Hamiltonian to account for the crystal field effect leads to warping of the APES. In such case  $SO(2)$  symmetry of the minima can be removed leaving only discrete minimum points. When these local minima are not very deep the system can tunnel between them and the JT effect remains dynamic. However, when warping is too large the system stabilizes in one of them. This situation is called *static Jahn-Teller effect*.

In fullerene materials the situation is a bit more complex. Electronic states in  $t_{1u}$  orbitals can couple to  $t \otimes t = A \oplus H \oplus T$  phonon modes [6]. From these three only  $H$  phonon modes are Jahn-Teller active ( $t \otimes H$ ). In particular,  $t_{1u}$  electronic orbitals couple to five-fold degenerate  $H_g^1$  modes [5, 6, 41]. The  $H_g$  modes deform  $C_{60}$  molecules corresponding to the spherical harmonics ( $Y_{LM}$ ) with  $L = 2$ . The basic  $H_g$  deformation can be expressed as  $H_0 = \frac{1}{2}(3 \cos^2 \theta - 1)$ , which corresponds to the compression or elongations along a certain axis. When this axis is along hexagon ring, the symmetry is  $D_{3d}$ , when it is along pentagon rings the symmetry is  $D_{5d}$ , and when it is perpendicular to the double bond the deformation symmetry is  $D_{2h}$  [6]. Such simple deformations are indeed present in fullerene molecules charged with a single electron. However, in case of triply-charged fullerenes ( $C_{60}^{3-}$ ) as is the case in  $A_3C_{60}$  deformations are bimodal [6, 41]. The most symmetric model for such deformation is  $D_{2h}$ . An example of such  $C_{60}$  deformations is shown in Fig. 1.5. In  $A_3C_{60}$  the Jahn-Teller coupling to  $H_g$  modes ( $t \otimes H$ ) has three APES in the five dimensional  $Q$  space. Similar to ( $\varepsilon \otimes E$ ) case the APES minimum is a continuum with the  $SO(3)$  spherical symmetry. A particular JT deformation in this case can be in principle represented with five parameters  $Q_i = Q_i(Q, \alpha, \gamma, \theta, \phi)$ . Due to spherical symmetry any deformation can be rotated along the surface, which is called a *pseudorotation* [6]. The spherical symmetry can be broken by warping terms in the JT Hamiltonian as was discussed above. In case of  $A_3C_{60}$  slight warping is caused by the cubic crystal field which results in a number of equivalent but discrete minima. Nevertheless, if JT effect is indeed present in real fullerene materials it is most probably dynamic. This is supported by the X-ray scattering measurements on  $A_3C_{60}$  which show no deviation

<sup>1</sup>in  $H_g$ ,  $g$  corresponds to "gerade" or even modes

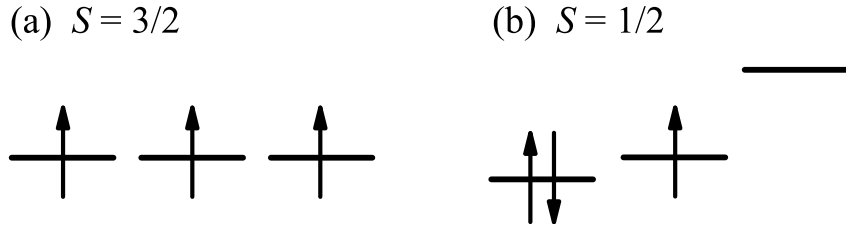


Figure 5.2: (a) High spin state in degenerate  $t_{1u}$  orbitals due to Hund's rule. (b) Low spin state due to JT deformation and removal of the  $t_{1u}$  degeneracy.

away from the ideal icosahedral symmetry of  $C_{60}$  molecules [14].

In the next two sections we will present the experimental evidence for the presence of JT effect in alkali-doped fulleride systems.

### 5.1.1 Low spin state, $S = 1/2$

In an isolated charged  $C_{60}$  molecule the JT effect is responsible for splitting of the triply-degenerate  $t_{1u}$  molecular orbitals. If the splitting is larger than the Hund's rule exchange then the high-spin state  $S = 3/2$  (Fig. 5.2a) would transform into the low-spin ground state,  $S = 1/2$ , where two out of three electrons would form a spin singlet in the lowest  $t_{1u}$  orbital and the remaining electron would be unpaired in the middle orbital (Fig. 5.2b). In fullerides the JT effect has been mostly studied theoretically [5, 6, 41]. Experimental, mainly indirect evidences of the JT were found. Some of them are presented below. In body-centred tetragonal compounds  $A_4C_{60}$  and  $A_2C_{60}$  a spin singlet-triplet transition has been observed in the spin susceptibility measured by NMR relaxation rate. The JT energy has been estimated to be 100 meV [15]. In  $NH_3K_3C_{60}$  and  $MAK_3C_{60}$  orthorhombic insulating compounds a Curie constant and the antiferromagnetic ground state was found to correspond to low-spin state  $S = 1/2$  [16, 18]. However, in all these non-cubic materials the low-spin state does not necessary originate from the JT effect. The anisotropic crystal field can similarly to the JT effect remove the degeneracy and split the  $t_{1u}$  levels leading to the low-spin state. Whether the low-spin state originates from the JT effect or the crystal field depends on the magnitude of their strength. In a cubic fullerene compounds the first experimental insight to JT effect was given by highly-expanded simple cubic fullerene,  $Li_3(NH_3)_6C_{60}$ . It has been shown that this material has an insulating ground state at ambient conditions with a Curie constant that correspond to  $S = 1/2$  [45]. However, this material has a complex unit cell with a large disorder in the position of Li anions and the random  $NH_3$  orientations. This can lead to rather strong local steric effects, which can remove degeneracy in similar way as the crystal field effect in  $NH_3K_3C_{60}$  or  $MAK_3C_{60}$ . Finally, the synthesis of the largest member of the cubic family  $Cs_3C_{60}$  gave an ultimate proof. At ambient pressure  $Cs_3C_{60}$  exhibits an antiferromagnetic insulating ground state. The Curie constant obtained from the temperature dependence of spin susceptibility corresponds to low spin  $S = 1/2$  ground state. This is the strongest evidence that the JT effect is present and prevails over the Hund's rule exchange interaction in the cubic fulleride systems [13, 14].

What remains to be seen is whether other JT effect could be seen more directly, for example, can a slight site symmetry reduction effect or the non-uniform electron spin density be observed with some local probes.

### 5.1.2 MAS NMR on $\text{Cs}_3\text{C}_{60}$ and $\text{Rb}_{0.5}\text{Cs}_{2.5}\text{C}_{60}$

If the JT effect is indeed present in the cubic fulleride compounds it would affect the local molecular symmetry. To investigate this effect we employed Magic Angle Spinning (MAS)  $^{13}\text{C}$  on *fcc*  $\text{Cs}_3\text{C}_{60}$  and *fcc*  $\text{Rb}_{0.5}\text{Cs}_{2.5}\text{C}_{60}$  (for details on materials composition and their physical properties see App. B.2). MAS technique employs a fast rotation ( $\nu_r = 25$  kHz) of the sample with rotation axis tilted for a magic angle ( $\theta_M = 54.7^\circ$ ) with respect to the external applied magnetic field. This technique averages out the major anisotropy terms of the Hamiltonian that broaden the NMR spectral lines. The result is a spectrum consisting of lines corresponding to non-equivalent nuclei whose number depend on the local symmetry (Sec. 3.3.6). The MAS spectra are, therefore, much narrower than the static ones (Fig. 5.3). Both  $^{13}\text{C}$  of  $\text{Cs}_3\text{C}_{60}$  (Fig. 5.3a) and  $\text{Rb}_{0.5}\text{Cs}_{2.5}\text{C}_{60}$  (Fig. 5.3b) consist of several lines corresponding to non-equivalent  $^{13}\text{C}$  nuclei. Due to better signal quality we now focus on  $\text{Cs}_3\text{C}_{60}$ . Room-temperature  $^{13}\text{C}$  MAS spectrum of  $\text{Cs}_3\text{C}_{60}$  (Fig. 5.3a) consists of three clearly resolvable peaks, with centres at 212.1 ppm (peak labelled as C3), 200.7 ppm (C2) and 183.7 ppm (C3). For peak details see Tab. 5.1. The average shift (200(1) ppm) is in excellent agreement with the first moment (196(5) ppm) of the corresponding static  $^{13}\text{C}$  NMR spectrum (Fig. 5.3a). The sample used for MAS NMR measurements contains also other impurity phases (App. B.1), which could give additional lines. However, the weakest C3 peak represents a relative intensity of 15.6% of total spectral intensity which is larger than the maximum impurity phase fraction of 7% (App. B.1). This rules out the possibility that any of these peaks exclusively originate from the impurity phases. Previous high-resolution  $^{13}\text{C}$  NMR study on  $\text{Cs}_4\text{C}_{60}$  found four peaks at 214 ppm, 189 ppm, 164 ppm, and 159 ppm, respectively. Since the last two peaks, which are well separated from the others, are completely missing in our  $^{13}\text{C}$  MAS NMR spectrum we conclude that the intensity of *bco*  $\text{Cs}_{3+x}\text{C}_{60}$  peaks is negligible. The other impurity A15  $\text{Cs}_3\text{C}_{60}$  phase is expected at 199 ppm [110] so its small contribution to C2 peak cannot be a priori excluded. The same conclusion can be made for the  $\text{CsC}_{60}$  peak at 179 ppm [111], which may overlap with C3 peak. Nevertheless, all three sites have similarly short spin-lattice relaxation times, 51 ms (C2), 52 ms (C3) and 80 ms (C1). This suggests that all three  $^{13}\text{C}$  peaks probe the same  $t_{1u}$  electron spin dynamics thus reassuring that they predominantly belong to the  $\text{C}_{60}^{3-}$  ions in the *fcc* phase. The spectra could be well fitted with three Gaussian function in the intensity ratio C1:C2:C3 = 1:2:2. Only small discrepancy could be observed at C3, which is most probably a small contribution of A15 impurity phase. Since the spectrum could be otherwise nicely fitted with three Gaussian function the contributions from the other impurity phases could be neglected.

In the expanded  $\text{Cs}_3\text{C}_{60}$  case the rotational dynamics of  $\text{C}_{60}^{3-}$  ions is frozen on the NMR time scale and thus all non-equivalent carbon nuclei can be resolved. In the  $\text{Fm}\bar{3}\text{m}$  structure the multiplicity of three chemically inequivalent carbon sites is 24:24:12. The relative intensity of C1 sites that correspond to about  $\sim 16$ -22% or  $\sim 10$ -13 out of 60 carbon sites per  $\text{C}_{60}$  molecule is thus in fair agreement with the expected intensity for carbon at the crystallographic position (0, 0.0491, 0.2407) [14]. The remaining two peaks C2 and C3 thus belong to carbons at (0.2051, 0.0767, 0.0987) and (0.1764, 0.1533, 0.0503) positions, but their final assignment is less certain. The inequivalent  $^{13}\text{C}$  sites in the *fcc* structure are expected to have different local charge densities [112] that mirror the symmetry of  $t_{1u}$  orbitals. Calculations predicted the smallest  $t_{1u}$  charge density for the C1 sites, which is compatible with its relatively small shift (180 ppm). On the other hand, same calculations gave the largest  $t_{1u}$  charge density for carbons at (0.2051, 0.0767, 0.0987)

positions, so we tentatively associate C2 peak with the largest shift of  $\sim 210$  ppm to this site. The remaining C3 peak at  $\sim 200$  ppm with the intermediate  $t_{1u}$  charge density is then attributed to (0.1764, 0.1533, 0.0503) carbon crystallographic sites.

	<i>fcc</i> Cs <sub>3</sub> C <sub>60</sub>			<i>fcc</i> Rb <sub>0.5</sub> Cs <sub>2.5</sub> C <sub>60</sub>		
<sup>13</sup> C peaks	C1	C3	C2	C1	C3	C2
Centre (ppm)	183.7(5)	200.7(5)	212.1(5)	180.56(1)	195.4(3)	207.6(2)
Width (ppm)	6.5(3)	9.0(8)	7.1(4)	4	13.3(3)	12.0(2)
Intensity (%)	20	40	40	20	40	40
$T_1$ (ms)	80(10)	52(3)	51(3)	80(10)	64(3)	64(3)

Table 5.1: Results of the analysis of MAS <sup>13</sup>C NMR spectrum of *fcc* Cs<sub>3</sub>C<sub>60</sub> and *fcc* Rb<sub>0.5</sub>Cs<sub>2.5</sub>C<sub>60</sub> at room temperature. Line positions are given relative to the TMS reference. In the bottom row measured spin-lattice relaxation times are given for each peak.

On cooling all three <sup>13</sup>C MAS NMR peaks show a dramatic broadening and are hardly recognized below  $\sim 150$  K (Fig. 5.3a). Similar effect can be observed for <sup>133</sup>Cs MAS spectra (Fig. 5.3b) implying that the two phenomena are closely related. In both cases the spinning frequency was kept without difficulties at  $\nu_R = 20$  kHz for all temperatures so the observed broadening is not an experimental artefact. Below  $\sim 100$  K <sup>13</sup>C spectra become very broad and fairly symmetric indicating a broad distribution of <sup>13</sup>C shifts. Since the anisotropic terms are cancelled out by MAS technique the low temperature <sup>13</sup>C spectra suggest that more than three chemically inequivalent carbon sites are present despite XRD investigations, which in this temperature range do not point to any lowering in the crystal symmetry. Therefore we conclude that the symmetry breaking must be local and random. C<sub>60</sub> molecular rotations are frozen on NMR time scale already well above room temperature so changes in merohedral disorder can be ruled out as the origin of such phenomena. Although Cs<sub>3</sub>C<sub>60</sub> is close to insulator-to-metal transition where charge fluctuations could account for the observed peak broadening, the sample remains insulating to low temperatures. The quadrupole effects are for <sup>13</sup>C nuclei with  $S = 1/2$  also not possible. The remaining degree of freedom is the JT effect. Therefore, as a plausible explanation for the anomalous broadening in low-temperature MAS NMR we suggest that on cooling JT inter-conversions between different energy minima gradually freeze out on the NMR time scale around 100 K. JT deformation of C<sub>60</sub><sup>3-</sup> largely increases the number of inequivalent <sup>13</sup>C resonances up to 30 – depending on the symmetry of JT deformed C<sub>60</sub><sup>3-</sup> ion - thus being in full agreement with the <sup>13</sup>C MAS NMR experiment.

Our results are in good agreement with very recent infra-red spectroscopy study [113] where static C<sub>60</sub> deformations have been observed on the time scale of the experiment ( $10^{-11}$  s) at temperatures as high as 400 K in Cs<sub>3</sub>C<sub>60</sub>. The deformations, most probably of the D<sub>2h</sub> symmetry, are still dynamic on the lower time scales which is implied from the observed interchange between different C<sub>60</sub> deformations established by the crystal field effect.

To summarize the experimental observations of the JT effect in Cs<sub>3</sub>C<sub>60</sub>, we have shown that the JT deformations are indeed present, supported by the low-spin state, infra-red measurements and the broadening of MAS spectra. Moreover, the JT effect is dynamic on the entire temperature range and at the same time it is slowing down with decreasing temperature on the NMR time scale (100 MHz). This implies that there are discrete minima in the APES, deep enough that the tunnelling between them is suppressed, and that at very low temperatures C<sub>60</sub> molecules stabilize in one of the minima appropriate

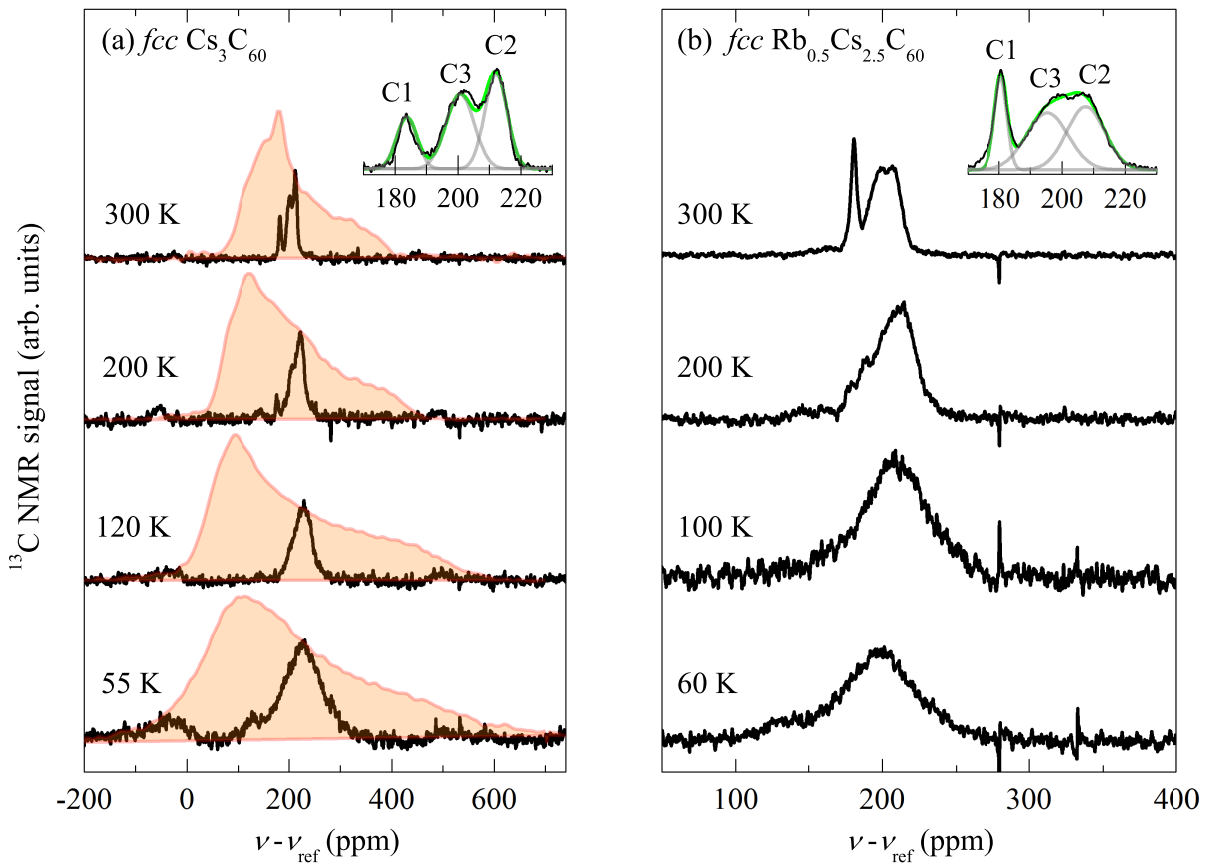


Figure 5.3: Temperature dependence of MAS  $^{13}\text{C}$  spectra on (a)  $\text{fcc Cs}_3\text{C}_{60}$  (black line) and (b)  $\text{fcc Rb}_{0.5}\text{Cs}_{2.5}\text{C}_{60}$  samples measured at rotation frequency of 25 kHz. For comparison spectra of static  $\text{fcc Cs}_3\text{C}_{60}$  are plotted in yellow/orange colour. Inset to (a) and (b) show a magnified  $^{13}\text{C}$  MAS spectra at 300 K, where three peaks corresponding to three non-equivalent carbons sites are clearly seen. Three Gaussian fits are shown as green and gray lines. In (a) smaller peaks in  $^{13}\text{C}$  MAS spectra separated from the main line for cca. 25 kHz are the side-bands due to magnetic broadening of static spectra.

for the static JT case. However, according to the XRD study the cubic crystal structure is maintained even at low temperatures. This can be justified by a random (glass-like) JT static deformations at very low temperatures driven by the frozen merohedral disorder. Merohedral disorder must be dominating over the cooperate JT effect, that favours orbital order and macroscopic crystal symmetry reduction.

So far, we have discussed JT effect only in the insulating alkali-doped fullerenes. Interesting question arises, whether JT effect can survive also in the metallic ground state close to MIT. It is clear that deep in the metallic state the fast conduction electrons will not remain on a molecules long enough to trigger JT deformation, however, close to the MIT they are much slower due to the effective mass enhancement. At this point we now return to  $\text{Rb}_{0.5}\text{Cs}_{2.5}\text{C}_{60}$  compound. The partial substitution of Cs ions with smaller Rb ions leads to a reduction of the unit-cell volume which brings it closer to the MIT. As we will show in Chap. 7 this compound is indeed very close to the MIT. Since the unit-cell contracts with decreasing volume this material, being in the insulating phase at room temperature, goes over MIT at  $\sim 110$  K (Tab. 7.1) into the metallic phase at lower temperatures. It is thus an ideal candidate to study the presence of JT effect close to the MIT border.  $^{13}\text{C}$  MAS NMR spectra of  $\text{Rb}_{0.5}\text{Cs}_{2.5}\text{C}_{60}$  are shown in Fig. 5.3b. It can be seen that  $\text{Rb}_{0.5}\text{Cs}_{2.5}\text{C}_{60}$  spectra closely resemble the behaviour of temperature dependent  $\text{Cs}_3\text{C}_{60}$  spectra. Three non-equivalent  $^{13}\text{C}$  spectral lines, resolved at room temperature, start to drastically broaden with decreasing temperature and become unresolved below  $\sim 200$  K. We note that in  $\text{Rb}_{0.5}\text{Cs}_{2.5}\text{C}_{60}$  there is substitutional disorder of Cs and Rb ions in the tetrahedral site as will be discussed in the next chapter. This can result in a small additional broadening, however, the Cs/Rb disorder does not change with the temperature and cannot be responsible for the large observed increase of the spectral width. We can, therefore, conclude that the broadening of  $\text{Rb}_{0.5}\text{Cs}_{2.5}\text{C}_{60}$   $^{13}\text{C}$  spectra with decreasing temperature is attributed to the enhanced number of inequivalent carbons caused by the JT deformation of  $\text{C}_{60}$  molecule, similar as in  $\text{Cs}_3\text{C}_{60}$ .

Our data suggest that JT effect can be also present in the metallic phase close to MIT. This is an important observation that might have a profound impact on the electronic properties of the metallic and superconducting phase close to MIT.

## 5.2 Steric effects

The cointercalation of molecules in the interstitial sites of the alkali doped fullerenes for example in  $\text{NH}_3\text{K}_3\text{C}_{60}$ ,  $\text{MAK}_3\text{C}_{60}$ , or  $(\text{NH}_3)_3\text{Li}_3\text{C}_{60}$  can lead to a short contact distance between molecules' protons and the fullerene anion. For example, in  $\text{NH}_3\text{K}_3\text{C}_{60}$  closest N-H...C distance is  $2.56 \text{ \AA}$  [35] and in  $\text{MAK}_3\text{C}_{60}$  this distance is  $2.25 - 2.32 \text{ \AA}$  [36]. It has been pointed out that in the later case distance is already in the range of a typical hydrogen-bond length and may thus have a notable impact on the electronic and magnetic properties of  $\text{MAK}_3\text{C}_{60}$ . One of the peculiarities of this material is for example a surprisingly low Néel temperature, compared to other compounds with similar unit-cell volume and crystal anisotropy.

### 5.2.1 High-pressure EPR study

To study the effects of interaction between protons and fullerene molecules we performed a high-pressure EPR measurement on  $\text{MAK}_3\text{C}_{60}$  up to 1 GPa at room temperature. EPR spectrum measured at ambient pressure consists of a single component, which can be well

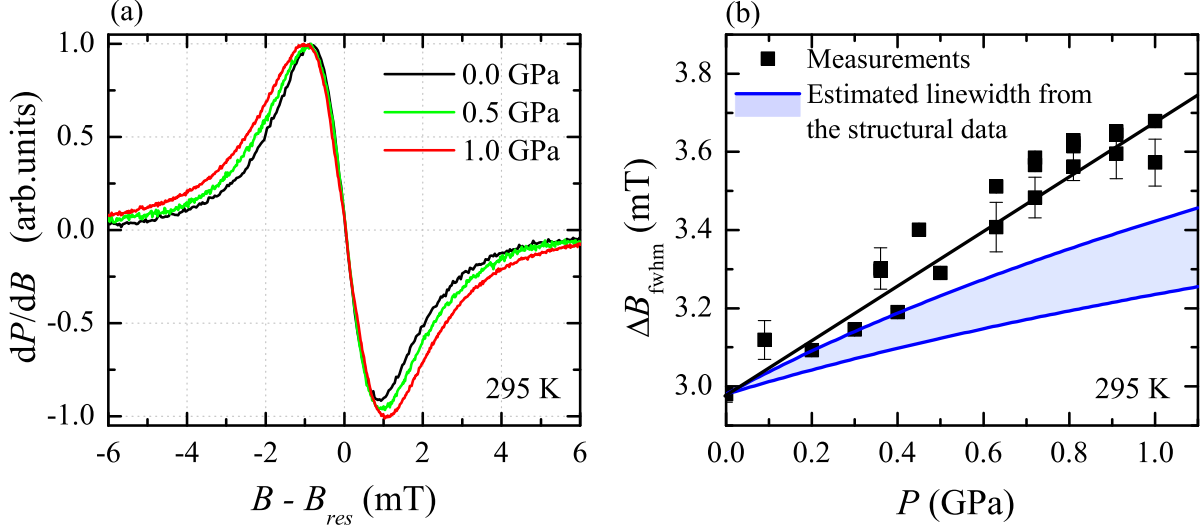


Figure 5.4: (a) Normalized EPR spectra of  $\text{MAK}_3\text{C}_{60}$  as a function of pressure at room temperature. Linewidth changes from 2.98 mT to 3.68 mT under applied pressure of 1.0 GPa. (b) EPR linewidth as a function applied pressure at room-temperature. Several points at the same pressure correspond to different measurements. Blue lines with the light blue area show the expected linewidth due to dipolar interaction using the XRD structural data under pressure (App. B.3.1).

approximated with a simple Lorentzian lineshape. Ambient pressure full width at half maximum of Lorentzian lineshape ( $\Delta B_{\text{fwhm}} = 2.98$  mT) is in a good agreement with the previously reported value [18]. Under applied pressures the lineshape remains Lorentzian and the linewidth monotonically increases with increasing pressure (Fig. 5.4a) and reaches 3.7(1) mT at 1.0 GPa. There is no indication of a sudden change in the lineshape or lineshift that would indicate the structural transformation.

Within the experimental accuracy the increase of linewidth is a linear function of pressure with a slope of 0.7(1) mT/GPa as shown in Fig. 5.4b. The exchange coupling constant  $J$  was determined from Eq. 3.24 by using the measured ambient pressure linewidth and calculated second moment,  $\sqrt{M_2(0)} = 50.7$  mT. The second moment was computed assuming dipolar interaction (Eq. 3.21) on the  $\text{MAK}_3\text{C}_{60}$  *fco* crystal structure (App. B.3.1). The obtained value of exchange coupling constant is  $J/k_B = 3.65(1)$  K. Assuming that  $J$  does not change substantially with pressure we can estimate how the linewidth would evolve with increasing pressure by using Eq. 3.24 and Eq. 3.21 together with the  $\text{MAK}_3\text{C}_{60}$  volume compressibility (App. B.3.2). The result is depicted in Fig. 5.4b where blue area indicates the uncertainty of the estimated values. We note that the measured linewidth does not correspond to the estimated linewidth's pressure dependence with a slope of almost half of the experimental one. There are two possible scenarios that can explain discrepancy between our estimate and measurements. In the first scenario the additional increase of the linewidth is a consequence of the enhancement of  $g$ -factor anisotropy observed in previous EPR measurements below the structural

phase transition [18]. Such a scenario would indicate that the structural phase transition temperature rapidly increases with the applied pressure. The structural phase transition at 220 K at ambient pressure should be within this scenario increased for 80 K to reach room temperature value under the applied pressure of 1 GPa. On the other hand, high-pressure  $^2\text{D}$  NMR experiments on  $\text{MAK}_3\text{C}_{60}$ , where MA dynamics was studied under pressure, have shown that under applied pressure of 0.7 GPa the structural phase transition indeed increases, but only to 250 K (A. Potočik, *et al.* unpublished). According to this results the phase transition is unlikely to reach the room temperature at 1 GPa and, therefore, the first scenario can be omitted. In the second scenario additional increase of the slope  $d\Delta B_{\text{fwhm}}/dP$  comes from a reduction of exchange coupling constant with increasing pressure (Eq. 3.24). In order to account for the measured  $d\Delta B_{\text{fwhm}}/dP$ ,  $J$  should be reduced for about 50% at 1 GPa. At the first sight this is counterintuitive since one would expect that  $J$  would increase with increasing pressure due to larger  $t_{1u}$  overlap between  $\text{C}_{60}^{3-}$  anions in the reduced unit cell. While this should indeed hold for the orbitally liquid state, it can get much more complicated when Jahn-Teller effect or steric effects due to proton–fullerene contact are taken into account. A certain orbital order induced by the JT effect or deformation of the  $\text{C}_{60}$  molecule due to steric effects can drastically change the overlap of electronic orbitals of the neighbouring fullerene molecules which could result in the reduced effective exchange interaction between them.

### 5.2.2 DFT study

To test these two proposed effects in  $\text{MAK}_3\text{C}_{60}$  compounds we carried out a DFT computations in the LDA approximation and search for the most probable explanation of the reduction of the effective exchange coupling constant. Technical details of DFT procedure are given in App. B.3.4.

Let us focus first on JT effect of  $\text{C}_{60}^{3-}$  anion. Orthorhombic crystal structures should provide a fertile ground for JT effect investigations within DFT. In order to isolate JT effect we consider an artificial enlarged face centered orthorhombic  $\text{C}_{60}^{3-}$  structure using the room-temperature  $\text{MAK}_3\text{C}_{60}$  lattice parameters multiplied by a factor of 1.5. To ensure charge neutrality, we add a uniform positive background in the DFT calculation. This positive background is not contributing to the orthorhombic crystal field, therefore, any removal of  $t_{1u}$  degeneracy at the  $\Gamma$  point should arise solely from the JT effect on top of the weak residual crystal field from the periodically replicated  $\text{C}_{60}^{3-}$  ions. The positions of  $\text{C}_{60}$  carbon atoms were relaxed in order to obtain molecular distortions. The  $\text{C}_{60}^{3-}$  ion deforms spontaneously into a structure with  $\text{D}_{2h}$  symmetry [Fig. 5.5(a)]. This is expected symmetry for  $t_{1u} \otimes \text{H}_g$  JT coupling involving  $\text{H}_g$  vibrational modes [6, 41, 42]. Distortions are small with the maximum value of 2 pm, which is in good agreement with the observed  $\text{C}_{60}$  distortions in  $\text{Cs}_4\text{C}_{60}$  [114]. We estimate the energy scale for deformation by realizing that the relaxed structure has  $\Delta E_{\text{tot}} = 170$  meV lower total energy than the starting structure with undistorted icosahedral  $\text{C}_{60}$ . Former threefold  $t_{1u}$  degeneracy of the LUMO is now removed, with  $t_{1u}$  levels split equally by  $\sim 50$  meV. The lowest  $t_{1u}$  orbital is doubly occupied, while the third electron goes into the central  $t_{1u}$  orbital, pinned at the Fermi level. The highest  $t_{1u}$  orbital is empty. The total energy difference,  $\Delta E_{\text{tot}}$ , has several contributions: the JT effect, the crystal-field effect and bond-length correction due to LDA approximation. To estimate only the JT energy scale we compare the above  $\Delta E_{\text{tot}}$  with the one obtained for a structural relaxation with equal and fixed occupations of the  $t_{1u}$  bands, which effectively hinders the JT effect. The difference in the total energy between these two calculations is 57 meV, a typical value for the JT

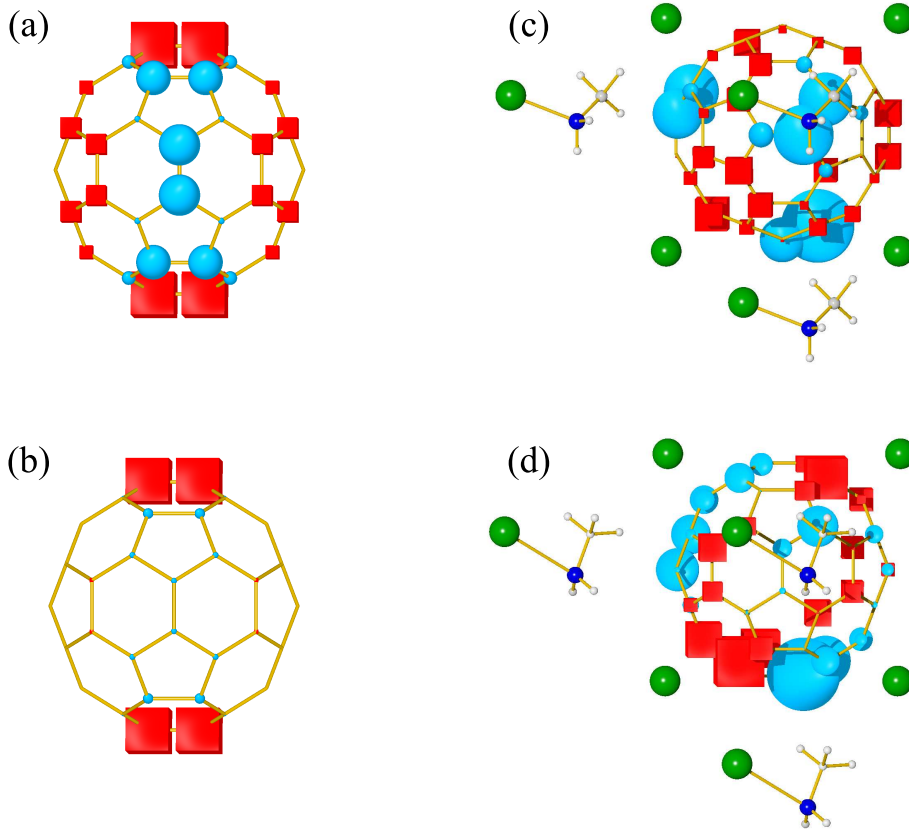


Figure 5.5: Radial molecular distortions of  $C_{60}^{3-}$  ions in (a) orthorhombic  $C_{60}^{3-}$  expanded structure, (b)  $K_3C_{60}$  orthorhombic environment, (c) room-temperature  $MAK_3C_{60}$  structure with relaxed  $C_{60}$  atom positions only, and (d)  $MAK_3C_{60}$  structure with where all atoms have been relaxed. Blue spheres correspond to inward distortions of the  $C_{60}$  cage and red boxes represent outward cage distortions. The sizes of the markers scale linearly with the amount of distortion.

effect [6, 42]. Proper energy scale, typical size of deformations, the right symmetry of  $C_{60}^{3-}$ , the splitting, and correct occupation of  $t_{1u}$  orbitals are all strong indications that the observed distortion is indeed a result of the JT effect.

The residual crystal field of  $C_{60}^{3-}$  ions is immediately seen for smaller lattice parameters, i.e. when room-temperature  $MAK_3C_{60}$  lattice parameters are for instance multiplied by a smaller factor of 1.25. Using the same procedure as above, the structural relaxation ended up with the same deformation of the  $C_{60}^{3-}$  molecule. The only difference is that the axis of JT deformation accidentally rotated from the crystal  $z$ - to  $y$ -direction. This indicates that we are dealing in both cases with the JT effect and that the change in the JT deformation axis is due to the existence of several equivalent minima in the lowest JT APES [6]. These minima become nearly degenerate for large lattice expansions. On the other hand, when lattice parameters are reduced down toward experimental  $MAK_3C_{60}$  values the orthorhombic crystal field starts to play a role by making some of the APES minima deeper, thus promoting a specific JT deformation.

Adding potassium atoms to the  $C_{60}^{3-}$  structure results in an artificial orthorhombic  $K_3C_{60}$  where even stronger orthorhombic crystal field due to the close contact between the  $K^+$  and  $C_{60}^{3-}$  ions are expected. The structural optimization of the  $C_{60}$  carbon positions when starting from the JT distorted  $C_{60}^{3-}$  atomic positions [Fig. 5.5(a)] leads to deformations of the  $C_{60}$  molecule shown in Fig. 5.5(b). Molecular deformations are slightly different because the crystal field additionally lifts the  $t_{1u}$  degeneracy, hence producing

pseudo-JT effect. Nevertheless, the resulting symmetry remains  $D_{2h}$  and the maximal distortions of 2.3 pm are similar to the previous cases. The same holds for the total-energy lowering,  $\Delta E_{\text{tot}} = 140$  meV. The JT effect is obviously still dominant over orthorhombic crystal field, which represents a smaller contribution to the total energy.

Finally we investigate  $C_{60}^{3-}$  deformations in the room-temperature  $MAK_3C_{60}$  structure where only  $C_{60}$  carbon atoms were allowed to relax. The presence of MA molecules has a dramatic effect on the  $C_{60}^{3-}$  shape [Fig. 5.5(c)]. The maximal cage distortions are significantly larger than in the previous cases - they reach up to 3.4 pm and the total energy is reduced by  $\Delta E_{\text{tot}} = 303$  meV during the structural optimization. In addition, even the  $D_{2h}$  symmetry of the distorted  $C_{60}$  molecule is lost. The maximal distortions are found for carbons facing methyl protons, at a closest-approach distance of 226 pm. Dramatically larger distortions compared to those obtained for  $C_{60}^{3-}$  or even for orthorhombic  $K_3C_{60}$  structure indicate that the additional crystal field produced by MA- $K^+$  groups plays a dominant role over the JT effect in  $MAK_3C_{60}$ .

We also address the possible hydrogen-bond formation by relaxing all atomic positions, including those of MA- $K^+$  groups. Hydrogen-bond traces can be detected on the tiny deformation of MA where C-H bond lengths of the  $CH_3$  group are 110.3 pm, 110.4 pm and 110.6 pm, the last one corresponding to the hydrogen with the closest contact to the fullerene molecule. However, with the structural relaxation, the MA- $K^+$  group rotates slightly away from the fullerene molecule, increasing the nearest H- $C_{60}$  distance to 228.5 pm, i.e. by 2.7 pm longer than in the experimental structure [Fig. 5.5(d)]. This distance still remains in the typical hydrogen-bond length range, but the  $C_{60}^{3-}$ -methyl proton contact elongation indicates that such bond must be very weak. However, due to the Born-Oppenheimer approximation used in DFT within each relaxation cycle an accurate treatment of a hydrogen-bond formation is not possible.

## 5.3 Conclusions

A high symmetry of fullerene molecules and consequently degenerated ground state of electrons make their electronic and magnetic properties sensitive to even slight molecular distortions either spontaneous due to Jahn-Teller effect or inflicted by the crystal field or steric effects. We have shown that the slow or even static Jahn-Teller effect is indeed present in  $Cs_3C_{60}$  as observed by MAS NMR experiments. We argue that JT deformations must be random and not cooperative since this would lead to a macroscopic crystal symmetry reduction, which is experimentally not observed. One possibility to obtain random JT effect is by random crystal field due to merohedral disorder. How strongly can merohedral disorder influence the electronic and JT properties will be studied in the next chapter. The presence of JT effect is in agreement with a low-spin ground state observed in insulating alkali-doped fullerenes as well as with recent infra-red spectroscopy measurements on  $Cs_3C_{60}$ . We have also shown that JT effect can survive the insulator-to-metal transition and can be even present in the metallic phase close to MIT. This can have profound implications since such metallic phase cannot be treated as Fermi-liquid metallic phase according to the theoretical study using DMFT. [5, 62]. The remaining question is how does the metallic phase close to the MIT behave. We will address this issue in Chap. 7.

On the other hand, we have shown that the cointercalation of anisotropic molecules e.g.  $NH_3$  or  $CH_3NH_2$  not only remove the cubic symmetry of the unit cell, but can also have a strong influence on the electronic and magnetic properties as is the case in

MAK<sub>3</sub>C<sub>60</sub>. Its anomalous pressure dependence of the EPR linewidth support an non-intuitive decrease of the effective exchange interaction constant under high-hydrostatic pressure despite having shorter C<sub>60</sub>-C<sub>60</sub> distance. Such behaviour can be rationalized by a drastic change of the hopping integrals caused by the presence of cointercalated molecules and possibly the formation of hydrogen-bonds between their protons and C<sub>60</sub><sup>3-</sup> anions. Further investigation by DFT-LDA technique shows that Jahn-Teller effect is indeed possible in alkali-doped fullerenes, even in the metallic state, however, as soon as the MA molecules are introduced, as is the case in the MAK<sub>3</sub>C<sub>60</sub> structure, JT effect is strongly dominated by the steric effects due to MA protons being in close contact to C<sub>60</sub><sup>3-</sup> anions. Relatively strong C<sub>60</sub> cage deformations compared to the JT deformations are in agreement with the previous experimental findings of strongly changed electronic pathways reflected by anomalously low Néel temperature of MAK<sub>3</sub>C<sub>60</sub>.

MAK<sub>3</sub>C<sub>60</sub> compounds, where JT effect is destroyed by strong steric effects, may also provide an important experimental evidence for the relevance of JT effect in the superconductivity of fullerenes. If the JT effect is crucial for superconductivity of fullerenes then exposing MAK<sub>3</sub>C<sub>60</sub> to much higher hydrostatic pressures, where the system would cross the metal-insulator boundary, must result in a metallic ground state without superconductivity appearing at low temperatures. This experiment is yet to be performed.

# 6 Importance of structural disorder

Structural disorder is an important effect that cannot be neglected when studying superconducting materials. Its effects are not entirely understood even today. In the early days of superconductivity, when only standard superconductors were known, disorder was associated with a suppression of the superconductivity [115]. In addition, disorder was attributed also the reduction of the superconducting phase fraction [116]. However, with discovery of high- $T_c$  cuprate superconductors an order of magnitude larger transition temperatures were obtained after doping which in fact created disorder in the material. Disorder is now believed to be an intrinsic property of cuprate superconductors where electronic and superconducting properties vary on a nanoscopic scale [117].

In fulleride superconductors the effect of structural disorder is still largely unknown. Since the controlling parameter is the unit-cell volume different phases in the phase diagram can be obtained without using doping technique, which is known to introduce large disorder. In fact, A15 polymorph of  $\text{Cs}_3\text{C}_{60}$  is completely disorder free superconductor under pressure [13]. In contrast to A15  $\text{Cs}_3\text{C}_{60}$  all *fcc*  $\text{A}_3\text{C}_{60}$  compounds have  $Fm\bar{3}m$  space-group which contains internal orientational disorder of  $\text{C}_{60}$  molecules, so-called *merohedral disorder*. In addition, some of the ternary *fcc* compounds can also have *substitutional disorder* between two different alkali metals, e.g.,  $\text{Rb}_x\text{Cs}_{3-x}\text{C}_{60}$ .

Although, disorder is present in the *fcc*  $\text{A}_3\text{C}_{60}$  compounds its effect on the electronic and superconducting properties was considered to be weak. However, as was suggested in the previous chapter the merohedral disorder might help to stabilize a particular JT deformation. In addition, structural disorder was also suggested to be the the origin of the mysterious T' line in the alkali metal NMR experiments [118]. In this chapter we will explore what is the role of structural disorder and to what extend it can effect  $\text{A}_3\text{C}_{60}$  properties.

## 6.1 Merohedral disorder

Merohedral disorder is a random distribution of two standard  $\text{C}_{60}$  orientations that differ by a  $90^\circ$  rotation around the molecular two-fold axis pointing along crystal axis. The two possible orientations are enforced by a relatively large alkali metals in small tetrahedral interstitial sites and are considered with equal probability. The merohedral disorder has been shown to have a notable influence on the electronic structure where two sharp peaks in the density of states calculated without disorder become smeared out when merohedral disorder was introduced [119].

A standard method that is used for studying local site symmetries and structural properties is a standard or high-resolution local probe NMR technique. Such experiments have been performed in the past on various, e.g.,  $^{87}\text{Rb}$  NMR on  $\text{Rb}_3\text{C}_{60}$  [120],  $\text{Rb}_2\text{CsC}_{60}$ ,  $\text{RbCs}_2\text{C}_{60}$ , etc. [7], where they found instead of two NMR lines corresponding

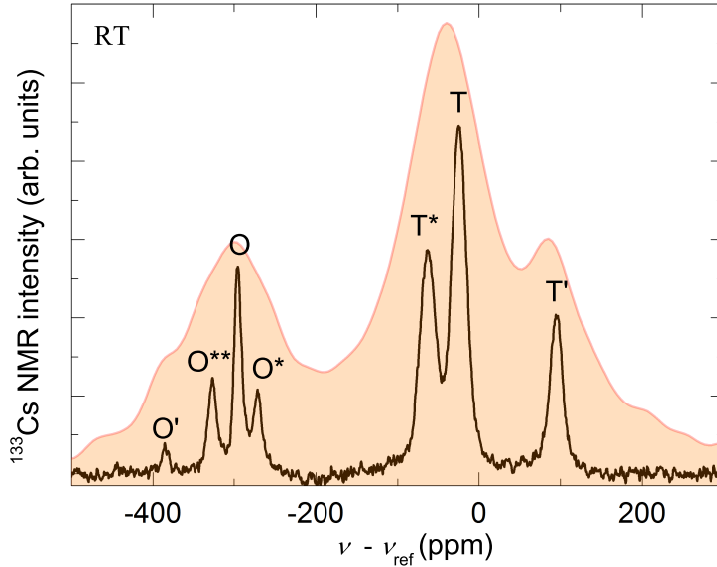


Figure 6.1: Room temperature  $^{133}\text{Cs}$  MAS NMR spectrum of *fcc*  $\text{Cs}_3\text{C}_{60}$  measured at a spinning frequency,  $\nu_r = 25$  kHz (black solid line). For comparison, we show the corresponding static ( $\nu_r = 0$  kHz) solid state  $^{133}\text{Cs}$  NMR spectrum (shaded area).

the octahedral and tetrahedral sites (Sec. 1.2) a third clearly resolvable line appearing at low temperature. The origin of the third line, denoted by T', was a long standing mystery. Many models have been proposed to explain its existence, such as the anion vacancies, alkali metal off-centre displacement, Jahn-Teller distortion, carrier density modulation, alkali metal clustering, and merohedral disorder [118]. The experiments performed in order to elucidate the T' problem have shown that T' and T lines merge into one at high temperatures where  $\text{C}_{60}$  rotational dynamics is fast. This suggest that T and T' have both the same tetrahedral environment at high temperatures [121]. T' lines were found to be an intrinsic property of  $A_3\text{C}_{60}$  and not originating from a phase segregated part of the sample or impurity [122]. In addition, thermally activated correlation effect has been observed between T and T' lines which indicates that these two lines are defined by molecular dynamics [120]. With this observations the existence of T' line has been proposed to originate from a special orientation of the neighbouring  $\text{C}_{60}$  molecules due to merohedral disorder of  $\text{C}_{60}$  molecules [118].

In order to study the role of merohedral disorder in more details we employed MAS  $^{133}\text{Cs}$  NMR on insulating *fcc*  $\text{Cs}_3\text{C}_{60}$  with much higher resolution than any published data on  $A_3\text{C}_{60}$  compounds up to now. The experimental procedure has been described in Sec. 5.1.2. The  $^{133}\text{Cs}$  MAS ( $\nu_r = 25$  kHz) and static ( $\nu_r = 0$  kHz) NMR spectra of the  $\text{Cs}_3\text{C}_{60}$  sample measured at room temperature are compared in Fig. 6.1. The  $^{133}\text{Cs}$  MAS NMR spectrum consists of 7 lines, whose positions coincide with O, T, and T' resonances as have been observed in the previous static NMR measurements (Fig. 6.1). The resonances of the  $A_{15}\text{Cs}_3\text{C}_{60}$  and *bco*  $\text{Cs}_4\text{C}_{60}$  phases are further suppressed by the appropriate choice of pulse sequence and pulse lengths [13, 14, 110], while that of  $\text{CsC}_{60}$  is very weak and shifted outside the spectral region shown in Fig. 6.1 (to  $\sim 900$  ppm) [31]. The measured  $^{133}\text{Cs}$  NMR spectrum thus arises entirely from the *fcc*  $\text{Cs}_3\text{C}_{60}$  polymorph.

The splitting of the tetrahedral resonance into two components (T, T') is already evident in the static  $^{133}\text{Cs}$  NMR spectra. The intensity of the T' peak is  $\sim 19\%$  of the total tetrahedral-site intensity (Tab. 6.1). Here, the high resolution of the MAS NMR experiments allows us to resolve a further component, T\* at  $-24.6(1)$  ppm in addition to

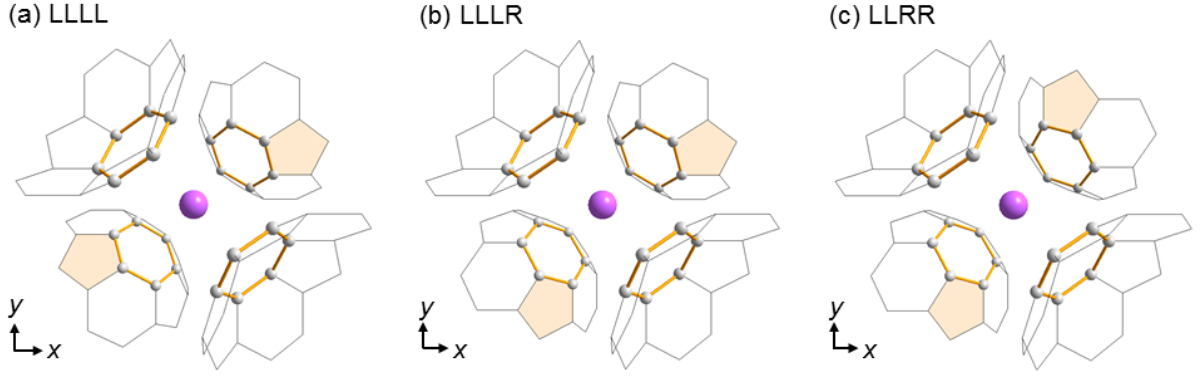


Figure 6.2:  $\text{Cs}^+$  ion (purple spheres) in the tetrahedral environment of the *fcc*  $\text{Cs}_3\text{C}_{60}$  structure (a) without merohedral disorder, where all first nearest neighbouring  $\text{C}_{60}$  molecules orient in the same way (LLLL configuration), (b) where one (i.e. lower left) of the  $\text{C}_{60}$  molecules is rotated by  $90^\circ$  around the cubic axis (LLLR configuration), and (c) when two  $\text{C}_{60}$  molecules are rotated (LLRR configuration). Please note the difference in the orientation of pentagon rings (shaded) for this molecule between LLLL and LLLR.

the T and T' peaks at  $-63.2(1)$  and  $94.8(1)$  ppm, respectively (Fig. 6.1). The spectral part corresponding to the octahedral site resonance shows an even more complex substructure than that of the tetrahedral site – the static NMR spectrum comprises a prominent O component with a lower-frequency weak O' shoulder. In the MAS NMR spectrum, the O' peak is now clearly resolved at  $-384.8(2)$  ppm. In addition, the main O resonance comprises three clearly distinguishable components – two additional weaker peaks, O\* and O\*\* are observed at  $-272.1(1)$  and  $-326.2(1)$  ppm, respectively, straddling the central O peak at  $-295.3(1)$  ppm. Although the O peak is still the most intense in the octahedral family, the combined intensity of the resolved O\* and O\*\* resonances matches its intensity (Tab. 6.1). Further definitive support for the general peak assignment of the observed resonances is obtained from the grouping of O and T peaks on the basis of their similar spin-lattice relaxation times and peak widths (Tab. 6.1).

$^{133}\text{Cs}$ peaks	O'	O**	O	O*	T*	T	T'
Centre (ppm)	$-384.8(2)$	$-326.2(1)$	$-295.3(1)$	$-272.1(1)$	$-63.2(1)$	$-24.6(1)$	$94.8(1)$
Width (ppm)	$10.9(4)$	$13.4(2)$	$10.9(2)$	$14.8(3)$	$21.2(2)$	$20.1(1)$	$17.7(2)$
Intensity (%)	$1.4(1)$	$6.1(1)$	$11.3(2)$	$5.8(1)$	$24.8(2)$	$36.3(2)$	$14.2(1)$
$T_1$ (ms)	$230(10)$	$340(10)$	$370(10)$	$380(10)$	$79(3)$	$72(3)$	$53(3)$

Table 6.1: Results of the analysis of MAS  $^{133}\text{Cs}$  NMR spectrum at room temperature. Line positions are given relative to the 0.1 M solution of  $\text{CsNO}_3$  in  $\text{D}_2\text{O}$  reference. In the bottom row measured spin-lattice relaxation times are given for each peak.

We first discuss the origin of three lines corresponding to tetrahedral sites. In the *fcc*  $A_3\text{C}_{60}$  structure  $\text{C}_{60}$  molecule is oriented such that eight of its hexagonal rings orient along the cubic  $\langle 111 \rangle$  directions. Four first neighboring  $\text{C}_{60}$  molecules face with their hexagon rings  $\text{Cs}^+$  ion in the T site as depicted in Fig. 6.2a. In the merohedrally disordered  $A_3\text{C}_{60}$  structure the two standard  $\text{C}_{60}$  orientations differ in positions of their pentagonal rings (Fig. 6.2) and are related by  $90^\circ$  rotations around the cubic axes. We denote these two standard orientations as L and R. Because  $\text{C}_{60}$  molecules are indistinguishable and L and R orientations are related by the  $Fm\bar{3}m$  symmetry operations it follows, for instance, that

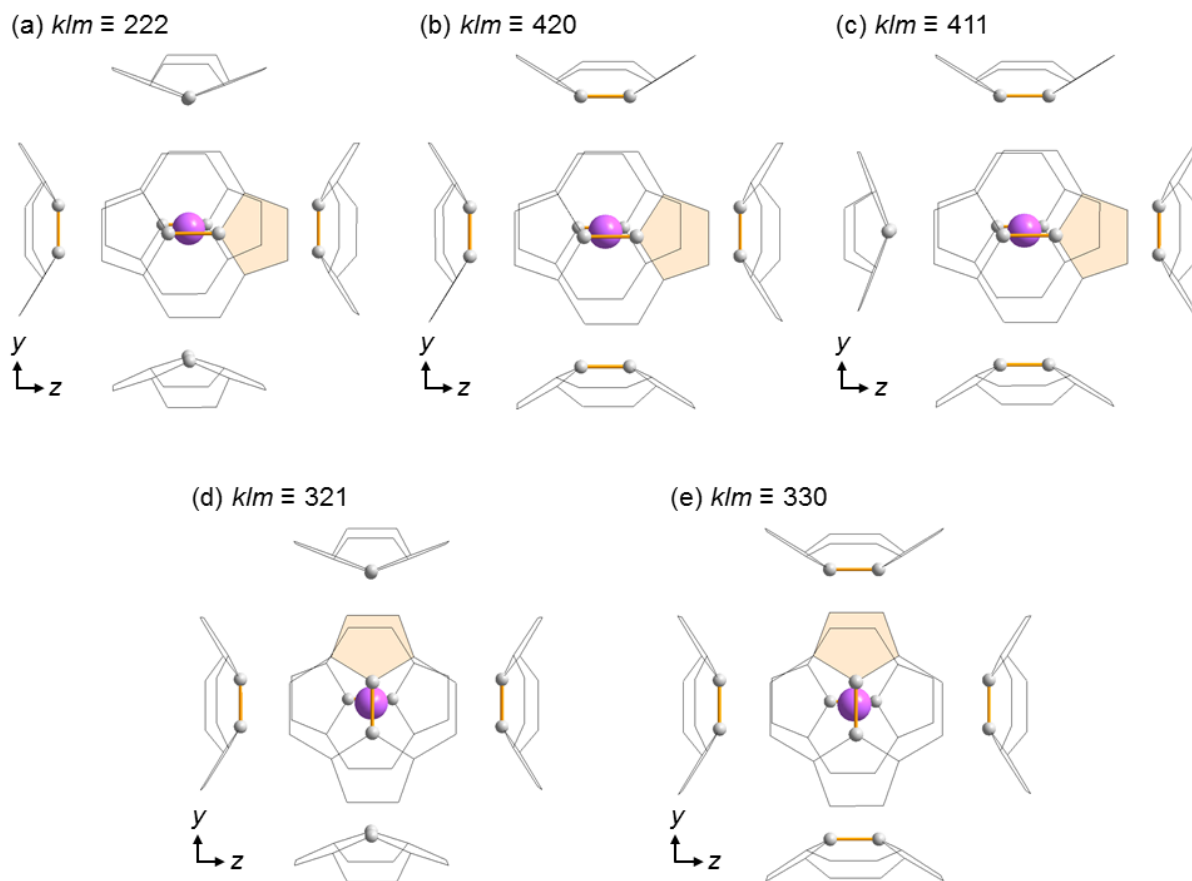


Figure 6.3:  $\text{Cs}^+$  ion (purple spheres) in the octahedral environment (a) without merohedral disorder (222 configuration), and with merohedral disorder for all inequivalent configurations:  $klm =$  (a) 420, (c) 411, (d) 321, and (e) 330. Please note the difference in the orientation of C=C double bond (marked with thick orange line) and the pentagon ring (shaded) for the front molecule.

Configurations	No. of possibilities	Probabilities	T-peak
LLL	2	$\alpha^4 + \beta^4$	T'
LLR	8	$4\alpha^3\beta + 4\beta^3\alpha$	T
LLRR	6	$6\alpha^2\beta^2$	T*

Table 6.2: Analysis of the  $^{133}\text{Cs}$  T-site intensities in merohedrally disordered *fcc*  $\text{Cs}_3\text{C}_{60}$ .  $\alpha$  and  $\beta$  are probabilities for each merohedral orientation,  $\alpha + \beta = 1$ . If  $\alpha = \beta$  ratio of probabilities T':T:T\* becomes the same as the ratio of possibilities.

LLL is completely equivalent to the RRRR configuration. Therefore, as first discussed in Ref. [118], out of  $2^4 = 16$  possible combinations for the T-site coordination only three are different from the  $^{133}\text{Cs}$  NMR point of view: LLL, LLR, LLRR with 2, 8 and 6 possibilities, respectively. If both  $\text{C}_{60}^{3-}$  merohedral orientations appear with the same probability, then the number of the above possibilities must also equal the relative intensities of different NMR peaks. The merohedral disorder model of *fcc*  $\text{Cs}_3\text{C}_{60}$  reasonably well fit with the experimental intensity ratio for the tetrahedral peaks T':T:T\* = 3:8:5 (Tab. 6.1). The strongest T peak is thus, for instance, assigned to the LLR configuration (Fig. 6.2b) and T' to the most symmetric LLL configuration (Fig. 6.2a). The agreement between experimental ratio and the calculated one can be improved if we allow non-equal probabilities for the two merohedral orientations. Writing probability for the first and the second merohedral orientation as  $\alpha$  and  $\beta$ <sup>1</sup> the probabilities for different tetrahedral configurations can be written as shown in the third column of Tab. 6.2. We note that in a special case when  $\alpha = \beta$ , the ratio T':T:T\* of probabilities becomes equal to the ratio of possibilities in the second column of Tab. 6.2. By allowing the merohedral probabilities to vary, a better agreement can be obtained with  $\alpha : \beta = 0.63(3) : 0.37(3)$  and the calculated ratio of T':T:T\* = 2.7 : 8.0 : 5.3. We note that this result is in violation with the *Fm* $\bar{3}$ *m* space group of  $A_3\text{C}_{60}$  which gives equal probabilities for the two merohedral orientations [34] and thus it should be taken lightly. Since we applied a rather crude model we cannot definitely conclude that obtained ratio is correct.

The fine structure of octahedral resonances for *fcc*  $\text{Cs}_3\text{C}_{60}$  (Fig. 6.1) has, to the best of our knowledge, not yet been observed nor discussed in  $A_3\text{C}_{60}$  family. We proceed by examining  $\text{Cs}^+$  ion, which is in the octahedral site surrounded by six  $\text{C}_{60}$  molecules as shown in Figs. 6.3. Merohedral disorder is manifested in the orientation of a  $\text{C}_{60}$  C=C double bond and the pentagon rings, which can take two mutually perpendicular orientations. We use the orientations of these C=C double bonds to characterize the O-site local coordination. In doing so we introduce a configuration number *klm*, which specifies how many C=C double bonds around the given O site have *x*-, *y*- or *z*-direction. For instance, where all surrounding  $\text{C}_{60}$  molecules are in the same standard orientation, two double bonds point along each of the crystallographic axes, hence we call such configuration 222 (Fig. 6.3a). However, when one of the  $\text{C}_{60}$  molecules freeze in the other merohedrally disordered orientation, its C=C double bond will orient differently. For instance, in Fig. 6.3d this is the case for the front  $\text{C}_{60}$  molecule and the corresponding configuration is 321. Merohedral disorder creates for the octahedral site altogether  $2^6 = 64$  possibilities, from which only five are non-equivalent (Figs. 6.3). We assume that the direction of a local magnetic field at O site, produced by the currents on the neighbouring fulleride, is given by the orientation of a C=C double bond. In this case the strength of interaction – that is, the total magnetic field at the O site – is a vector sum of all six magnetic field

---

<sup>1</sup> $\alpha + \beta = 1$

$klm$	No. of possibilities	Relative $B_{loc}$ magnitude	O-peak
420	6	$\sqrt{20}$	O'
411 & 330	12	$\sqrt{18}$	O**
321	36	$\sqrt{14}$	O
222	10	$\sqrt{12}$	O*

Table 6.3: Analysis of the  $^{133}\text{Cs}$  O-site intensities in merohedrally disordered *fcc*  $\text{Cs}_3\text{C}_{60}$ . A configuration number  $klm$  (first column) specifies how many C=C double bonds around the given O site have  $x$ -,  $y$ - or  $z$ -direction. The corresponding numbers of different possibilities are in the second column. The relative magnitude of O site local magnetic field ( $B_{loc}$ , third column) is calculated as a vector sum of all six contributions related to the orientation of C=C double bonds on neighbouring  $\text{C}_{60}$  molecules (see text for details). The assignment to the observed O-peaks is in the fourth column.

contributions. Under these assumptions we find only four different local O site magnetic fields (Tab. 6.3), which lead to the corresponding splitting of the octahedral resonances. Their intensities are predicted to be in the ratio 6:12:36:10, which is not far from the experimental O':O\*\*:O:O\* = 4:16:30:15. Moreover, the calculated relative magnitudes of total magnetic fields at O-site for different  $klm$  configurations comply with the observed shifts of O peaks (Fig. 6.1, Tab. 6.1). Similar analysis of the peak intensity ratios as have been performed for T-peaks where probabilities for two merohedral orientations were not equal is also possible for O resonances. However, these lines have much larger overlap which puts additional uncertainty on the extracted peak intensities. The experimental error is too large to be able to obtain an accurate merohedral orientation probabilities.

## 6.2 Substitutional disorder in $\text{Rb}_x\text{Cs}_{3-x}\text{C}_{60}$

The other type of disorder present in some of the ternary alkali-doped fullerenes is the substitutional disorder between different alkali ions occupying octahedral or tetrahedral sites. An example of such compounds is  $\text{Rb}_x\text{Cs}_{3-x}\text{C}_{60}$  series where  $x$  can take any real value between 0 and 3, prepared in order to gradually change the unit-cell volume, which is a controlling parameter of this family. Even-though, alkali metals, by themselves, are not considered to strongly influence the electronic structure [7] the presence of smaller alkali ions in the interstitial sites surrounded by larger nearest neighbour alkali ions can lead to a local site symmetry reduction and thus to a change of the crystal field surrounding  $A_3\text{C}_{60}$  molecules. To what extent the local site symmetry is affected by the substitutional disorder will be studied in this section.

In  $\text{Rb}_x\text{Cs}_{3-x}\text{C}_{60}$  compounds the substitutional disorder between  $\text{Cs}^+$  and  $\text{Rb}^+$  ions is expected for compositions  $0 < x < 2$  and  $2 < x < 3$ . Let us focus first on the  $0 < x < 2$  compounds. In this analysis the one  $\text{Cs}^+$  ion per unit cell that is always in the octahedral site can be ignored. The level of disorder can be regarded as a number of possible configurations where either  $\text{Rb}^+$  or  $\text{Cs}^+$  ion occupy each site on an arbitrary lattice. The number of configurations is obtained with a binomial coefficient  $\binom{n}{k}$ , where  $n$  is number of lattice sites and  $k = \alpha n$  where  $\alpha = x/2$  is a probability for  $\text{Rb}^+$  ion to occupy a lattice site. The maximal number of combinations or a degree of disorder have  $x = 1$  compounds with  $\binom{n}{n/2}$  combinations. For larger or smaller  $x$ , disorder monotonically decreases until it vanishes for  $x = 2$  or 0, i.e.  $\text{Rb}_2\text{CsC}_{60}$  and  $\text{Cs}_3\text{C}_{60}$  compounds, respectively. For  $2 < x < 3$  compounds a similar analysis can be done. Here two  $\text{Rb}^+$  ions in tetrahedral

sites are ignored since small amount of large  $\text{Cs}^+$  ions will occupy only octahedral sites. This sets the probability for  $\text{Rb}^+$  ion to  $\alpha = x - 2$ . The maximal disorder in this case is for  $x = 2.5$  or  $\text{Rb}_{2.5}\text{Cs}_{0.5}\text{C}_{60}$  and no disorder is present in  $\text{Rb}_3\text{C}_{60}$ .

To study the effects of substitutional disorder on the local scale we have performed MAS  $^{133}\text{Cs}$  NMR on  $\text{Rb}_{0.5}\text{Cs}_{2.5}\text{C}_{60}$  sample, a sample with considerable level of disorder. For structural details see App. B.2. Partial replacement of  $\text{Cs}^+$  with smaller  $\text{Rb}^+$  ions does not affect main room temperature MAS  $^{133}\text{Cs}$  NMR spectral features shown in Fig. 6.4. One can still recognize all seven major peaks grouped in the tetrahedral and octahedral groups. With respect to  $\text{Cs}_3\text{C}_{60}$  these peaks systematically slightly shift to lower frequencies for about 10–15 ppm (Tab. 6.4). In addition, all peaks are considerably broader compared to  $\text{Cs}_3\text{C}_{60}$ , i.e. the widths are now about 20 and 30 ppm for octahedral and tetrahedral peaks, respectively. This suggests a presence of an additional effect of disorder caused by the Rb intercalation at the local scale. Spin-lattice relaxation times get longer after Rb substitution an effect that seems to be more pronounced than in the case of spectral line effects. Namely,  $T_1$  is typically in the range between 400–450 ms and 70–100 ms for octahedral and tetrahedral sites, respectively. This implies that  $\text{Rb}^+$  substitution does not strongly perturb local-site symmetry, but may have more pronounced effect on the electron spin dynamics that defines nuclear spin-lattice relaxation times. Apart from 7 recognized resonance lines an additional very sharp line labelled here as T'' on the high frequency side of T' peak can be observed at 127 ppm of the MAS  $^{133}\text{Cs}$  NMR room temperature spectrum. Its low intensity of about 2% of the total spectrum and the narrow linewidth may suggest that it belongs to some unidentified impurity phase or less likely to a T' site in a part of the sample without extra strain caused by the Rb/Cs site disorder (Rb-rich region). We also note that in order to simulate spectrum we have to include a broad background (width 150 ppm) with a centre at -18 ppm and a non-negligible intensity of about 27.5%. An analogous broad peak can also be found beneath octahedral peaks with an intensity of 11% (Fig. 6.4). Based on their joint intensity (38.5%), which is more than estimated amount of impurity phases, we suspect that these two peaks belong to Cs sites with  $\text{Rb}^+$  ions located in the nearest neighbouring tetrahedral site. The probability of finding at least one  $\text{Rb}^+$  ion in the nearest neighbouring site<sup>2</sup> is  $1 - \delta^6 = 82\%$ , where  $\delta = 1 - x/2 = 0.75$  is probability for finding a Cs ion in the tetrahedral site, and exponent corresponds to 6 such neighbours. If  $T_b$  would consist of Cs sites with at least one Rb ion as the nearest neighbour the  $T_b : T$  ratio would be much larger than the experimental one. A better agreement is obtained if  $T_b$  spectral line consist of Cs sites with at least two Rb neighbours.

### 6.3 *fcc* and A15 crystal symmetries

It is interesting to compare two  $\text{Cs}_3\text{C}_{60}$  superconducting polymorphs with different crystal symmetries, the face-centred cubic, *fcc*, and body-centred cubic, A15 from the structure disorder point of view. The A15 polymorph was found to have a disorder-free crystal structure where all  $\text{C}_{60}$  molecules are orientationally ordered and there is negligible amount of cation vacancies [13]. On the other hand, *fcc* polymorph has, as we have described above, merohedral  $\text{C}_{60}$  orientational disorder. From the superconducting point of view, both compounds exhibit similar superconducting domes on the  $(V, T)$  phase diagram, which after appropriate rescaling fall on the same universal superconducting

<sup>2</sup>Each tetrahedral site has 6 nearest neighbour tetrahedral sites that have two shared  $\text{C}_{60}$  molecules in direction of three crystallographic axis.

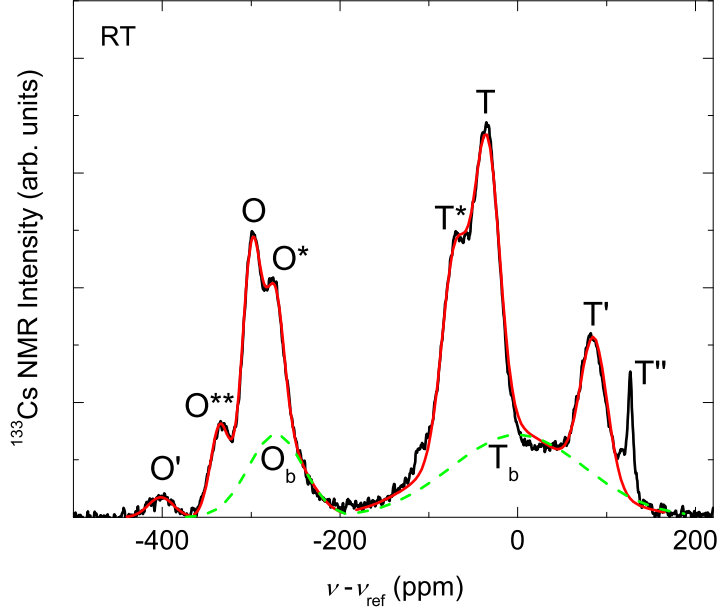


Figure 6.4: Room temperature  $^{133}\text{Cs}$  MAS NMR spectrum of *fcc*  $\text{Rb}_{0.5}\text{Cs}_{2.5}\text{C}_{60}$  measured at a spinning frequency,  $\nu_r = 25$  kHz (black solid line). For comparison, we show the corresponding static ( $\nu_r = 0$  kHz) solid state  $^{133}\text{Cs}$  NMR spectrum (shaded area).

curve [14]. In addition, both polymorphs show similar superconducting shielding fractions under pressure with *fcc* having even slightly larger fraction than disorder-free A15 polymorph [14]. This indicates that the superconducting mechanism must be similar in both polymorphs. The differences are accounted to the different density of states and to the frustration effects which are both related to the crystal structure. The effect of the merohedral disorder seems to be negligible.

The most notable difference between the two polymorphs is, apart from their structure, the magnetically ordered phase in the insulating part of the phase diagram [14]. A15 polymorph has Néel temperature of  $T_N = 46$  K and Weiss temperature of  $\theta = -68(1)$  K [13]. Similar  $T_N$  and  $\theta$  temperatures support long-range magnetic order, which is in agreement with experiment [13]. In contrast *fcc* polymorph has Néel temperature of  $T_N = 2.2$  K and much larger Weiss temperature of  $\theta = -105(2)$  K [14]. A large difference between the two temperatures is typical for samples with strong frustration effects. This is indeed true for the *fcc* structure which is geometrically frustrated. Based on high-cubic symmetry and the icosahedral symmetry of the  $\text{C}_{60}$  molecules one would expect that strong frustration would be present down to the lowest temperatures and, therefore, no magnetic ordering would occur. The experimental evidence of the presence of magnetic ordering at 2.2 K is thus remarkable and speaks for an additional symmetry lowering mechanism that reduces frustration effects. Since the volume fraction of magnetically ordered state at 2.2 K is above 70% as is evident from the  $\mu\text{SR}$  measurements [14] we can ignore impurity phases as the source of the symmetry breaking. The remaining internal degree of freedom in *fcc* compounds are the merohedral disorder and JT effect. Comparing Néel temperatures of the two polymorphs the effect of merohedral disorder or JT on the hopping integrals is only approximately 5% (1/20 of the effective hopping integral between neighbouring molecules in A15 polymorph).

$^{133}\text{Cs}$ peaks	O'	O**	O	O*	O <sub>b</sub>
Centre (ppm)	-401.6(4)	-335.5(6)	-299.3(2)	-273.2(3)	-272(6)
Width (ppm)	28.5(8)	20.8(9)	20.8(1)	20.8(6)	62(5)
Intensity (%)	1.20(2)	3.5(6)	9.5(9)	6.0(5)	11(2)
$T_1$ (ms)	590(10)	450(10)	430(10)	400(10)	
$^{133}\text{Cs}$ peaks	T*	T	T'	T''	T <sub>b</sub>
Centre (ppm)	-71	-35	85.8(3)	126.9(1)	-15(2)
Width (ppm)	29	29	30	9(1)	150
Intensity (%)	12.5(3)	18.2(8)	8.9(2)	2.0(1)	27.5(6)
$T_1$ (ms)	94(5)	84(5)	74(5)	91(5)	

Table 6.4: Results of the analysis of MAS  $^{133}\text{Cs}$  NMR spectra of  $\text{Rb}_{0.5}\text{Cs}_{2.5}\text{C}_{60}$  at room temperature, shown in Fig. 6.4. Line positions are given relative to the 0.1 M solution of  $\text{CsNO}_3$  in  $\text{D}_2\text{O}$  reference. Values without errorbar estimate were kept fixed to reduce the number of free parameters. Measured spin-lattice relaxation time ( $T_1$ ) for each resonance is added in the 5th and 10th row.

## 6.4 Conclusions

We measured high-resolution  $^{133}\text{Cs}$  NMR MAS spectrum of insulating *fcc*  $\text{Cs}_3\text{C}_{60}$  and *fcc*  $\text{Rb}_{0.5}\text{Cs}_{2.5}\text{C}_{60}$  samples with the highest resolution up to now. We have shown that its fine structure is in excellent agreement with the local variations in the T- and O-site coordination arising from the  $\text{C}_{60}$  merohedral disorder. The agreement could be further improved if we would allow the probabilities of the two merohedral  $\text{C}_{60}$  orientations to be slightly different (0.6:0.4). It is surprising that the effect of different merohedral orientations on the  $^{133}\text{Cs}$  lineshift is so large, namely the lineshift difference between T and T' is  $\sim 130$  ppm (Tab. 6.1). This value is comparable to the mean difference between O and T sites which have completely different site symmetries. Such a large difference suggests that the ring currents on the surface of  $\text{C}_{60}^{3-}$  ions, responsible for the magnetic field at  $\text{Cs}^+$  ion, must be very strong. This is, however, not compatible with the theoretical study on the isolated  $\text{C}_{60}$  molecules where it was argued that ring currents have negligible effect on the NMR lineshift [123]. Further discussion on this matter will be given in Chap. 7.

Experiments on  $\text{Rb}_{0.5}\text{Cs}_{2.5}\text{C}_{60}$  compound that contains substitutional disorder between  $\text{Rb}^+$  and  $\text{Cs}^+$  ions show that there are two effects related to this disorder. A moderate broadening of the linewidths (30–50%) and the appearance of two broad components (width  $> 100$  ppm) one at T and the other at O site. Whereas the former broadening could be attributed to the higher order effects, e.g. next nearest alkali neighbours, the later broadening is argued to come from the presence of more than two different nearest alkali neighbours that are expected to strongly distort the local crystal symmetry. Whether this large broadening is a direct consequence of local symmetry reduction or perhaps an indirect consequence of disturbed ring currents is not clear. Additional insight can be obtained from  $^{13}\text{C}$  MAS NMR measurements on  $\text{Rb}_{0.5}\text{Cs}_{2.5}\text{C}_{60}$  presented in the previous chapter. Room-temperature  $^{13}\text{C}$  spectrum consists of three distinguishable lines corresponding to three non-equivalent carbons in  $\text{C}_{60}$  molecules, as was discussed for  $\text{Cs}_3\text{C}_{60}$ . With an exception of C1 line, the other two are slightly broader ( $\sim 50\%$ ) and all are shifted for  $\sim 5$  ppm to lower values with respect to  $\text{Cs}_3\text{C}_{60}$  (Tab. 5.1). Moderate changes in the  $^{13}\text{C}$  spectrum of  $\text{Rb}_{0.5}\text{Cs}_{2.5}\text{C}_{60}$  is not compatible with the strong symmetry

reduction argument and, therefore, favour the disturbed ring currents argument.

Comparison between merohedrally disordered *fcc* and disorder-free A15 polymorph of  $\text{Cs}_3\text{C}_{60}$  gives an estimate that merohedral disorder affects only up to  $\sim 5\%$  of an average hopping integral between two  $\text{C}_{60}$  molecules. This suggests that merohedral disorder only weakly distorts the electronic pathways.

To conclude, the substitutional disorder lowers the site symmetry, however, the changes in the crystal fields are only moderate or weak compared to electronic energy scale. Both merohedral and substitutional disorder, therefore, do not considerably affect macroscopic electronic properties of *fcc*  $A_3\text{C}_{60}$ . On the other hand, we argue that there are relatively strong magnetic fields at the interstitial sites arising from ring currents. These are controlled by the merohedral orientation and indirectly by local site symmetry reduction due to substitutional disorder. Observed relatively strong local inhomogeneities could additionally warp JT lowest APES in a random fashion and lead to the stabilization of JT distortion (static JT effect) without showing long-range orbital ordering.

# 7 Importance of electron correlations

The presence of strong electron correlations in superconducting alkali-doped fullerenes has been suspected already from the early investigations on these materials [7]. The reason is that large on-site Coulomb repulsion between two electrons is comparable or even larger than the width of a narrow conduction  $t_{1u}$ -derived band. Nevertheless, it has been believed that strong screening and retardation effects, later coming from rich phonon spectra of  $C_{60}$ , cause strong renormalization of the repulsion interaction and, therefore, do not considerably effect the metallic or superconducting state at low temperatures.

Recent developments related to the synthesis of hyper-expanded  $A_3C_{60}$  compounds [13, 14, 124, 125], where strong electron correlations are clearly present, call for reconsideration of previous believes. The underlying superconducting state, previously believed to be of standard BCS type, now closely resembles that of unconventional superconductors where strong electron correlations and close proximity to the MIT are the main properties. To relate the fullerene superconductors to the unconventional ones the role of electron correlations is discussed next.

## 7.1 Bandwidth vs. on-site correlations

### 7.1.1 Bandwidth

With the intercalation of alkali atoms their electron in the outer  $s$ -orbital is transferred to  $t_{1u}$ -derived band of  $C_{60}$  molecules. Having three alkali atoms per  $C_{60}$  molecule in the unit-cell after electron transfer each  $C_{60}$  becomes triply charged,  $C_{60}^{3-}$ . The electron transfer occurs due to a strong electron affinity of  $C_{60}$  molecules. This has been shown theoretically by *ab initio* calculations [24, 51] and confirmed by the photoemission experiments [51, 126]. An almost complete transfer of electrons is maintained by very small back transfer due to small  $C_{60}$ - $A$  hopping probabilities. This is a result of a large anti-bonding nature of  $t_{1u}$  orbitals where the wavefunction sign changes drastically over hexagon rings, that are facing tetrahedral alkali ions, and over carbons connected by double bond, that are facing octahedral ions. At the same time small back transfer is a result of only a few percent admixture of alkali-metal  $s$ -orbitals into the molecular  $t_{1u}$  orbitals [51]. The electron hopping is, on the other hand, considerably larger between neighbouring  $C_{60}$  molecules. This is due to mostly  $p_r$  character of  $t_{1u}$  orbitals that point radially out of the molecules and thus have large overlap with neighbouring molecules [127].

The electron's kinetic energy is given by a hopping integral,  $t$ , which is related to the conduction electron bandwidth. This is easy to show in the second quantisation where the kinetic term of non-interacting electrons is written as

$$\mathcal{H}_{\text{kin}} = - \sum_{\langle i,j \rangle} t_{i,j} c_i^\dagger c_j + h.c. \quad (7.1)$$

Here the summation goes over all the neighbouring sites,  $c_i^\dagger$  and  $c_i$  are creation and annihilation operators, respectively, and *c.c.* represent complex conjugated terms. By transforming the above Eq. 7.1 to  $q$ -space one obtains

$$\mathcal{H}_{\text{kin}} = - \sum_{\vec{q}} \varepsilon_{\vec{q}} c_{\vec{q}}^\dagger c_{\vec{q}} + h.c., \quad \varepsilon_{\vec{q}} = \sum_n^z t_n e^{-i\vec{q} \cdot \vec{a}_n}, \quad (7.2)$$

where  $\vec{a}_n$  is a vector pointing to the nearest neighbours and  $z$  is the number of nearest neighbours. In case of cubic structure where all hopping integrals are equal the kinetic energy can be written as  $E_{\text{kin}} = 2dt \cos(\vec{q} \cdot \vec{a}_n)$ , where  $d = z/2$  is system dimensionality. The bandwidth, being a difference between maximal and minimal energy, is for simple cubic structure equal to  $W = 4dt = 2zt = 12t$ . On the other hand, for *fcc* with  $z = 12$  and A15 with  $z = 8$  the bandwidth is in both cases equal to  $W = 16t$ .

The bandwidth in  $A_3C_{60}$  materials have been mostly studied using *ab initio* procedures. The computed bandwidth for *fcc*  $K_3C_{60}$  is  $W \simeq 0.6$  eV [39, 50, 51, 128], for *fcc*  $Rb_3C_{60}$  is  $W \simeq 0.4$  eV [128, 129], for *fcc*  $Cs_3C_{60}$  is  $W \simeq 0.3$  eV [54, 128, 129] and for A15  $Cs_3C_{60}$  is  $W \simeq 0.5$  eV [54, 128]. There were several attempts to measure the bandwidth experimentally, however, the results were less conclusive. For instance, the angular-resolved photoemission spectroscopy could not give reliable data [5], due to merohedral disorder and small size of the Brillouin zone. Angular integrated techniques gave very broad spectra due to many-body effects and the presence of satellites originating from strong electron-phonon interactions. The experiments on  $K_6C_{60}$  and ordered monolayer of  $C_{60}$  on a Ag(111) substrate, where many-body effects are reduced, gave, on the other hand, bandwidths consistent to the *ab initio* calculations for non-interacting electrons [130].

### 7.1.2 Coulomb repulsion

When two electrons are put on  $C_{60}$  molecule they will repel each other due to the Coulomb interaction. The magnitude of the Coulomb interaction energy can be obtained in several ways depending on what approximations are used. In a completely classical picture two point charge electrons put on a sphere would move away from each other and maintain a distance of sphere diameter,  $d$  ( $d = 7$  Å for  $C_{60}$ ). In this approximation the Coulomb energy between the two electrons is  $U = e^2/(4\pi\varepsilon_0 d) = 2$  eV. In semi-classical approximation we take a smeared charge uniformly over a sphere as a thin shell. The Coulomb energy is then obtained as

$$U = \int d^3\vec{r}_1 \int d^3\vec{r}_2 \frac{\rho(\vec{r}_1)\rho(\vec{r}_2)}{4\pi\varepsilon_0|\vec{r}_1 - \vec{r}_2|} = \frac{e^2}{4\pi\varepsilon_0 R}. \quad (7.3)$$

Taking  $C_{60}$  radius,  $R = 3.5$  Å, the Coulomb energy is  $U = 4$  eV. A more realistic estimate of the Coulomb repulsion energy is obtained by the density functional theory where a total energy of a molecule with different number of added electrons is studied. By such treatment the obtained Coulomb energy was  $U \simeq 3$  eV, depending on a research group [5]. Experimentally, the Coulomb parameter was determined from the ionization and absorption energy measurements and photoabsorption experiments which gave  $U = 3.3$  eV [5]. The experimental result is in fair agreement with theoretical calculations.

When charged  $C_{60}$  molecules are put in a solid material the screening effects reduce the Coulomb repulsions energy. It has been theoretically shown that the Coulomb parameter in solid state can be reduced down to  $U = 0.8$ – $1.3$  eV [5]. The experimental estimate

of  $U$  in a material was done by the Auger spectroscopy on  $K_3C_{60}$  film. They obtained a value of  $U = 1.6 \pm 2$  eV [131]. However, measurements on the surface do not correctly represent the behaviour inside a bulk material since screening on the surface is smaller due to a smaller number of neighbouring molecules. It has been suggested that the Coulomb parameter would be for  $\sim 0.3$  eV [132] smaller inside the material compared to the surface. If this is true the Coulomb energy in solid would be  $U = 1.1\text{--}1.5$  eV. This experimental estimate is somewhat larger than theoretical results, however, both are in a fairly good agreement. Even-though, the Coulomb repulsion energy in solid considerably reduced it is still larger than the electron kinetic energy measured by the bandwidth. This strongly suggest strong electron correlations and close proximity to the MIT of the  $A_3C_{60}$  compounds.

Finally, we note that the inter-molecular Coulomb interaction was estimated to be of the order of 0.3 eV [132]. This is smaller than the on-site Coulomb repulsion and can be thus neglected in the first calculations. However, in the final result this interaction should also be considered. On the other hand, it has also been shown that inter-molecular interaction does not in any specific way influence the MIT [133].

## 7.2 MIT transition

As we have shown in the previous section the Coulomb repulsion energy between two electrons on  $C_{60}$  molecules is larger than their kinetic energy. In a picture where each molecule has one electron in a single orbital this would result in an electron localization, since the energy gained by hopping to a neighbouring molecule would be smaller than the Coulomb potential energy required for two electrons being on the same molecule. Such a state is called the Mott-insulating state [5]. However, despite the above consideration most  $A_3C_{60}$  compounds exhibit metallic ground state, suggesting that the proposed picture is not appropriate. Only with the synthesis of the largest member,  $Cs_3C_{60}$ , where kinetic energy of electrons is sufficiently reduced by large intermolecular separation, the electrons become localized and forming Mott-insulating state [13, 14]. Assuming  $Cs_3C_{60}$  is at the MIT we can estimate the critical ratio  $(U/W)_c$  for *fcc*  $A_3C_{60}$  compounds from already determined  $U = 0.8\text{--}1.5$  eV and  $W = 0.3$  eV. The obtained critical ratio  $(U/W)_c = 2.7\text{--}5$  is much larger than 1 as would be naïvely expected for the above single-band model and which has been found for cuprate superconductors [5].

In this section we will show that such large critical ratio can be explained by triple orbital degeneracy of  $t_{1u}$  orbitals and the frustration effects in the geometrically frustrated *fcc* structure. Next, we will study how local properties determined by NMR experiments behave when going from insulating to the metallic state over MIT and finally try to characterise the transition.

### 7.2.1 $(U/W)_c$ for *fcc* $A_3C_{60}$

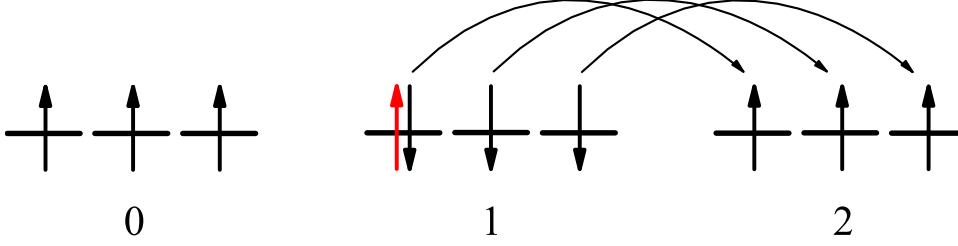


Figure 7.1: After adding an spin up electron (red arrow) to the site 1 of the antiferromagnetic ground state  $|\text{anti}\rangle$  and paying the energy  $U$  the three spin down electrons on this site can now freely move to the neighbouring site without paying an additional energy  $U$ .

Gunnarsson *et al.* [106] showed that  $t_{1u}$  orbital degeneracy allows multiple hopping channels to the neighbouring molecules and thus effectively increase the hopping integral in a single-particle picture and consequently widen the relevant bandwidth by a factor of  $\sqrt{N_d}$ , where  $N_d$  is the number of degenerate  $t_{1u}$  orbitals. This can be easily shown in a half-filled Hubbard model in the limit of large  $U$

$$\mathcal{H} = - \sum_{i m \sigma, j m' \sigma'} t_{i m, j m'} c_{i m \sigma}^\dagger c_{j m' \sigma'} + U \sum_i \sum_{m \sigma < m' \sigma'} n_{i m \sigma} n_{i m' \sigma'}, \quad (7.4)$$

where  $\sigma$  is spin number,  $m$  counts  $N_d$  degenerate orbitals and  $n = c^\dagger c$  is the number operator. We consider a simple case where electrons can hop only to the neighbouring sites with the same orbital number

$$t_{i m, j m'} = \begin{cases} t \delta_{m, m'} & \text{if } i \text{ and } j \text{ are nearest neighbours,} \\ 0 & \text{otherwise.} \end{cases} \quad (7.5)$$

If we add an additional spin up electron to site 1,  $m = 1$ , of antiferromagnetic ground state (Fig. 7.1) the wavefunction can be expressed as

$$|1\rangle = c_{11\uparrow}^\dagger |\text{anti}\rangle. \quad (7.6)$$

After the electron is added and the required Coulomb energy  $U$  has been paid the other three electrons on this site can now freely hop to the neighbouring sites  $i = 0, 2$ . Such state is described by

$$|i\rangle = \frac{1}{\sqrt{N_d}} c_{11\uparrow}^\dagger \sum_m c_{i m \uparrow}^\dagger c_{1 m \uparrow} |\text{anti}\rangle. \quad (7.7)$$

The matrix element between the the two states is then

$$\langle i | \mathcal{H} | 1 \rangle = \sqrt{N_d} t, \quad (7.8)$$

which means that the matrix element between state 1 and state  $i$  is by a factor  $\sqrt{N_d}$  larger than the single-particle hopping matrix element. Since the single-particle bandwidth ( $W$ ) is proportional to the matrix element  $\langle i | \mathcal{H} | 1 \rangle = t$  in case of multiple hopping channels the effective single-particle bandwidth is  $\widetilde{W} = \sqrt{N_d} W$ . An effective critical  $(U/W)_c$  ratio is due to multiple orbital degeneracy, therefore, expressed as  $(U/W)_c \sim \sqrt{N_d}$ . The same result is obtained when allowing also intraband hopping  $t_{1m, 2m'} \neq 0$  and when considering

the trail of rotated spins behind moving electrons in the limit where number of neighbours is larger than  $N_d$  [5].

Considering orbital degeneracy the critical ratio for  $A_3C_{60}$  with  $N_d = 3$  is  $(U/W)_c \sim 1.7$ , which is still smaller than the estimated one,  $(U/W)_c = 2.7-5$ . An additional increase of  $(U/W)_c$  ratio has been accounted to the frustration effects present in the *fcc* structure. Quantum Monte-Carlo study on a cluster of 32  $C_{60}$  molecules gave  $(U/W)_c = 2.3$  for frustrated *fcc*  $A_3C_{60}$  structure and  $(U/W)_c = 1.3$  for unfrustrated *bcc* (A15)  $A_3C_{60}$  crystal structure [134]. High critical ratio determined for *fcc*  $A_3C_{60}$  compounds is, therefore, a combination of orbital degeneracy and frustration effects.

## 7.2.2 NMR measurements on $Cs_3C_{60}$ and $Rb_xCs_{3-x}C_{60}$

Previous NMR measurements on  $A_3C_{60}$  compounds with smaller unit-cell volumes are consistent with a metallic state described by Fermi liquid theory where orbital and spin degrees of freedom are neglected and possibly weak electron-electron interaction causes only a minute renormalization of  $N(E_F)$  [7, 135, 136]. On the other hand, measurements on the largest member,  $Cs_3C_{60}$ , reveal low-spin Mott-insulating ground state where spin, orbital, and lattice degrees of freedom play a crucial role [13, 14, 110, 124, 125]. Having such a different contributions on either side of MIT it is interesting to inquire how the system evolves from metallic to Mott-insulating state and how this is related to the underlying superconductivity with non-conventional properties. Being similar to other unconventional superconductors, e.g., cuprates, heavy fermions, new exotic states, like pseudogap, strange-metal, spin-liquid, or antiferromagnetic state, found in those materials [137] could be also present in  $A_3C_{60}$ .

To explore the properties of *fcc*  $A_3C_{60}$  in the vicinity of MIT we employed high-pressure  $^{13}C$ ,  $^{133}Cs$  NMR experiments on  $Cs_3C_{60}$  and  $^{13}C$ ,  $^{133}Cs$  and  $^{87}Rb$  NMR experiments on  $Rb_xCs_{3-x}C_{60}$  samples. Being able to change the unit-cell volume, which was found to be the only controlling parameter in  $A_3C_{60}$  system, we can scan the phase diagram in a controlled manner. High-pressure NMR technique is presented in Sec. 3.4.2 and the experimental details are given in App. B.1 and App. C.1. NMR measurement on a series of  $Rb_xCs_{3-x}C_{60}$  samples were partial substitution of Cs with Rb atoms alters the unit-cell volume, can be also considered as an effective chemical pressure. The structural details of  $Rb_xCs_{3-x}C_{60}$  samples used for positioning the NMR results on the phase diagram are summarized in App. B.2. Details regarding spin-lattice relaxation rate analysis are given in App. C.

### Spin-lattice relaxation rate

A representative  $^{13}C$  spin-lattice relaxation rates divided by temperature are summarized in Fig. 7.2 from both high-pressure NMR on  $Cs_3C_{60}$  and NMR on  $Rb_xCs_{3-x}C_{60}$ . Selected  $^{133}Cs$  and  $^{87}Rb$  results are added as empty symbols to Fig. 7.2a and Fig. 7.2b, respectively, to emphasise an equivalence between different local NMR probes,  $^{13}C$ ,  $^{133}Cs$ , or  $^{87}Rb$ . Another equivalence can be found by comparing physical and chemical pressure. Both techniques give qualitatively similar results. A quantitative comparison is not possible since the temperature dependences of the two techniques follow different paths on the phase diagram (Fig. 7.15). Our results are also consistent with the previous ambient pressure  $^{13}C$  NMR results on *fcc* rich  $Cs_3C_{60}$  sample [14] and high-pressure  $^{133}Cs$  NMR measurements on multiphase  $Cs_3C_{60}$  sample [124, 125].

Measurements in the over-expanded part of the phase diagram ( $P \simeq 0$  kbar,  $x = 0$ )

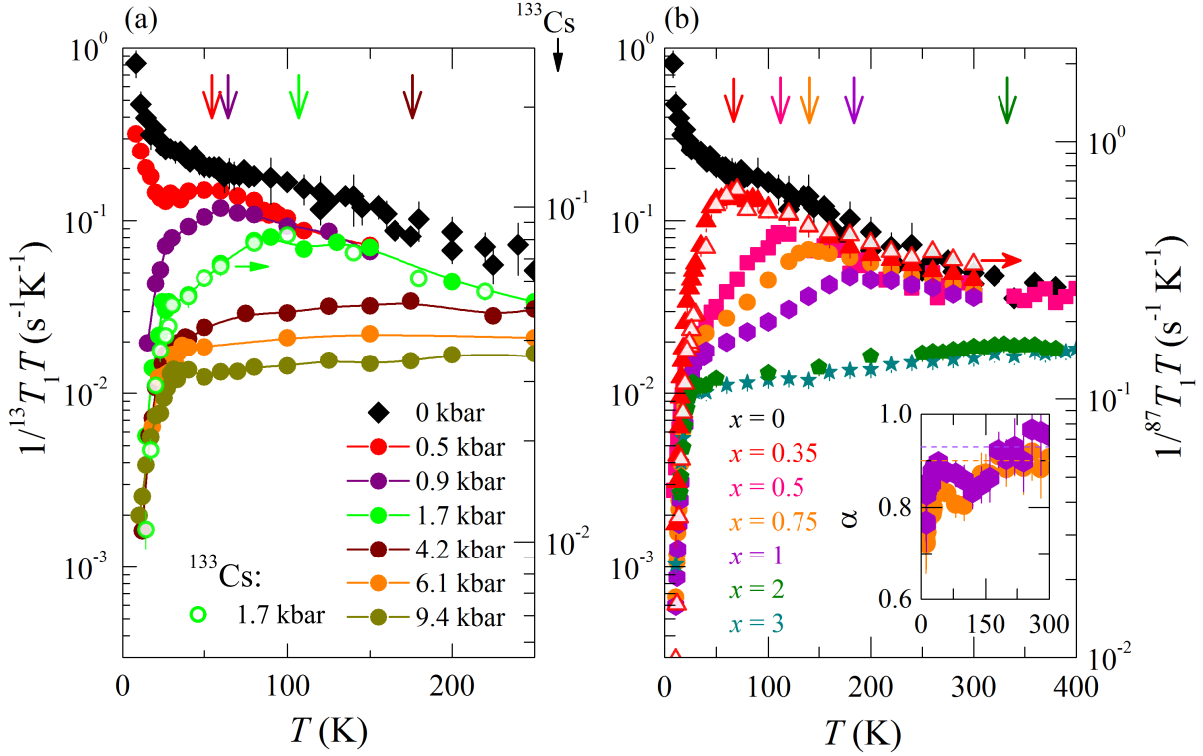


Figure 7.2:  $1/T_1T$  results of (a)  $^{13}\text{C}$  high-pressure NMR on  $\text{Cs}_3\text{C}_{60}$  and (b)  $^{13}\text{C}$  NMR on  $\text{Rb}_x\text{Cs}_{3-x}\text{C}_{60}$ . Coloured arrows in (b) indicate the position of maximum corresponding to MIT ( $T_{\text{MIT}}$ ). Inset to (b) show a stretch parameter used for fitting recovery of nuclear magnetization and indicates an enhancement of  $T_1$  distribution below  $T_{\text{MIT}}$ .  $^{133}\text{Cs}$  data points at  $P = 1.7$  kbar are added to (a) as empty circle and  $^{87}\text{Rb}$  data points for  $x = 0.35$  are added to (b) as empty triangles.

show a monotonic increase of  $1/T_1T$  with decreasing temperature, which is characteristic of an exchange-coupled antiferromagnetic insulator [14, 125] (Sec. 3.3.3). Assuming low-spin state ( $S = 1/2$ ), as determined by the bulk susceptibility measurement [14], the exchange coupling constant for the over-expanded  $\text{Cs}_3\text{C}_{60}$  is  $J = 25(5)$  K (Eq. 3.63) which is in agreement with the previous measurements [14]. Going from larger towards smaller volumes (increasing  $P$  or  $x$ ) data follows the insulating behaviour only at high temperatures. At a certain temperature  $1/T_1T$  reaches a maximum below which it drops exponentially towards a value of  $1/T_1T \sim 0.01 \text{ s}^{-1}\text{K}^{-1}$  (Fig. 7.2b). This is a typical value for metallic compounds, e.g.,  $\text{Rb}_3\text{C}_{60}$  [47, 135]. The maximum in  $1/T_1T$  data can thus be assigned to MIT and the corresponding temperature as  $T_{\text{MIT}}$ . This conclusion was made before [125] by comparing  $1/T_1T$  temperature dependence to a similar behaviour observed in organic SC where metallic and insulating phases manifest as separate NMR lines [138]. At low temperatures,  $T \sim 30$  K,  $1/T_1T$  data again drops and vanishes as  $T \rightarrow 0$ . Such a drop is characteristic for a superconducting state where exponential decay in  $1/T_1T$  is a consequence of the superconducting gap opening below  $T_c$ . In the high-pressure experiments the low temperature drop can be observed already at 1.0(5) kbar (Fig. 7.2a) which is not entirely consistent with bulk susceptibility measurements where superconducting state appears at 1.3 kbar [14]. However, since NMR is a local probe technique a drop in  $1/T_1T$  could be a result of a non-connected filamentary type of superconductivity that appears at lower pressures or possible non-hydrostatic pressure conditions.

When going further towards smaller volumes we can follow four different effects. (1) The high-temperature part, above  $T_{\text{MIT}}$ , only approximately fall on the same curve. In fact,  $1/T_1T$  become less steep for smaller volumes. This can be best seen by comparing  $1/T_1$  data which is approximately temperature independent in this temperature region. For  $x = 0$ ,  $1/T_1 = 15(3) \text{ s}^{-1}$  which is again in good agreement with previous measurements ( $1/T_1 = 18(1) \text{ s}^{-1}$  [14]). With increasing stoichiometric ratio,  $x$ ,  $1/T_1$  decreases and reaches  $1/T_1 = 8(2) \text{ s}^{-1}$  for  $x = 2$ , see Tab. 7.1. A reduction  $1/T_1$  for a factor of cca. 2 can according to Eq. 3.63 come from either increase of the exchange frequency, which depends on the effective exchange coupling constant, or from the decrease of an effective magnetic moment. In these compounds both mechanisms are possible and cannot be distinguished by NMR alone. (2)  $T_{\text{MIT}}$  is increasing with decreasing unit-cell volume (increasing  $P$  or  $x$ ). From  $T_{\text{MIT}} = 65 \text{ K}$  for  $x = 0.35$  the transition shifts to  $T_{\text{MIT}} = 330 \text{ K}$  for  $x = 2$  and  $T_{\text{MIT}} \simeq 400 \text{ K}$  for  $x = 3$ , see Tab. 7.1. The slope of  $T_{\text{MIT}}$  as a function of volume or pressure will be further discussed in Sec. 7.2.3. (3) The exponential drop below  $T_{\text{MIT}}$  is a function of the unit-cell volume. The slope in the logarithmic plot (Fig. 7.2b) reduces from  $\alpha = 0.054(2) \text{ K}^{-1}$  for  $x = 0.35$  to  $\alpha = 0.0016(1) \text{ K}^{-1}$  for  $x = 3$  assuming  $1/T_1T = A + Be^{\alpha T}$ , see Tab. 7.1. (4)  $1/T_1T$  just above  $T_c$  is strongly varying with the unit-cell volume. Being  $1/T_1T_c = 0.046(5) \text{ s}^{-1}\text{K}^{-1}$  for  $x = 0.35$  the  $1/T_1T$  drops to a typical value of  $1/T_1T_c = 0.01 \text{ s}^{-1}\text{K}^{-1}$  for  $x = 3$ , consistent with previous experiments, see Tab. 7.1. According to the Korringa expression and Pauli susceptibility for metals, the increase of  $1/T_1T$  with increasing volume is expected as  $N(E_F)$  is increasing with volume, however, such strong dependence close to MIT is not expected. Further discussion on this subject will be given in Sec. 7.3.

Compound	$T_{\text{MIT}}$ (K)	$1/T_1$ ( $\text{s}^{-1}$ ), $T > T_{\text{MIT}}$	$\alpha$ ( $\text{K}^{-1}$ )	$1/T_1T_c$ ( $\text{s}^{-1}\text{K}^{-1}$ )
$x = 0$	-	15(3)	-	-
$x = 0.35$	65(5)	13(1)	0.054(2)	0.046(5)
$x = 0.5$	110(10)	11(2)	0.0182(5)	0.020(1)
$x = 0.75$	140(10)	11(1)	0.0118(2)	0.019(1)
$x = 1$	180(5)	10(1)	0.0075(1)	0.016(1)
$x = 2$	330(5)	7.5(5)	0.0018(1)	0.0107(5)
$x = 3$	400(10)	7(1)	0.0016(1)	0.0099(5)

Table 7.1: Summary of results from  $1/^{13}\text{C}T_1T$  measurements analysis. See text for details.

So far, measurements in the over-expanded limit where the system is in exchange-coupled insulating state and in the under-expanded limit where compounds like  $\text{Rb}_3\text{C}_{60}$  show a metallic behaviour are reasonably well understood. In the intermediate region, on the other hand, the state below  $T_{\text{MIT}}$  cannot be simply explained. To obtain a further insight into this state we show in inset to Fig. 7.2b the stretch exponent,  $\alpha$ , obtained when fitting NMR magnetization recovery data. An example and description of magnetization recovery data analysis is given in App. C. For magnetic systems described by a single  $T_1$  parameter stretch exponent equals  $\alpha = 1$ , however, when  $T_1$  is distributed the stretch exponent becomes  $\alpha < 1$ . In  $^{13}\text{C}$  NMR on fullerene systems the spin-lattice relaxation rate is expected to be slightly distributed due to three non-equivalent carbon atoms. A value of  $\alpha \simeq 0.9$  is expected in static  $^{13}\text{C}$  NMR measurements. As can be seen in the inset to Fig. 7.2b the stretch exponent is for  $x = 0.75$  and  $x = 1$  samples close to 0.9–1 only at high temperatures, whereas, below  $T_{\text{MIT}}$  it drops to  $\alpha \simeq 0.8$ . Below  $T_c$   $\alpha$  drops again due to appearance of vertices in the superconducting state. A reduction of  $\alpha$  when entering the

metallic state signals an enhanced distribution of spin-lattice relaxation rates, or in other words, a development of local-site inhomogeneities. The appearance of inhomogeneities is most probably related to the symmetry breaking below the phase transition. This is reminiscent to the phase coexistence observed for the second order phase transitions. To determine the order of the phase transition in  $A_3C_{60}$  we searched for the hysteresis on  $x = 0.35$  and  $x = 1$  samples by measuring spin-lattice relaxation times on cooling and on heating. After performing the temperature cycle on both sample we could not observe any hysteresis. We, therefore, conclude that the MIT phase transition in  $A_3C_{60}$  is of the second order, similar to magnetic phase transitions.

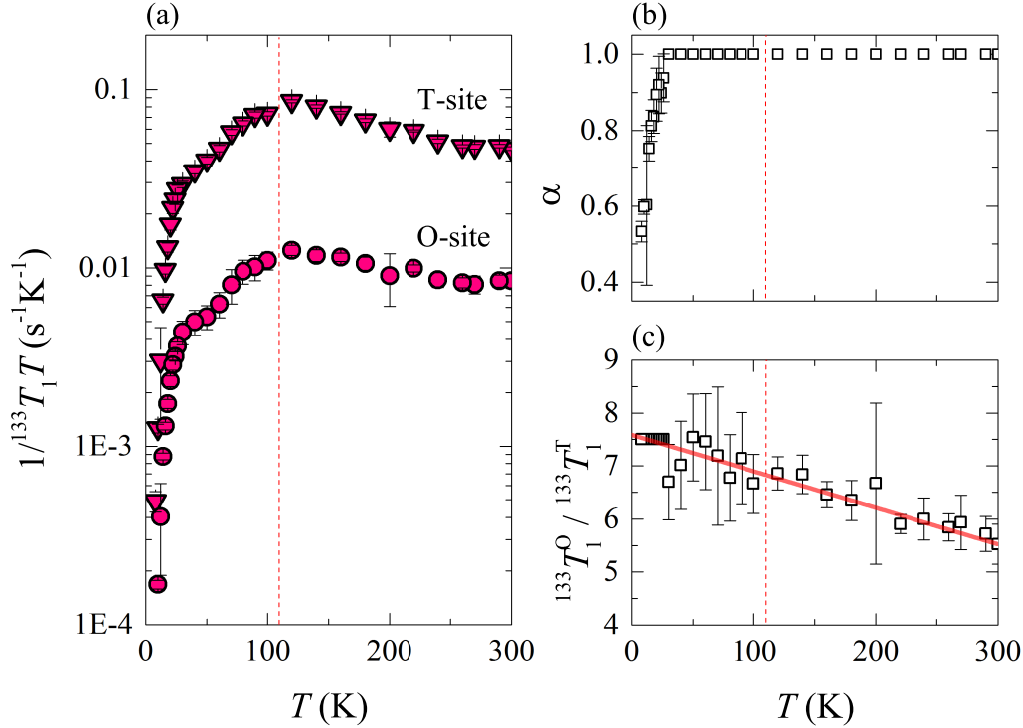


Figure 7.3:  $1/T_1T$  results of (a)  $^{13}\text{C}$  high-pressure NMR on  $\text{Cs}_3\text{C}_{60}$  and (b)  $^{13}\text{C}$  and  $^{87}\text{Rb}$  static NMR on  $\text{Rb}_x\text{Cs}_{3-x}\text{C}_{60}$ . Coloured arrows in (b) indicate the position of maximum accounted to the MIT ( $T_{\text{MIT}}$ ). Inset to (b) show a stretch parameter used for fitting recovery of nuclear magnetization and indicates an enhancement of  $T_1$  distribution below  $T_{\text{MIT}}$ .

Next, we briefly discuss  $^{133}\text{Cs}$  spin-lattice relaxation rates for O and T sites as a function of temperature. A representative data for  $x = 0.5$  sample are shown in Fig. 7.3. Two spin-lattice relaxation rates, one for each site, were obtained by fitting the magnetization recovery data with two exponential functions where amplitudes ( $B_i$ ) have been fixed to the number of Cs ions in O to T sites. In the normal state the stretch exponent was kept equal to 1 since no spin-lattice relaxation time distribution is expected. The obtained  $1/T_1T$  for both sites have the same temperature evolution comparable also to  $^{13}\text{C}$  measurements. Below  $T_c$  stretch exponent was released in order to account for the field distribution caused by the presence of vortices in the superconducting state. The only difference between the spin-lattice relaxation rates of different probes is in the magnitude which is according to Moriya expression (Eq. 3.53) proportional to the hyperfine coupling constant squared. To determine how the hyperfine coupling constants for O and T site develop with temperature we plot the ratio  $T_1^{\text{O}}/T_1^{\text{T}}$  as a function of temperature in Fig. 7.3c. The spin-lattice relaxation times ratio is nearly temperature independent with a very small negative slope of  $-0.005(1)$  s/K and  $T = 0$  value of  $^{133}\text{T}_1^{\text{O}}/^{133}\text{T}_1^{\text{T}} = 6.7(1)$ .

Assuming that dynamic spin susceptibility is not peaked at the edge of the Brillouin zone corresponding to the antiferromagnetic fluctuations<sup>1</sup> and that no other mechanism relax the nuclei polarization besides the hyperfine interaction the spin-lattice relaxation rate ratio is directly proportional to the hyperfine constant ratio squared

$$\frac{T_1^O}{T_1^T} = \left| \frac{A^T}{A^O} \right|^2. \quad (7.9)$$

The hyperfine coupling constant of the T site is for  $x = 0.5$  sample equal to

$$A^T = \sqrt{7.6(1) - 0.0069(5)T}A^O. \quad (7.10)$$

Ratios between tetrahedral and octahedral hyperfine coupling constants for different samples are summarized in Tab. 7.2.

Compound	$^{133}A^T/^{133}A^O$
$x = 0$	$\sqrt{6.3(2) - 0.0019(17)T}$
$x = 0.35$	$\sqrt{7.0(1) - 0.0053(6)T}$
$x = 0.5$	$\sqrt{7.6(1) - 0.0069(5)T}$
$x = 0.75$	$\sqrt{6.9(2) - 0.006(1)T}$
$x = 1$	$\sqrt{7.1(1) - 0.0067(7)T}$

Table 7.2:  $^{133}A^T/^{133}A^O$  ratio as a function of temperature obtained by a linear fit to the experimental  $^{133}T_1^T/^{133}T_1^O$  ratio for different  $\text{Rb}_x\text{Cs}_{3-x}\text{C}_{60}$  samples. See text for details.

## NMR resonances and their lineshifts

Next we focus on NMR spectral shape and position measured by different local probes. In this section we will consider only  $\text{Rb}_x\text{Cs}_{3-x}\text{C}_{60}$  sample measurements due to better data quality. The on-site  $^{13}\text{C}$  probe gives similar spectra to what has been observed before in  $\text{Rb}_2\text{CsC}_{60}$  sample with spectral position shifted away from TMS standard for  $\sim 190$  ppm and the linewidth of  $\sim 80$  ppm [112]. We note that in samples with smaller unit-cell volumes the spectral shape is narrower due to the fast rotational dynamics of  $\text{C}_{60}$  molecules and can thus not be easily compared to our measurements. As has been pointed out before and directly shown by our MAS NMR experiments (Sec. 5.1.2)  $^{13}\text{C}$  resonance consists of three non-equivalent sites. Corresponding three NMR lines are broadened due to the dipolar interaction resulting in an anisotropic second-order tensors. Due to their strong overlap they cannot be resolved by the static NMR measurements and, therefore, we cannot determine their tensor components individually. Our temperature dependent MAS NMR measurements also indicate that spectra gets additionally broadened at low temperatures due to JT molecular symmetry lowering. There are many unknown parameters, which are required to correctly describe the  $^{13}\text{C}$  spectra and since they cannot be determined by our NMR measurements we limit our analysis to a simple moment analysis.

<sup>1</sup>Since different NMR probes give the same qualitative spin-lattice relaxation rate as a function of temperature we argue that the dynamic spin susceptibility is not strongly enhanced at  $\vec{q}$  vector corresponding to the antiferromagnetic spin fluctuations. If this would not be the case, e.g., when antiferromagnetic fluctuations would become enhanced at low temperatures, different local probes would show different temperature dependences since their form factors would differently filter out antiferromagnetic fluctuations. In curates, for example, the spin-lattice relaxation notably differs for different due to antiferromagnetic fluctuations [139].

The selected spectra (for  $x = 0.5, 0.75,$  and  $1$  samples) and corresponding first and second moments are as a function of temperature shown in Fig. 7.4. The first moment, Fig. 7.4b, seems temperature independent above  $T_c$ , however, this result must be taken lightly as large spectral linewidth (Fig. 7.4c) prevents an accurate determination of the line position. The second moment (Fig. 7.4c) corresponding to the effective linewidth, on the other hand, shows an interesting behaviour. At high temperatures the linewidth increases with decreasing temperature, reaches a maximum and then decreases on further cooling. Below  $T_c$  linewidth again increases which can be explained by the presence of inhomogeneous magnetic field in the type-II superconductor. In the normal state, the maximum of the second moment shifts to higher temperatures for samples with larger unit-cell volumes, in the same way as has been observed in the spin-lattice relaxation rate measurements. The second moment ( $\sqrt{M_2}$ ) is for the same reasons as the Knight shift (the first moment) proportional to the static spin susceptibility (Eq. 3.59). The observed behaviour in the second moment can thus be attributed to the temperature behaviour of the static spin susceptibility. The same qualitative behaviour of the averaged dynamics spin susceptibility (measured by  $T_1$ ) and the static spin susceptibility (measured by  $\sqrt{M_2}$ ) further support the the argument that dynamic spin susceptibility does not contain a contribution from the antiferromagnetic spin fluctuations.

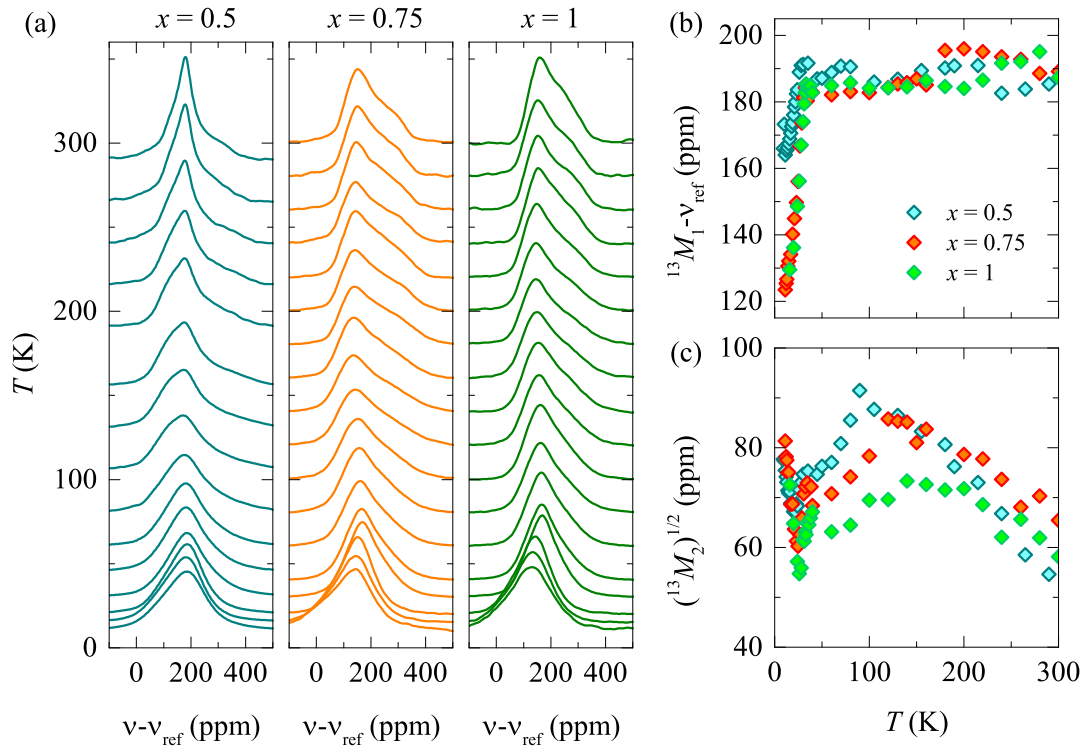


Figure 7.4:  $^{13}\text{C}$  spectra and moment analysis for  $x = 0.5, 0.75,$  and  $1$  samples. (a) Temperature dependence of  $^{13}\text{C}$  spectra. (b) The first moment of  $^{13}\text{C}$  spectra, related to the lineshift. (c) Square root of the second moment of  $^{13}\text{C}$  spectra, equivalent to the spectral linewidth.

More detailed information can be extracted from the  $^{133}\text{Cs}$  and  $^{87}\text{Rb}$  NMR measurements, where several resonance lines are resolved at high temperatures.  $^{133}\text{Cs}$  and  $^{87}\text{Rb}$  spectra as a function of  $x$  at room temperature are shown in Fig. 7.5.  $^{133}\text{Cs}$  static NMR spectrum at room temperature exhibits four out of seven spectral lines observed by MAS NMR experiment (Fig. 7.5a). By comparing room-temperature spectra of both probes one can see that larger Cs ions favour larger O octahedral interstitial sites (Fig. 7.5a) and

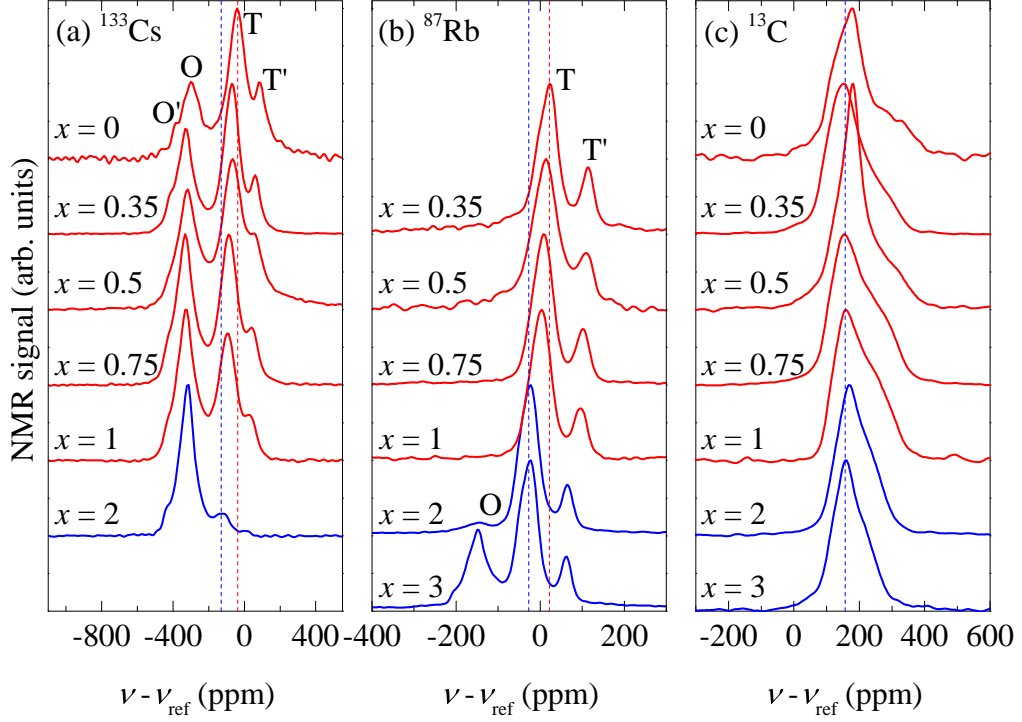


Figure 7.5: Room-temperature (a)  $^{133}\text{Cs}$ , (b)  $^{87}\text{Rb}$ , and (c)  $^{13}\text{C}$  NMR spectra of  $\text{Rb}_x\text{Cs}_{3-x}\text{C}_{60}$  samples. Blue and red colours correspond to metallic and insulating phase, respectively. Dashed vertical lines are added to better follow the lineshifts as a function of  $x$ .

smaller Rb ions favour smaller tetrahedral sites (Fig. 7.5b). With decreasing the amount of  $\text{Rb}^+$  ions a small shift to higher frequencies ( $\sim 100$  ppm for  $^{133}\text{Cs}$  and  $\sim 50$  ppm for  $^{87}\text{Rb}$ ) can be observed for both probes.

With decreasing temperature both O and T site lines shift to lower frequencies (Fig. 7.6), however, below  $T_{\text{MIT}}$  O site suddenly moves upwards. The direction change causes a strong overlap between the two sites at cca. 50 K where a precise line position is difficult to determine. We solved this problem by a concomitant measurement of spin-lattice relaxation time. Since T resonance has cca. 6-times shorter  $T_1$  compared to the O site, the spectrum was decomposed by following the amount of shorter and longer  $T_1$  components along the spectra (Further details are given in App. C.2). The decomposition is depicted in Fig. 7.6a. With such treatment we were able to obtain the positions of O, T lines from  $^{133}\text{Cs}$  and T, T' lines from  $^{87}\text{Rb}$  measurements. The line positions are as a function of temperature for all  $\text{Rb}_x\text{Cs}_{3-x}\text{C}_{60}$  samples shown in Fig. 7.7.

Measured lineshifts of  $\text{Rb}_x\text{Cs}_{3-x}\text{C}_{60}$  samples have a regular behaviour with respect to Rb concentration. For all samples temperature dependence of the lineshift changes at  $T_{\text{MIT}}$  (colour arrows in Fig. 7.7). The transition temperatures ( $T_{\text{MIT}}$ ) are increasing with increasing  $x$ , which is in agreement with bulk susceptibility (Sec. B.2) and spin-lattice relaxation time measurements (Sec. 7.2.2). At low temperature a notable transition occurs which is related to the emergence of the superconducting state. A change in the lineshift below  $T_c$  corresponds to the vanishing of the Knight shift, since the conducting electrons who are responsible for the Knight shift transform into non-magnetic Cooper pairs.

In the normal state the isotropic lineshift is a sum of chemical and Knight shift. The latter is further proportional to the uniform static spin susceptibility,

$$\alpha\delta_{\text{iso}} = \alpha\sigma_{\text{iso}} + \alpha K_{\text{iso}} = \alpha\sigma_{\text{iso}} + \alpha A\chi_s. \quad (7.11)$$

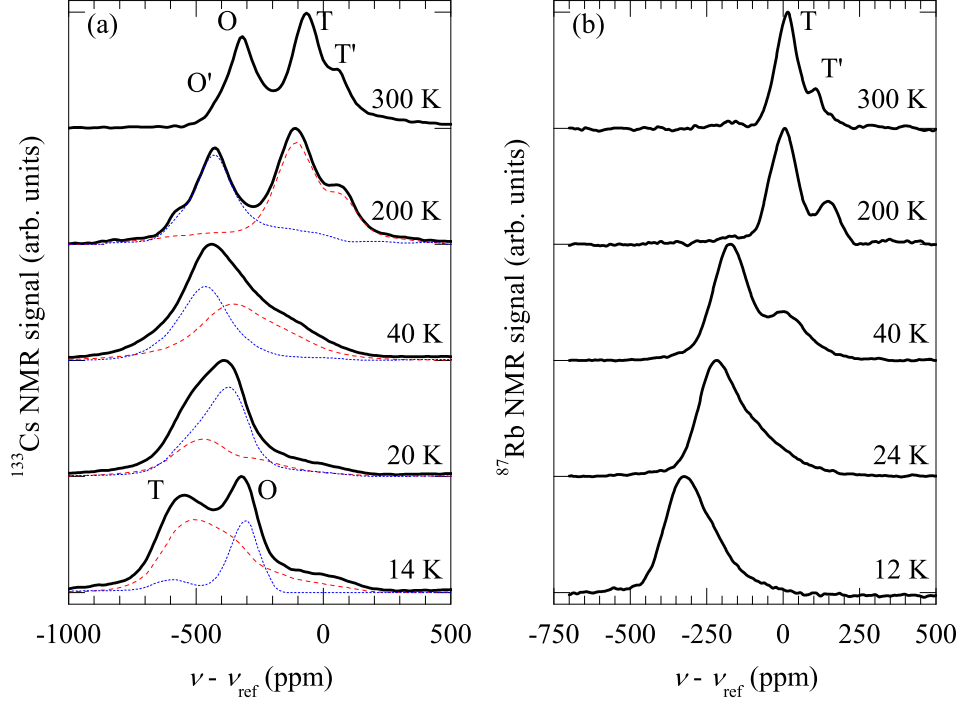


Figure 7.6: (a)  $^{133}\text{Cs}$  and (b)  $^{87}\text{Rb}$  spectral lines as a function of temperature measured on  $\text{Rb}_{0.5}\text{Cs}_{2.5}\text{C}_{60}$  sample. The four observed  $^{133}\text{Cs}$  lines, O', O, T, and T', are marked at room temperature spectrum. Similarly two T and T' lines are marked at  $^{87}\text{Rb}$  room temperature spectrum. The decomposition using spin-lattice relaxation times of T and O resonances in the  $^{133}\text{Cs}$  measurement are depicted with red dashed and blue dotted lines, respectively.

Here  $\alpha$  represents any molecular site (O, T, T'). Strong temperature dependence of line position is in non-magnetic systems normally attributed to a temperature dependent Knight shift, whereas the chemical shift is treated as a molecular property and is, therefore, rarely temperature dependent. To test the correlation between measured lineshifts and the bulk spin susceptibility we perform a standard Jaccarino-Clogston plot [140] where lineshift is plotted against the bulk susceptibility (Fig. 7.8b). The assumption related to this analysis is that the chemical shift is temperature independent. In our Jaccarino-Clogston plot analysis only  $^{133}\text{O}$ -site lineshift falls on a straight line. This suggest that O site hyperfine constant is temperature independent and negative. Data points from  $^{133}\text{T}$ ,  $^{87}\text{T}$  and  $^{87}\text{T}'$  sites, on the other hand, do not show such a good correlation to the bulk susceptibility. At high temperatures these points still follow a line, however, close to  $T_{\text{MIT}}$  they drift away and at lower temperatures form another line with a different slope (hyperfine constant) and offset (chemical shift). A drift near  $T_{\text{MIT}}$  suggest a drastic change of hyperfine coupling constants and the chemical shifts both in magnitude and sign. Results of a linear fitting to both high and low temperature data points in Jaccarino-Clogston plot for different sites are summarized in Tab. 7.3. Results for other  $\text{Rb}_x\text{Cs}_{3-x}\text{C}_{60}$  samples give qualitatively similar results with an exception of  $^{133}\text{O}$ -site behaviour where it can also exhibit a break at  $T_{\text{MIT}}$  with a strongly varying low-temperature hyperfine constant ranging between  $-2.5 \text{ kOe}/\mu_{\text{B}}$  for  $x = 0.35$  and  $0 \text{ kOe}/\mu_{\text{B}}$  for  $x = 1$  sample.

Such a drastic change of hyperfine constant and chemical shift at  $T_{\text{MIT}}$  proposed by the Jaccarino-Clogston plot analysis is not observed in any direct experimental data. The lineshifts, linewidths, and the spin-lattice times for all sites and samples seem to evolve rather smoothly when crossing MIT. Moreover, a constant chemical shift given by the

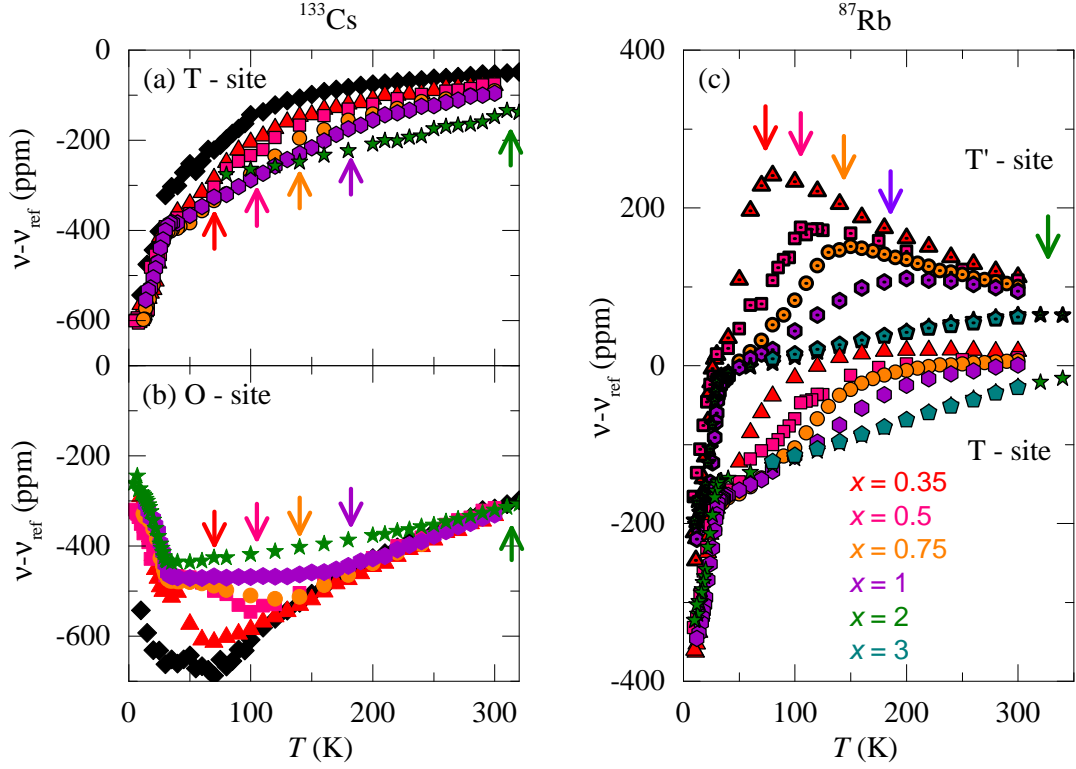


Figure 7.7: Spectral line positions of (a) T- and (b) O-sites in the  $^{133}\text{Cs}$  spectra as a function of temperature and (c) T and T' lines in the  $^{87}\text{Rb}$  spectra as a function of temperature for samples  $x = 0.35, 0.5, 0.75, 1, 2,$  and  $3$ . The transition temperatures where the lineshift behaviour changes (above  $T_c$ ) are marked by appropriate coloured arrows corresponding to different samples. The temperature of a transition point corresponding to a certain sample is independent on the probe used for NMR measurements.

low-temperature Jaccarino-Clogston plot ( $T < T_{\text{MIT}}$  in Tab. 7.3) is not in agreement with the lineshift deep in the superconducting state ( $T \rightarrow 0$ ) where it is determined only by the chemical shift<sup>2</sup>. All this suggests that Jaccarino-Clogston plot analysis is inadequate for  $\text{Rb}_x\text{Cs}_{3-x}\text{C}_{60}$  lineshift analysis and that hyperfine coupling constants or chemical shifts are probably temperature dependent.

An alternative explanation could be a two-fluid model used in heavy-fermion systems where a similar anomaly in the Jaccarino-Clogston plot was explained [141]. In this theory a uniform spin susceptibility and local spin susceptibility measured by the Knight shift have two contributions<sup>3</sup> with different weights. Different weights causes the two measured quantities to have different temperature dependences and thus an anomaly in the Jaccarino-Clogston plot. We have shown that the second moment of the  $^{13}\text{C}$  spectra which is proportional to the Knight shift resembles the uniform spin susceptibility in the same way as the spin-lattice relaxation rate. Therefore, the temperature dependences of the static local spin susceptibility and the uniform spin susceptibility are comparable and thus the two-fluid model cannot be applied.

<sup>2</sup>Here we neglect the reduction of the magnetic field due to the Meissner screening currents, since its estimated value is at least an order of magnitude smaller than the chemical or the Knight shift.

<sup>3</sup>One from localized and the other one from coherent heavy fermions.

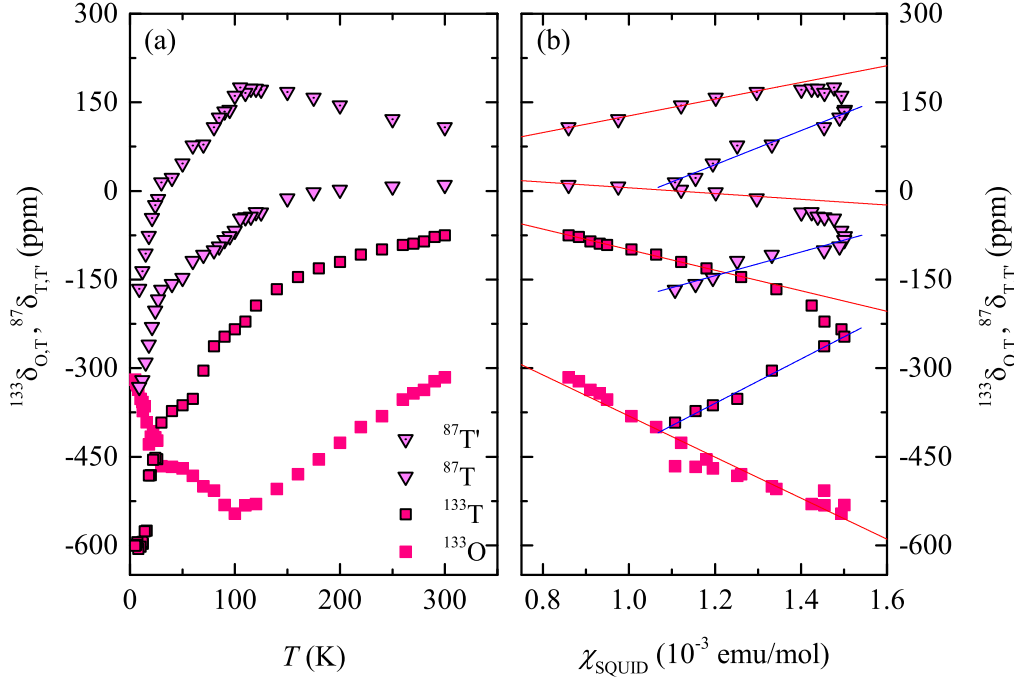


Figure 7.8:  $\text{Rb}_{0.5}\text{Cs}_{2.5}\text{C}_{60}$  lineshifts of  $^{133}\text{O}$ ,  $^{133}\text{T}$ ,  $^{87}\text{T}$ , and  $^{87}\text{T}'$  sites as a function of (a) temperature and (b) bulk magnetic susceptibility (Jaccarino-Clogston plot). The bulk susceptibilities used for Jaccarino-Clogston plot are presented in App. B.2. The hyperfine constant and chemical shift have been determined from a linear fit to Jaccarino-Clogston plot as a slope and the intercept with  $y$ -axis, respectively, for  $T > T_{\text{MIT}}$  (red line) and for  $T < T_{\text{MIT}}$  (blue line). The fitting parameters are summarized in Tab. 7.3.

	$T > T_{\text{MIT}}$		$T < T_{\text{MIT}}$	
Site	$A_{\text{iso}}$ (kOe/ $\mu_B$ )	$\sigma_{\text{iso}}$ (ppm)	$A_{\text{iso}}$ (kOe/ $\mu_B$ )	$\sigma_{\text{iso}}$ (ppm)
$^{133}\text{O}$	-1.9(3)	-34(24)	-1.9(3)	-34(24)
$^{133}\text{T}$	-1.0(3)	75(4)	2.1(1)	-810(20)
$^{87}\text{T}$	-0.2(3)	54(2)	1.1(1)	-390(30)
$^{87}\text{T}'$	0.8(3)	-14(6)	1.6(1)	-300(30)

Table 7.3: Fitting parameters used to determine the hyperfine constant and the chemical shift in Jaccarino-Clogston plot for  $\text{Rb}_{0.25}\text{Cs}_{2.5}\text{C}_{60}$  samples. The hyperfine constant for individual sites is proportional to the line slope (where we used  $\text{kppm}/(\text{emu}/\text{mol}) = 5.5848 \cdot 10^{-3}$  kOe/ $\mu_B$ ) and the chemical shift is equal to the intercept with  $y$ -axis. For each site data points above  $T_{\text{MIT}}$  and below  $T_{\text{MIT}}$  where fitted.

Let us proceed with two simple models where we first assume temperature independent chemical shift and later temperature independent hyperfine interaction. In the first model the chemical shift is determined from the low temperature lineshifts ( $T \rightarrow 0$ ). In the superconducting state an additional shift is present due to the magnetic field reduction caused by Meissner screening currents. This shift was estimated by several groups to be  $\Delta B/B = -35 - -17$  ppm [142], 10 ppm [143], and the latest 2.3 ppm [112]. Being an order of magnitude smaller than the estimated chemical shifts we will neglect this contribution. At the lowest temperature that we were able reach ( $\sim 10$  K) the Knight shift at not completely removed. To extract the Knight shift and consequently the chemical shift we fit the drop of lineshift below  $T_c$  with an exponential function,  $K = K_0 \exp(-\Delta/T)/\exp(-\Delta/T_c)$ , appropriate for gap behaviour. The extracted chem-

ical and Knight shifts by such treatment are summarized in Tab. 7.4.

$x$	$^{133}\text{O}$		$^{133}\text{T}$		$^{87}\text{T}$		$^{87}\text{T}'$	
	$\sigma$	$K$	$\sigma$	$K$	$\sigma$	$K$	$\sigma$	$K$
0.35	-280	-230	-610	210	-380	190	-240	240
0.5	-330	-140	-610	210	-340	170	-190	190
0.75	-330	-150	-650	250	-370	190	-280	250
1	-310	-160	-580	190	-360	190	-220	190
2	-300	-140	-	-	-320	170	-180	180
3	-	-	-	-	-350	210	-160	130

Table 7.4: Chemical shifts ( $\sigma$ ) and Knight shifts ( $K$ ) in units of ppm obtained by fitting Knight shift drop below  $T_c$  for all measured  $\text{Rb}_x\text{Cs}_{3-x}\text{C}_{60}$  samples and for all sites,  $^{133}\text{O}$ ,  $^{133}\text{T}$ ,  $^{87}\text{T}$ , and  $^{87}\text{T}'$ . An estimated relative error is 15% based on the scattering of the data.

We first note that the all Knight shifts of O sites are negative. The upturn of the O-site lineshift below  $T_c$  for all studied samples is in agreement with the previous measurements [7, 144]. A negative Knight shift is rather surprising since it is by its definition a positive quantity [67]. A possible explanation could come from the core-polarization effect which is, like the Knight shift, proportional to the static spin susceptibility but with a negative factor [7, 145]. If the core polarization effects are dominating over the positive contact interaction hyperfine constant for the O-site nuclei the result could be a negative total hyperfine constant. Interestingly, C.P. Pennington, *et. al* [7] estimated the amount of the Knight shift for T- and O-site nuclei from the probability density of the Bloch wavefunctions obtained from electronic band-structure calculations. They estimated very large theoretical Knight shift value of  $\sim 6000$  ppm and  $\sim 300$  ppm for T and O site, respectively. An order of magnitude difference between theoretical and experimental Knight shift values could not be rationalized by the same authors. However, we argue that the large theoretical Knight shift is compensated by the core-polarization effect which leads to the reduced shift values. For T site the two contributions almost cancel out leaving a small positive shift of  $\sim 200$  ppm, whereas, for O-site the core polarization effect exceeds that of the contact interaction effect resulting in a negative net shift of  $\sim -200$  ppm.

To obtain temperature dependent hyperfine constants in the first simplified model we subtract the chemical shifts from the lineshift data (Tab. 7.4) and divide with bulk susceptibility,  $A(T) = (\delta(T) - \sigma) / \chi_s(T)$ . The hyperfine coupling constants obtain in such a way are presented in Fig. 7.9. For the T site hyperfine coupling constants decrease with decreasing temperature almost linearly from  $\sim 3.5$  kOe/ $\mu_B$  at RT to 1 kOe/ $\mu_B$  at 30 K (Fig. 7.9). In case of O site the temperature dependence is reversed. The amplitude of the O-site hyperfine coupling constant is increasing with decreasing temperature having a negative sign. The temperature dependence for both sites seems not to be correlated with the amount of intercalated Rb ions.

To test the validity of the first simplified model we show in inset to Fig. 7.9 a hyperfine constant ratio between T and O site for a characteristic  $x = 0.5$  sample. The hyperfine constant ratio is strongly temperature dependent, being more than 30 at RT and 1.3 at 30 K. Such a strong reduction for a factor of  $\sim 30$  at low temperatures is not consistent with a ratio obtained from the spin-lattice relaxation times (Tab. 7.2) where  $|A^{\text{T}}/A^{\text{O}}|$  is only weakly increasing from RT to 30 K, for a factor  $\sim 1.2$ . Disagreement between the two results cast doubts on proposed simplified model.

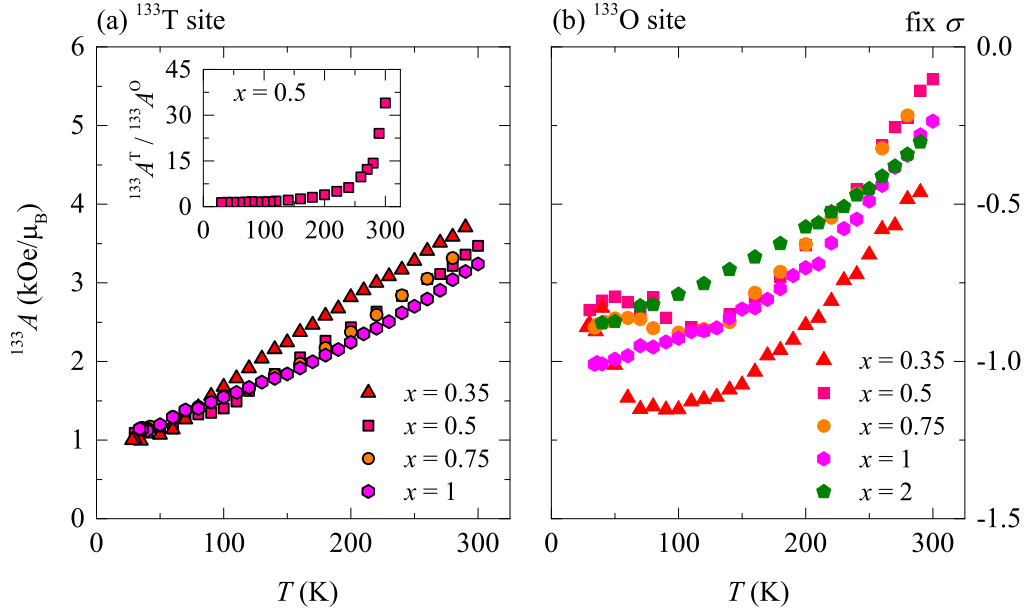


Figure 7.9: Hyperfine coupling constants obtained from (a)  $^{133}\text{T}$  and (b)  $^{133}\text{O}$  lineshift data for all  $\text{Rb}_x\text{Cs}_{3-x}\text{C}_{60}$  samples assuming a temperature independent chemical shift,  $\sigma$ . Inset shows temperature dependence of hyperfine constant ratio of T- and O-site for  $x = 0.5$  sample.

The second simple model assumes that the hyperfine coupling constants are temperature independent and allow the chemical shifts to be temperature dependent. We take the isotropic hyperfine coupling constants for different sites and samples from the extracted Knight shift at low temperatures (Tab. 7.5) and use them for computing Knight shift as a function of temperature,  $K(T) = A\chi_s(T)$ . The chemical shift is then a difference between lineshift and Knight shift,  $\sigma(T) = \delta(T) - K(T)$ . The results for characteristic  $x = 0.5$  sample are shown in Fig. 7.10. The obtained chemical shifts (strong black line) are negative and decrease with decreasing temperature. At low temperatures ( $T \rightarrow 0$ ) the obtained chemical shifts are consistent with measured lineshift. The drop of the chemical shift between RT and 30 K is the smallest in case of  $^{133}\text{O}$  site ( $\sim 100$  ppm), and the largest in case of  $^{133}\text{T}$  site ( $\sim 400$  ppm). The measurements on  $^{87}\text{Rb}$  give somewhat smaller drop of  $\sim 250$  ppm for  $^{87}\text{T}$  and  $\sim 150$  ppm for  $^{87}\text{T}'$  site. We note that for all sites the slope reduces below  $T_{\text{MIT}}$ . The inflation point corresponds rather well with  $T_{\text{MIT}}$ . Another interesting observation is almost temperature independent  $^{87}\text{T}'$  site chemical shift at high temperatures. Such a behaviour is not observed for any other sites and is probably related to the highly symmetric environment of the T site produced by the neighbouring  $\text{C}_{60}$  hexagons (Sec. 6.1).

The chemical shifts obtained for all measured  $\text{Rb}_x\text{Cs}_{3-x}\text{C}_{60}$  samples are shown in Fig. 7.11. For all T sites a regular decrease of the chemical shift can be observed with increasing  $x$  with a concomitant transformation towards a straight line. O-site chemical shifts, on the other hand, are much less dependent on the amount of Rb ions. Only for the largest  $x = 2$  sample the O-site chemical shift slightly moves to higher values. A weak temperature dependence of  $^{87}\text{T}'$  site at high temperatures, as previously noted for  $x = 0.5$  sample, is observed also for  $x = 0.35$  sample. Samples with smaller unit-cells ( $x > 0.5$ ) show small temperature dependence (Fig. 7.11d) and becomes qualitatively comparable to the  $^{87}\text{T}$  site. In general, the overall slope of all the sites is reduced with increasing amount of added Rb ions, which is most clearly seen for  $^{133}\text{T}$  and  $^{87}\text{T}$  sites. Temperature independent hyperfine coupling constants and the chemical shift drop between RT and

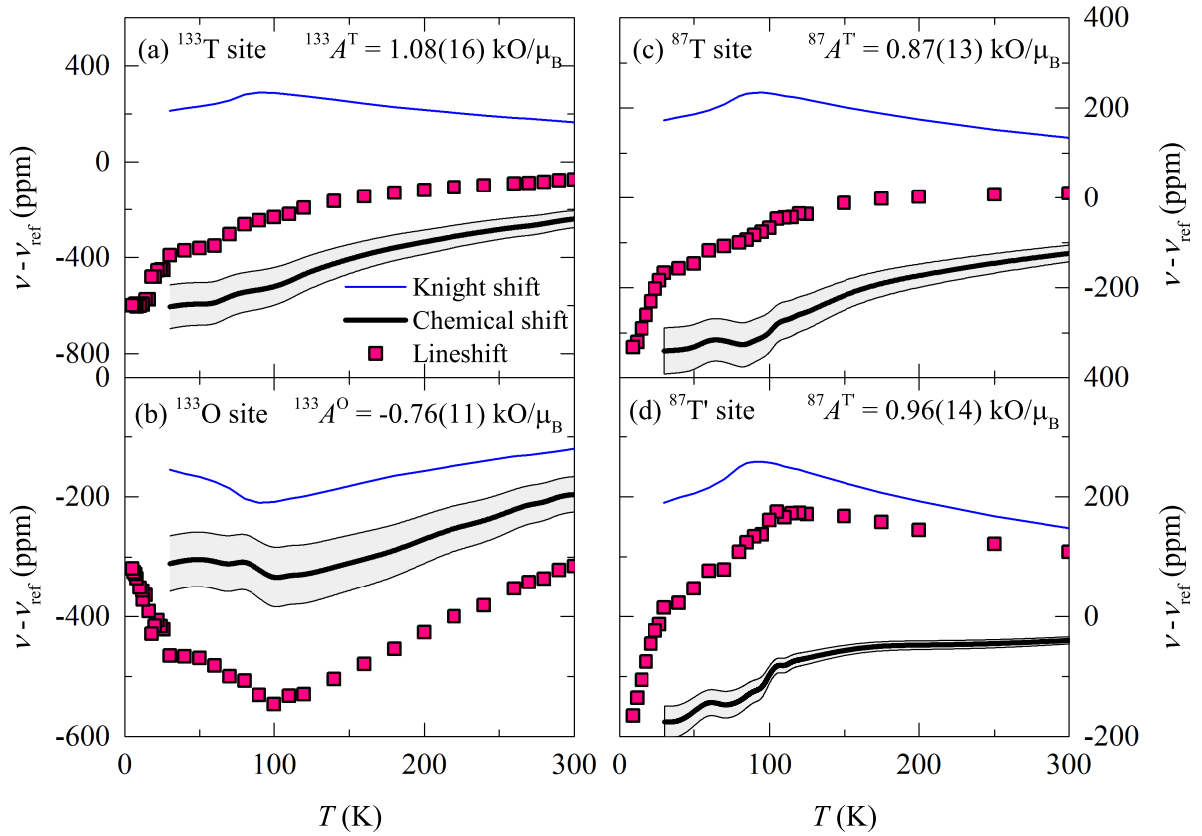


Figure 7.10:  $x = 0.5$ . sample's lineshift, Knight shift (thin blue line), and chemical shift (thick black line) calculated from the temperature independent hyperfine coupling constant for (a)  $^{133}\text{T}$ , (b)  $^{133}\text{O}$ , (c)  $^{87}\text{T}$ , and (d)  $^{87}\text{T}'$  sites. The uncertainty of the chemical shift is shown as gray area and is obtained by the uncertainty of the hyperfine coupling constant.

30 K obtained by the second simple model are summarized in Tab. 7.5.

$x$	$^{133}\text{O}$		$^{133}\text{T}$		$^{87}\text{T}$		$^{87}\text{T}'$	
	$A$ ( $\frac{\text{kOe}}{\mu_B}$ )	$\Delta\sigma$						
0.35	-0.88(13)	80(70)	0.82(12)	410(120)	0.73(11)	290(70)	0.94(14)	220(40)
0.5	-0.76(11)	120(80)	1.08(16)	380(130)	0.87(13)	220(70)	0.96(14)	140(30)
0.75	-0.78(12)	100(80)	1.36(20)	350(140)	1.07(14)	220(70)	1.39(21)	180(60)
1	-0.92(14)	110(80)	1.12(17)	320(130)	1.11(17)	200(80)	1.11(17)	150(40)
2	-0.77(12)	100(70)	-	-	0.95(14)	130(80)	1.00(15)	180(40)

Table 7.5: Temperature independent hyperfine coupling constants ( $A$ ) and chemical shift difference ( $\Delta\sigma$ ) in ppm units between 300 K and 30 K for all sites and all measured  $\text{Rb}_x\text{Cs}_{3-x}\text{C}_{60}$  samples. The hyperfine coupling constants were calculated from the Knight shift extracted at low temperatures (Tab. 7.4) divided by the bulk susceptibility given at  $T_c$  (Sec. B.2.2). The chemical shift change was obtained by using second simple model. See text for details.

Strong temperature dependence of the chemical shift proposed by the second model is rarely encountered in NMR experiments. In case of fullerene superconductors a lineshift drop of 110 ppm for  $^{133}\text{O}$  and 150 ppm for  $^{87}\text{Rb}$  site in  $x = 2$  sample were initially explained by the decrease of local spin susceptibility at lower temperatures reflecting the decrease in  $N(E_F)$  due to thermal contraction of the unit-cell [144]. It was later realized that the spin susceptibility measured by EPR does not drop sufficiently at lower

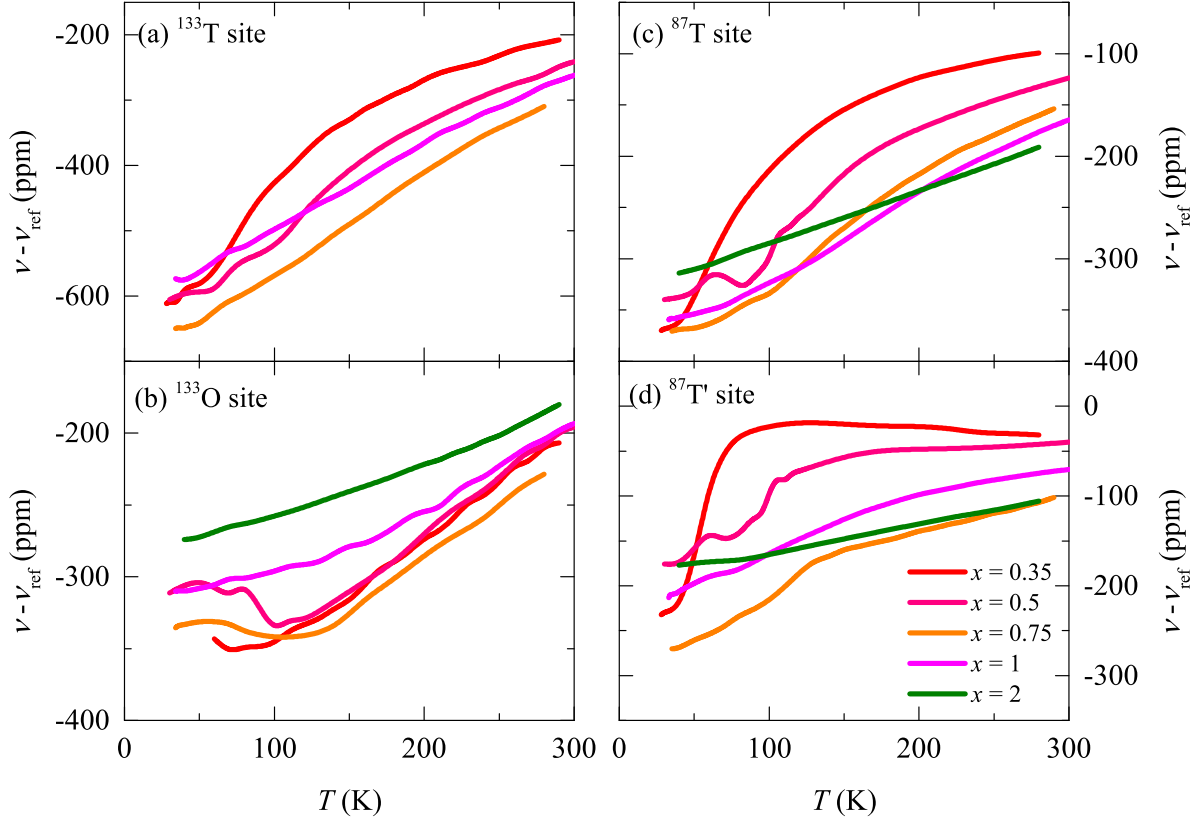


Figure 7.11: Chemical shifts calculated from the temperature independent hyperfine coupling constant for (a)  $^{133}\text{T}$ , (b)  $^{133}\text{O}$ , (c)  $^{87}\text{T}$ , and (d)  $^{87}\text{T}'$  sites for different  $\text{Rb}_x\text{Cs}_{3-x}\text{C}_{60}$  samples.

temperatures to explain the measured drop of the NMR lineshifts. An alternative explanation was proposed to be the temperature dependent chemical shift [142]. There are three known sources of the chemical shift in the  $A_3\text{C}_{60}$  systems [7]. (1) The core electron contribution, which is an atomic property and is thus not expected to be temperature dependent. (2) The admixture of neighbouring  $t_{1u}$  (Wannier) orbitals in order to form an orthogonalized basis set for Slater determinant used as the many-electron wavefunction. Since this contribution is difficult to calculate it is not clear what chemical shift would be obtained in case of fullerene systems. Since this mechanism depends on the overlap of the neighbouring orbitals and their relative energy difference one would expect it to be predominately a function of unit-cell volume rather than temperature. Our second simplified model, however, shows that chemical shift changes more with temperature than the unit-cell volume. We argue that this contribution is not the primary source of the temperature dependent chemical shift. (3) Ring currents on the neighbouring  $\text{C}_{60}$  ions produce magnetic field that can yield additional chemical shifts. Pasquarello *et al.* [123] calculated ring currents induced shift at various positions around  $\text{C}_{60}$  molecule. They observed large shift near the surface of the molecule of  $\sim 12$  ppm in the plane of pentagon and  $\sim -5$  ppm in the plane of a hexagon. This are rather small to account for the observed chemical shifts, however, their analysis was done on an isolated charge neutral icosahedral molecule where some currents are cancelled out due to high molecular symmetry. As has been pointed out by Pasquarello *et al.* the local currents are strongly dependent on the electronic structure. In addition, the currents probably depend on molecular symmetry reduction caused, for example, by the JT effect. The presence of strong molecular currents is also suggested by our MAS  $^{133}\text{Cs}$  NMR spectral analysis on  $\text{Cs}_3\text{C}_{60}$  sample, where

T' site was shown to be a tetrahedral site with a specially symmetric arrangement of the neighbouring molecular merohedral orientations. A large distance between T and T' lines in room-temperature spectra of  $\sim 130$  ppm (Tab. 6.1) is most probably due to molecular currents which are either summed up or cancelled out in case of T' site. Following this interpretation  $\sim 130$  ppm is an order of magnitude estimate of the ring currents effect, which should contribute to the chemical shift of alkali-metal nuclei. The obtained chemical shift values and the estimate of ring currents effect are indeed of the same order of magnitude, however, a detailed numerical study is needed to show whether ring currents are strong enough to be the main source of the observed chemical shift.

The presented two simple models are meant to give an insight into a complicated lineshift behaviour. It is indeed possible that the lineshift consists of both chemical and Knight shift that are temperature dependent. Nevertheless, our discussion favours the chemical shift to be the main source of temperature dependent lineshift.

## Discussion

The MIT transition and peculiar phase close to  $T_{\text{MIT}}$  are far from being understood. So far, we understand the insulating phase of highly-expanded samples and the metallic phase of under-expanded samples, however, in the intermediate region close to  $T_{\text{MIT}}$  where the spin susceptibility drops from the insulating value to the metallic in an exponential manner is far from being clear. At the same time our lineshift data and high resolution spectra suggest that molecular deformations, probably due to the JT effect, are present throughout the MIT.

Such a peculiar  $1/T_1T$  behaviour has been observed before in organic BEDT-TTF superconductors [138, 146]. In those materials the increase of the  $1/T_1T$  with decreasing temperature was explained by the presence of antiferromagnetic fluctuations, which became suddenly reduced below MIT [147]. Other proposed possibilities for reduction of  $1/T_1T$  below  $T_{\text{MIT}}$  are the opening of a pseudogap or the coexistence of insulating and metallic phases. In case of organic superconductors more experimental evidence point towards the pseudogap model. For example, a reduction of the Knight shift and the bulk spin magnetic susceptibility below  $T_{\text{MIT}}$ , as well as the depression of the linear specific heat coefficient,  $\gamma$  when closing the MIT, are all in agreement with a reduction of the  $N(E_F)$  due to the opening of a pseudogap. Comparing these observation with  $A_3C_{60}$  system we note that the only similarity is in  $1/T_1T$  data. Our Knight shift and bulk magnetic susceptibility resemble  $1/T_1T$  data which is not the case in organic superconductors. Nonetheless, following BEDT-TTF's example we next search for any experimental evidence of the antiferromagnetic spin fluctuations.

We proceed by comparing the spin-lattice relaxation rates measured on different nuclei in the unit-cell. Due to their different position within the crystal structure, they have different form factors (Eq. 3.53) and consequently different sensitivity to the antiferromagnetic fluctuations (Sec. 3.3.2). The presence of antiferromagnetic fluctuations was determined by such analysis in cuprate superconductors where Cu nuclei having an on-site charge and spin carriers displayed substantially different  $1/T_1T$  temperature dependence then the O nuclei where the contribution from the antiferromagnetic fluctuations were filtered out by the form factors [139]. In case of fullerenes similar comparison was performed in the past on  $\text{Rb}_2\text{CsC}_{60}$  compound [47]. They observed no difference in the behaviour of the  $1/T_1T$  data of  $^{13}\text{C}$ ,  $^{87}\text{Rb}$ , and  $^{133}\text{Cs}$  NMR probes and concluded that there is no "form factor effect" and, therefore, no direct proof of the presence of antiferromagnetic spin fluctuations. We are now able to extend their analysis to compounds

much closer to MIT. Our data show that all local probes,  $^{13}\text{C}$ ,  $^{87}\text{Rb}$ , and  $^{133}\text{Cs}$  give the same qualitative behaviour as is shown in Fig. 7.2 and directly compared for  $x = 0.35$  sample in Fig. 7.12. We, therefore, conclude that there is no "form factor effect" in  $A_3\text{C}_{60}$  family and no direct proof of the antiferromagnetic fluctuations.

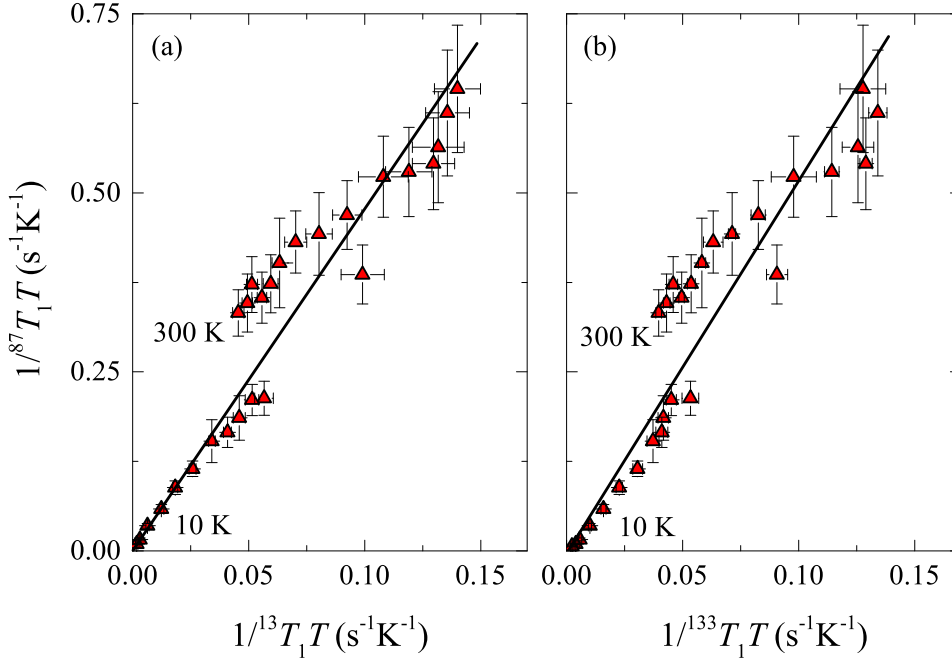


Figure 7.12: Comparison of  $1/T_1T$  data on  $x = 0.35$  sample between different probes: (a)  $^{87}\text{Rb}$  vs.  $^{13}\text{C}$  and (b)  $^{87}\text{Rb}$  vs.  $^{133}\text{Cs}$ . Red line has been added as a guide to the eye.

Another method for testing the effect of spin correlations is a deviation from the Korringa relation measured by the Korringa phenomenological factor  $\beta$  (Eq. 3.83)

$$(T_1T) K^2 = \frac{\hbar}{4\pi k_B} \frac{\gamma_e^2}{\gamma_n^2} \beta.$$

Such analysis has been employed on several  $A_3\text{C}_{60}$  samples limited to the  $^{13}\text{C}$  NMR probe. Obtained  $\beta$  are 0.4 [148], 0.58 [112] for  $\text{K}_3\text{C}_{60}$  and 0.37 [148], 0.48 [112] for  $\text{Rb}_3\text{C}_{60}$ . In all cases the Korringa parameter was smaller than 1, which means that the enhancement of  $1/T_1T$  is due to the antiferromagnetic rather than ferromagnetic spin fluctuations. To explore spin correlations in the region close to MIT we have performed the same analysis on all  $\text{Rb}_x\text{Cs}_{3-x}\text{C}_{60}$  samples. We used  $^{133}\text{O}$  site spin-lattice relaxation rates and the extracted  $^{133}\text{O}$  site Knight shift from the second model. The results are shown in Fig. 7.13. We note that Korringa relation was derived for the Fermi-liquid state and thus its validity is questionable in the insulation phase. For this reason, data points corresponding to the metallic phase are in Fig. 7.13 filled with colour. First, we observed that in contrast to past analysis the obtained Korringa factor is weakly temperature dependent, however, we have to note that the plotted data points have large uncertainty of 30% and that the temperature dependence might not be so pronounced as may be seen in Fig. 7.13. In general, the obtained Korringa factors are comparable to the past observations. Samples closer to the MIT show smaller Korringa factor, which indicates that the antiferromagnetic fluctuations become enhanced when closing MIT.

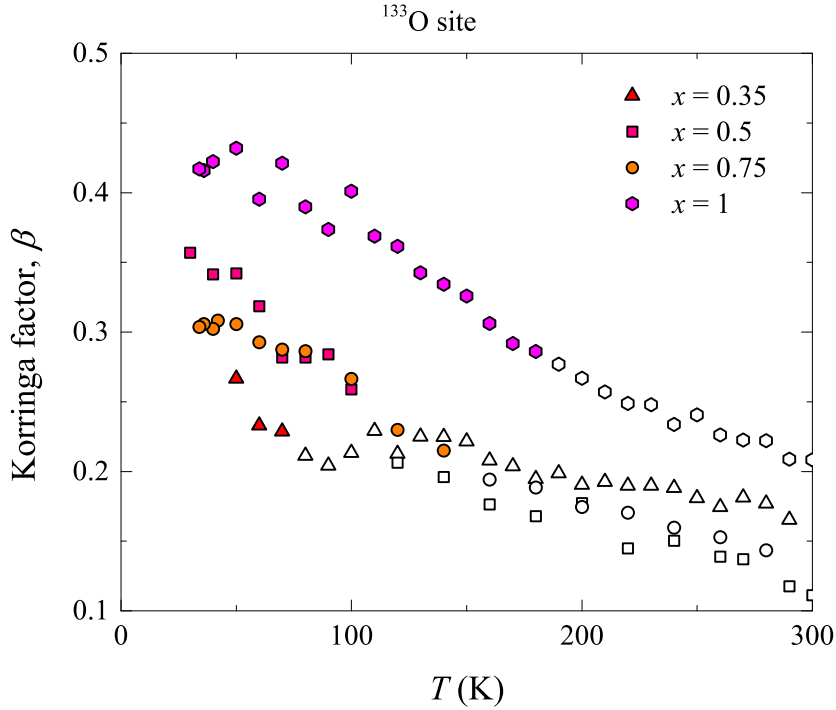


Figure 7.13: Korringa factor as a function of temperature for several  $\text{Rb}_x\text{Cs}_{3-x}\text{C}_{60}$  samples. Empty symbols correspond to data points in the insulating state where validity of Korringa relation is questionable. The Korringa factor was calculated using the Knight shift and spin-lattice relaxation rate of the  $^{133}\text{O}$  site. The uncertainty of data points is 30%.

Finally, we discuss the temperature dependence of the measured spin susceptibility. The increase of  $1/T_1T$  with decreasing temperature above  $T_{\text{MIT}}$  is most probably not due to the antiferromagnetic spin fluctuations as observed by BEDT-TTF organic superconductors, since its behaviour is reflected by static spin susceptibility measured by the Knight shift or the bulk spin susceptibility. The later experiment is proportional only to static  $\vec{q} = 0$  part of the spin susceptibility and is thus insensitive to the contribution from antiferromagnetic fluctuations. It is far more reasonable to treat the high temperature spin susceptibility on the insulating site by the Curie-Weiss law. The reduction of the spin susceptibility below  $T_{\text{MIT}}$  is, on the other hand, far from trivial. To our knowledge there are 3 possible models that could explain such behaviour.

(1) The opening of a pseudogap below  $T_{\text{MIT}}$  is consistent with a reduction of  $1/T_1T$ , Knight shift, and bulk susceptibility measurements. In case of  $\text{A}_3\text{C}_{60}$  system a pseudogap has also been proposed by DMFT [62, 149]. In this theory pseudogap emerges at low energies when three spins on  $\text{C}_{60}^{3-}$  molecules initially screened by conducting electrons in Kondo state become coupled by the effective exchange interaction (difference between JT and Hund's rule exchange) and form a low-spin state ( $S = 1/2$ ) which is followed by reduction of  $N(E_{\text{F}})$ . Kondo screening is lost when the system is so close to the Mott-insulating state that the renormalized coherent bandwidth becomes smaller than the effective on-site exchange interaction. According to the theory this transition happens at the maximum of the superconducting dome in the phase diagram. The phase between this transition and MIT is argued to be in a non-Fermi liquid state. The pseudogap remains a valid model to describe the drop in the measured quantities, however, it does not directly explain a continuous evolution of spin susceptibility as a function of temperature when crossing MIT.

(2) Another model that could also explain measured spin susceptibility is the coexis-

tence of the insulating and metallic phases. The coexistence is also consistent with the observed decrease of the spin-lattice stretch parameters below  $T_{\text{MIT}}$  (inset to Fig. 7.2). However, the phase segregation is normally observed for the first order phase transition. In our case, as we have noted above, we observe no hysteresis when slowly crossing  $T_{\text{MIT}}$  on cooling or on heating and, therefore, the phase transition between metallic and insulating states is most probably of the second order. We thus argue that there is no coexistence of phases below  $T_{\text{MIT}}$ .

(3) The last model is based on the interpretation of Kanoda *et al.* [146] who argued that the reduction of the spin susceptibility in the half-filled conduction band material that is initially in the Mott-insulating state comes from the reduction of the magnetic moments when electrons start to hop. In a simple picture, after an electron hops to a neighbouring site where there is already an electron with opposite spin direction they form a non-magnetic spin singlet state. In such model the magnetic moment and the spin susceptibility would get reduced when moving towards the metallic state where more electrons will hop and form spin singlet state. This model is, however, valid only in the limit of large  $U$  where electron mobility is small and they can be still considered to be in the low-spin state. If they are slow enough the unpaired electrons can still be considered as free paramagnetic spins giving Curie-like susceptibility only their number is reduced. This model predicts a continuous development of the spin susceptibility when crossing the MIT. To accurately predict the development in the larger temperature and unit-cell volume range a more rigorous model should be considered that correctly accounts the effects of both metallic and insulating states.

Such model that treats electronic correlations and the coherent electronic behaviour on equal footing is the DMFT. In collaboration with M. Capone and E. Tosatti, we performed a simple one band Hubbard model DMFT computations on a Bethe lattice in a half field case. After obtaining a converged solution for a given temperature and  $U$  using exact diagonalization with the finite temperature extension of the Lanczos method [150] we calculated the static local spin susceptibility using [63]

$$\chi_{\text{loc}}(\omega = 0) = \frac{1}{Z} \sum_{n,m} |\langle n | S_z | m \rangle|^2 e^{-\beta E_m} \begin{cases} 2\text{Re} \left( \frac{1}{E_n - E_m} \right) & E_n - E_m \neq 0, \\ \beta & E_n - E_m = 0, \end{cases} \quad (7.12)$$

where  $|n\rangle$  and  $E_n$  are  $n$ -th eigen state and eigen energy of Anderson impurity model solved in the final iteration of DMFT procedure. In Fig. 7.14 we show the static local spin susceptibility as a function of temperature and the proximity to Mott-state ( $U/W$ ). In the insulating ( $U/W \gg 1$ ) and metallic ( $U/W \ll 1$ ) state the Curie and Pauli temperature independent behaviour correctly reproduce experimentally observed spin susceptibility. Interestingly, for  $U/W$  values close to critical values the spin susceptibility is increasing with increasing temperature which is again consistent with our experimental behaviour of  $1/T_1T$ , Knight shift and bulk spin susceptibility. We note that the discontinuity at MIT is due to the numerical instability. The increase of spin susceptibility is, therefore, intrinsic to a single band Hubbard model on a Bethe lattice.

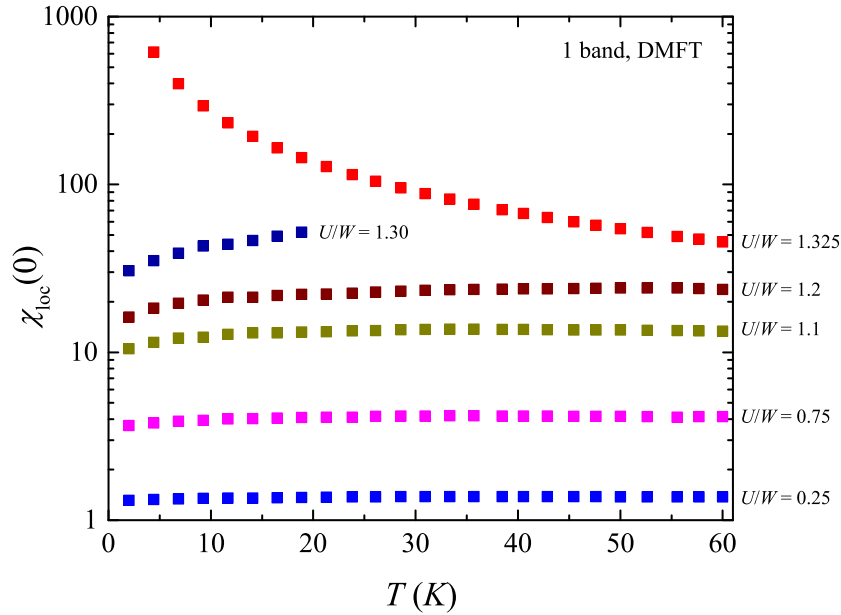


Figure 7.14: Temperature dependent local static spin susceptibility computed by a half filled single band DMFT with  $N_s = 7$  bath states for several  $U/W$  ratios. The critical value at which the system becomes Mott-insulator is  $(U/W)_c = 1.325$ ; This result was obtained in collaboration with M. Capone and E. Tosatti.

The decrease of spin susceptibility below  $T_{\text{MIT}}$  as a function of temperature can have at least two contributions, the opening of a pseudogap or the partial localization of electrons given by the Hubbard model. To further understand their role the local static spin susceptibility would need to be computed on the three-band Hubbard model with exchange interaction as has been used for computing the phase diagram for  $A_3C_{60}$  [62].

### 7.2.3 MIT border on the Phase diagram

Joint NMR measurement on  $\text{Rb}_x\text{Cs}_{3-x}\text{C}_{60}$  and high-pressure measurements on  $\text{Cs}_3\text{C}_{60}$  allow us to construct a phase diagram from the superconducting and MIT critical points. To position our measured critical points on the  $(V, T)$  phase diagram we use measured unit-cell volume for  $\text{Rb}_x\text{Cs}_{3-x}\text{C}_{60}$  samples as a function of temperature (Sec. B.2) and calibrated hydrostatic pressures and corresponding temperatures for high-pressure experiments. How the unit-cell volume was determined from calibrated pressures and temperatures is described in Sec. B.1. The obtained  $(V, T)$  phase diagram is shown in Fig. 7.15a. The superconducting dome is in good agreement with the previously published data [14] represented by a red curve. A small shift to lower values ( $\sim 3$  K) can be observed for  $\text{Rb}_x\text{Cs}_{3-x}\text{C}_{60}$  samples. This is probably due to substitutional disorder which are known to reduce  $T_c$  [115]. In addition to the critical points we added on the phase diagram two characteristic paths that were taken by high pressure experiment run on cooling for  $P = 2.3$  kbar at low temperatures (red dotted line) and another one taken by  $x = 0.75$   $\text{Rb}_x\text{Cs}_{3-x}\text{C}_{60}$  sample on cooling. We can see that the two paths can be quite different and thus a direct comparison between high pressure and  $\text{Rb}_x\text{Cs}_{3-x}\text{C}_{60}$  sample measurement is not trivial, however, critical points from both  $\text{Rb}_x\text{Cs}_{3-x}\text{C}_{60}$  and high pressure experiments are consistent implying that the physical and chemical pressures are equivalent and that the alkali ions do not participate in the electronic structure.

The metal-insulator border, determined by the maxima in  $1/T_1T$  data, is positioned

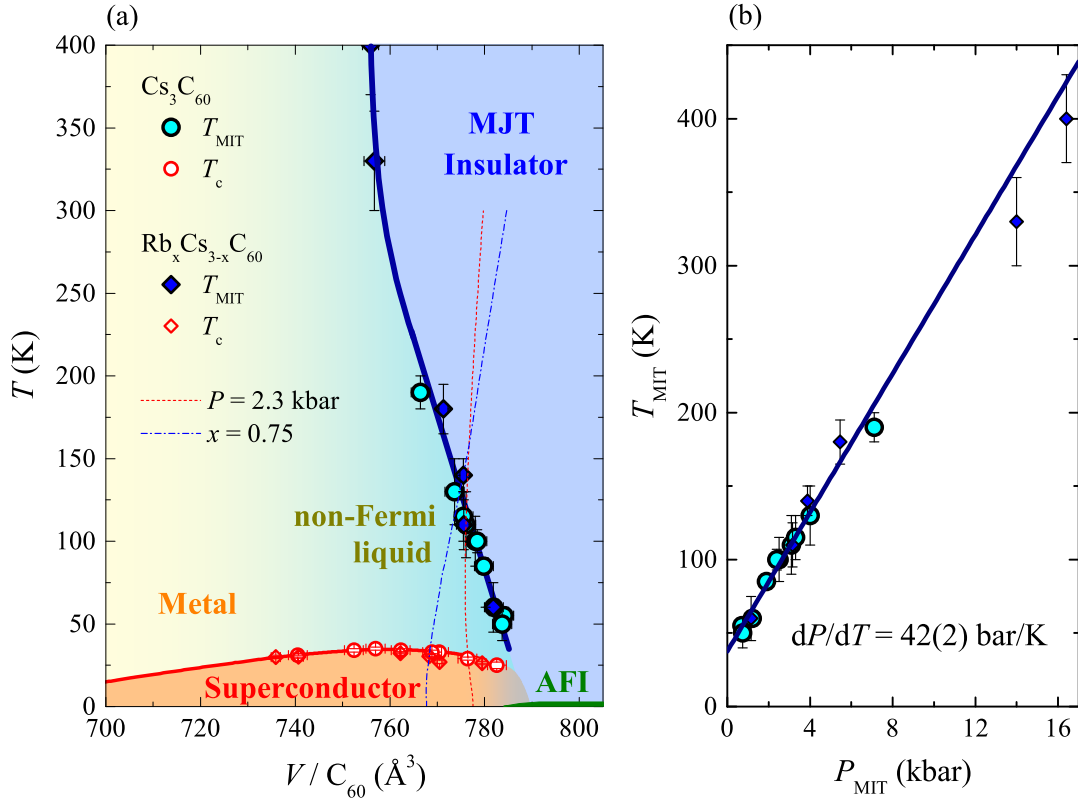


Figure 7.15: (a)  $(V, T)$  phase diagram of  $A_3C_{60}$  with critical superconducting temperature  $T_c$  (red empty symbol) and critical MIT temperature,  $T_{MIT}$  (full symbols) determined from joint NMR measurements on  $Rb_xCs_{3-x}C_{60}$  samples (diamond symbols) and high-pressure NMR measurements on  $Cs_3C_{60}$  sample (circle symbols). Two paths are shown for  $P = 2.3$  kbar high-pressure experimental run on cooling (red dotted curve) and experimental run on cooling for  $x = 0.75$   $Rb_xCs_{3-x}C_{60}$  sample (blue dash-dotted curve). The MIT transition border is shown by thick blue curve and meant as a guide to the eye. (b) Critical MIT temperature as a function of appropriate pressure. In case of  $Rb_xCs_{3-x}C_{60}$  samples the hypothetical pressure was determined using  $Cs_3C_{60}$  compressibility data (Sec. B.1). Blue line is a linear fit with an inverse slope of  $dP/dT = 42(2)$  bar/K.

above the superconducting dome on the phase diagram (Fig. 7.15a). The MIT border is a straight line with a negative slope of  $-7.42$  K/ $\text{\AA}^3$  at lower temperatures. At higher temperatures the border seems to become steeper. Transforming MIT critical points on the  $(P, T)$  phase diagram (Fig. 7.15b) an inverse slope of  $dP/dT = 42(2)$  bar/K is obtained. Determined slope of MIT border is, however, in qualitative disagreement with the previous measurements [125] where MIT border was claimed to be a vertical line. This is less likely since the entropy of the metallic and insulating phases are not expected to be equal. The slope of MIT boundary line can be discussed by a thermodynamic analysis using Clausius-Clapeyron relation [151]

$$\frac{dP}{dT} = \frac{\Delta S}{\Delta V}, \quad (7.13)$$

where  $dP/dT$  is the MIT boundary slope in the  $(P, T)$  phase diagram (Fig. 7.15b),  $\Delta S$  is the difference between metallic and insulating state entropy and  $\Delta V$  is a difference between metallic and insulating state unit-cell volume.

The entropy of the metallic state is expressed as  $S_m = \gamma T$ , where  $\gamma$  is a Sommerfeld linear coefficient of the metallic contribution to the heat capacity. For simple metals

this is of the order of  $\sim 1$  mJ/mol/K<sup>2</sup> [70]. In case of fullerene compounds a linear term in the heat capacity is difficult to extract since its contribution is small compared to numerous strong vibrational contributions. However, in case of superconducting materials a subtle jump in specific heat can be observed at  $T_c$  which is caused by the opening of the superconducting gap. The jump in specific heat is related to the normal state metallic contribution and for the BCS superconductors it is expressed as [46]  $\Delta C/T_c = 1.43\gamma$ . We can estimate  $\gamma$  for fullerene superconductors from the specific heat jump measured on  $K_3C_{60}$  ( $\Delta C/T_c = 68(13)$  mJ/mol/K<sup>2</sup> [152]). Using this value we obtain metallic entropy of  $S_m = 0.68$  mJ/mol/K at 10 K, 6.8 mJ/mol/K at 100 K and 20.4 mJ/mol/K at 300 K. The entropy of a paramagnetic insulating state is calculated using the general formula for entropy,  $S = k_B \ln(\Omega)$ , where  $\Omega$  is the size of the phase space or the number of possible states of the system. Assuming a low  $S = 1/2$  spin in the paramagnetic insulating state as has been discussed in Sec. 5.1, the only degrees of freedom are spin up or spin down states. This gives  $2^N$  possible states, where  $N$  is number of  $C_{60}$  molecules in a sample. The temperature independent insulator entropy is  $S_i = N_A k_B \ln(2)$  per mole, or  $S_i = 5.7$  mJ/mol/K. At low temperatures the metallic entropy can be neglected compared to the insulating entropy and thus the entropy difference calculated per  $C_{60}$  molecule is  $\Delta S \simeq 8 \cdot 10^{-24}$  J/K. The volume difference between the insulating and metallic phase is obtained from the XRD data on the  $Rb_xCs_{3-x}C_{60}$  samples where a volume drop of  $\Delta V = 3.5(5)$  Å<sup>3</sup> has been observed when crossing the MIT border (Sec. B.2). Using these values we estimate low temperature slope of  $dP/dT \simeq 23(3)$  bar/K, which is almost two times smaller as the measured one  $(dP/dT)_{\text{exp}} = 42(2)$  bar/K (Fig. 7.15b). In addition, due to fairly large  $\gamma$  of fulleride systems the MIT border would become vertical at temperature of  $\sim 100$  K and change sign at higher temperature. Such behaviour is, for example, observed in BEDT-TTF organic superconductors [146]. However, in fullerides the MIT border is a straight line at least up to  $\sim 200$  K.

Experimentally determined large slope of  $(dP/dT)_{\text{exp}} = 42(2)$  bar/K suggest that the proposed simple model at low temperature with insulating paramagnetic  $S = 1/2$  electrons is not correct. To reproduce the experimental values one would need to include additional degrees of freedom to the insulating phase. Since low-spin state has been determined by experiment and the merohedral orientational disorder is static in the highly expanded  $A_3C_{60}$  samples, the only known effect that might contribute additional entropy is the JT effect. Larger entropy of the insulating state would also shift the MIT border inflection point to higher temperatures which would be in agreement with our observations.

The difference in the entropies and the unit-cell volumes of the insulating and metallic phases are not restraint to a narrow temperature range as is the case of the first order phase transitions with a finite latent heat. Instead, the transition seems to be smeared over a larger temperature range, which is best seen in the unit-cell volume temperature dependence of the  $Rb_xCs_{3-x}C_{60}$  samples (Fig. B.5). This is reminiscent of the second order phase transition, where an order parameter is developing below critical temperature over the large temperature range as observed in magnetic or superconducting phase transitions. And is in agreement with the absence of the hysteresis observed when crossing MIT on cooling and on heating for  $x = 0.35$   $Rb_xCs_{3-x}C_{60}$  sample.

### 7.3 $N(E_F)$ in normal state

The presence of strong electron correlations in  $A_3C_{60}$  family has been anticipated even before the arrival of insulating  $Cs_3C_{60}$ . At that time the only evidence of electronic correlations was from an experimentally determined  $^{13}C$  Korringa factor [112, 148, 153], or from enhanced density of states at the Fermi energy assuming Pauli mechanism for magnetic susceptibility [47, 136, 152, 154, 155]. Although the correlation effects were found to be small (a factor of  $\sim 2$ ) all the experimental data was at that time successfully explained. Stenger *et al.* [47] observed that all spin-lattice relaxation rates known at that time fit on a universal curve when plotted as a function of unit-cell site with temperature and dopant ion as implicit parameters. He argued that all spin-lattice relaxation measurements could be explained with a simple Pauli susceptibility and enhanced calculated density of states by the Stoner enhancement.

With the synthesis of the largest member  $Cs_3C_{60}$  that shows Mott-insulating properties at ambient pressures the role of electron correlations became evident. To further characterise the Mott-Hubbard metal-to-insulator transition we extend the analysis by Stenger *et al.* [47] adding high-pressure  $Cs_3C_{60}$  and  $Rb_xCs_{3-x}C_{60}$   $^{13}C$  NMR results. In Fig. 7.16 we show  $1/^{13}T_1T$  data measured in the metallic state (full symbols in Fig. 7.16), just above the superconducting transition. For comparison with the previous work we added data of  $K_3C_{60}$ ,  $Rb_3C_{60}$ , and  $RbCs_2C_{60}$  [47, 135] as grey symbols. We can see that all measured  $1/T_1T$  points do not lay on an universal curve as has been argued before. This is, however, true if we limit our analysis only to the low temperature points for each compound (with smaller volume). All data points are not uniquely determined by the density of states only and other effects should be considered. To further emphasise this claim we plot  $1/^{13}T_1T$  measured at  $T_{MIT}$  (empty symbols in Fig. 7.16) for  $Rb_xCs_{3-x}C_{60}$  samples where  $1/^{13}T_1T$  is at the maximum. We can see that these points follow a path set by the high temperature points of the  $RbCs_2C_{60}$  sample [47]. At higher temperatures the spin-lattice relaxation rate cannot be modelled by a simple Pauli theory for metals where spin susceptibility is a function of density of states. In this temperature range other effects should be considered, e.g. pseudogap, phase segregation, enhanced uncorrelated spin fluctuations. However, if we limit our analysis to the low temperatures (just above  $T_c$ ) a single universal curve is obtained. We will use low temperature data for further analysis.

Low-temperature spin-lattice relaxation rate divided by temperature is monotonically increasing with increasing of the unit-cell volume. Assuming that Korringa relation (Eq. 3.83) for normal metals holds and that Korringa factor is kept constant<sup>4</sup> then  $1/T_1T$  data is proportional to the Pauli spin susceptibility squared. Since Pauli susceptibility is also proportional to the  $N(E_F)$  the measured increase of  $1/T_1T$  can be directly related to the increase of  $N(E_F)$  with increasing volume. This is expected since with larger unit-cell volume the overlap between neighbouring  $C_{60}$  molecules decrease which leads to reduced electron wavefunction overlap, the hopping integral and the  $t_{1u}$  bandwidth. Since the number of  $t_{1u}$  states is unchanged decrease of the bandwidth requires increase of density of states. To test if our data follows this simple non-interacting model we added dashed line to Fig. 7.16 calculated as  $1/T_1T \propto \chi_s^2 \propto |N(E_F)|^2$ . DFT-LDA  $N(E_F)$  was adapted from [54] and the data was scaled in order to fit the measurements at low volumes. The agreement is rather good up to the volume  $\sim 760 \text{ \AA}^3/C_{60}$  above which it fails to follow its

<sup>4</sup>The Korringa factor obtained in the previous subsection 7.2.2 is at low temperatures not changing for more than 30% (Fig. 7.13)

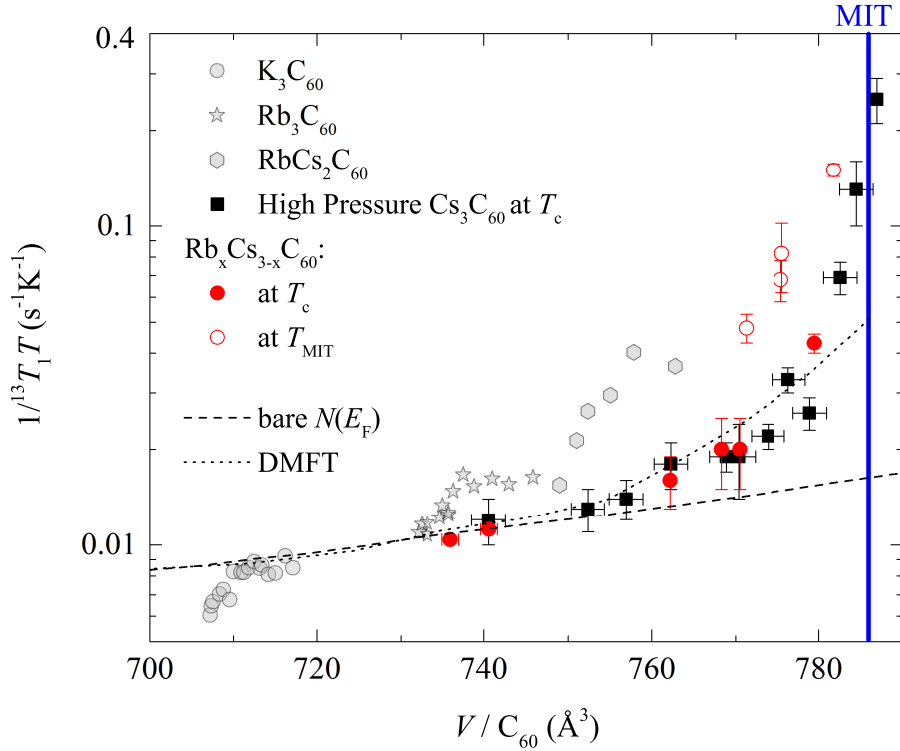


Figure 7.16:  $1/T_1T$  as a function of unit-cell volume per  $C_{60}$  molecule for high-pressure measurements on  $Cs_3C_{60}$  (black squares) and  $Rb_xCs_{3-x}C_{60}$  samples (red circles) just above  $T_c$  (full symbols). For  $Rb_xCs_{3-x}C_{60}$  samples  $1/T_1T$  points at  $T_{MIT}$  (empty symbols) were also added. For comparison previous  $1/T_1T$  data has been adapted and added,  $K_3C_{60}$  [135] (grey circles),  $Rb_3C_{60}$  [135] (grey stars) and  $RbCs_2C_{60}$  [47] (grey hexagons). Fits: (dashed line) using Korringa relation (Eq. 3.83) and bare density of states computed by DFT-LDA [54] and (dotted line) scaled uniform spin susceptibility obtained by DMFT [62].

rather strong increase when closing on MIT. This clearly shows that the spin susceptibility is enhanced close to the MIT probably due to strong electron correlations.

The enhancement of the spin susceptibility in the vicinity of the Mott-Hubbard transition is well known effect, which has vastly been studied on Ti-doped  $V_2O_3$  systems [156]. Neglecting the high-energy physics when solving the Hubbard model Brinkman and Rice [157] showed that the spin susceptibility is proportional to an effective electron mass or the quasiparticle residuum in the Fermi liquid theory picture. By using Gutzwiller approximation where the high energy incoherent Hubbard bands were neglected their result gave a divergent uniform ( $\vec{q} = 0$ ) spin susceptibility at the MIT. After the DMFT has been developed the correctly computed uniform spin susceptibility show similar enhancement when closing the MIT, however, the spin susceptibility does not diverge at MIT but rather saturate to a value proportional to the Hubbard exchange parameter ( $J = 2t^2/U$ ). This effect comes from the polarization of the high energy Hubbard bands and the corresponding uniform spin susceptibility is written as  $\chi^{-1} \simeq 0.4(1 - U/U_c) + J$  [63]. However, the spin susceptibilities measured by NMR are local, on-site susceptibilities,  $\chi_{loc} = \sum_q \chi(q)$ . In this case the the enhancement at the MIT is not saturated by the exchange term and it, therefore, diverges for  $T = 0$  [63].

To test our data for the effect of strong electron correlations we added dotted line to Fig. 7.16, which we calculated using the DMFT results of  $A_3C_{60}$  system [62]. The adapted uniform spin susceptibility was squared as required by the Korringa relation and

scaled to best fit the data. As it can be seen, the agreement is much better confirming the presence of strong electron correlations. A small discrepancy can be found for a couple of points closest to the MIT. This could arise from saturation effects of used uniform spin susceptibility rather by local which is measured by NMR. Another possibility would be an additional enhancement due to the  $\vec{q}$  dependent antiferromagnetic fluctuations which are not considered within DMFT. We note that simple Brinkman-Rice expression,  $\chi \propto (1 - U/U_c)^{-1}$ , does not fit our data successfully.<sup>5</sup> This could be due to fact that  $A_3C_{60}$  are complex three orbital systems with intra-orbital exchange interaction which reduce the  $S = 3/2$  high spin state to the  $S = 1/2$  low-spin state when close to the MIT. This additionally modifies the spin susceptibility which results in a plateau near the MIT [62] and a better agreement with our data.

Finally we note, that no critical point in the phase diagram could be found. Isothermal paths on the phase diagram give for all the temperatures a finite derivative of the order parameter,  $1/T_1T$ , as a function of the unit-cell volume, not even at the lowest temperature (Fig. 7.16). The lack of critical point suggest that the transition is of the second order. This is in agreement with the absence of the hysteresis in  $1/T_1T$  measurements. The second order phase transition at low temperatures is uncommon for the Mott-Hubbard transitions, unless disorder effects are present [158]. In *fcc*  $Rb_xCs_{3-x}C_{60}$  samples there is the merohedral and the alkali metal substitutional disorder which were until now considered not to influence the electronic properties apart from observed reduction of  $T_c$  for a few degrees. The second order phase transition is, therefore, the most probable scenario in the  $A_3C_{60}$  family.

## 7.4 Conclusions

In this chapter we have studied the MIT of  $A_3C_{60}$  system both experimentally and theoretically. We stress that strong electron correlations have been expected in  $A_3C_{60}$  even before the appearance of the insulating  $Cs_3C_{60}$  due to large on-site Coulomb repulsion between the electrons. Even-though strong correlations are present, the absence of the insulating state for critical  $(U/W)_c$  of more than 2 has been explained by the three-fold orbital degeneracy providing a three hopping channels and the effectively increase the electron bandwidth.

The high pressure NMR on  $Cs_3C_{60}$  and NMR on  $Rb_xCs_{3-x}C_{60}$  samples allowed us to scan the phase diagram around the MIT in controlled manner. The metallic and the insulating bordering phases were rather straight forward to analyse and discuss within standard models, however, in the intermediate region the explanation of the experiments is far more challenging. In this region we have found that the spin-lattice relaxation rate divided by temperature,  $1/T_1T$ , exhibits a maximum which can be related to the on-set of MIT. In addition, below a temperature corresponding to the MIT,  $T_{MIT}$ , there is an exponential decay of  $1/T_1T$  as a function of temperature. The reason for this decay is still not known, however, we proposed several models to explain the observed behaviour. These are the pseudogap model, a less probable phase segregation model, or the reduction of the uncorrelated spin susceptibility in the metallic site due to the formation of spin singlet pairs. We also showed that there is no direct indication for the presence of the antiferromagnetic fluctuations, since the spin lattice relaxation rates of different nuclei,

---

<sup>5</sup>Brinkman-Rice expression can be transform from the  $U$  dependence to the  $V$  dependence by realizing that the relevant parameter is proximity to the MIT determined either by  $U/W$ ,  $U/U_c$ ,  $W_c/W$ , or even  $V/V_c$ , since ( $V \propto W^{-1}$ ).

having different form factors, do now show different temperature evolutions as is expected when strong antiferromagnetic fluctuations are present. We see only the indirect evidences of its presence, namely, there is an inconsistency between the hyperfine constants of different nuclei obtained by the Knight shift and the spin-lattice relaxation rates for different alkali metal sites and another evidence is that the extracted Korringa factor is less than one. However, both arguments are based on the assumption of the temperature independent hyperfine coupling constants which leads to a strong temperature dependent chemical shift, a rear effect.

A strong temperature dependent lineshift of the alkali nuclei only partially resembles temperature dependent bulk susceptibility as would be the case of temperature independent chemical shift and the hyperfine coupling constants which is normally the case. In order to explain the complex lineshifts temperature dependence we studied two simple models to reduce the number of free parameters. In the first model we assumed temperature independent chemical shift. The obtained strongly temperature dependent hyperfine coupling constants would result in the strong temperature evolution of the ratio between O- and T-site coupling constants which not realistic based on the spin-lattice relaxation time ratio. The second model assumes temperature independent hyperfine coupling constants and results in a strong chemical shift variation as a function of temperature. Even-though, this is uncommon, such effect has been proposed before and could be a result of strong ring currents of the deformed  $C_{60}$  molecules induced by the Jahn-Teller effect. The second model, therefore, seems more plausible having less disagreements with the minimum amount of the free parameters. However, we can not definitely reject the first model. It may well be that in reality both chemical shift and hyperfine coupling constants are temperature dependent.

We have also investigated the shape of the MIT border on the phase diagram. A negative slope of the border on the  $(P, T)$  phase diagram is consistent with metallic entropy being smaller than the paramagnetic insulating state at low temperatures. However, the magnitude of the slope does not agree well with the paramagnetic low-spin insulating state. To remove the discrepancy the insulating phase would have to be in the high-spin state, however, a low spin insulating phase has been shown experimentally. The other possibility is the reduction of orbital degrees of freedom when passing the MIT. This can only be related to the Jahn-Teller which is known to be present in the insulating state and only expected to slowly fade away in the metallic state. The slow disappearance of the Jahn-Teller effect is therefore suggested by MIT border analysis.

At the end we focused on the  $1/T_1T$  values as a function of the unit cell volume. It has been argued before, that  $A_3C_{60}$  samples could be discussed within a simple Pauli theory where the spin susceptibility is uniquely determined by the density of states and temperature independent. By extending their analysis to include also samples in the vicinity of the MIT we have shown that  $A_3C_{60}$  family cannot be treated within a simple Fermi-liquid theory since spin susceptibility in the vicinity of MIT is not only a function of density of states but also temperature. In addition, we have shown that the increase of the spin susceptibility with increasing unit-cell volume is follows the increase of the non-correlated density of states at smaller volumes, however, close to the MIT this description fails where experimental susceptibility becomes strongly enhanced near MIT showing almost a divergent tendency. Such behaviour is common for the Mott-Hubbard systems where the spin susceptibility increase approximately inversely proportional to the proximity to the MIT,  $\chi \propto (1 - U/U_c)^{-1}$ . However, a simple single band Hubbard model does not successfully reproduce our data. Far better agreement is obtained by the DMFT results of a three band Hubbard model with an intraband exchange interaction

developed for  $A_3C_{60}$  system. Compared to the single band simple Hubbard case the susceptibility in this model is partially suppressed when approaching MIT from the metallic side, due to a crossover from the high-spin to the low-spin state which theoretically and experientially found in the insulating state.

The metal to insulating transition in the  $A_3C_{60}$  system is a result of a rather rich physics. In addition to the strong electron correlations that are driving the metal to the insulating transition we have found evidence of the Jahn-Teller effect and only an indirect evidence of antiferromagnetic fluctuations which could be a result of large geometric frustration. The order of the phase transition is most probably of the second order since we could not observed a hysteresis in the order parameter or a critical point in the phase diagram. This is uncommon for Mott-insulating-to-metallic transitions, however, it is possible in the presence of disorder.

# 8 Superconductivity

Alkali-doped fullerenes are molecular superconductors with the highest known  $T_c$  of 38 K [13]. With the discovery of superconductivity in  $A_3C_{60}$  [9] and the fact that  $T_c$  is increasing with increasing unit-cell volume they received a lot of attention as possible candidates for room-temperature superconductors. Measured superconducting properties of the under-expanded  $A_3C_{60}$  compounds were explained by the BCS framework and thus alkali-doped fullerenes have been considered to be a special case of phonon-mediated standard superconductors with high  $T_c$ . However, increasing number of theoretical and experimental arguments suggested that  $A_3C_{60}$  cannot be correctly described by the standard BCS theory or its extensions. The strongest evidence came with the discovery of the largest member,  $Cs_3C_{60}$ , with a Mott-insulating ground state and a metallic or superconducting ground state under moderate hydrostatic pressure of  $\sim 2$  kbar [13, 14]. Measurements at higher pressures revealed a non-monotonic behaviour of  $T_c$ , which is reminiscent to the unconventional superconductors, like cuprates, iron pnictides, or heavy fermion systems [49].

This raises an important question: are  $A_3C_{60}$  standard superconductors that can be adequately explained by the BCS framework even in the vicinity of MIT, or are they unconventional superconductors where other effects, that are not included in the BCS framework, play a dominant role. In order to address this important question we present in this chapter an extensive study of superconducting properties measured by local probe high-pressure NMR on *fcc*  $Cs_3C_{60}$  and NMR on *fcc*  $Rb_xCs_{3-x}C_{60}$  compounds.

## 8.1 Superconducting dome

Recently synthesised largest member of  $A_3C_{60}$  family, *fcc*  $Cs_3C_{60}$  [36], finally answered the long standing question: will the superconducting transition temperature keep increasing with increasing unit-cell volume or will it stop on approaching MIT at some critical volume,  $V_c$ .

High-pressure SQUID magnetization measurements on *fcc*  $Cs_3C_{60}$  reveal that  $T_c$  increases with increasing volume up to  $V_{\max} \simeq 760 \text{ \AA}^3$ , where it reaches  $T_c = 35$  K, and then  $T_c$  decreases until at  $V_c$  it goes over the MIT [14]. Equivalent behaviour is observed also in A15  $Cs_3C_{60}$  polymorph, where  $T_c$  reaches a record high value of  $T_c = 38$  K [13], which is the highest  $T_c$  known for molecular superconductors. Such a non-monotonic – a "dome shaped" superconducting region – is reminiscent to unconventional superconductors like cuprates, heavy fermions, or iron pnictides [49].

In NMR experiments the onset of the superconductivity is observed either in the spectra where their Knight shift starts to decrease and completely vanishes for  $T \rightarrow 0$  or in the spin-lattice relaxation rate which is suppressed in the superconducting state due to the vanishing number of thermally excited normal state electrons. The spin-

lattice relaxation rate, however, strongly depends on the shape of the density of states and can display Hebel-Slichter coherence peak just below  $T_c$  before it steeply drops for  $T \rightarrow 0$ . This makes the determination of  $T_c$  from spin-lattice relaxation rates ambiguous, so we decided to determine  $T_c$  in the NMR experiments from the drop of the Knight shift. Discussion on the Knight shift in the superconducting state can be found in Sec. 3.3.5 and representative measured lineshifts for  $\text{Rb}_x\text{Cs}_{3-x}\text{C}_{60}$  samples are summarized in Fig. 7.7.  $T_c$  extracted from the high-pressure NMR experiments on  $\text{Cs}_3\text{C}_{60}$  and ambient-pressure NMR experiments on  $\text{Rb}_x\text{Cs}_{3-x}\text{C}_{60}$  samples as a function of the unit-cell volume are shown in Fig. 8.1. In this superconducting phase diagram we include also  $T_c$  from previous experiments on various  $A_xA'_{3-x}\text{C}_{60}$  samples [30] and high-pressure SQUID results on *fcc*  $\text{Cs}_3\text{C}_{60}$  sample [14]. We can see that results from our NMR measurements agree well with previous measurements. A slight discrepancy observed for  $\text{Rb}_x\text{Cs}_{3-x}\text{C}_{60}$ ,  $x \geq 1$  samples will be discussed later.

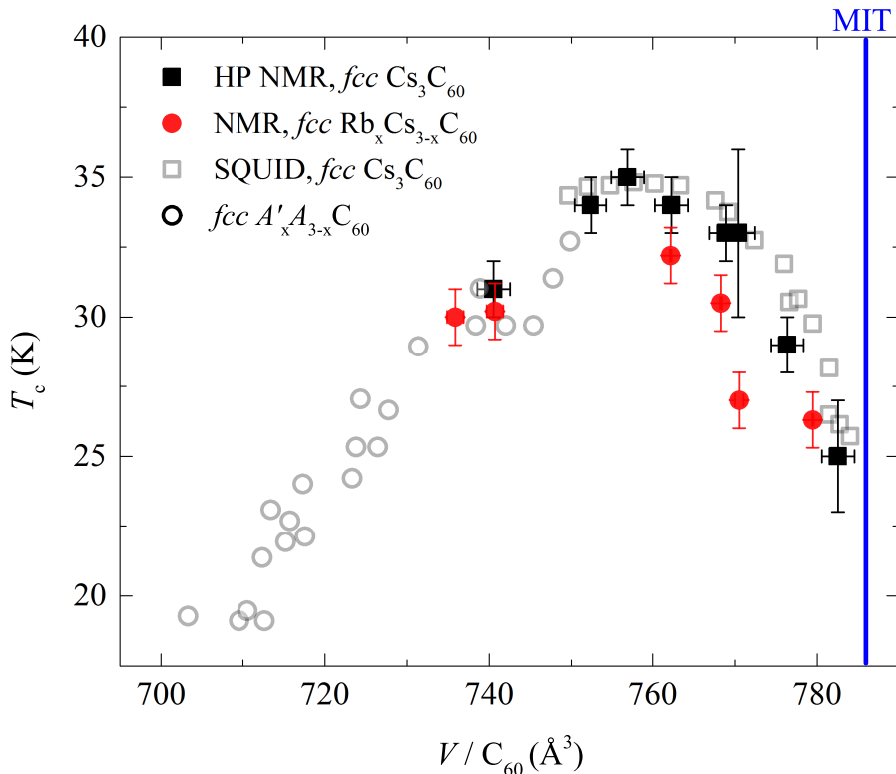


Figure 8.1: Superconducting  $(V, T_c)$  phase diagram of the  $A_3\text{C}_{60}$  family. Displayed are  $T_c$  points from (black solid squares) high-pressure NMR on  $\text{Cs}_3\text{C}_{60}$ , (red solid circles) NMR on  $\text{Rb}_x\text{Cs}_{3-x}\text{C}_{60}$  samples, (empty gray squares) high-pressure SQUID measurements on *fcc*  $\text{Cs}_3\text{C}_{60}$  sample [14] and (empty gray circles)  $T_c$  values of various  $A_xA'_{3-x}\text{C}_{60}$  samples adapted from [30].

In the previous chapter (Sec. 7.3) we have shown that the spin susceptibility in the metallic phase measured by the spin-lattice relaxation rate just above  $T_c$  (Fig. 7.16) shows a monotonic increase with the increasing unit-cell volume.

Since in the Fermi-liquid theory Pauli spin susceptibility is proportional to  $N(E_F)$ , we can conclude that  $N(E_F)$  is as well monotonically increasing function of the unit-cell volume. According to standard BCS theory (Eq. 2.11) or Migdal-Eliashberg extension (Eq. 2.13) where Coulomb parameter  $U$  is assumed to be volume independent, a monotonic behaviour of  $N(E_F)$  can lead only to a monotonic behaviour of  $T_c$ . This is in odds with the experimental observation which suggests that standard BCS theory is inadequate to explain superconductivity of  $A_3\text{C}_{60}$ .

In principle, a qualitative description of the non-monotonic behaviour of  $T_c$  is possible within the Migdal-Eliashberg theory assuming that the Coulomb parameter becomes notably enhanced in the over-expanded region. This could be justified since the screening effects that reduce the on-site Coulomb repulsion in the solid state (Sec. 7.1.2) become less effective in the expanded crystal structure where quasiparticles are strongly renormalized. However, a quantitative determination of  $T_c$  in this region would require strong retardation effects which are possible only when low energy phonon modes, e.g. optical or even lower in energy, take part in the superconducting pairing [5]. As will be discussed later, the involvement of low energy phonons in  $A_3C_{60}$  superconductivity is questionable.

### 8.1.1 Chemical vs. hydrostatic pressure

Let us now come back to the discussion of the observed slight difference between high pressure NMR on  $Cs_3C_{60}$  and  $Rb_xCs_{3-x}C_{60}$  samples. Where  $Cs_3C_{60}$  superconducting transition temperatures agree well with the ones measured by SQUID magnetometer at low magnetic fields,  $Rb_xCs_{3-x}C_{60}$  samples show a slight reduction of cca. 2 K for samples in the vicinity of MIT ( $x \leq 1$ ). A lower transition temperature would be expected in the presence of large magnetic fields used for NMR experiments, however, since  $Cs_3C_{60}$  samples show that such reduction is negligible in the over-expanded region this argument is invalid. Negligible effect on  $T_c$  by a considerable magnetic field used in the NMR experiment (9.4 T) is consistent with very large critical magnetic fields determined for  $K_3C_{60}$  and  $Rb_3C_{60}$  of  $B_{c2} = 50$  and 70 T, respectively [159], and since  $B_{c2}$  is increasing with the unit-cell volume one might expect that it would be even larger for highly expanded samples. Another mechanism that can suppress  $T_c$  is structural disorder [115]. The absence of discrepancy in  $x = 3$  and 2 compounds is in agreement with this argument, since we have shown (Chap. 6) that these two compounds exhibit no substitutional disorder.

Another difference between high-pressure  $Cs_3C_{60}$  and  $Rb_xCs_{3-x}C_{60}$  compounds is the size of alkali ions when both have the same unit-cell volume. For example, at a certain high pressure, where the unit-cell volume is the same as in, e.g.,  $Rb_3C_{60}$  the larger  $Cs^+$  ions occupy more space in the interstitial sites than  $Rb^+$  ions. This results in a stronger crystal field exerted on  $C_{60}$  molecules in case of  $Cs_3C_{60}$  under high pressure. A consequence of stronger crystal field would be a higher structural transition temperature below which  $C_{60}$  molecular dynamics freezes. For  $Rb_3C_{60}$  compound  $C_{60}$  dynamics freeze around room temperature [7], whereas, in case of  $Cs_3C_{60}$  with similar volume this transition would be shifted to much higher temperatures. The crystal field effect would also affect the JT deformations by enhancing the minima in APES which would favour the static JT effect. However, stronger crystal field due to larger alkali metals does not change the cubic symmetry of these materials and the triple degeneracy of  $t_{1u}$  electronic orbitals is maintained. From the electronic structure point of view the alkali metals are known to have negligible effect on the electronic structure near Fermi energy. This is a result of a small admixture of their outer  $s$  orbitals in the  $t_{1u}$  molecular (Wannier) orbitals, of the order of 1% [7]. In case of high-pressure  $Cs_3C_{60}$  at the same unit-cell volume, large size of Cs  $6s$  orbitals could lead to a larger admixture of  $6s$  orbitals in the  $t_{1u}$  molecular (Wannier) orbitals. A possible consequence of this could be an enhanced Knight shift, which is yet to be determined.

## 8.2 Hebel-Slichter coherence peak

The Hebel-Slichter (H-S) coherence peak observed in NMR spin-lattice relaxation rate below  $T_c$  is a hallmark of BCS superconductors and comes from the logarithmic divergence in the BCS density of state. According to the BCS theory the ratio between superconducting and normal state spin-lattice relaxations rates would have on the top of the peak a maximum of  $(R_s/R_n)_{\max} = 2-3$  [160] (Fig. 8.6a). The absence of Hebel-Slichter peak in the early NMR measurements on  $K_3C_{60}$  [135], therefore, came as a surprise and initiated scepticism about the BCS theory as the appropriate theory of  $A_3C_{60}$  superconductors. It has been later revealed that the H-S peak is indeed present but its suppression strongly depends on the magnetic fields used, e.g., in the NMR experiments [47, 91, 161]. However, also in small magnetic fields the H-S peak is not recovered completely. Its maximum is only  $(R_s/R_n)_{\max} \sim 1.2$  as observed by the  $\mu$ SR experiments done at  $B = 1$  T [91, 161]. Such a strong damping of the H-S peak is not common among standard BCS superconductor and thus suggests that additional effects are present but not taken into account in the standard BCS theory.

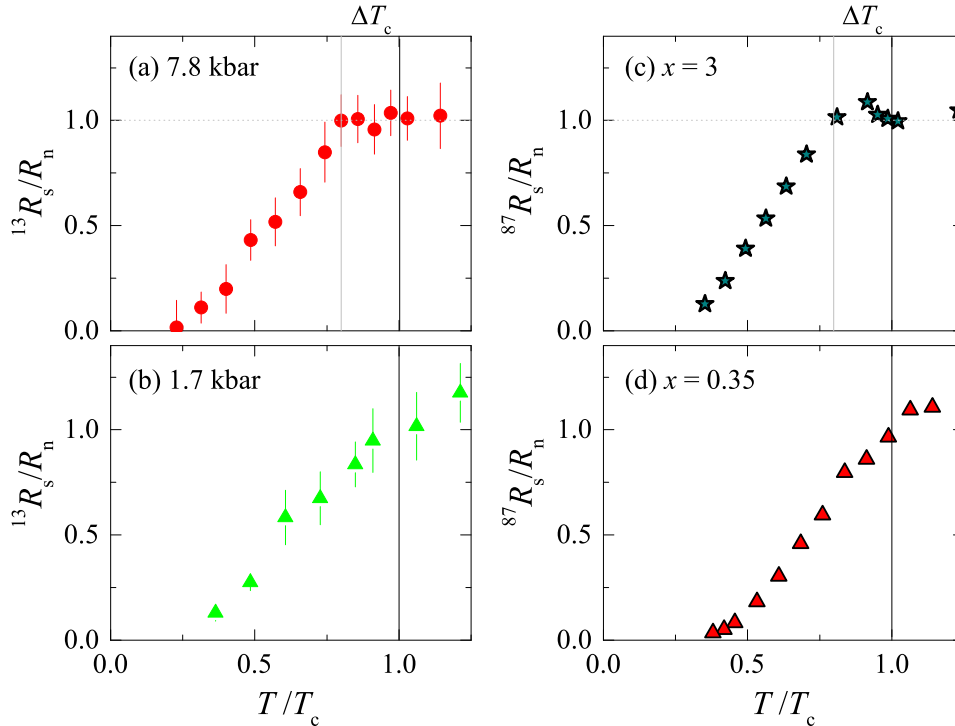


Figure 8.2: Normalized spin-lattice relaxation rate divided by temperature ( $R_s/R_n = T_1^n T_c / T_1^s T$ ) as a function of normalized temperature from high pressure (a) 7.8 kbar and (b) 1.71 kbar experiments and from  $Rb_xCs_{3-x}C_{60}$  (c)  $x = 3$  and (d)  $x = 0.35$  sample NMR measurements. Delayed drop of spin-lattice relaxation rate due to H-S peak is indicated with  $\Delta T_c$ .

Based on the past observations H-S peak is anticipated to be strongly damped in the magnetic field used in our NMR experiments. This is indeed true for our high pressure NMR measurements as can be seen in Fig. 8.2a. For the highest pressure, in the under-expanded region, there is no observable peak, only a notable suppression of  $1/T_1 T$ ,  $\Delta T_c \simeq 4$  K below  $T_c$ . Such a delayed drop was also observed in previous NMR measurements on multiphase  $Cs_3C_{60}$  [124] as well as in other  $A_3C_{60}$  compounds [135]. Since the actual peak is recovered in smaller magnetic fields [47] we associate the observed offset

( $\Delta T_c$ ) to strongly damped H-S peak. For smaller pressures, when closing MIT the temperature difference  $\Delta T_c$  becomes reduced and completely vanishes just before the MIT. This indicates that H-S peak damping is further enhanced approaching MIT.

Spin-lattice relaxation time measurements on  $\text{Rb}_x\text{Cs}_{3-x}\text{C}_{60}$  samples with large  $x$ , that are in the under-expanded region, in contrast to high-pressure experiments actually exhibit a small H-S peak (Fig. 8.2b). For  $x = 3$  sample the peak maximum exceeds the normal state value for  $\sim 10\%$  and the data drops below the normal value at  $\Delta T_c \simeq 5$  K below  $T_c$ . This temperature difference is similar to the high-pressure experiments. For more expanded samples  $x \rightarrow 0$  the H-S peak is gradually fading away and completely vanishes at the MIT. The disappearance of the peak can be followed in both the peak maximum and  $\Delta T_c$ . The same behaviour is observed for all measured local probes,  $^{13}\text{C}$ ,  $^{133}\text{Cs}$ , and  $^{87}\text{Rb}$ .

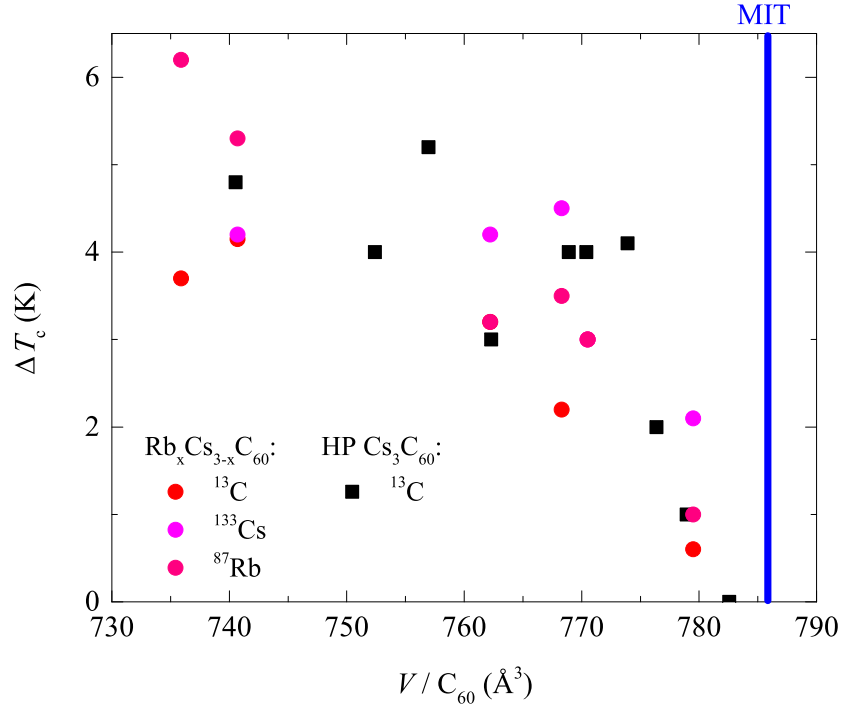


Figure 8.3: Summary of  $\Delta T_c$  as a function of unit-cell volume obtained by high pressure  $^{13}\text{C}$  NMR measurements on  $\text{Cs}_3\text{C}_{60}$  (black squares) and  $^{13}\text{C}$ ,  $^{133}\text{Cs}$ , and  $^{87}\text{Rb}$  NMR measurements on  $\text{Rb}_x\text{Cs}_{3-x}\text{C}_{60}$  samples (coloured circles).

All measurements of  $\Delta T_c$  on  $\text{Rb}_x\text{Cs}_{3-x}\text{C}_{60}$  samples and on  $\text{Cs}_3\text{C}_{60}$  under high pressure are summarized in Fig. 8.3. One can see that  $\Delta T_c$  as a function of the unit-cell volume shows a universal behaviour, where in the under-expanded region  $\Delta T_c$  is almost volume independent having a value of  $\Delta T_c \sim 5$  K, around  $760 \text{ \AA}^3 / \text{C}_{60}$   $\Delta T_c$  starts to decrease, and vanishes close to MIT. Such a universal behaviour furthermore supports the claim that the unit-cell volume is the only controlling parameter of this system and for the first time shows that H-S peak damping is strongly enhanced close to the MIT, independent of the magnetic field<sup>1</sup> or the sample quality<sup>2</sup>. We note that the absence of H-S peak is commonly observed among unconventional superconductors, e.g., cuprates [162], heavy fermion systems [163], or iron-pnictides [164], which suggest that similar effects might be responsible for the enormous H-S peak damping in  $\text{A}_3\text{C}_{60}$  near MIT.

<sup>1</sup>All experiments were performed in the same magnetic field of  $B_0 = 9.4$  T.

<sup>2</sup>The same sample was used for all high-pressure experiments.

There are several factors that could suppress the H-S peak: momentum anisotropy of the superconducting gap, time-reversal symmetry breaking by magnetic impurities or applied magnetic field, and the damping effects in the superconducting state.

In case of anisotropic gap function the superconducting density of states is obtained by averaging over all angles. As a result the H-S peak is reduced and the low temperature Arrhenius slope [ $R_s \propto \exp(-\Delta/k_B T_c)$ ] can be modified relative to the isotropic case. For large anisotropies (such that the angular momentum of the Cooper pairs is finite) the density of states becomes gapless due to the nodal structure of the gap function. In such case the H-S peak can be completely eliminated and the low temperature exponential dependence can be replaced by the power law dependence, e.g., typically  $R_s \propto T^3$  for  $d$ -wave superconductors [145]. Such behaviour is observed in  $\text{YBa}_2\text{Cu}_3\text{O}_{6.91}$  [162]. However, all experiments on  $A_3\text{C}_{60}$  samples so far [7] and as we shall see also for samples near MIT show that the superconducting pairing symmetry is of  $s$ -wave type. Therefore, the effects of the gap function anisotropy on the H-S peak can be omitted in further discussion.

The time reversal effects in  $A_3\text{C}_{60}$  samples can only come from applied magnetic field since no magnetic impurities are present. The effects of applied magnetic field are modelled in two ways. The first is by considering Zeeman energy in the expression of  $T_1$  in superconducting state (Eq. 3.96)

$$\frac{1}{T_1} = \frac{2\pi}{\hbar} M^2 \int_0^\infty \text{Re} \left\{ N(E_i) \sqrt{\frac{E_i E_f + \Delta^2}{E_i^2 - \Delta^2}} \right\} \text{Re} \left\{ N(E_f) \sqrt{\frac{E_i E_f + \Delta^2}{E_f^2 - \Delta^2}} \right\} f(E_i) [1 - f(E_f)] dE,$$

where  $\Delta E = E_f - E_i = \hbar(\gamma_e + \gamma_n)B_0$  is the total Zeeman energy. However, this effect is not strong enough to explain the experimentally observed strong field dependence [90]. The second model uses a simple weighted average of the spin relaxation rate in BCS superconductor and temperature independent relaxation rate appropriate for normal metallic state. The later comes from vortex cores. Their weight is determined from vortex core size which is a known function of applied external magnetic field. Such treatment can successfully reproduce the experimental field dependent suppression of the H-S peak [7, 47]. However, our measurements show that H-S peak is additionally suppressed when approaching MIT, even-though we used the same magnetic field in all experiments. This suggests that other suppression mechanism should be considered. We note, that the additional suppression could come from increased sensitivity to the magnetic field when approaching MIT. However, the same reduction of H-S peak as observed by our experiments have been obtained also by  $\mu\text{SR}$  experiments on  $\text{Rb}_x\text{Cs}_{3-x}\text{C}_{60}$  samples [165]. This confirms that the additional suppression close to MIT does not come from the magnetic field effects.

The remaining mechanism known to suppress the H-S peak is the damping of quasi-particles when these are scattered by phonons, impurities or other electrons. In case of phonons the electron-phonon interaction in  $A_3\text{C}_{60}$  is not strong enough to explain strongly suppressed H-S peak. To obtain experimental values of  $(R_s/R_n)_{\text{max}}$  the electron-phonon dimensionless coupling constant would have to be  $\lambda \sim 2$  [90] which is much larger than  $\lambda = 0.5-1$  that is expected for  $A_3\text{C}_{60}$  [7, 25, 90]. The effect of impurities can be omitted since they are not present. The only remaining effect is the scattering among electrons due to strong Coulomb interaction. This idea was verified by the self-consistent Eliashberg-Nambu calculations [90], which yield strongly suppressed H-S peak of magnetic field comparable to the experimental values of  $(R_s/R_n)_{\text{max}} \sim 1.2$ . The Eliashberg-Nambu calculations were performed for the zero magnetic field, typical values of the electron-phonon interaction, and the Coulomb repulsion energy for under-expanded

$A_3C_{60}$  samples. They showed that the inclusion of the Hubbard parameter,  $U$ , causes an increase in the imaginary part of the energy dependent gap function, which broadens the superconducting density of states and suppresses the H-S peak.

Two main contributions found to suppress the H-S peak in under-expanded  $A_3C_{60}$  samples are magnetic field and strong electron-electron interaction. Since in our experiments the magnetic field was kept constant the observed additional suppression can only originate from the electron-electron interaction. To explain the enhanced suppression and finally the disappearance of the H-S peak near the MIT the effects of strong electron-electron interaction must be further enhanced when approaching MIT. This is in agreement with the observed enhancement of the spin susceptibility close to the MIT and the Mott localisation of electrons on the insulating side of MIT.

### 8.3 Superconducting ratio, $2\Delta/k_B T_c$

Another parameter that characterizes the coupling strength of superconductors is a superconducting ratio  $2\Delta/k_B T_c$ . The BCS theory developed in the weak-coupling regime predicts  $2\Delta/k_B T_c = 3.53$  (Sec. 2.2) which was also experimentally confirmed for numerous elemental superconductors, such as Al for instance. To determine the superconducting ratio in  $A_3C_{60}$  samples several experiments were conducted. NMR experiments on  $K_3C_{60}$ ,  $Rb_3C_{60}$ , and  $Rb_2CsC_{60}$  gave  $2\Delta/k_B T_c = 3.0 - 4.3$  [47, 135, 166],  $\mu$ SR on  $Rb_3C_{60}$  gave  $2\Delta/k_B T_c = 3.6$  [161], scanning tunnelling microscopy on  $Rb_3C_{60}$  yields  $2\Delta/k_B T_c = 2 - 5.3$  [48, 167] and optical measurements on  $K_3C_{60}$ , and  $Rb_3C_{60}$  gave  $2\Delta/k_B T_c = 3.44 - 4.2$  [168, 169]. Even-though the values strongly depend on the sample quality and the technique used, it is generally accepted that  $A_3C_{60}$  samples in the under-expanded region have BCS superconducting ratio,  $2\Delta/k_B T_c = 3.5$  [5].

In the NMR experiments the superconducting ratio can be obtained by measuring the value of the superconducting gap ( $\Delta$ ) at low temperatures. This can be done by following the evolution of the Knight shift or the spin-lattice relaxation rate below  $T_c$ . In case of the Knight shift, the gap is obtained by fitting Yosida function (Eq. 3.91) to the measured shift as shown in Fig. 8.4. However, in our case the lack of measured points at lowest temperatures does not allow to precisely separate the chemical shift from the Knight shift. The error introduced by estimating the chemical shift as was done in Sec. 7.2.2 is too large to give a meaningful value of  $2\Delta/k_B T_c$ .

Alternative method is to employ the spin-lattice relaxation rate where  $s$ -wave superconducting gap can be extracted from the Arrhenius behaviour at low temperatures (Eq. 3.98)

$$\frac{1}{T_1} \propto \exp(-\Delta/k_B T).$$

The deviations from such behaviour can come from the anisotropic gap function, where for  $d$ -wave symmetry  $1/T_1 \propto T^3$  as mentioned in the previous section. Other effects known to distort the Arrhenius behaviour are the H-S peak for temperatures close to  $T_c$ , inhomogeneous gap function due to dense vortex lattice close to upper critical field  $B_{c2}$  and additional relaxation channel at very low temperatures from the electronic excitations in the vortex cores [91]. Considering all these distortion effects the Arrhenius behaviour is expected to be valid at fields smaller than  $B_{Arr} = 0.4B_{2c} \simeq 20-30 T^3$ , temperatures higher than  $T_{||} \simeq 0.2T_c = 6 K$  and lower than  $T_{hl} \simeq 0.6T_c = 20 K$  [91]. These limits

---

<sup>3</sup>We took  $B_{c2} = 50 T$  and  $70 T$ , for  $K_3C_{60}$  and  $Rb_3C_{60}$ , respectively [159]. As  $B_{c2}$  seems to increase with increasing unit-cell volume the upper field limit for Arrhenius behaviour would be even higher.

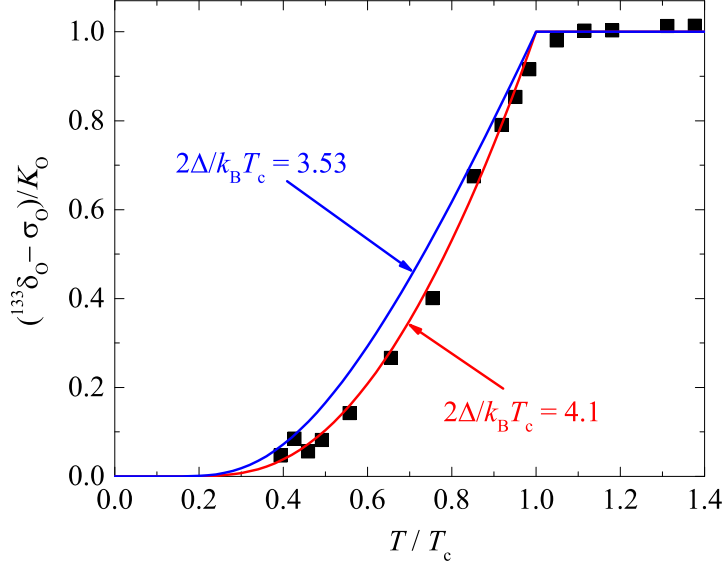


Figure 8.4: Rescaled  $^{133}\text{Cs}$  O-site lineshift for  $x = 0.75$  as a function of renormalized temperature. Red curve represents fit to the data with Yosida function yielding  $2\Delta/k_{\text{B}}T_{\text{c}} = 4.1$ . Yosida function calculated for BCS value  $2\Delta/k_{\text{B}}T_{\text{c}} = 3.53$  is added as a blue curve for comparison. We note that obtained superconducting ratio strongly depends on the estimated chemical shift  $\sigma_{\text{O}}$ . This method is thus not appropriate for determining  $2\Delta/k_{\text{B}}T_{\text{c}}$ .

are obtained using an average  $T_{\text{c}}$  of  $\sim 30$  K for  $A_3\text{C}_{60}$ . In our case the magnetic field used for NMR experiments was smaller than the critical field  $B_0 = 9.4 \text{ T} < B_{\text{Arr}}$  and the lowest measurements temperatures did not go below  $T_{\text{H}}$ . We can, therefore, reliably apply Arrhenius analysis to our relaxation rate measurements for  $T_{\text{c}}/T > T_{\text{c}}/T_{\text{H}} = 1.5$ .

In Fig. 8.5 we plot normalized spin-lattice relaxation rate as a function of the inverse normalized temperature for high-pressure  $\text{Cs}_3\text{C}_{60}$  experiments (Fig. 8.5a) and  $\text{Rb}_x\text{Cs}_{3-x}\text{C}_{60}$  experiments (Fig. 8.5b). Both experiments show that measured data fall on a straight line corresponding to Arrhenius behaviour and isotropic gap. Comparison with a  $T^3$  behaviour, indicated as a dashed-dotted line in Fig. 8.5a, gives much worst agreement with our data. If we now focus on the samples in the under-expanded region ( $P = 14.1$  kbar and  $x = 3$ ) we see that the data correspond to the BCS ratio  $2\Delta/k_{\text{B}}T_{\text{c}} = 3.53$ . The isotropic gap and the BCS superconducting ratio for under-expanded samples is consistent with previous experiments. When we increase sample volume and move towards MIT (for  $P = 1.7$  kbar or  $x = 0.35$ ) our data show that the superconducting gap is still isotropic, however, the superconducting ratio is increased to values  $2\Delta/k_{\text{B}}T_{\text{c}} > 5$ . We note, that the Arrhenius behaviour, as seen from our data, is not limited by  $T_{\text{c}}/T_{\text{H}} = 1.5$  but rather goes to  $T_{\text{c}}/T \simeq 1.2$ . This could be a result of strong damping effects and the absence of H-S coherence peak. Results from all high-pressure  $\text{Cs}_3\text{C}_{60}$  and  $\text{Rb}_x\text{Cs}_{3-x}\text{C}_{60}$  measurements are summarized as a function of the unit-cell volume in Fig. 8.7. As we can see the enhancement of  $2\Delta/k_{\text{B}}T_{\text{c}}$  close to MIT is a general behaviour given by both experiments. The high-pressure experiments, on the other hand, give less scattered results that show BCS values up to the volume  $\sim 760 \text{ \AA}^3$  and for larger volumes a strong monotonic increase to value of more than  $2\Delta/k_{\text{B}}T_{\text{c}} = 5$ . We note that superconducting ratio can be sensitive to the sample quality and the technique used for measuring. However, our high-pressure experiments were for the first time performed by the same technique on the same samples over a larger range on the phase diagram. For this reason the high-pressure results are much more reliable than  $\text{Rb}_x\text{Cs}_{3-x}\text{C}_{60}$  or from previous experiments.

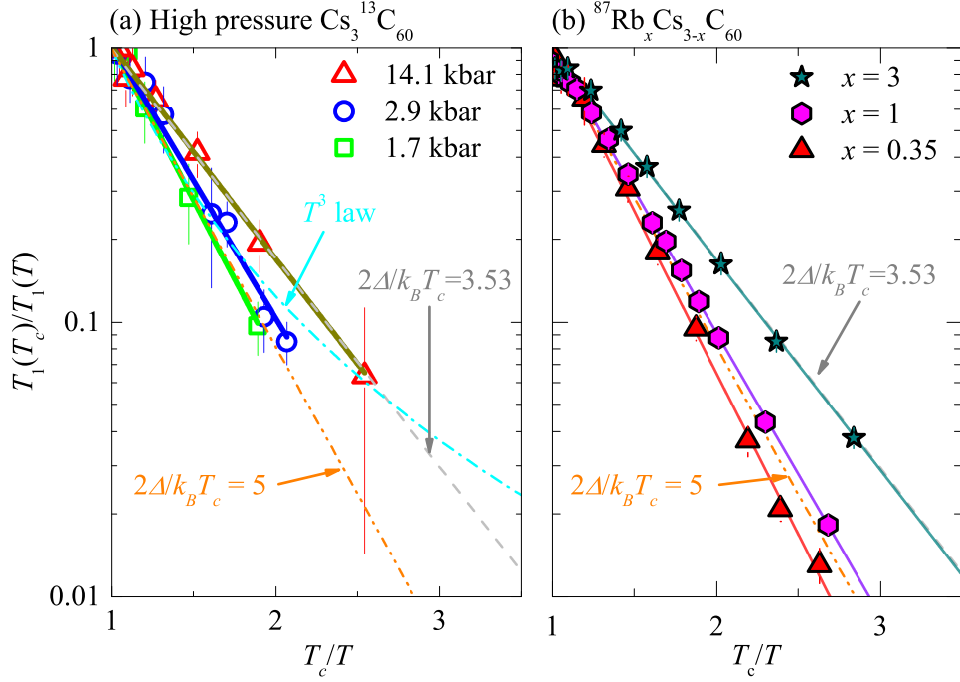


Figure 8.5: The temperature dependence of the normalized spin-lattice relaxation rates in the superconducting state for (a) selected pressures in high-pressure  $^{13}\text{C}$  NMR experiments and (b) selected  $^{87}\text{Rb}$  NMR measurements on  $\text{Rb}_x\text{Cs}_{3-x}\text{C}_{60}$ . The gray dashed line represent a BCS result of  $2\Delta/k_{\text{B}}T_c = 3.53$ , orange dash-dot-dotted line represent result of  $2\Delta/k_{\text{B}}T_c = 5$  and cyan dash-dotted line represent a result of  $d$ -wave power law  $T^3$ .

We also checked if enhancement of the superconducting ratio is an experimental artefact coming from other effects not related to the coupling strength. An effect known to distort spin-lattice relaxation rate in the superconducting state are as discussed above the magnetic field, and various broadening mechanisms either from strong electron-phonon or electron-electron interaction [91]. We tested these effects in a simplified model, where the superconducting gap function contains imaginary term ( $\Delta_2$ ) to account for damping ( $\Delta = \Delta_1 + i\Delta_2$ ) or an inclusion of an additional imaginary term ( $i\Gamma$ ) in the superconducting density of states (Eq. 3.96) accounting for the short lifetime effects due to scattering of electrons [91] (Fig. 8.6).

$$N_{\text{D}}(E, T, \Gamma) = N(E) \text{Re} \left\{ \frac{E + i\Gamma}{\sqrt{(E + i\Gamma)^2 - \Delta(T)^2}} \right\}. \quad (8.1)$$

This model was argued not to be exact where the imaginary gap function ( $\Delta = \Delta_1 + i\Delta_2$ ) should be used instead [170]. Nevertheless, we tested this effect. All tests including various temperature dependences expected for  $i\Gamma$  and  $\Delta_2$  [91] show that  $2\Delta/k_{\text{B}}T_c$  is decreasing when increasing either  $i\Gamma$  or  $\Delta_2$  (Fig. 8.6). We, therefore, conclude that the measured enhancement of  $2\Delta/k_{\text{B}}T_c$  is indeed due to the enhanced coupling strength.

The enhancement of  $2\Delta/k_{\text{B}}T_c$  in the over-expanded region is surprising and cannot be rationalized within the weak-coupling standard BCS theory. However, the maximal value,  $2\Delta/k_{\text{B}}T_c \approx 5$ , could be obtained for the strong electron-phonon coupling according to Eq. 2.15

$$\frac{2\Delta}{k_{\text{B}}T_c} = 3.53 \left[ 1 + 12.5 \left( \frac{T_c}{\omega_{\text{ln}}} \right)^2 \ln \left( \frac{\omega_{\text{ln}}}{2T_c} \right) \right],$$

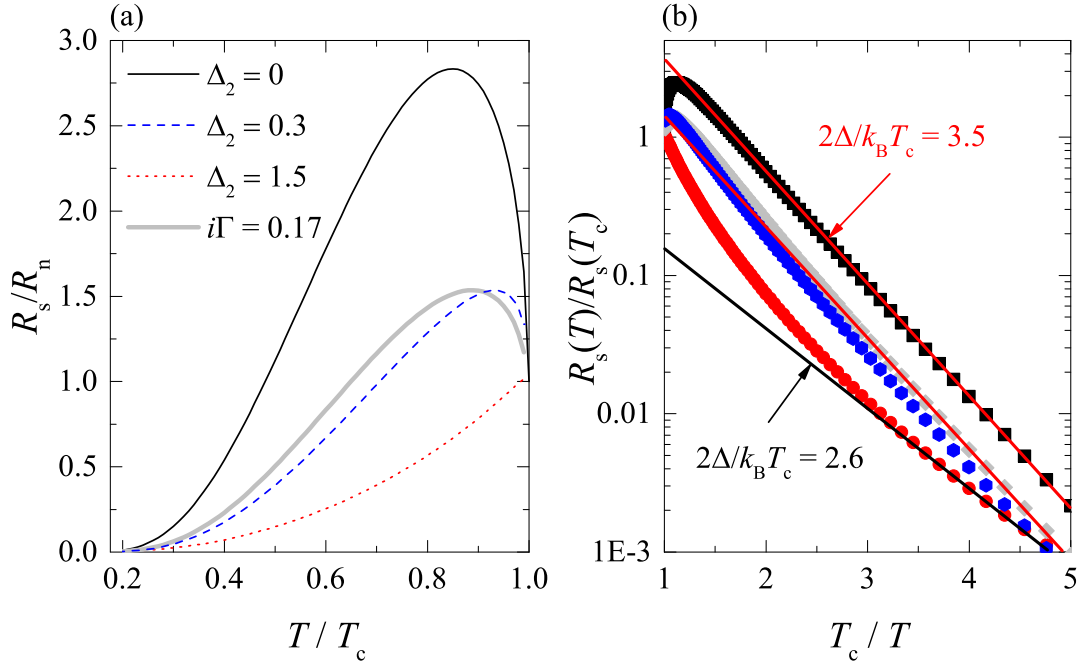


Figure 8.6: (a) Calculated spin-lattice relaxation rate using Eq. 3.96 and  $2\Delta/k_B T_c = 3.5$  in order to simulate damped Hebel-Slichter peak. Solid black curve corresponds to BCS H-S peak without damping. Blue dashed and red dotted curves show damped H-S peak with  $\Delta_2 = 0.3$  and  $\Delta_2 = 1.5$ , respectively. For comparison damping from Eq.8.1 and  $\Gamma = 0.17$  is shown in thick gray curve. (b) Data from (a) presented in Slichter plot. It can be seen that strong damping would result in a smaller  $2\Delta/k_B T_c$  as obtained by fitting with Arrhenius law (Eq. 3.98).

but would require optical phonons ( $\sim 100 \text{ cm}^{-1}$ ) to take part in the superconducting pairing mechanism [5, 7]. This is, however, less likely since several experiments point towards intra-molecular phonons [5].

## 8.4 Conclusions

In this chapter we studied three different superconducting parameters of  $A_3C_{60}$  close to the MIT: the evolution of  $T_c$ , H-S coherence peak, and the superconducting ratio  $2\Delta/k_B T_c$  as a function of unit-cell volume.

The study of H-S peak shows that it is strongly damped in the magnetic field used in our experiments. Nevertheless, it can still be observed for under-expanded compounds as a delayed suppression of  $1/T_1 T$  below  $T_c$ . When approaching MIT the H-S peak becomes additionally damped until it completely vanishes at volumes closest to the MIT. We have shown that this additional damping is most probably a consequence of strong electron-electron correlations as has been predicted by self-consistent Eliashberg-Nambu calculations [90] for  $A_3C_{60}$ . The presence of strong electron correlations in the superconducting state is in agreement with strongly enhanced spin susceptibility measured by  $1/T_1 T$  just above  $T_c$  as a function of unit-cell volume (Sec. 7.3). These observations alone are not compatible with the BCS framework, where strong electron correlations are known to compete with superconducting pairing, yielding a smaller  $T_c$  when correlations are present [5, 62].

We have shown that the non-monotonic behaviour of  $T_c$  and enhanced superconducting ratio,  $2\Delta/k_B T_c$  close to MIT are also not compatible with the standard weak-coupling

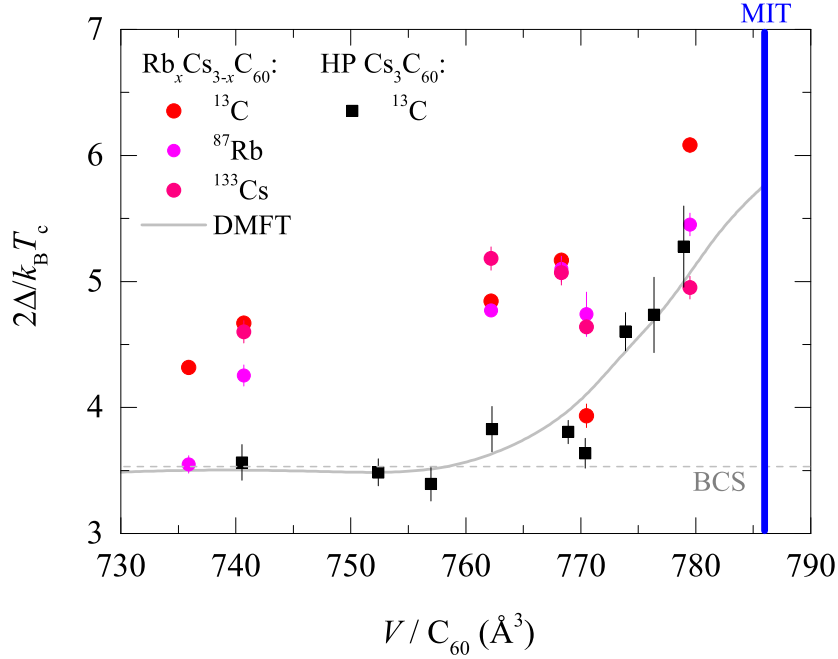


Figure 8.7: Summary of  $\Delta T_c$  as a function of unit-cell volume obtained by high pressure  $^{13}\text{C}$  NMR measurements on  $\text{Cs}_3\text{C}_{60}$  (black squares) and  $^{13}\text{C}$ ,  $^{133}\text{Cs}$ , and  $^{87}\text{Rb}$  NMR measurements on  $\text{Rb}_x\text{Cs}_{3-x}\text{C}_{60}$  samples (coloured circles). The BCS value is depicted by gray dashed line and the DMFT calculated value by solid gray line (Capone *et al.* unpublished.)

BCS theory. However, they could be in principle explained by the extended BCS, the Migdal-Eliashberg theory. As the superconducting properties in the under-expanded region agree with the weak-coupling BCS theory the observed properties close to MIT require strong coupling that is possible only with optical phonons to take part in the superconducting pairing mechanism. However strange that the relevant phonon modes would be suddenly changed at a certain  $N(E_F)$  within Migdal-Eliashberg theory, let us discuss the presence of the optical phonons from the experimental point of view.

Optical phonons are intermolecular vibrations between alkali ions and  $\text{C}_{60}$  ions. The optical phonon frequency would depend on the mass of both objects. First, let us note that within the experimental uncertainty no isotope effect with respect to alkali atoms has been observed in  $A_3\text{C}_{60}$  [171, 172]. Furthermore, the superconducting border in the phase diagram seems to be a universal function of the  $V$  and does not depend on the alkali atom dopants. If optical phonons would be important,  $T_c$  would depend on the optical phonon frequency (Eq. 2.11) and consequently on the mass of alkali atoms. In the simplest model of two body vibration ( $A\text{-C}_{60}$ ) the frequency in case of  $A = \text{Rb}$  ion would be 20% higher than in case of  $A = \text{Cs}$ . This would mean that  $T_c$  of  $\text{Cs}_3\text{C}_{60}$  would be cca. 6 K smaller when pressed to volumes of  $\text{Rb}_3\text{C}_{60}$  than that of  $\text{Rb}_3\text{C}_{60}$ . However, according to our measurements,  $T_c$  of  $\text{Rb}_3\text{C}_{60}$  and  $\text{Cs}_3\text{C}_{60}$  under pressure are the same within the experimental error (Fig. 8.1). This unambiguously rule out optical phonons as the bosons that mediate superconducting pairing.

The Migdal-Eliashberg theory could in principle explain the superconducting parameters in the under-expanded region, but it would largely fail to do so on the whole phase diagram. We stress that this has been argued before from the theoretical point of view. Namely, the Migdal theorem is valid only for  $\omega_{\text{ph}} \ll W$ , Coulomb repulsion is represented by a single effective parameter  $\mu^*$ , and the approximate treatment of the electron-phonon interaction neglects JT effect which has been recognized as an important effect in alkali-

doped fullerenes [25]. We now conclude that  $A_3C_{60}$  family cannot be correctly explained by the BCS framework and thus this materials show *unconventional superconductivity*.

The failure to describe our NMR data within BCS formalism prompt us to use DMFT where electron-phonon and electron-electron interaction are considered on equal grounds together with the intramolecular JT phonons and the Hund's rule exchange [62]. In contrast to the BCS formalism DMFT correctly reproduces the dome-shape structure of the superconducting part of the phase diagram, gives a better agreement with our  $1/T_1T$  data just above  $T_c$  and agrees surprisingly well with  $2\Delta/k_B T_c$  measured by high-pressure NMR experiment. Having several advantages over Migdal-Eliashberg theory, DMFT is a local theory and thus cannot precisely treat  $\vec{q}$  dependent effects, e.g., the antiferromagnetic spin fluctuations in the normal state and the anisotropy of the superconducting gap function. Nevertheless, DMFT theory seems to consider the important properties relevant to  $A_3C_{60}$  family.

Finally we note, that all our measured superconducting properties start to deviate away from the BCS predictions at the superconducting dome maximum,  $V_{\max} \sim 760 \text{ \AA}^3$ , where at the same time our results in the normal state suggest that JT effect is present also in the metallic state and spin susceptibility below  $T_{\text{MIT}}$  resembles pseudogap behaviour. These experimental observations are also in agreement with the strongly correlated superconductivity proposed by M. Capone, *et al.* [62]. DMFT results show that Fermi-liquid behaviour is present far from MIT, however, when closing the MIT a proximity to quantum critical point at  $V_{\max}$  would change this behaviour to a non-Fermi liquid where also pseudogap is expected [62]. So far, the agreement with DMFT study is surprisingly good, however, more experimental results and quantitative calculations are still needed in order to fully accept this theory as a theory of superconducting of  $A_3C_{60}$ .

# 9 Discussion

The main experimental findings of this thesis are

- $A_3C_{60}$  family has strongly correlated electrons in the normal and superconducting phase. Its effects are Mott-insulating phase and related Curie-Weiss spin susceptibility (Fig. 9.1e), enhanced spin susceptibility close to MIT in the metallic phase, and suppression of H-S coherence peak in the spin-lattice relaxation rate measured in the superconducting phase (Fig. 9.1b,f) close to MIT. Due to strong electron correlations even small macroscopic structural deformations lead to an insulating ground state.
- Merohedral or substitutional disorder have no major impact on the electronic and magnetic properties of  $A_3C_{60}$ . However, they are important on the local scale. The mysterious T' line observed in the alkali-metal NMR spectra comes from a special configuration of neighbouring  $C_{60}$  molecular merohedral orientations. We argue that  $C_{60}^{3-}$  molecules possess strong ring currents.
- JT effect is present in the Mott-insulating phase as well as in the metallic phase close to MIT (inset to Fig. 9.1d). JT dynamics is slowing down with decreasing temperature on the NMR timescale (100 MHz).
- MIT transition is of the second order over the entire measured phase diagram (Fig. 9.1d). There is no direct proof of the phase coexistence.
- Antiferromagnetic spin fluctuations in the metallic phase can be observed only indirectly by Korringa phenomenological factor. We have no definite proof of its existence.
- Static and dynamic local, as well as, static uniform spin susceptibility have equivalent temperature dependences.
- Spin-lattice relaxation rate close to MIT exhibits pseudogap-like behaviour (Fig. 9.1e).
- $A_3C_{60}$  are *unconventional superconductors* that cannot be explained correctly by the BCS framework. Their coupling strength enhances when approaching MIT (Fig. 9.1c,g).

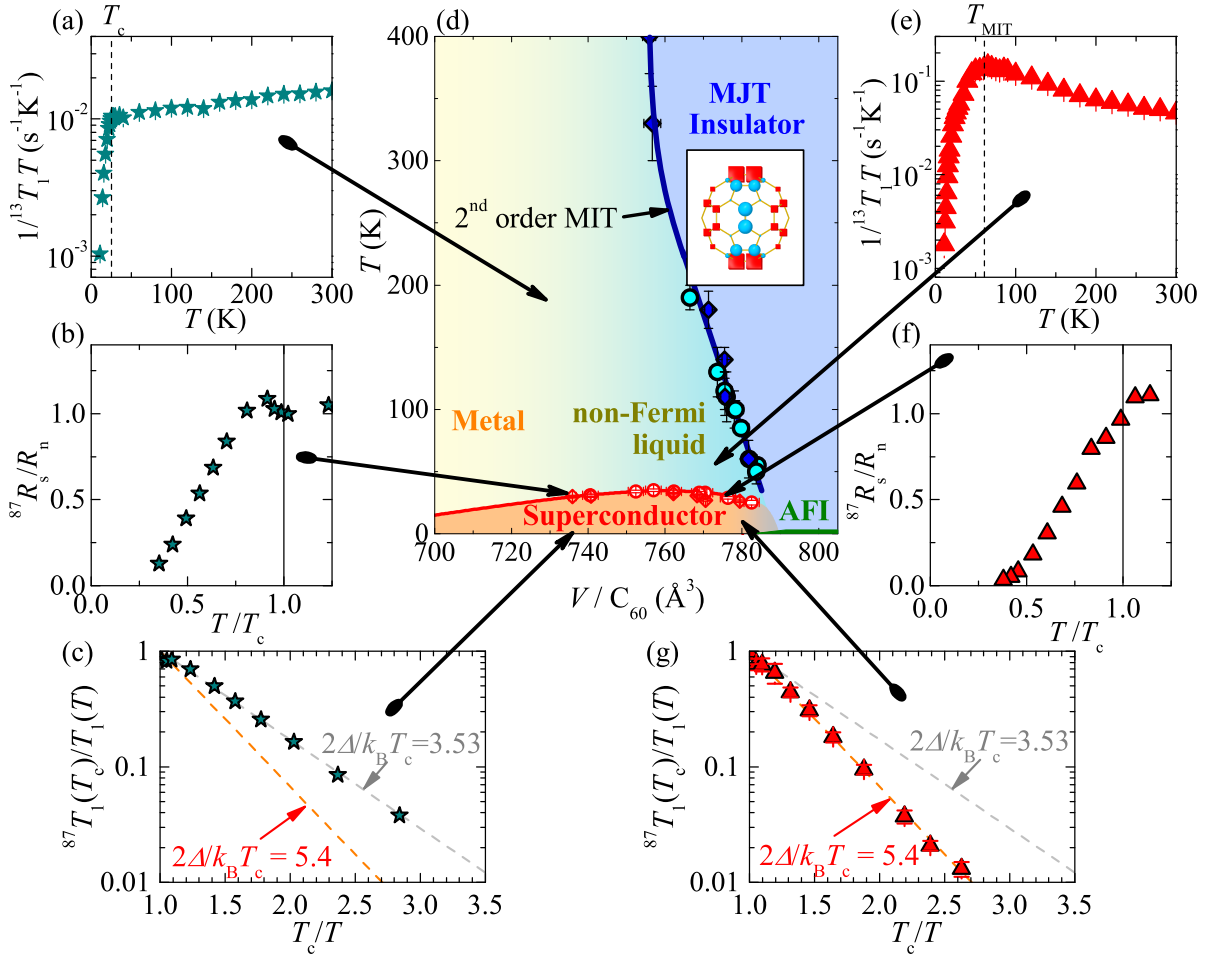


Figure 9.1: Illustration of main experimental findings showing a  $A_3C_{60}$  phase diagram (d) with selected temperature dependent quantities in the under-expanded region (left-hand side) and the over-expanded region (right-hand side). Presented quantities are (a,e)  $^{13}\text{C}$  NMR spin-lattice relaxation rate divided by temperature, (b,f) normalized  $^{87}\text{Rb}$  spin-lattice relaxation rates, and (c,g) normalized  $^{87}\text{Rb}$  spin-lattice relaxation rate as a function of normalized inverse temperature. Inset to (g) shows a typical JT distorted  $C_{60}$  molecules.

In this chapter we will discuss the presented main experimental properties of  $A_3C_{60}$  superconductors in connection with the other unconventional and light elements superconductors. We will search for general properties of unconventional superconductors.

## 9.1 Comparison to other unconventional superconductors

Unconventional superconductors in contrast to standard superconductors cannot be described by the BCS framework, either by standard weak-coupling BCS theory or its extensions like the Migdal-Eliashberg theory. In practice, unconventional superconductors differ in at least one of several BCS properties: phonon-driven pairing mechanism, isotropic superconducting gap function, strongly screened electron-electron interaction, absence of magnetic interactions, and a Fermi-liquid metallic state above  $T_c$ .

The archetypal family of unconventional superconductors are the high- $T_c$  cuprates. Soon after the discovery by Bednorz and Müller [57] the cuprates received much attention

mostly due to their unexpectedly high  $T_c$  which holds the record even today of  $T_c \simeq 133$  K at ambient pressure [21]. Extensive scientific work on these materials showed that they are indeed of unconventional nature that differ in most of the above states properties of standard superconductors. High- $T_c$  cuprates are layered two dimensional system with a single relevant band near the Fermi level. A general consensus is that they have strongly anisotropic superconducting gap function most probably with nodal points consistent with a  $d$ -wave symmetry [173]. Even-though the origin of the pairing mechanism is still contentious, it is believed that it comes from the coupling to the antiferromagnetic spin fluctuations, which is responsible for  $d$ -wave symmetry, however, the coupling to phonons can not be *apriori* excluded as the role of JT effect and associated structural instabilities continue to be observed in various experiments [174, 175]. In cuprates the controlling parameter was found to be the level of doping or the carrier concentrations. By doping the antiferromagnetic insulating ground state of a parent compound appears at lower Néel temperatures until it vanishes or goes directly to the superconducting state. The gradual emergence of superconducting phase upon doping reaches a maximum at a critical doping level and gradually vanishes again at higher doping levels (Fig. 9.2a). Proximity to the magnetically ordered insulating state and a non-monotonic behaviour of  $T_c$  are all in odds with the BCS framework showing that strong electronic and magnetic interactions are important properties of the unconventional cuprate superconductors. Other experimental evidences that can be understood in this view are the localizations of electrons for low doping, the absence of the H-S peak, enhanced superconducting ratio observed, for examples, by the Knight shift in the superconducting state [176]. In addition, the normal state above the superconducting dome show peculiar properties like pseudogap behaviour in the under-doped region and strange/bad metal properties directly above the maximum of the superconducting pocket (Fig. 9.2a). The later is being associated with the quantum fluctuations arising from the quantum critical point below the dome maximum [177]

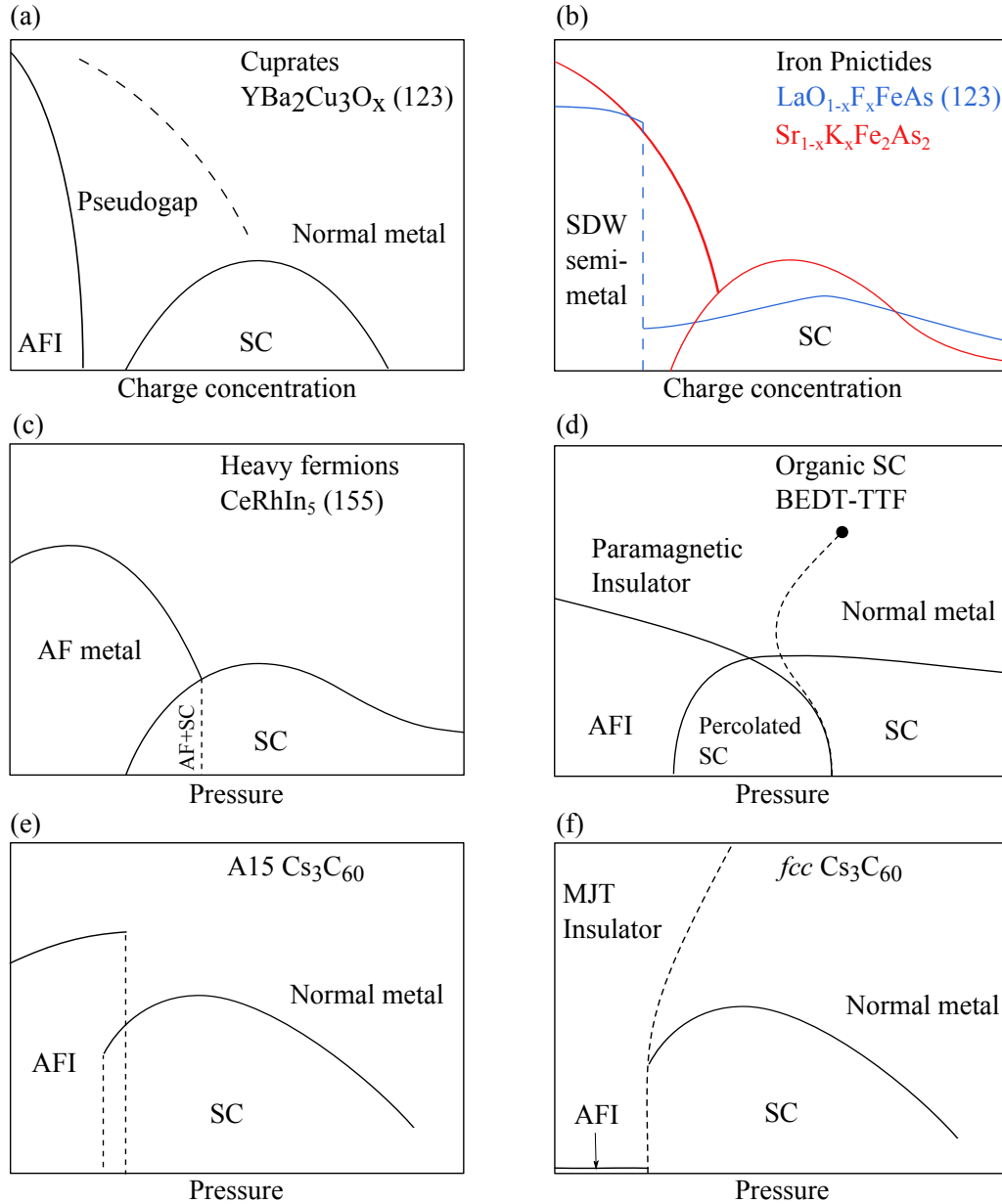


Figure 9.2: Phase diagrams of several superconducting families: (a) cuprates, (b) iron-pnictides, (c) heavy fermions, (d) BEDT-TTF organic superconductors, (e) A15  $\text{Cs}_3\text{C}_{60}$ , and (f)  $\text{fcc Cs}_3\text{C}_{60}$   $\text{A}_3\text{C}_{60}$ . They all show dome-shaped superconducting region bordering magnetically ordered state. Adapted from [49].

Another family of unconventional superconductors that has been discovered only recently is the family of iron-pnictides. Holding the second place among the highest  $T_c$  superconductors with the maximum of  $T_c = 56$  K [20] ignited an intense research on these materials. Similar to cuprates the iron-pnictides have layered quasi two-dimensional geometry and exhibit magnetically ordered ground state. By changing the doping level magnetically ordered phase (spin density wave or antiferromagnetic state) goes to the superconducting phase, showing a familiar dome-shape behaviour of  $T_c$  (Fig. 9.2c). It has been argued that weak electron-phonon interaction cannot lead to such high  $T_c$  using the BCS theory. A more probable pairing mechanism is believed to originate from the antiferromagnetic spin fluctuations [178]. Although, considerable sensitivity to the crystal symmetry change, which appears just above the magnetically ordered state, could provide an indirect involvement of the phonons in the pairing mechanism [179, 180]. In

contrast to cuprates, iron-pnictides are multi-orbital system, where five orbitals cross the Fermi level. The multi-orbital nature is reflected in the superconducting order parameter that is believed to be of  $s^\pm$ -wave symmetry, i.e., two  $s$ -wave gaps with opposite sign surrounding  $\Gamma$  and  $M$  point in the two dimensional  $\vec{q}$  space. Along the third dimension, which is supposed to show no dispersion for the two dimensional systems, nodal lines in the order parameter have been observed in over-doped region for some materials [181]. This suggests that the order parameter can vary in different parts of the phase diagram, as well as, between different iron-pnictide compounds. We note that recently similar band-structure dependent superconductivity has been proposed for  $A_3C_{60}$  [182]. The presence of strong electron correlations in iron-pnictides is still under debate. On one hand, the metallic ground state of the parent compounds speak against strong electron correlations [179], however, on the other hand, some experiments show that electron correlations are indeed present [183]. It has been argued that the presence of metallic state is possible even with the strong electron correlations when multi-orbital effects and strong Hund's rule exchange interaction is considered [64]. This is similar to the  $A_3C_{60}$  where triple orbital degeneracy has been shown shift MIT to larger values of  $(U/W)_c$  (Sec. 7.2.1). In the NMR spin-lattice relaxation rate iron-pnictides show similar to cuprates a pseudogap-like behaviour [184]. Whether the underlying physics of this behaviour is comparable to that of cuprates is not yet clear. Finally we note, that increasing theoretical and experimental evidence support the presence of a quantum critical point placed between the magnetic and superconducting phases in iron-pnictides [181].

Similar phase diagram containing magnetic phase and dome-shape-like superconducting phase was observed also in other unconventional superconductors like BEDT-TTF<sup>1</sup> superconductors [146] or heavy fermion systems [185] (Fig. 9.2d). Both materials show strong electron correlations effects and the presence of antiferromagnetic spin fluctuations. In addition, in heavy fermions quantum critical fluctuations have been observed [185].

The fullerene superconductors, initially believed to be conventional BCS-type superconductors, exhibit similar phase diagram as other unconventional superconductors (Fig. 9.2b). Despite the fact that the superconducting pairing mechanism is still probably mediated by the intramolecular phonons, we have shown that  $A_3C_{60}$  cannot be explained within the BCS framework and is thus considered to be unconventional. Our measurements indicate that strong electron-electron correlations, that ultimately lead to the electron localization and the Mott-insulating state, cannot be ignored in the superconducting state close to the MIT transition. In addition, we have shown that JT effect, known to couple lattice and spin degrees of freedom, is present in the insulating and metallic phase close to MIT. Being at the border with the antiferromagnetic phase, one would expect to observe antiferromagnetic fluctuations close to the magnetic transition. The fact that we did not directly observe the presence of spin fluctuations could be explained by the strong frustration effects present in the geometrically frustrated *fcc* lattice. It would be interesting to repeat our work on the non-frustrated A15 polymorph and check for antiferromagnetic fluctuations there. Another peculiar and also important observation provided by fullerene superconductors is that superconductivity is rather insensitive to the long range magnetic order as A15 and *fcc* polymorphs both have similar superconducting domes that can be scaled to a universal curve [14]. This suggests that the superconducting mechanism might not be directly related to the magnetism and that magnetism is merely a consequence of other effects, e.g., strong correlations.

---

<sup>1</sup>bis(ethylenedithio)tetrathiafulvalene.

Alkali-doped fullerenes, as a new family of unconventional superconductors, are distinguished by a relatively simple and highly-symmetrical cubic unit cell which allows to control the system by a single parameter, the unit-cell volume ( $V$ ). Since there is no need for doping, no additional disorder is introduced which makes fulleride superconductors an ideal model system for studying electron correlations and unconventional superconductivity. For example, as we have shown the suppressed H-S peak observed in  $A_3C_{60}$  is a result of broadening of the superconducting density of states that arises from the energy dependent complex gap function induced by strong electron correlations. Similar effects are expected to occur close to MIT also in other unconventional superconductors, however, due to other effects, like anisotropic gap function or disorder, this cannot be observed directly.

### 9.1.1 Unconventional superconductivity

Common phase diagrams of various unconventional superconductors including  $A_3C_{60}$  imply that there is a general physical law behind all unconventional superconductors. Relevant properties responsible for their common phase diagram could be obtained by searching for the common ones. The number of relevant orbitals is most probably not important for the general behaviour as cuprates are single-band systems, iron pnictides and heavy fermions are non-degenerate multiband systems and fullerenes are degenerate multiband systems. Next, dimensionality of unconventional superconductors is also not important as cuprates, iron pnictides, and BEDT organic superconductors are two or quasi-two dimensional systems while heavy fermions and fullerides are three-dimensional systems. There are speculations that low dimensionality is responsible for the high- $T_c$  of cuprates and iron pnictides, as quantum fluctuations are enhanced in low-dimensional systems, however, this is not a general property of unconventional superconductors. The quantum critical points have been identified for both heavy fermions [186] and fullerene superconductors [62, 149] which is in both case related with the Kondo effect. If these description is valid, additional quantum fluctuations might be present and important for the superconductivity.

Next, let us discuss the role of strong electron correlations. Strong electron correlations have been identified in all unconventional superconductors, cuprates, heavy fermions, organic superconductors, and fullerenes, whereas, in iron-pnictides its strength is not yet clearly understood. Their presence is most directly proved by a Mott-insulating phase bordering metallic phase. This is, in principle, not true for iron-pnictides where the ground state of parent compounds is metallic with commensurate or incommensurate magnetic order. Nevertheless, despite metallic ground state strong correlations might be indeed present [187, 188]. It has been shown that for multiorbital systems Hund's rule exchange interaction can drastically modify the effects of correlations [64]. If electron correlations are directly involved with the unconventional superconductivity their role is not transparent. Having maximum of a superconducting dome distant from the on-set of electron localization implies that there is another relevant energy scale that sets the distance between superconducting maximum and MIT.

Yet another common property is a pseudogap phase. A pseudogap phase was first observed in cuprates and was later due to similar behaviour identified also in pnictides where it is denoted as pseudogap-like phase or in fullerenes where a peculiar drop of spin susceptibility below  $T_{MIT}$  resembles that of a pseudogap. However, we cannot confirm that this is indeed the same phase as in cuprates, since other models could explain observed peculiar behaviour. The theoretical study of strongly correlated superconductivity in

$A_3C_{60}$  suggest that the phase in the over-expanded region, above the dome maximum, has non-Fermi liquid properties since large mass of the quasiparticles reduces the screening of the spin degrees of freedom [62]. Such model could also be relevant for cuprates and iron-pnictides. The non-Fermi liquid phase above the superconducting dome is becoming more frequently associated with the quantum critical point below the superconducting dome. In fullerenes this is within the strongly correlated superconducting theory related to the point where the bandwidth becomes of the same size as the Kondo temperature which is related to the effective intramolecular exchange interaction constant ( $J_{\text{eff}} = J_{\text{Hund}} + J_{\text{JT}}$ ) [62]. According to the theory the exchange interaction also sets the additional degree of freedom that positions the superconducting maximum relative to MIT.

At the end we note that there is yet another property that might be common to all unconventional superconductors, namely the structural instability. In cuprates some believe that JT effect can be relevant for the superconducting pairing mechanism [175]. In iron-pnictides there is a structural phase transition from tetrahedral to octahedral symmetry just above the magnetic transition at low doping levels [179]. In fullerenes the structural instability can be view in terms of dynamic Jahn-Teller effect which spontaneously breaks the symmetry of a molecule and causes a reduction of the net spin from  $S = 3/2$  to  $S = 1/2$ . It would seem the relevance of lattice degrees of freedom cannot be *a priori* excluded.

## 9.2 Comparison to other light-elements superconductors

$A_3C_{60}$  are one of a few superconductors composing of light elements such as carbon. Other light-elements superconductors are graphite intercalated compounds, doped diamonds, BEDT organic superconductors [146], and recently discovered  $\text{MgB}_2$  [19]. The last two are especially interesting as they exhibit unconventional superconducting phase diagram (BEDT organic superconductors) and unexpectedly high- $T_c$  ( $\text{MgB}_2$ ). Apart from containing light and non-toxic elements these materials are interesting as they show magnetic and/or superconducting properties arising from  $s$ - $p$  hybridized orbitals which is a rare occasion, since, strong magnetism and superconductivity normally occur from  $d$  or  $f$  electrons.

The family of BEDT organic superconductors has been widely studied as they are similar to other unconventional superconductors close [146]. The phase diagram of  $\kappa$ -( $\text{ET}$ ) $_2\text{Cu}[\text{N}(\text{CN})_2]\text{Cl}$  has been studied in details using hydrostatic pressure. Their phase diagram consists of paramagnetic insulating, paramagnetic metallic, superconducting, percolated superconducting, and antiferromagnetic insulating phase. The phases are separated with a curved MIT border containing a critical temperature at which the first order phase transition goes into the second order phase transition for higher temperatures. Different slopes of the MIT border have been described by different entropies corresponding to different phases.

BEDT superconductors differ from fullerenes by their quasi two-dimensional triangular structure. NMR measurements on these systems show similar spin-lattice relaxation rate behaviour to that of  $A_3C_{60}$ , following a Curie-Weiss law at high temperatures and a sharp decrease towards metallic value below MIT, followed by the superconducting transition at low temperature [189]. Interestingly, such behaviour is not observed in either the Knight shift or the bulk spin susceptibility. These two show nearly temperature independent susceptibility at high temperatures and gradually suppression below  $T_{\text{MIT}}$ .

Discrepancy between spin-lattice relaxation rates which is proportional to the averaged  $\vec{q}$ -vector dependent dynamic spin susceptibility and the Knight shift proportional to the local spin susceptibility was justified by the emergence antiferromagnetic spin fluctuation peak at a finite  $\vec{q}$  in the dynamic spin susceptibility. Another difference with respect to the fullerenes is the independent spin-lattice relaxation rate just above  $T_c$  as a function of proximity to MIT. In fullerenes this parameter is increasing when closing to the MIT, reflecting the enhancement of a renormalized electron mass. In organic superconductors independent spin susceptibility was rationalized by strong frustration in the Hubbard model [189]. The peculiar drop of  $1/T_1T$  below  $T_{\text{MIT}}$  has been in organic superconductors suggested to be due to a pseudogap, since a concomitant drop of the Knight shift reflects the reduction of  $N(E_F)$  caused by pseudogap. Finally we note that organic superconductors in the superconducting state the show power law behaviour of  $1/T_1 \propto T^3$  consistent with strongly anisotropic gap function possibly of  $d$ -wave symmetry. The presence of antiferromagnetic fluctuations and anisotropic gap function is consistent with the reduced symmetry of these systems. This is probably the largest difference between BEDT and fulleride superconductors.

At the end we briefly comment on the superconducting properties of  $\text{MgB}_2$ . A discovery of high  $T_c = 39$  K [19] came as a surprise since  $\text{MgB}_2$  is expected to be a standard phonon-driven superconductor. It has been found that there are two isotropic  $s$ -wave gaps with different magnitudes denoted by  $\sigma$  and  $\pi$  gaps [190]. There have been several claims that the superconductivity of  $\text{MgB}_2$  is of unconventional nature [191]. However, NMR measurements show that both the Knight shift and the spin-lattice relaxation rates are temperature independent and thus consistent with the Fermi-liquid theory [192]. Interestingly, it has been found that  $\text{MgB}_2$  shows a small H-S peak and enhanced coupling strength measured by the superconducting ratio [193].

The presence of two gaps is a consequence of multi-orbital system similar to the alkali-doped fullerenes. However, the presence of electron correlations and magnetic phase have not yet been observed. This is in contrast to  $A_3C_{60}$  systems and thus we speculate that superconducting mechanism strongly differ from that of  $A_3C_{60}$ .

# 10 Concluding remarks

The subject of this thesis is a study of normal and superconducting properties of molecular superconductors, the alkali-doped fullerenes, close to the metal-to-insulator transition. These materials show the highest superconducting transition temperature among molecular superconductors with the maximum of  $T_c = 38$  K being close to the metal-to-insulator transition. In order to elucidate the nature of normal and superconducting state that yields such high transition temperatures we focus on several different aspects that are believed to be important for these family. These are the role of relevant orbital degeneracy, the importance of  $C_{60}$  molecular distortions related to the Jahn-Teller effect, the role of merohedral and substitutional disorder, the importance of electron correlations, and the properties of superconducting state.

In respect with the importance of orbital degeneracy, we have found that all alkali-doped fullerenes are strongly correlated materials where already small reduction of the cubic symmetry leads to the Mott-insulating ground state. The metallic state is realized despite larger on-site Coulomb repulsion energy compared to the single-electron hopping energy, due to the orbital degeneracy of the half-filled  $t_{1u}$ -derived band. Triple degeneracy allow multiple hopping channels which effectively increase the single-particle bandwidth. However, experiments show that already small crystal symmetry reduction results in the electron localization. Such a strong sensitivity is possible only if strong electron correlations, within the Fermi-liquid theory, renormalise the quasiparticle bandwidth ( $W \rightarrow zW$ ) to such a small value that is comparable to the level splitting induced by the anisotropic crystal field. As a result the orbital degeneracy is lost which leads to the Mott-insulating state state. We used high hydrostatic pressure of 7 kbar at low temperatures in order to increase the bandwidth of face-centred orthorhombic  $MAK_3C_{60}$  compound and to push the system to the metallic state, however, we were unsuccessful. In this process we constructed the MSDT phase diagram, from where it is evident that  $A_3C_{60}$  systems are indeed strongly correlated with an estimated renormalization factor of  $z = 0.2-0.3$ .

In respect to the importance of molecular distortions we have shown that  $C_{60}$  molecules in *fcc*  $A_3C_{60}$  are subject of JT effect. This has been concluded based on the low-spin state observed in insulating alkali-doped fullerenes, as well as, from enhanced broadening of the high-resolution  $^{133}\text{Cs}$  NMR spectra on  $Cs_3C_{60}$  upon lowering the temperature. Our findings are in agreement with recent infrared measurements where JT distortions were observed in  $Cs_3C_{60}$ . In addition, we have shown that JT dynamics is slowing down with decreasing temperature observed on the NMR timescale of  $\sim 100$  MHz. This suggest that JT becomes static at very low temperatures. Furthermore, high-resolution  $^{133}\text{Cs}$  NMR measurements on  $Rb_{0.5}Cs_{2.5}C_{60}$  compound show that JT effect survives also in the metallic state close to MIT. Apart from JT distortion, we have shown that steric effects can cause  $C_{60}$  deformations that can even prevail over the JT effect. This effect was found in  $MAK_3C_{60}$  by high-pressure EPR measurements and electronic structure calculation

study.

In respect with the importance of structural disorder, we have found that merohedral and substitutional disorder have negligible effect on the macroscopic electronic and magnetic properties. These effects are estimated to be of the order of a few percent. Merohedral disorder can be responsible for finite Néel temperature of strongly frustrated *fcc* crystal structure. By comparing the Néel temperature with the Weiss temperature an upper value of disorder effect can be obtained. Effect of substitutional disorder can be estimated from a relative reduction of the superconducting transition temperature in  $\text{Rb}_x\text{Cs}_{3-x}\text{C}_{60}$  samples which contain substitutional disorder. On the other hand, locally, on the nanoscopic scale, disorder has more drastic effects. We have found that fine-structure of high-resolution  $^{133}\text{Cs}$  NMR spectra can be quantitatively explained by different merohedral orientation configurations surrounding  $\text{Cs}^+$  ion in the interstitial site. In this model mysterious T' spectra line corresponds to a highly symmetric configuration of merohedral orientations of surrounding  $\text{C}_{60}$  molecules. In addition, we argue that large spectral shifts separating fine-structure lines come from the non-negligible ring currents on  $\text{C}_{60}^{3-}$  ions.

In respect to the importance of electron correlations we have shown that spin susceptibility exhibit peculiar behaviour at temperatures below  $T_{\text{MIT}}$  where it resembled pseudogap-like behaviour. Interestingly, similar temperature dependence of spin susceptibility can be obtained by different techniques: SQUID magnetization measurements, the Knight shift, and the spin-lattice relaxation rate for all sites and nuclei. This observation suggest that no antiferromagnetic fluctuations are present in *fcc* samples. Indirect proof of antiferromagnetic spin fluctuations have been obtained by the Korringa phenomenological factor. However, we note that Korringa analysis requires information about the temperature dependence of the Knight shift, which we obtained using oversimplified model. This model assumes temperature independent hyperfine coupling constant and allows chemical shift to be temperature dependent. As a result the obtained chemical shift is strongly temperature dependent which is uncommon. We argue that this dependence comes from the non-negligible ring currents on the surface of  $\text{C}_{60}^{3-}$  ions that are also responsible for the fine-structure spectral shifts controlled by the merohedral configurations of neighbouring  $\text{C}_{60}$  molecules. We note that in principle both hyperfine coupling constant and the chemical shift could be temperature dependent. Also, a two fluid model proposed for heavy fermion systems might be applicable, but less likely. In addition, we have shown that MIT border is tilted towards smaller volumes. Quantitative analysis suggest that in the insulating state and additional source of entropy is required. This can be attributed to the JT effect. Our measurements show that the MIT border corresponds to the second order phase transition down to  $\sim 50$  K. Finally, we note that spin susceptibility just above superconducting transition temperature is monotonically increasing when approaching MIT with a drastic enhancement that cannot be explained by the non-interacting electronic structure calculations.

In respect to the superconductivity of  $A_3\text{C}_{60}$  family we have shown that it cannot be correctly described by the BCS framework and thus it is considered to be unconventional. We have measured the evolution of superconducting transition temperature, the presence of Hebel-Slichter coherence peak and the superconducting ratio,  $2\Delta/kBT_c$  as a function of the unit-cell volume. The suppression of Hebel-Slichter peak close to metal-to-insulator transition can only be accounted for the presence of strong electron correlations. Together with measured enhancement of spin susceptibility just above  $T_c$  we can conclude that strong electron correlations are present in the superconducting state. In addition, we have shown that superconducting ratio having BCS value of 3.53 in the under-expanded

region becomes enhanced (up to  $\sim 5$ ) close to MIT. Such enhancement could be explained in the strong coupling limit of BCS framework, but would require optical phonons to participate in the pairing mechanism. At the same time the non-monotonic behaviour of  $T_c$  as a function of the unit-cell volume could also be explained by the BCS framework, however, it would again require optical phonons close to MIT. We have shown, from the experimental point of view, that optical phonons cannot be present and thus the BCS framework fails to describe  $A_3C_{60}$  superconductivity. At the same time dynamical mean field theory results computed for  $A_3C_{60}$  are in much better agreement with the experimental observations. DMFT predicts a non-monotonic behaviour of  $T_c$  as a function of unit-cell volume. Its spin susceptibility is in good agreement with the enhanced spin-lattice relaxation rate or the spin susceptibility just above  $T_c$  in vicinity of MIT. An finally, superconducting ratio predicted by DMFT is in excellent agreement with our measured data.

Despite being a mean field theory where spatial degrees of freedom are not considered DMFT is in surprisingly good agreement with our experimental data. It is, therefore, the best candidate to explain  $A_3C_{60}$  superconductivity. However, to accept DMFT as a valid theory of superconductivity of  $A_3C_{60}$ , more quantitative computations and detailed experiments have to be performed. One such experiment that would unambiguously test the limits of DMFT is applying even higher pressures to  $MAK_3C_{60}$  in order to push it over to the metallic side. We have shown that  $MAK_3C_{60}$  have very strong steric effects that dominate over JT effect. If JT has indeed a central role in the superconductivity of  $A_3C_{60}$ , as is assumed in DMFT, then at such high pressures superconductivity would not be observed. If this is not the case, other effects are important that are not considered within DMFT.

Comparison of  $A_3C_{60}$  to other unconventional superconductors yields several common characteristics that might be central to all unconventional superconductors with the characteristic phase diagram. One of such characteristic is strong electron correlations, although its role is not completely clear and it can as well be indirectly related to the superconductivity as is suggested for iron-pnictides. The presence of antiferromagnetic spin fluctuations or quantum fluctuations arising from the quantum critical point is another characteristics. The former case is believed to be relevant for cuprates, iron-pnictides, and BEDT organic superconductors where enhanced antiferromagnetic fluctuations come from reduced dimensionality of a system. The later are associated more with heavy fermions and  $A_3C_{60}$  since both are expected to show Kondo physics within their theoretical models. These are a few selected common characteristics of the unconventional superconductors that might be relevant and considered in the future general theory of unconventional superconductors.



# A High Pressure Cells

## A.1 High Pressure EPR cell

In Chapter 3 we introduced the working principle of the high-pressure EPR cell. In this appendix we give technical description and the construction details of the high-pressure EPR clamped-type cell. At the end a discussion about coupling between microwave source and the dielectric resonator is given.

### A.1.1 Construction details

The high-pressure clamped-type cell for EPR measurements was constructed to operate in magnetic fields up to 1.5 T and reach high hydrostatic pressures. For this reason special materials were chosen for the construction of the cell. Most of the cell's parts are made out of non-magnetic hardened BeCu with large Be content (cca. 2%), hardness of 32 HRC and tensile strength of cca. 1.2 GPa. Different material was used only for piston since it is moving through the body during the loading and unloading procedure. During this procedure piston must not expanded and get stuck at the highest pressures. To avoid this problems we used non-magnetic wolfram carbide (WC) with much higher hardness of 77 HRC and elastic modulus of 600 GPa for piston.

High-pressure EPR cell (Fig. A.1) was designed to fit into an Oxford CF935 Cryostat with the inner diameter of 43 mm. For this reason the cell's outer diameter was set to 36 mm. The inner diameter was determined by an analysis of the infinitely long cylinder with outer and inter radius  $r_o$  and  $r_i$ , respectively. The maximum pressure that a cylinder with yield strength of  $\sigma_y$  can withstand is [194]

$$p_{\max} = \frac{\sigma_y}{2} \frac{\alpha^2 - 1}{\alpha^2}, \quad \alpha = \frac{r_o}{r_i}. \quad (\text{A.1})$$

Since the maximal stress is at the inner wall ( $r_i$ ), large values of outer diameter do not considerably increase the cylinder performance. An empirical limit, which we used in our design, is  $r_o/r_i = 3$ , where the maximal pressure is around 90% of the theoretical limit ( $\sigma_y/2$ ). In reality, the actual high-pressure cell is not an infinite cylinder, but rather a short one, resembling a spherical geometry. Such geometry naturally withstands larger loading pressures. The maximal pressure could be further increased by the autofrettage procedure. During this procedure the high-pressure cell is slowly and repeatedly exposed to high pressures which plastically deforms the most inner layers of the body. Effectively, these structure deformations cause a redistribution of the stress from the inner layers to a large volume of the cell and consequently increase the maximum achievable pressures even by a factor of  $\sim 1.6$  [194].

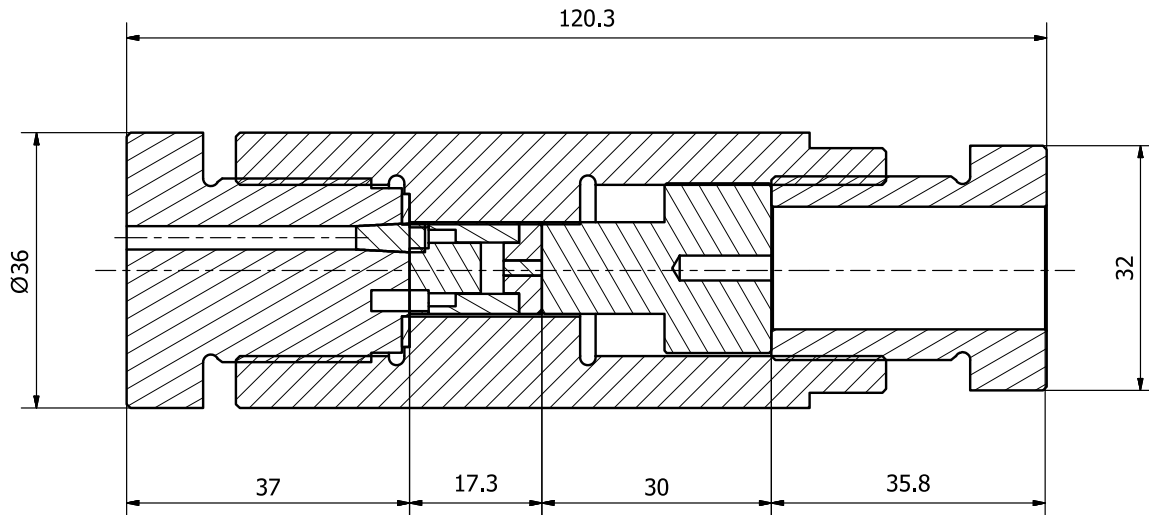


Figure A.1: Overview of assembled high-pressure EPR cell in sectional view.

Initially, the body (Fig. A.2), the piston (Fig. A.3b) and the anti-extrusion ring (Fig. A.3d) were made with smaller diameter  $d = 11.5$  mm, and the bottom plug was made without any holes. This piston was made out of cheaper hard magnetic alloy. During the autofrettage procedure the indium metal was used as a pressure transmitting medium inside the cell. The cell was then slowly pressurised and released (20 min per cycle) twelve times, and each time the maximum pressure was increased for 0.1 GPa. The procedure was stopped at 1.1 GPa and consequently the limit for the highest pressure used in experiments was set to 1 GPa. After the autofrettage procedure the inner hole of the body was honed to diameter of  $d = 12.05$  mm with less than 0.01 mm precision. The WC piston (Fig. A.3b) and the auto-extrusion rings (Fig. A.3d) were then made with the diameter of  $d = 12$  mm and tolerance of 0.01 mm.

The leakage of the pressure transmitting medium from the central chamber was suppressed by the copper washer (Fig. A.3e) placed between the bottom screw and the body. The washer was previously heated to very high temperatures until it irradiated visible red light and after this it was rapidly cooled in the water. With this procedure the copper became "softer" and better filled any remaining holes. At the piston site the central chamber was sealed with an anti-extrusion ring (Fig. A.3d). Under pressure this ring seals the remaining small openings between the piston and the body.

In the final step the holes were drilled in the bottom screw (Fig. A.4a). The one going all the way through the screw was used for the coaxial line waveguide which was made with ceramic ( $\text{ZrO}_2$ ) conical cork (Fig. A.4b), a quartz tube (with diameter of 3 mm and length 30 mm), and 1 mm thick electrical wire. All parts were glued together with the special low-temperature two-component epoxy resin, Stycast 1266AB from Emerson & Cuming. In the outer part of the bottom screw the electrical wire was mounted to a SMA connector. In the inner part the electrical wire was formed in the shape of an antenna (see Sec. A.1.2). The ceramic conical cork was introduced to suppress the leakage of the pressure transmitting medium through the cracks in the waveguide.

To obtain high hydrostatic pressure conditions in the central cavity Teflon holder and pressure transmitting medium was used. The Teflon holder for dielectric resonator and the sample constitutes of 5 pieces (Fig. A.5). The bottom part (Fig. A.5a) has two holes that fit exactly onto the two holes at the top of the bottom screw. The hole at the 4.3 mm distance from the center contains the head of ceramic cork and provides access

for the antenna. The second hole is positioned on top of the second hole of the screw by a small Teflon rod. The middle part of the Teflon holder (Fig. A.5b) fits to the bottom part of the holder in such a way that the larger opening (diameter of 10 mm) is facing two holes of the bottom Teflon part and the bottom screw. Between the bottom and the middle Teflon holder there is 3.5 mm high tube-shape space where L-shaped antenna is positioned. On the top of the bottom part, a 6.7 mm diameter hole is produced by both the bottom and the middle holder together. In this hole the dielectric resonator and the sample is placed. This hole is closed with the top Teflon holder (Fig. A.5d). After pouring pressure transmitting medium into the chamber and evacuating the remaining air the cover is sealed with a small Teflon cork (Fig. A.5c).

In our high-pressure EPR experiments the transmitting medium was a 1:1 mixture of Fluorinert FC70 and FC770 oils from 3M company. This combination yields hydrostatic conditions up to cca. 1 GPa [101] and in addition has no EPR signal. The dielectric constant of the pressure transmitting medium (1.9) is similar to that of Teflon (2.0–2.1) which simplifies the cavity's electromagnetic eigenmode analysis.

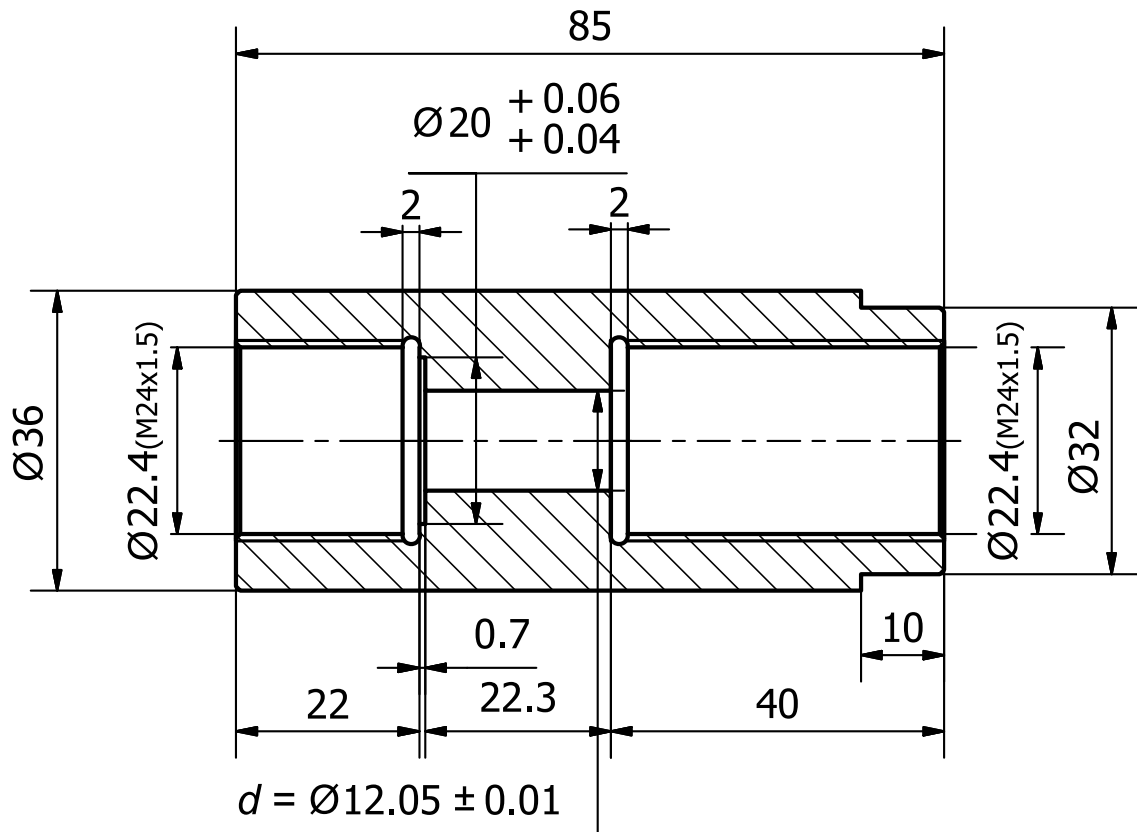


Figure A.2: Drawing of the body of the high-pressure EPR cell. The material used for the body was BeCu.

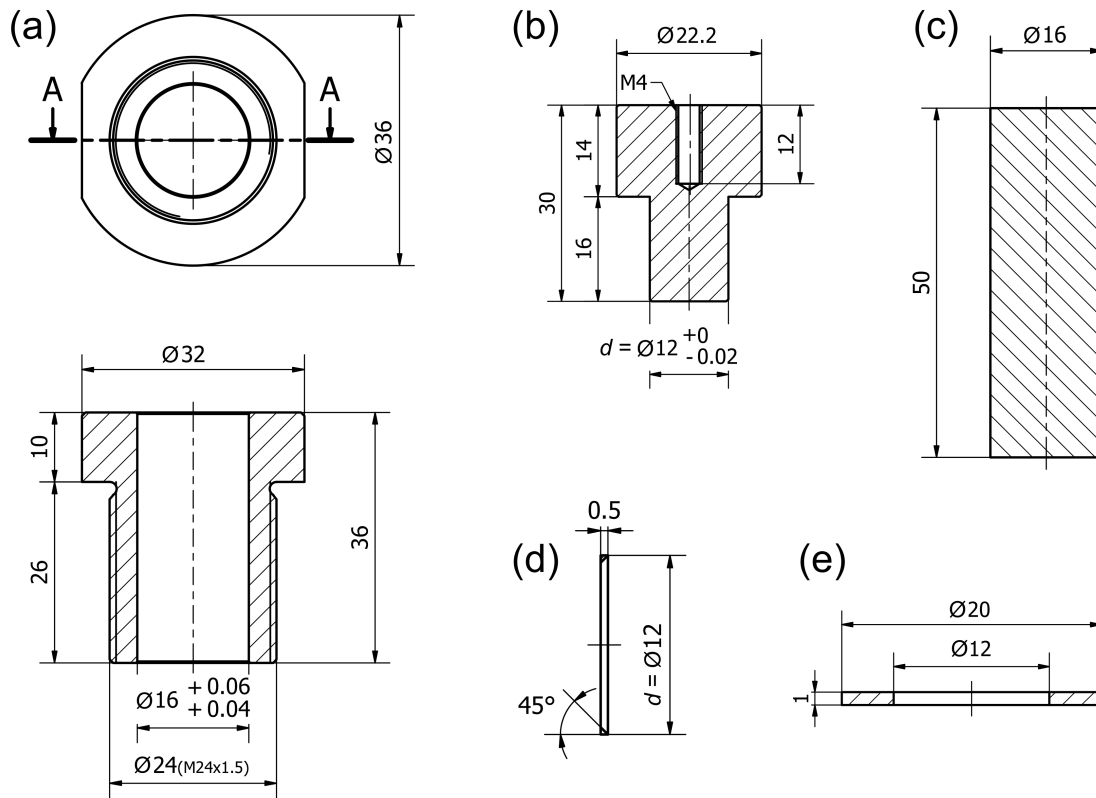


Figure A.3: Drawings of other pieces of the high-pressure EPR cell: (a) the locknut represented in the top view (top) and sectional view (bottom), (b) piston in sectional view, (c) plunger in sectional view, (d) anti-extrusion ring in sectional view, and (e) copper washer in sectional view. Pieces (d) and (e) have larger scale ratios than other pieces.

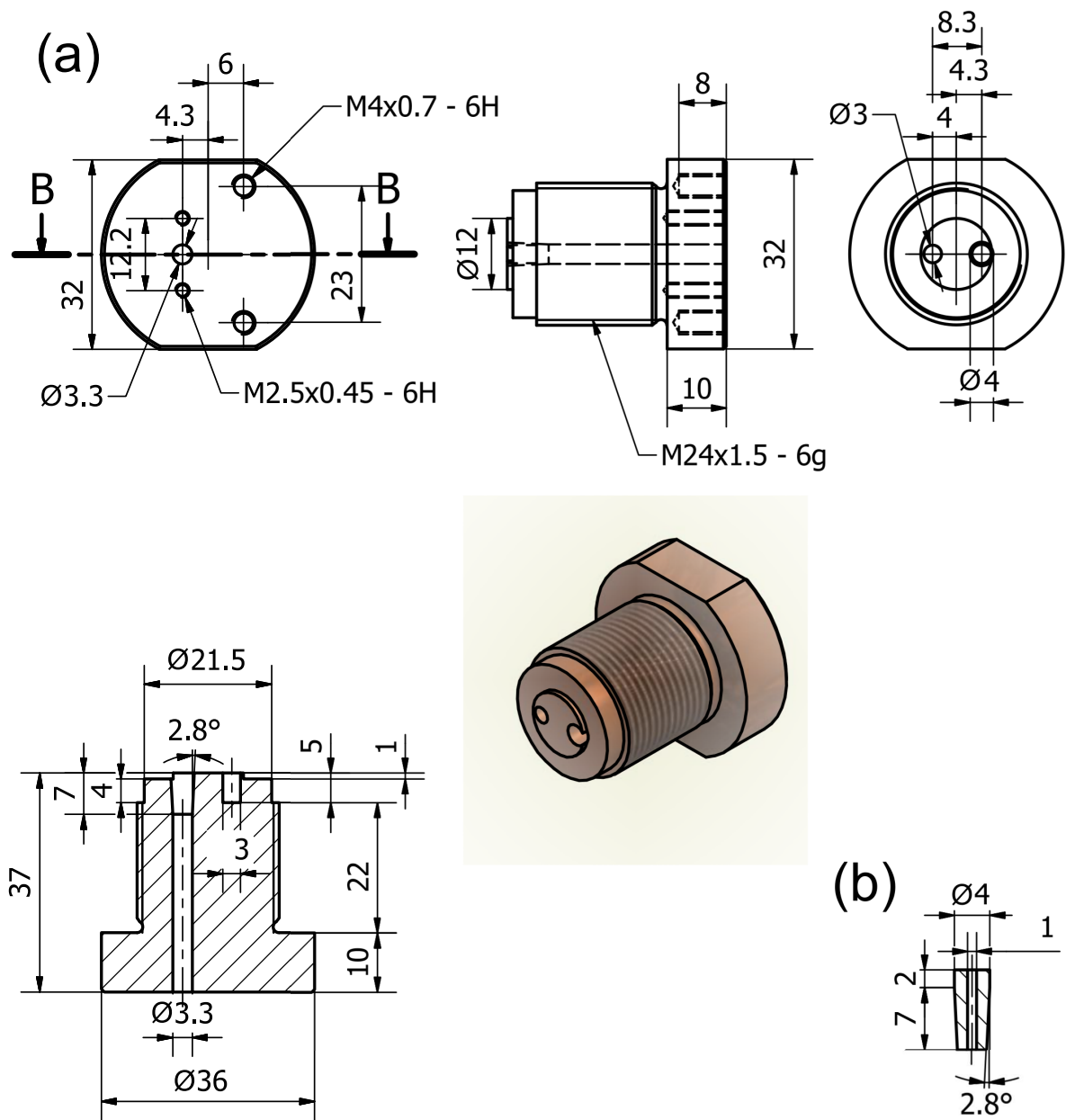


Figure A.4: (a) Drawings of the bottom screw of the high-pressure EPR cell. The piece is given in the ground view (top left), side view (top middle), top view (top right), and sectional view (bottom left). 3D shaded representation can be seen in the bottom right side of the figure. (b) ZrO<sub>2</sub> ceramic conical cork in sectional view. The cork fits into the conical opening at the top of the bottom screw. After insertion 2 mm of the ceramic cork is looking outside of the screw. This drawing is not in scale with the drawings of the bottom screw.

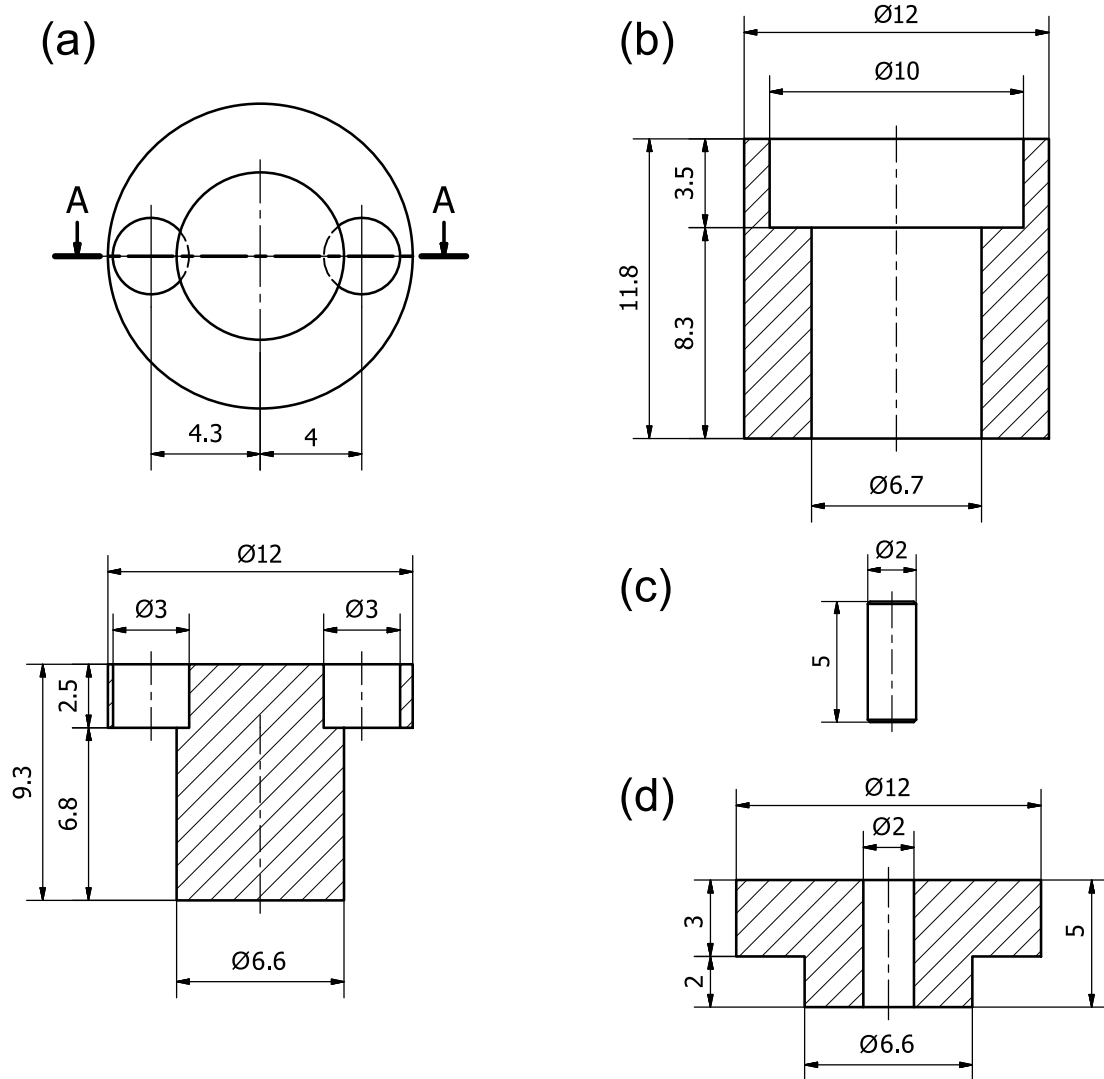


Figure A.5: Drawings of the Teflon holder of the high-pressure EPR cell. (a) Bottom part of the Teflon holder in the top view (top) and sectional view (middle). Two holes fit on top of the two holes of the bottom screw. The hole at the 4.3 mm distance from the center contains the head of ceramic cork and provides access for the antenna. The second hole is fixed to the second hole of the screw by a Teflon rod for better positioning. (b) The middle part of the Teflon holder. The larger opening (diameter 10 mm) is facing two holes of the bottom Teflon part. (c) Teflon cork for sealing the Teflon holder after introduction of the pressure transmitting medium. (d) Top and the covering part of the Teflon holder.

### A.1.2 Microwave Cavity and Coupling

One of the most important parts of the high-pressure EPR cell is the MW resonator and its coupling system. In our design we used dielectric resonator (DR) in an oversized cylindrical cavity coupled to the waveguide by an antenna (electric coupling, Fig. A.6a). Such configuration gave the maximal resonator quality factor of  $Q \approx 3000 - 6000$  and consequently the largest signal to noise ratio. We used cylindrical DR with a hole in the middle from muRata company (part number: DRT0650288R30A00T-S). The resonator's dielectric constant is  $\epsilon = 30.57$ , outer diameter 6.50 mm, inner diameter 2.06 mm, and

length of 2.88 mm. Its nominal  $Q$ -factor and the resonant frequency of the dielectric resonator is 18,735 and 9.2 GHz, respectively. The eigenmode that we used for EPR measurements is  $TE_{01\delta}$  [95] with the largest magnetic field in the center for the resonator directed along the cylindrical axis (Fig. A.6b).

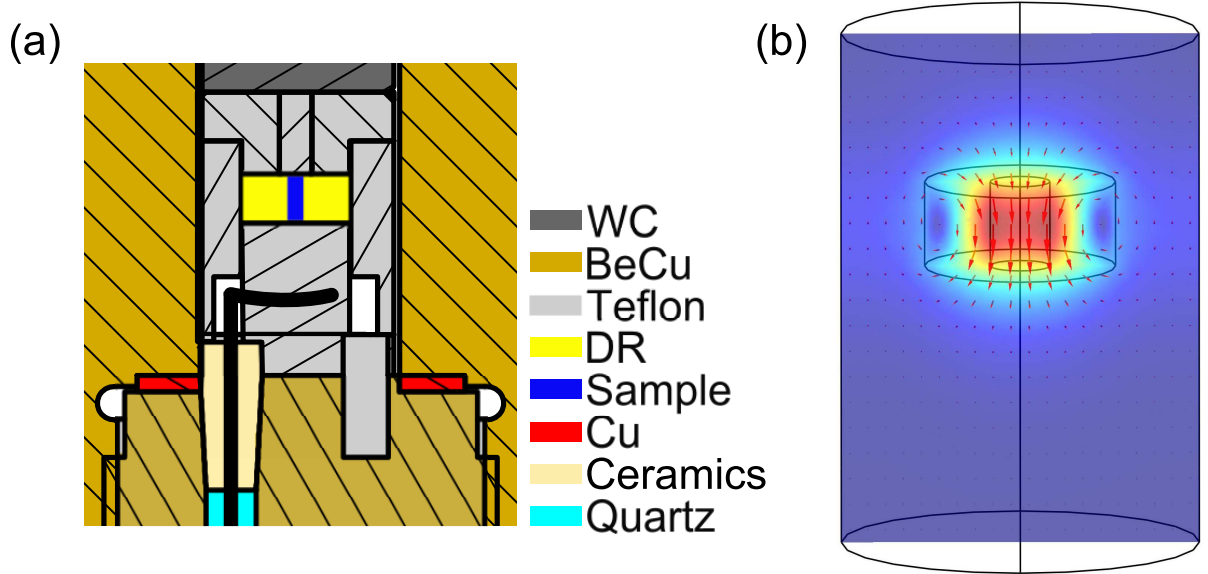


Figure A.6: (a) The central cavity containing dielectric resonator (DR) together with the electric coupling system. (b) Magnetic field component of  $TE_{01\delta}$  eigenmode solution at  $\nu = 9.297$  GHz. This result is calculated for actual non-pressurised cavity dimensions containing dielectric resonator by a Comsol finite element software package. The colour represents norm of the magnetic field, where blue denotes small and red large magnetic fields. Arrows indicate the direction of the magnetic field.

This eigenmode is similar to  $TE_{011}$  mode of cylindrical resonator, but in this case outside the DR the electromagnetic field decays exponentially [95]. Because of this the effect of conducting cavity walls only slightly influence the eigenmode solution. We determined the cavity length in such a way that the resonant frequency falls into the spectrometer frequency range of 9.0 – 9.9 GHz even for high-pressure experiments where the cavity length is reduced.

The optimal coupling between the DR and the waveguide was achieved with monopole L-shaped antenna (Fig. A.6b) where the horizontal part of the antenna with a length of  $\lambda/4 = 5.6$  mm was aligned along the  $TE_{01\delta}$  electrical field line. The antenna was positioned 6.3 mm below the center of the DR. The coupling strongly varies with the DR slight off-center position or the sample placed in the DR inner hole. A direct coupling optimization is in our design not possible since all inner parts have to be static to avoid pressure medium leakage. An indirect coupling optimization is realized by using external slide-screw tuner.

## A.2 High Pressure NMR cell

In chapter 3 we introduced the working principle of a high-pressure NMR cell. Here we give technical details and description of construction of the high-pressure NMR clamped-type cell.

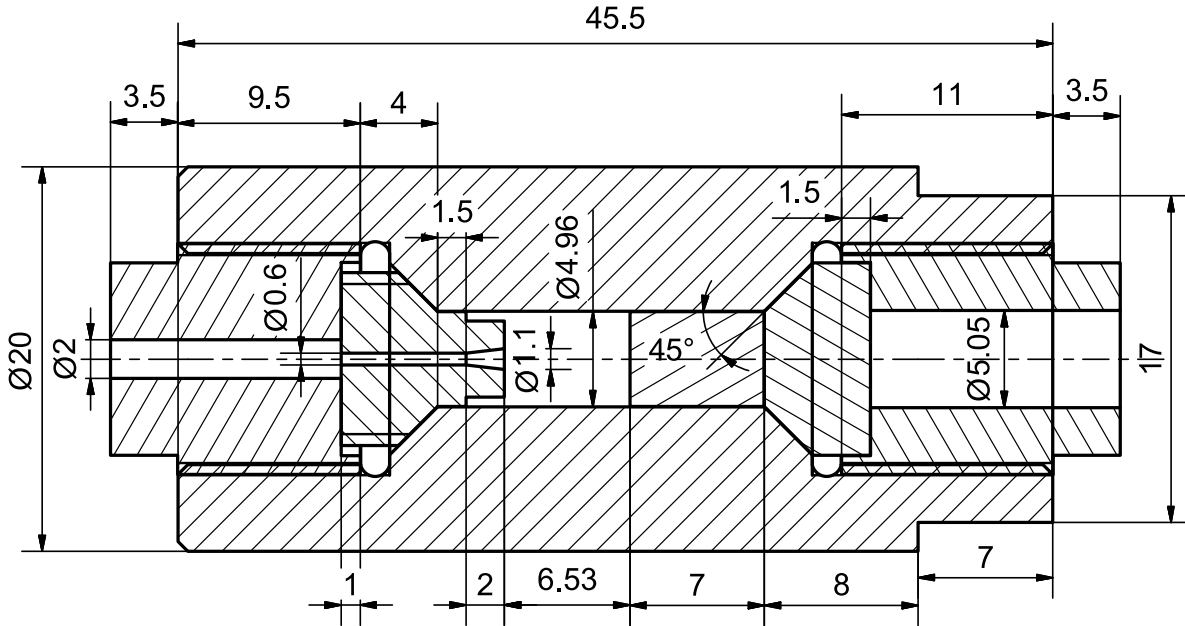


Figure A.7: Overview of assembled high-pressure NMR cell in sectional view.

## A.2.1 Construction details

An overview of the NMR high-pressure cell is given in Fig. A.7. The cell was designed to fit horizontally into the NMR SPE62HT600 cryostat with the inner diameter of 62 mm, which was also the limit for the cell's maximal dimension. The ratio between inner and the outer diameter of the cell was chosen to be  $r_o/r_i = 4$ ; see discussion in Sec. A.1.1. For this high-pressure cell three types of materials were used to maximize the maximal achievable pressure. A special material used for the cell's body (Fig. A.8) is non-magnetic NiCrAl alloy. This material is one of the hardest materials containing the smallest amount of magnetic moments know to date [99]. After the body was machined from pre-sintered NiCrAl it was hardened by a special sintering protocol provided by the manufacturer. The final hardness of the body was cca. 55 HRC. The other parts, namely, two lock nuts (Fig. A.9), the feed-through (Fig. A.10a), and anti-extrusion rings (Fig. A.10b) were made from non-magnetic hardened BeCu. Only the piston (Fig. A.10d) was made from WC. Details of BeCu and WC were given in Sec. A.1.1. The plunger (Fig. A.11b) was made of FeC and other tools (Fig. A.11a and Fig. A.11c) from brass. Very large hardness and consequently large Poisson's modulus allow very high pressures without preceding auto-fretage procedure. The maximal working pressures of 2.0 GPa could be reached repeatedly even at lower temperatures.

The NMR coil and the optical 50  $\mu\text{m}$  fibre were glued to the feed-through (Fig. A.10a) using special low temperature two component epoxy resin - Stycast®1266A/B by Emerson & Cuming. The NMR coil was made of an isolated copper leads with a diameter of 0.6 mm. The optical fibre with the outer diameter of 250  $\mu\text{m}$ , used for the pressure calibration, had pieces of ruby powder glued to the end of the correctly cut fibre using Loctite®406™ Instant Adhesive glue.

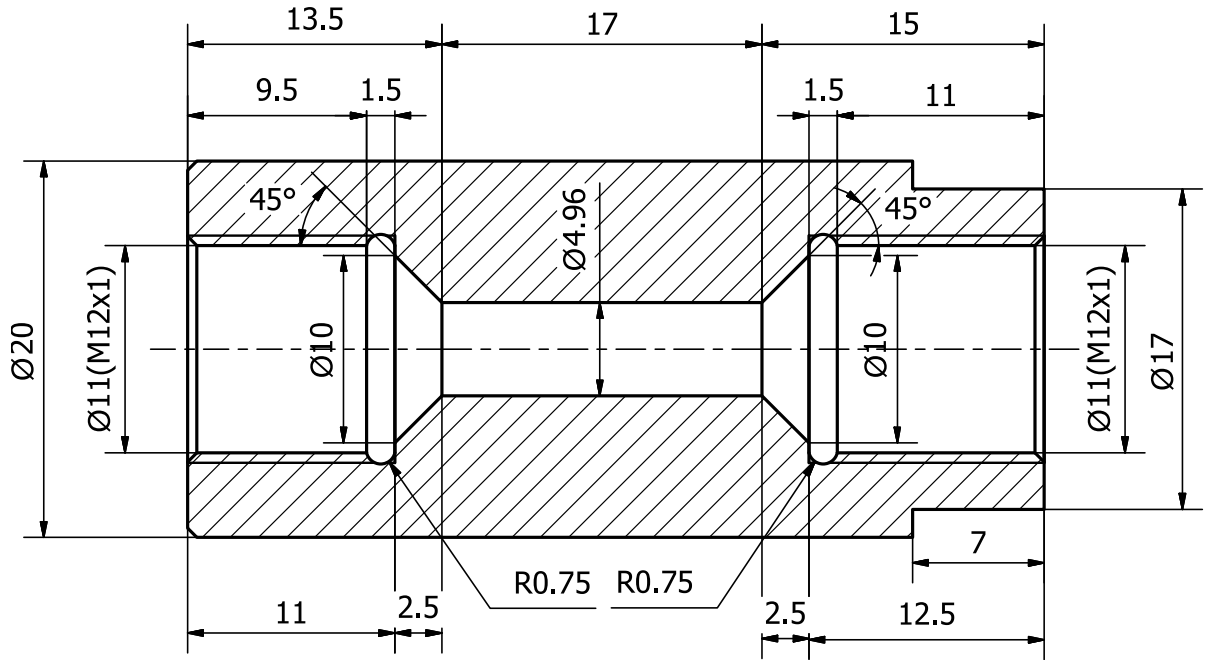


Figure A.8: Drawing of the body of the NMR high-pressure cell in sectional view. The tools used for threading should be blunt in order to avoid micro-crack formation which can propagate and even break the cell at very high pressures.

## A.2.2 Spectrometer for Ruby fluorescence

Ruby powder fluorescence was used for pressure measurements. The fluorescence was measured by the two channel spectrometer setup (Fig. 3.6). A diode pumped solid state green laser light with 532 nm wavelength (Fig. 3.6-1) is by silver mirrors (Fig. 3.6-2) guided to the dichroic mirror (Fig. 3.6-3) that reflects below and transmits above 605 nm wavelength. The reflected green light is by means of FiberPort collimator (Fig. 3.6-4) transferred to the multimode optical fibre with core diameter of 50  $\mu\text{m}$ . The fibre is then connected to the optical switch (OSW12-488E - MEMS 1x2 Fiber Optic Switch Kit, 480-650 nm by Thorlabs, Fig. 3.6-5), which was modified to work for higher wavelengths. There are two outputs from the switch, one goes to the ruby sample in the high-pressure cell and the other to the reference ruby sample. The red ruby fluorescent light is returned through the fibres and the optical switch to the dichroic mirror. There the light is transmitted and guided to the optical spectrometer (HR4000 by OceanOptics). To protect the spectrometer from direct laser beam a long-pass filter with cutoff wavelength of 600 nm was inserted before the spectrometer. For each pressure and each temperature the spectre of ruby inside the cell and the reference ruby was automatically measured between 690 and 710 nm with a resolution of 0.03 nm.

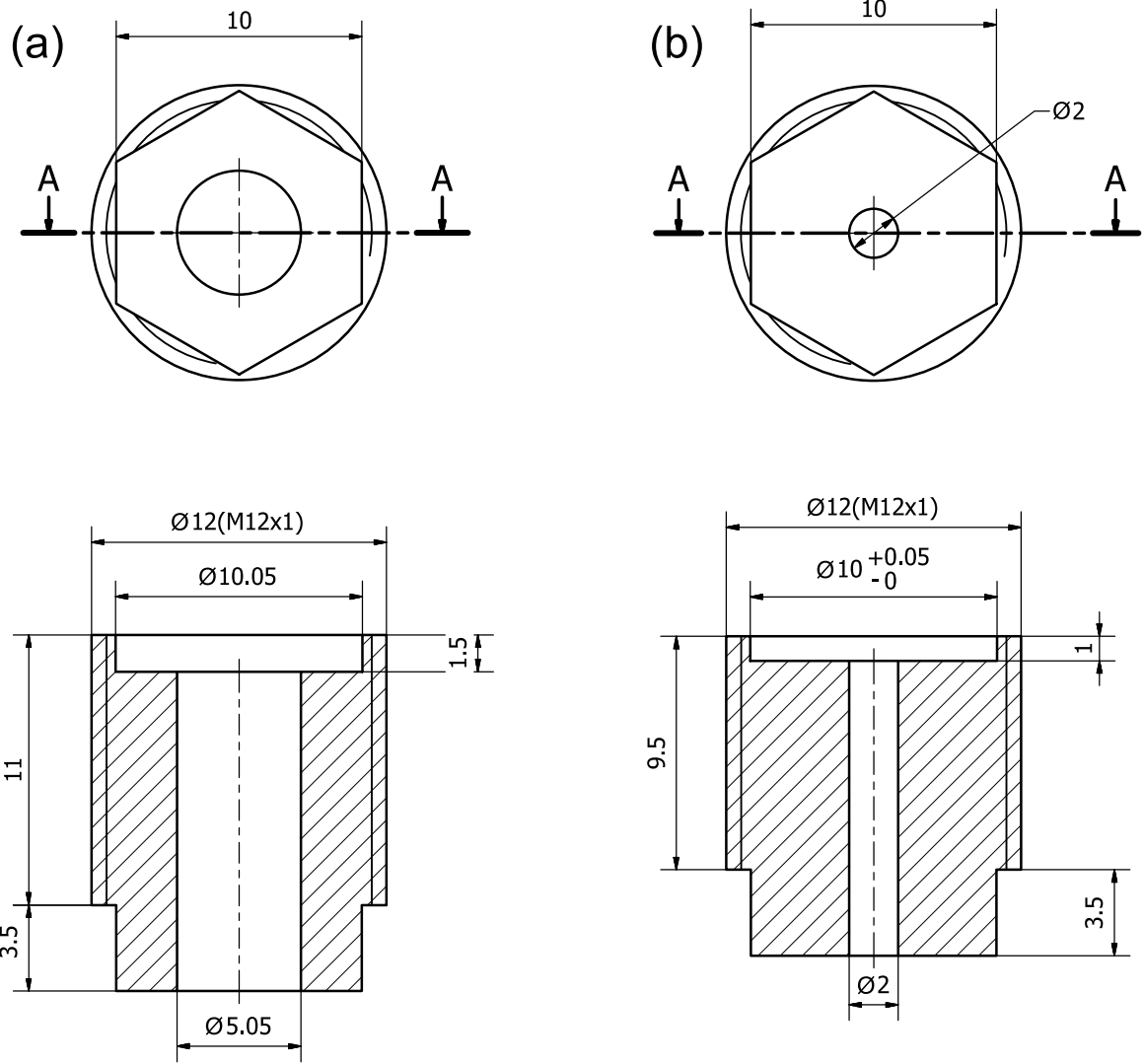


Figure A.9: Drawings of the two locknut screws of the high-pressure NMR cell, at the feed-through site (a) and at the piston side (b). The pieces are given by top (top) end sectional view (bottom)

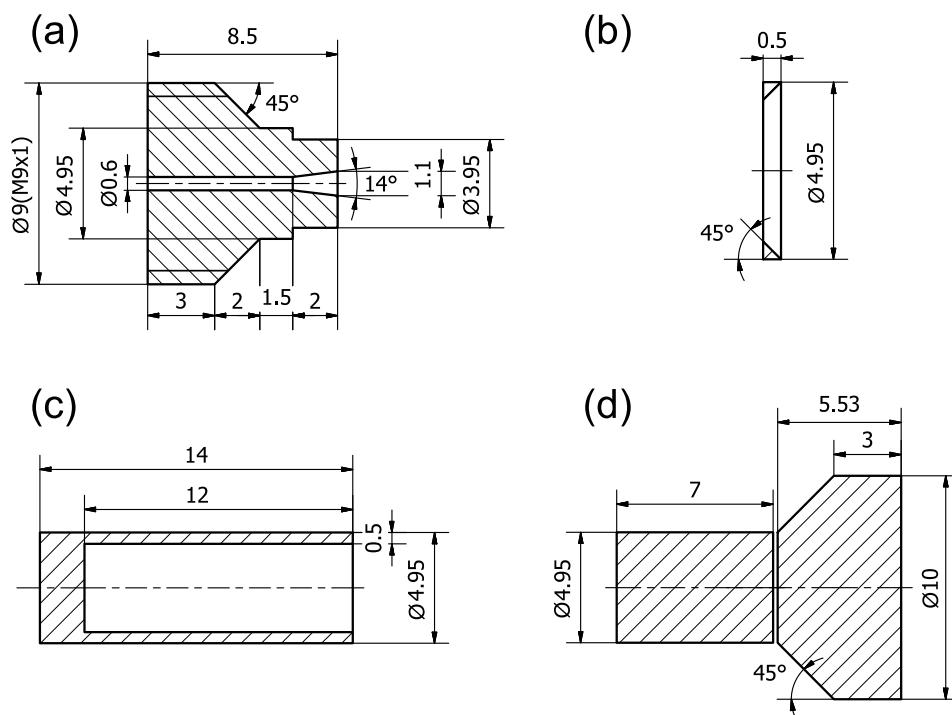


Figure A.10: Drawings of other pieces of the high-pressure NMR cell, all in a sectional view: (a) the feed-through, (b) anti-extrusion ring, (c) Teflon cap and (d) piston, made from two parts, to avoid breaking when unloading from the highest pressures.

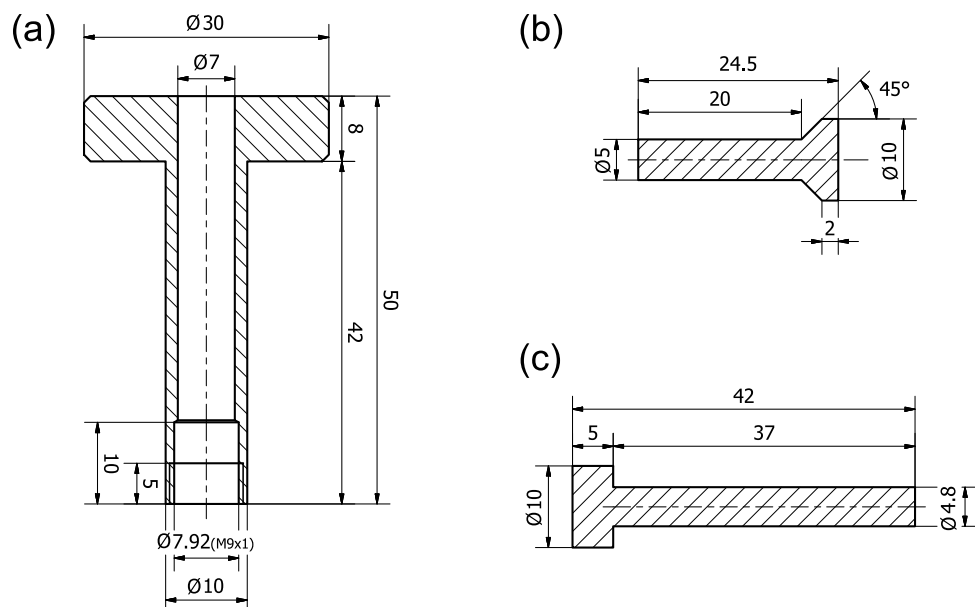


Figure A.11: Drawings tools used for assembling and disassembling the NMR cell, all in sectional view: (a) screw for pulling out the feed-through, (b) plunger, and (c) rod for cleaning the the body. Plunger is made from cheap hard magnetic alloy.



# B Materials

## B.1 *fcc* Cs<sub>3</sub>C<sub>60</sub>

### Structural characterization

Cs<sub>3</sub>C<sub>60</sub> compound grows in the face-centred cubic (space group  $Fm\bar{3}m$ ) polycrystalline structure with a lattice parameter of  $a = 14.76151(8)$  Å and the unit-cell volume of  $V = 804.14(1)$  Å<sup>3</sup> per C<sub>60</sub> at ambient pressure and temperature. The fullerene anions are orientationally disordered (merohedral disorder). Cs ions are intercalated in the interstitial sites between fullerene molecules. In one unit cell two Cs ions occupy the smaller tetrahedral sites (red balls in Fig. B.1) and one occupies the larger octahedral site. The XRD data do not show any deviation away from the icosahedral symmetry. The sample used in the present work was structurally characterised by the synchrotron X-ray powder diffraction (XRPD) which showed that the phase fraction of *fcc* Cs<sub>3</sub>C<sub>60</sub> is 86 % [14] The fractions of minority co-existing A15 Cs<sub>3</sub>C<sub>60</sub>, body-centred orthorhombic (*bco*) Cs<sub>4</sub>C<sub>60</sub>, and CsC<sub>60</sub> phases are 3%, 7%, and 4%, respectively.

The unit-cell volume per C<sub>60</sub> molecule as a function of temperature at ambient pressure and applied pressure at 15 K is shown in Fig. B.2. The unit-cell volume as a function of temperature (Fig. B.2a) is for A<sub>3</sub>C<sub>60</sub> structure sufficiently well described by an expression based on the Debye model [195]

$$V(T) \simeq V_0 + ATF(\theta_D/T), \quad F(t) = \frac{3}{t^3} \int_0^t \frac{x^3}{e^x - 1} dx, \quad (\text{B.1})$$

where  $\theta_D$  is Debye temperature and  $A$  is a material specific parameter. Parameter  $A$  is temperature independent in the approximation used to derive the above formula. Since Eq. B.1 has to be calculated numerically it is not convenient for fast fitting procedures.

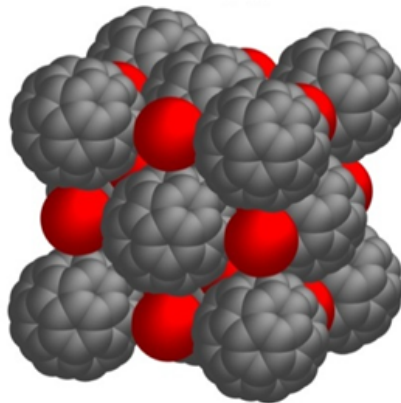


Figure B.1: A<sub>3</sub>C<sub>60</sub> crystal structure. Alkali atoms in tetrahedral sites can be seen in red.

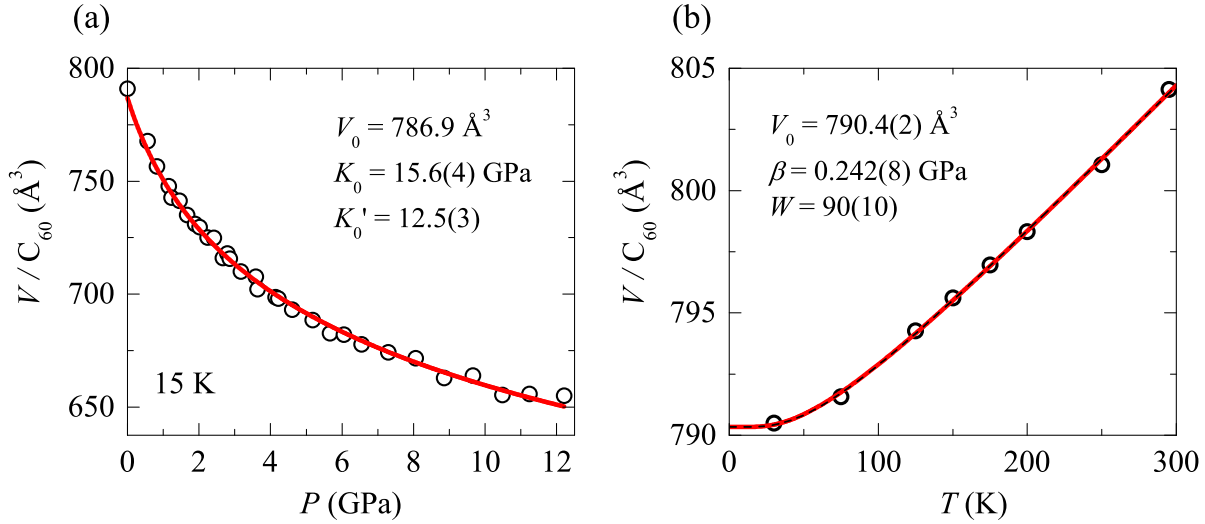


Figure B.2: *fcc*  $\text{Cs}_3\text{C}_{60}$  unit-cell volume as a function of the hydrostatic pressure at 15 K (a) and the temperature (b) at ambient pressure. The fit to the pressure dependent data was made by Murnaghan equation of state (Eq. B.3 shown in red solid line). The temperature dependent data was fitted by the Debye model (Eq. B.1) shown in black dashed line and analytical approximation function (Eq. B.2) shown by red solid line. The experimental data shown in these figures was obtained by our collaborators from University of Durham.

We found an analytical approximation which gives excellent accuracy in the parameter range appropriate for temperature dependence of  $\text{Cs}_3\text{C}_{60}$  unit-cell volume. The analytical approximation which we used for fitting to the data is

$$V = V_0 + \beta T e^{-W/T}. \quad (\text{B.2})$$

The maximal deviation between the Debye model (Eq. B.1) and the analytical approximation function (Eq. B.2) is  $0.2 \text{ \AA}^3$ , which is less than the experimental uncertainty. In Fig. B.2 we show fit of the Debye model with  $V_0 = 790.4 \text{ \AA}^3$ ,  $\theta_D = 216 \text{ K}$  and  $A = 0.738 \text{ \AA}^3/\text{K}$  depicted by a black dashed line and fit to the analytical approximation model with  $V_0 = 790.4(2) \text{ \AA}^3$ ,  $\beta = 0.252(8) \text{ \AA}^3/\text{K}$  and  $W = 90(10)$  depicted by a red solid line. Finally, we note that the cubic symmetry is retained at low temperatures, since no structural phase transition was detected at low temperatures.

The pressure dependence (Fig. B.2b) can be successfully fitted with a Murnaghan equation of states

$$V = V_0^m \left( 1 - \frac{K'_0}{K_0} P \right)^{-\frac{1}{K'_0}}, \quad (\text{B.3})$$

with  $V_0^m = 786.9 \text{ \AA}^3$ ,  $K_0 = 15.6(4) \text{ GPa}$ , and  $K'_0 = dK_0/dP = 12.5(3)$ . As will be shown in Sec. B.2, the unit-cell volume in the metallic state is smaller than that in the insulating state for  $\Delta V = 3.5(5) \text{ \AA}^3$  per  $\text{C}_{60}$ . Since the transition to the metallic state happens already for small pressures ( $P_c \simeq 2 \text{ kbar}$ ) all but the first ( $P = 0$ ) data point are measured in the metallic state. To treat all pressure dependent data points in metallic state we fix  $V_0^m$  value when fitting to a metallic equivalent that is lower for the observed volume change  $V_0^m = V_0 - 3.5 \text{ \AA}^3 = 786.9 \text{ \AA}^3$ . Such treatment introduces error in the insulating state which is  $3.5 \text{ \AA}^3$  at  $P=0$  and vanishes around  $P \simeq 2 \text{ kbar}$ . Since our high-pressure results have a similar resulting unit-cell volume uncertainty the additional error for very low pressure data points were neglected.

To obtain the final expression for the unit-cell volume as a function of temperature and pressure we assumed temperature independent compressibility parameters ( $K_0$  and  $K'_0$ ) and pressure independent volume expansion parameters ( $\beta$  and  $W$ ). The final expression that we used for calculation of the unit-cell volume from the pressure and temperature during high-pressure NMR measurements is thus

$$V(P, T) = \begin{cases} V_0^m \left(1 - \frac{K'_0}{K_0} P\right)^{-\frac{1}{K_0}} + \beta T e^{-W/T} & \text{if } P > 0, \text{ metallic state,} \\ V_0 + \beta T e^{-W/T} & \text{if } P = 0, \text{ insulating state.} \end{cases} \quad (\text{B.4})$$

### Unit-cell volume during high-pressure experiments

During high-pressure NMR experiments we measured temperature with standard ITC503 temperature controller and the internal pressure using pressure calibration technique described in Sec. 3.4.2. The temperature gradient was measured separately with the use of two thermocouples, one inside the cell and the other above the cell, on the other side of the blowing coolant. The temperature difference is below the experimental error down to 50 K. At cca. 30 K the temperature difference is 1 K and at 15 K this difference is 3 K. We estimate that difference between reported and actual temperature at the sample is lower than the above given value since the coolant gas (liquid He) was in a direct thermal contact with the high-pressure cell which was not the case for the upper thermocouple that was mounted cca. 3 cm higher on the plastic holder.

The obtained pressure calibration measurements as a function of temperature during the high-pressure NMR experiments are shown in Fig. B.3a for  $^{13}\text{C}$  and in Fig. B.3b for  $^{133}\text{Cs}$  runs.

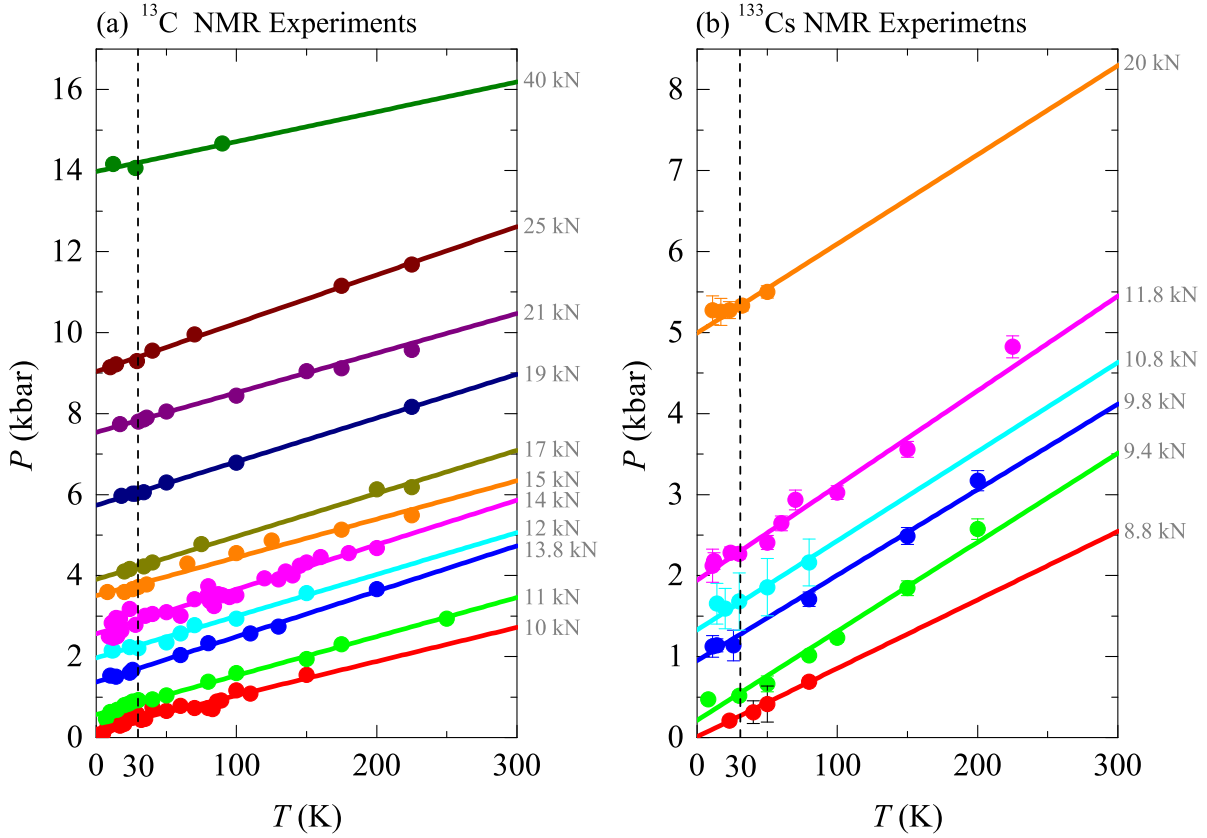


Figure B.3: Calibrated internal pressures as a function of temperature for high-pressure (a)  $^{13}\text{C}$  and (b)  $^{133}\text{Cs}$  NMR experimental runs. For each experiment the applied force is written in grey. 30 K is marked with dashed line.

Rather scattered pressures as a function of temperature were fitted with a linear function. For every pressure run the unit-cell volume was calculated using Eq. B.4 together with the linear pressure trend and the corresponding temperatures. The calculated unit-cell volumes are for  $^{13}\text{C}$  and  $^{133}\text{Cs}$  depicted in Fig. B.4a and Fig. B.4b, respectively. Considering the pressure uncertainty of our calibration technique ( $\sim 0.3$  kbar) the volume errorbars were added to Figs. B.4a,b represented by a gray area along the volume curves. The typical volume uncertainty is  $2 - 3 \text{ \AA}^3$ .

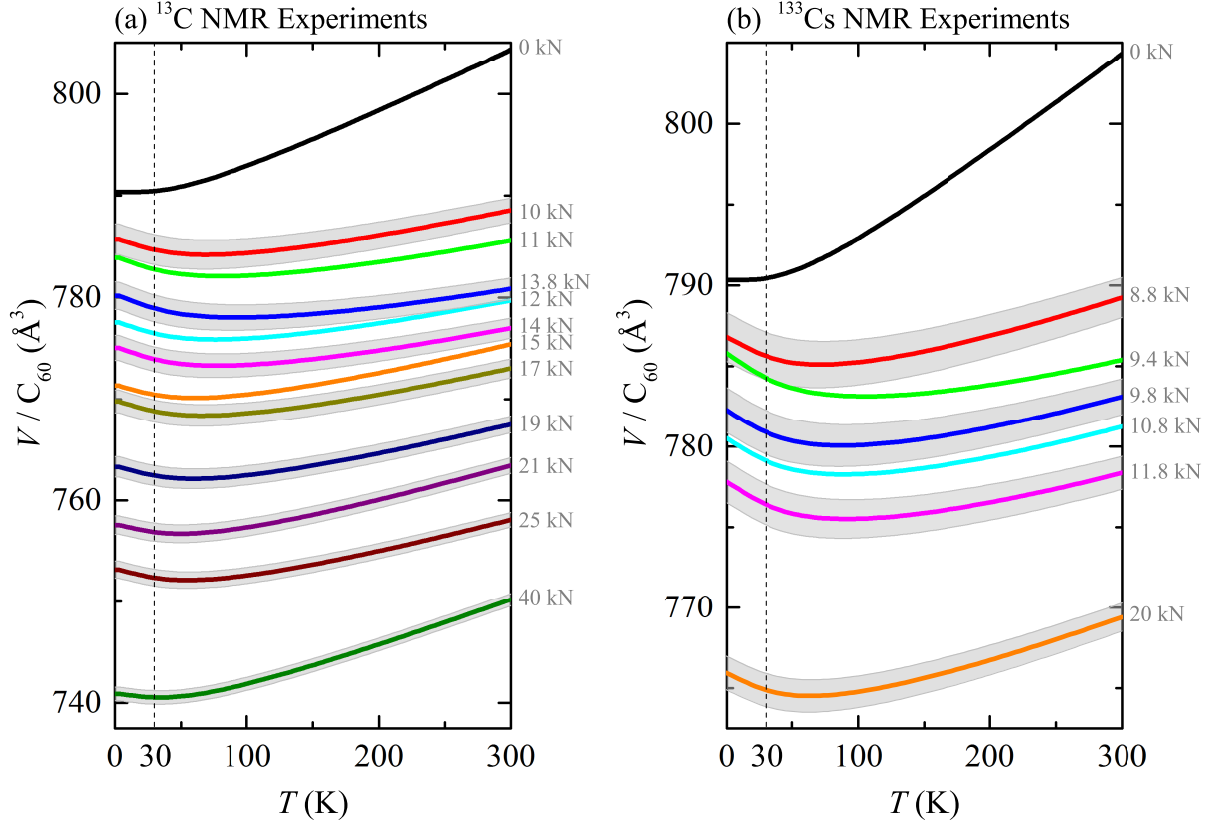


Figure B.4: Calculated unit-cell volume as a function of temperature for high-pressure (a) <sup>13</sup>C and (b) <sup>133</sup>Cs NMR experimental runs. The estimated volume uncertainty is depicted as a gray area for selected high-pressure runs. For each experiment the applied force is written in grey. 30 K is marked with dashed line.

## B.2 *fcc* Rb<sub>x</sub>Cs<sub>3-x</sub>C<sub>60</sub>

### B.2.1 Structural characterisation

Rb<sub>x</sub>Cs<sub>3-x</sub>C<sub>60</sub> compounds grow in the *fcc* lattice with  $Fm\bar{3}m$  space group. All samples were characterised by a synchrotron X-ray diffraction experiment performed at temperatures between 295 and 12 K using the high-resolution powder diffractometers on beamline ID31 at the European Synchrotron Radiation Facility (ESRF), Grenoble, and on beamline I11 at the Diamond synchrotron, UK. All structural characterization was done by Durham and Liverpool groups. Rb<sub>x</sub>Cs<sub>3-x</sub>C<sub>60</sub> samples' phase fractions are given in Tab. B.1 together with unit-cell volume at 30 K and measured  $T_c$  by NMR. We note that these temperatures are due to large magnetic fields used in NMR (9.4 T) somehow smaller than the one obtained by SQUID magnetometer at low temperatures.

Compound	<i>fcc</i>	A15	<i>bco</i>	AC <sub>60</sub>	$V_{30\text{K}}$ ( $\text{\AA}^3/\text{C}_{60}$ )	$T_c$ (K)
Cs <sub>3</sub> C <sub>60</sub> (AM2_4)	86%	3%	7%	4%	790.5	-
Rb <sub>0.35</sub> Cs <sub>2.65</sub> C <sub>60</sub> (RZ024_5)	76.5%	-	10.0%	13.5%	779.4	26
Rb <sub>0.5</sub> Cs <sub>2.5</sub> C <sub>60</sub> (AG159_3)	79.5%	1.1%	19.4%	-	774.5	27
Rb <sub>0.75</sub> Cs <sub>2.25</sub> C <sub>60</sub> (RZ021_4)	93.8%	-	-	6.2%	768.2	31
RbCs <sub>2</sub> C <sub>60</sub> (RZ018_4)	98.7%	-	1.3%	-	762.2	32
Rb <sub>2</sub> CsC <sub>60</sub> (RZ025_3)	98.3%	-	-	1.7%	750.8	32
Rb <sub>3</sub> C <sub>60</sub> (MR025_4)	94.4%	-	-	5.6%	731.2	29

Table B.1: Summary of structural sample characterization of Rb<sub>x</sub>Cs<sub>3-x</sub>C<sub>60</sub> compounds. The superconducting critical temperature  $T_c$  is determined from NMR experiments performed in a large magnetic field (9.4 T) and are thus for a few K lower than the one obtained using SQUID measurements at low magnetic fields.

Temperature dependence of the unit-cell volume for different Rb<sub>x</sub>Cs<sub>3-x</sub>C<sub>60</sub> are shown in Fig. B.5. Empty data points are approximate points estimated using data with similar  $x$ . For example for  $x = 0.5$  sample data points of  $x = 0.75$  were used and for  $x = 2$  and 3 data points from another  $x = 2$  sample (now shown) were used. Samples that show no anomalies ( $x = 0, 2, 3$ ) were fitted by Eq. B.2 over the entire temperature range. The parameters  $\beta = 0.25$  and  $W = 80$  are within the fitting uncertainty equal for all three samples and were, therefore, kept fixed when fitting the volumes of other samples. Samples in the range  $0.35 < x < 1$  show a clear change in behaviour below  $T_{\text{MIT}}$  determined by NMR  $1/T_1T$  results.<sup>1</sup> They indicate that the unit-cell volume changes when going from the insulating to the metallic state. Data points for these samples were fitted in two parts. In the first part the high temperature data points were fitted using Eq. B.2 with only  $V_0$  as a free parameter (strong solid lines in Fig. B.5) and in the second part the whole data range was fitted with the following double function (narrow black solid lines in Fig. B.5).

$$V(T) = f(T)V_{01} \left( 1 + \frac{\beta}{V_{01}} T e^{-W/T} \right) + [1 - f(T)]V_{02} \left( 1 + \frac{\beta}{V_{02}} T e^{-W/T} \right), \quad (\text{B.5})$$

where we introduce an empirical crossover function

$$f(T) = \frac{1}{e^{(T-T_0)/\Delta T} + 1}. \quad (\text{B.6})$$

For  $x = 0.5$  sample the additional parameters in Eq. B.5 were estimated based on the fitting results of other compounds. Its unit-cell volume dependence is thus least accurate. Fitting parameters are summarized in Tab. B.2

<sup>1</sup>Temperatures corresponding to the MIT determined from  $1/T_1T$  are connected by a dashed line in Fig. B.5

Compound	$V_{01}$	$\beta$	$W$	$V_{02}$	$T_0$	$\Delta T$
$x = 0$ (AM2_4)	790.4(2)	0.25(1)	90(10)	-	-	-
$x = 0.35$ (RZ024_5)	781.4(1)	0.25	80	778.2(2)	36(2)	8(2)
$x = 0.5$ (AG159_3)	772.8(1)	0.25	80	769.8	59	21
$x = 0.75$ (RZ021_4)	770.5(1)	0.25	80	767.5(2)	67(6)	25(4)
$x = 1$ (RZ018_4)	764.2(1)	0.25	80	761.8(2)	80(10)	33(5)
$x = 2$ (RZ025_3)	740.6(1)	0.246(2)	78(3)	-	-	-
$x = 3$ (MR025_4)	735.6(1)	0.246(2)	78(3)	-	-	-

Table B.2: Temperature dependent unit-cell volume fitting results for  $\text{Rb}_x\text{Cs}_{3-x}\text{C}_{60}$  compounds. For  $x = 0, 2, 3$  the model Eq. B.2 was used and for  $x = 0.35, 0.5, 0.75, 1$  the model used was Eq. B.5. Parameters without error values were fixed during fitting procedure.

From the above results we can estimate the unit-cell volume difference between metallic and insulating state. In average this difference is  $3.5(5) \text{ \AA}^3/\text{C}_{60}$ .

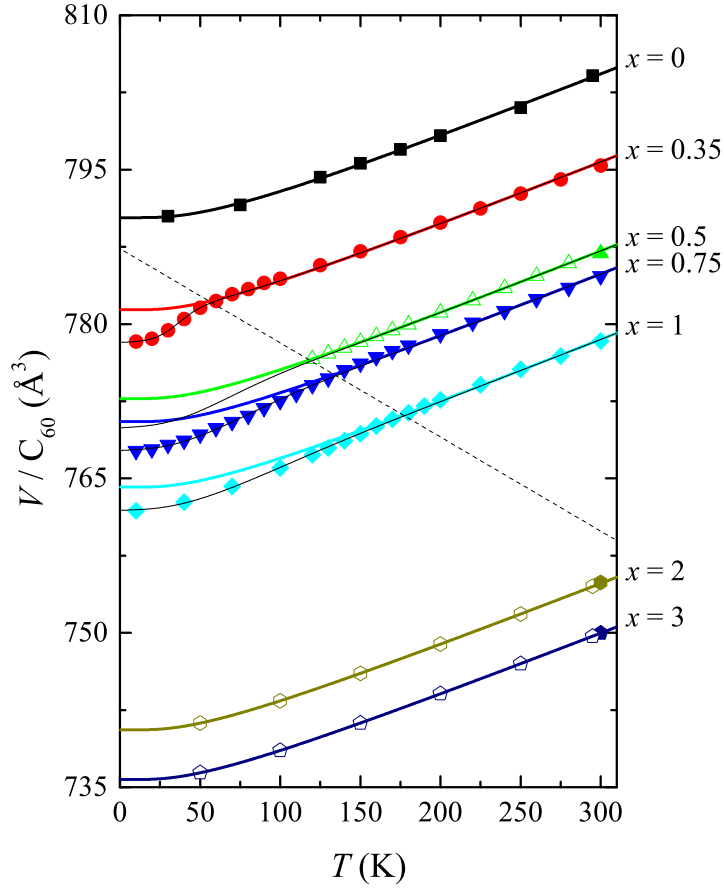


Figure B.5: Unit-cell volume as a function of temperature for  $\text{Rb}_x\text{Cs}_{3-x}\text{C}_{60}$  samples with  $x = 0, 0.35, 0.5, 0.75, 1, 2,$  and  $3$ . Solid points are the actual measured points. Empty points are estimated data points. Solid lines are fits of Eq. B.2 to the points at high temperature ( $T > T_{\text{MIT}}$ ). Dotted lines are fits to the lowest temperature data point. The dashed black line represents the MIT determined from the maximum in  $1/T_1T$  measurements. The experimental data shown in this figure was obtained by our collaborators from University of Durham.

## B.2.2 SQUID magnetization measurements

The magnetic properties of all prepared samples were measured by SQUID magnetometer. The results are shown in Fig. B.6. The presented bulk magnetic susceptibility was obtained first by taking a difference between magnetization measurements at 5 T and 3 T. In this way the contribution from the ferromagnetic impurities is eliminated. Later the core contributions were subtracted that come from the alkali ions and the carbon atoms. Later, for samples  $x < 1$  high temperature points (above maximum) were fitted with the Curie-Weiss law and a constant

$$\chi(T) = \frac{C}{T - \theta} + \chi_{\text{imp}}, \quad (\text{B.7})$$

where the constant ( $\chi_{\text{imp}}$ ) was later subtracted from the measured data in order to remove a temperature independent contribution from the impurity phases. For samples with higher Rb content such analysis is not required since they have less amount of impurity phases (Tab. B.2). Details of bulk susceptibility measurements can be found in [165].

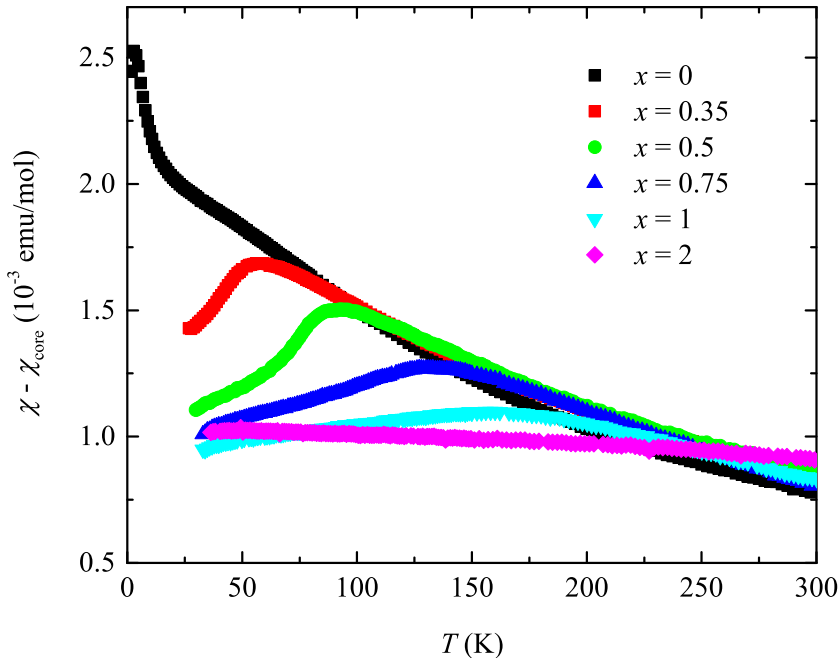


Figure B.6: Bulk magnetic susceptibility measurements on  $\text{Rb}_x\text{Cs}_{3-x}\text{C}_{60}$  samples. These results were obtained by subtracting core contributions, ferromagnetic impurities and Pauli-like impurities. See text for details. The measurement on  $x = 0.5$  was not done on the same sample (RZ016\_3) as were NMR measurements (AG159\_3), however, the nominal Rb content was the same. The experimental data shown in this figure were obtained by our collaborators from University of Durham.

## B.3 *fco* $\text{CH}_3\text{NH}_2\text{K}_3\text{C}_{60}$ ( $\text{MAK}_3\text{C}_{60}$ )

### B.3.1 Crystal structure

Methylamine cointercalated potassium fullerides were initially used as a precursor in the synthesis route for the highly expanded  $A_3\text{C}_{60}$  synthesized. However, it was soon realized that the cointercalation of a larger anisotropic molecule can strongly distort the

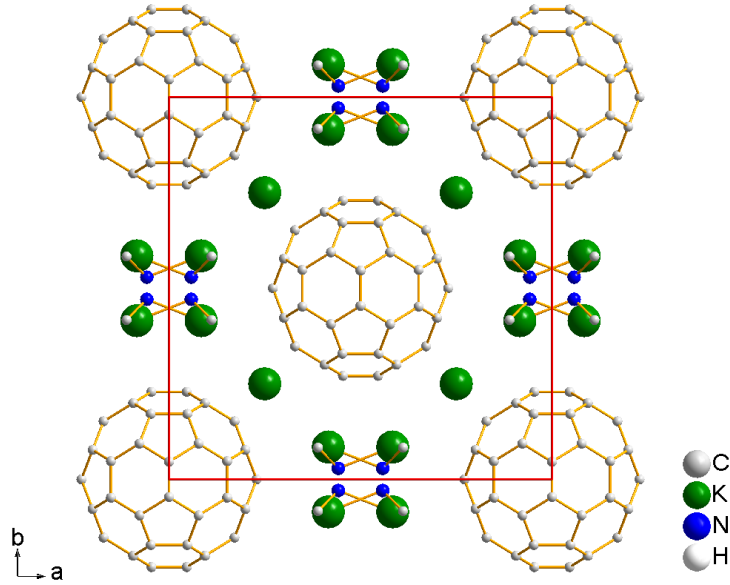


Figure B.7: The unit-cell atom arrangement of the  $\text{MAK}_3\text{C}_{60}$  compound.  $\text{MA}^-\text{K}^+$  groups are disordered between four equivalent positions in the octahedral interstitial sites. All four possible configurations are shown. In addition,  $\text{C}_{60}$  molecules are merohedrally disordered, not shown.

cubic symmetry which is interesting for studying the effects of orbital degeneracy on the superconductivity of alkali-doped fullerenes.

$\text{CH}_3\text{NH}_2\text{K}_3\text{C}_{60}$  or shortly  $\text{MAK}_3\text{C}_{60}$  grows in the face-centred orthorhombic unit cell (space group  $Fmmm$ ) with the unit-cell parameters  $a = 15.2027(8) \text{ \AA}$ ,  $b = 15.1800(9) \text{ \AA}$ ,  $c = 13.5032(3) \text{ \AA}$  and unit-cell volume of  $V = 779.057 \text{ \AA}^3$  [36]. The  $\text{MA}^-$  coordinated with  $\text{K}^+$  occupy large octahedral interstitial sites. They are disordered between eight equivalent positions (Fig B.7). The random Markovian-type dynamics of MAK groups freeze below cca. 220 K [107]. As indicated from the XRD measurements (Takabayashi et al., unpublished), below that temperature MAK groups most probably orientationally order leading to a double or even larger unit-cell similar as in  $\text{NH}_3\text{K}_3\text{C}_{60}$  [38]. However, the actual low temperature crystal structure has not been solved so far. The two remaining potassium cations occupy smaller tetrahedral interstitial sites. As is the case with all *fcc*  $\text{A}_3\text{C}_{60}$  the fullerene molecules are merohedrally disordered also in  $\text{MAK}_3\text{C}_{60}$ . The cointercalation of MA molecules modifies the  $\text{K}_3\text{C}_{60}$  in three ways: (i) the unit-cell volume is increased for 7.6%, the unit cell becomes anisotropic with  $b/a = 0.99851$  and  $c/a = 0.88821$ , and a new interaction is introduced between  $\text{C}_{60}\text{-H-CH}_2\text{NH}_2$ . All these effects should have profound implications for the electronic and magnetic properties. For example,  $\text{MAK}_3\text{C}_{60}$  is not metallic at ambient pressures. It was found the ground state is antiferromagnetic insulating ground state with a drastically lower Néel temperature of  $T_N = 11 \text{ K}$  compared to other non-cubic triply-doped fullerenes [37, 108].

### B.3.2 Compressibility

A high-hydrostatic pressure XRD study show that due to anisotropic crystal structure the unit-cell lattice parameters have different compressibility coefficients [inset to Fig. B.8(a)]. Volume per  $\text{C}_{60}$  molecule can be successfully fitted with a Murnaghan equation of states (Eq. B.3) with parameters  $K'_0 = dK_0/dP = 12(2)$  and  $K_0 = 14(4) \text{ GPa}^{-1}$ .  $\text{MAK}_3\text{C}_{60}$  linear compressibility is, therefore,  $\kappa = 1/K_0 = 0.083(12) \text{ GPa}^{-1}$ . This is quite large

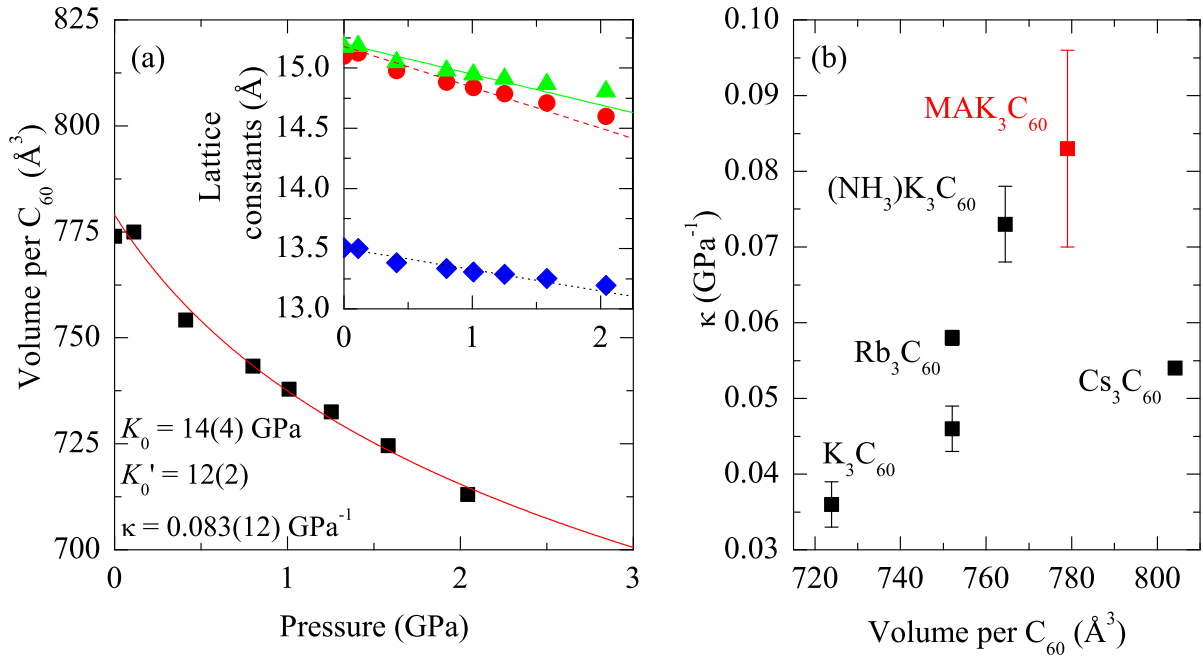


Figure B.8: (a) Lattice constants as a function of hydrostatic pressure from an approximate model for  $MAK_3C_{60}$  (Takabayashi, Y., *et al.*, unpublished 2012). (b) Comparison of compressibilities as a function of volume per  $C_{60}$  for *fcc* compounds:  $K_3C_{60}$  [196],  $Rb_3C_{60}$  [196, 197],  $(NH_3)K_3C_{60}$  [198],  $Cs_3C_{60}$  [14], and  $MAK_3C_{60}$  (red point). The experimental data shown in these figures were obtained by our collaborators from University of Durham.

compressibility compared to face-centred cubic  $A_3C_{60}$ , however, it is comparable to the compressibility of the expanded orthorhombic  $NH_3K_3C_{60}$  [Fig. B.8(b)]. It would seem that the presence of organic molecules in the interstitial sites increase the compressibility probably by rearranging its position.

### B.3.3 Low temperature structure

The low temperature crystal structure has not yet been solved exactly. XRD data taken at low temperatures suggest a long range order of the MAK groups yielding a double or even larger unit cell (Y. Takabayashi, *et al.*, unpublished 2012). Similar behaviour has also been found for  $NH_3K_3C_{60}$  compound [38, 199]. Although, exact structure is not yet known the unit-cell parameters could still be extracted using Le Bail analysis assuming room-temperature model (space group  $Fmmm$ ). The unit-cell parameters at 25 K obtained in such a way are  $a = 15.1106(7)$   $\text{\AA}$ ,  $b = 15.0769(3)$   $\text{\AA}$ , and  $c = 13.4013(2)$   $\text{\AA}$ . The unit-cell volume is  $V = 763.3(1)$   $\text{\AA}^3$ . The contraction of the unit-cell volume on cooling from room temperature to 25 K is thus 15.8  $\text{\AA}$  per  $C_{60}$  molecule or 2.0%. This is comparable to the  $NH_3K_3C_{60}$  compound where a contraction of 1.3% was found when cooling from room temperature to 15 K [199].

### B.3.4 DFT calculation parameters

We executed DFT calculations using the Quantum Espresso software package (pwscf program) [200] with the ultrasoft pseudo potentials appropriate for the Perdew-Zunger exchange-correlation functional (LDA). The pseudo Bloch functions were expanded over plane waves with an energy cutoff of 50 Ry on a  $5^3$  Monkhorst-Pack  $k$ -space mesh, such

that the total energy is within 250 meV of its converged value, while the conduction bands are within 0.1 meV of their converged value. The Fermi surface was smeared with a “temperature” parameter of 2 meV using the Gaussian smearing method. The density of states (DOS) is evaluated with the tetrahedron method, sampling  $k$ -space with a uniform  $8^3$  mesh. For the relaxation of the atomic positions, we adopted a damp (quick-min Verlet) procedure on a  $2^3$   $k$ -space mesh with a plane-waves energy cutoff of 30 Ry and the same smearing of the Fermi surface.

Unit-cell parameters and atomic positions used in our calculations were based on the XRD data [36]. The real structure including the merohedral disorder and the eight possible orientations of MAK group in each octahedral site is too immense to be computed in given time. For this reason we simplified the structure by taking only one chemical unit per unit cell. The  $C_{60}$  atoms were taken in a standard  $y$ -orientation and a random orientation was used for MAK group. The atomic positions used in our calculations are summarized in Tab. B.3. The hydrogen atom positions were calculated from a known  $CH_3NH_2$  molecule structure. Only  $C_{60}$  carbon positions were relaxed to account for the crystal field effects and bond-length corrections due to the LDA approximation.

The maximally-localized Wannier orbitals were obtained using the Wannier90 package [201]. The three Wannier orbitals are computed in the  $t_{1u}$  energy window, using  $5^3$   $k$ -points on Monkhorst-Pack grid with Bloch phases as initial projections. All three Wannier orbitals were positioned on the central  $C_{60}$  molecule and have a similar spread of  $\sqrt{\Omega} \sim 0.4$  nm. The projected DOS (PDOS) on the three Wannier orbitals were evaluated using the Gaussian smearing method with a “temperature” parameter of 8 meV. The use of two different methods for evaluation of DOS and PDOS gives rise to a slight mismatch between the two. The mismatch does not affect the conclusions of this work. We tested the convergence of Wannier orbitals’ hopping integrals as a function of the number of  $k$ -points and negligible changes of less than 0.01 meV are found for  $k$ -space mesh finer than  $5^3$

Atom	x (Å)	y (Å)	z (Å)	Atom	x (Å)	y (Å)	z (Å)
C1	0.23390	0.65295	3.61461	C36	-0.64087	2.62056	-2.08203
C2	0.25011	-0.74031	3.59087	C37	-0.59651	-2.53336	-2.17773
C3	0.07653	-0.62619	-3.31367	C38	0.79036	2.63471	-2.11273
C4	0.05649	0.76198	-3.26891	C39	-0.52249	2.54312	2.50527
C5	0.82727	3.47397	0.18973	C40	0.94517	-2.58271	2.38028
C6	-0.51326	-3.43028	0.10583	C41	2.72497	2.31806	0.84492
C7	0.87936	-3.40244	0.06920	C42	-2.38054	-2.31859	0.88934
C8	-0.56727	3.45501	0.22370	C43	2.73632	-2.23759	-0.67366
C9	1.37923	1.38999	3.14883	C44	-2.45603	2.28898	-0.47079
C10	-0.91715	-1.46447	3.16139	C45	-2.42034	-2.29487	-0.55116
C11	1.25421	-1.34081	-2.91836	C46	2.69074	2.34376	-0.59501
C12	-1.09811	1.46903	-2.80914	C47	-2.41285	2.26272	0.96545
C13	-1.07053	-1.36407	-2.85417	C48	2.76778	-2.25580	0.76391
C14	1.22028	1.48105	-2.83032	C49	2.50488	0.70864	2.68655
C15	-0.94160	1.37104	3.22011	C50	-2.06095	-0.77005	2.77557
C16	1.40272	-1.43718	3.11120	C51	2.39282	-0.63891	-2.50015
C17	1.57536	3.01936	1.32594	C52	-2.21553	0.75101	-2.36691
C18	-1.20906	-3.03339	1.29652	C53	-2.19510	-0.68419	-2.39000
C19	1.56863	-2.95133	-1.10030	C54	2.37369	0.79164	-2.46803
C20	-1.31337	3.02517	-0.92682	C55	-2.07436	0.66220	2.79904
C21	-1.26959	-2.99283	-1.03559	C56	2.52069	-0.72252	2.66300
C22	1.52075	3.06357	-0.99479	C57	3.63394	0.03549	0.77038
C23	-1.25056	2.98604	1.39381	C58	-3.25338	-0.03801	0.92635
C24	1.61887	-2.97582	1.21898	C59	3.59963	0.05717	-0.63807
C25	3.18959	1.17712	1.50953	C60	-3.31069	-0.01374	-0.47038
C26	-2.79743	-1.19939	1.61322	K1	3.80067	3.79500	3.37580
C27	3.14298	-1.08971	-1.36374	K2	6.32432	1.28726	0.00000
C28	-2.89869	1.16316	-1.17715	K3	-3.80067	-3.79500	-3.37580
C29	-2.87902	-1.15338	-1.21450	N1	8.48311	0.44022	0.00000
C30	3.11854	1.22345	-1.31446	C61	9.28885	1.25994	0.91822
C31	-2.80379	1.10883	1.65183	H1	9.89696	2.04399	0.35081
C32	3.21126	-1.13450	1.47624	H2	9.90608	0.70299	1.53707
C33	0.90622	2.55968	2.47056	H3	8.60564	1.93272	1.58582
C34	-0.48377	-2.60992	2.42292	H4	8.49375	-0.52523	0.29842
C35	0.83445	-2.51316	-2.21212	H5	8.88294	0.46603	-0.92767

Table B.3: MAK<sub>3</sub>C<sub>60</sub> atomic positions used for DFT computations.

# C NMR spin-lattice relaxation rate analysis

Spin-lattice relaxation rate was measured using *inversion recovery* pulse sequence [67] where initially reversed magnetization (obtained with a  $\pi$  pulse) is measured (with solid echo pulse sequence) at later times (Fig.C.1a). In the simplest case magnetization is recovered as an exponential function with a characteristic time  $T_1$  – the spin-lattice relaxation time. In practice, the spin-relaxation time is not always equal in all parts of the spectra. In order to take into account small variations in spin-lattice relaxation rate a stretch factor ( $\alpha$ ) is introduced in the magnetization recovery expression,

$$M_z(t) = A + B [1 - \exp(-t/T_1)^\alpha]. \quad (\text{C.1})$$

Here  $A$  and  $B$  are the initial magnetization and the recovered magnetization constants, respectively. To obtain magnetization values at given time the spectrum is integrated over a specified interval (red lines in Fig.C.1a). The resulting magnetization values as a function of time are then fitted with Eq. C.1 in order to obtain  $T_1$  or  $\alpha$ .

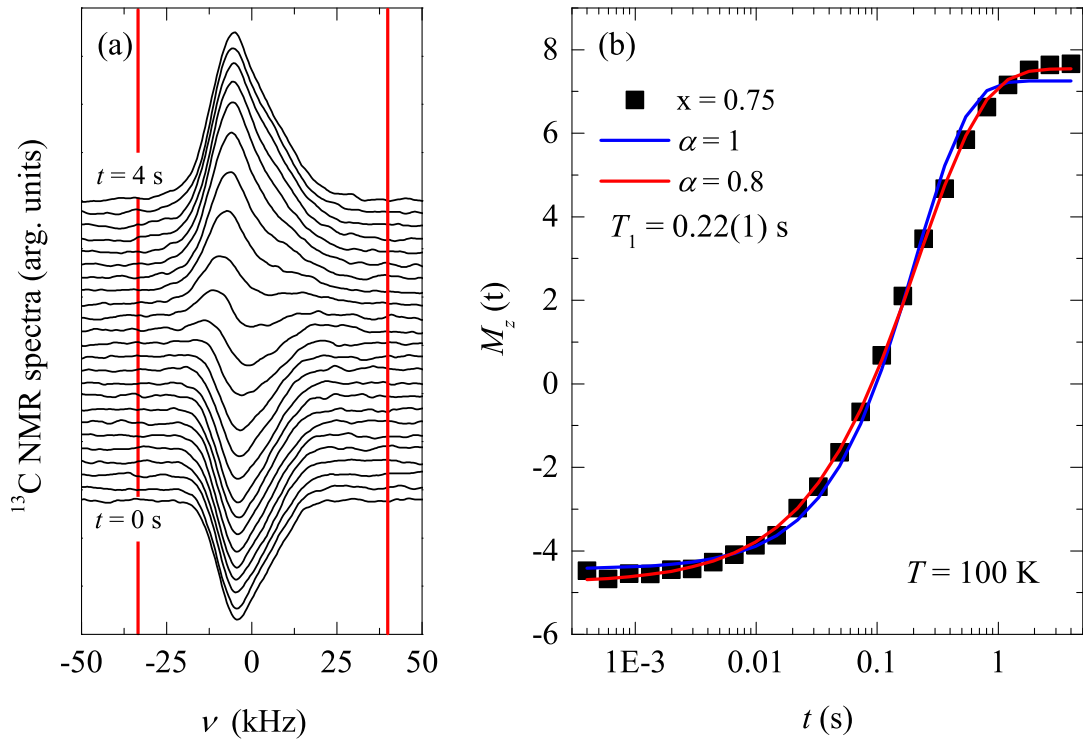


Figure C.1: (a)  $^{13}\text{C}$  NMR inversion recovery spectra for  $\text{Rb}_x\text{Cs}_{3-x}\text{C}_{60}$   $x = 0.75$  compound at  $T = 100$  K. (b) Integral between two red lines of each spectra is fitted with Eq. C.1.

## C.1 High Pressure NMR $1/^{13}T_1$ analysis

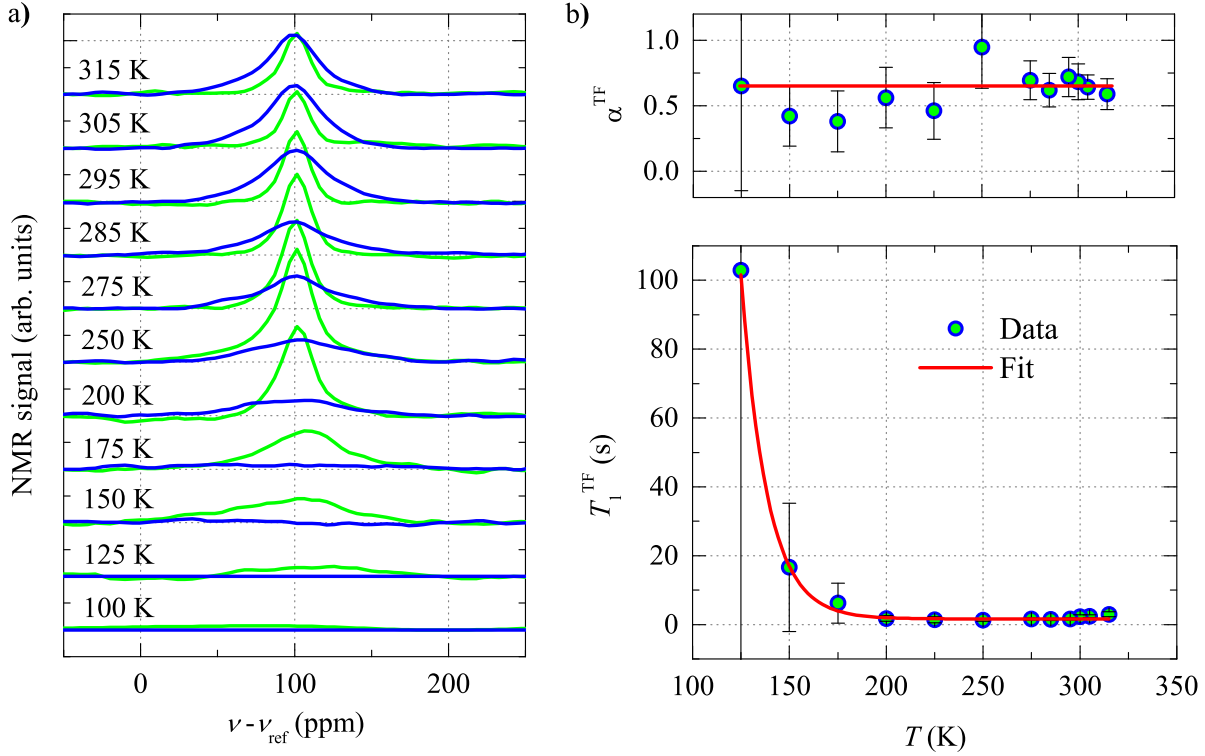


Figure C.2: (a)  $^{13}\text{C}$  NMR signal of a Fluorinert (green) and a Teflon holder (blue). (b) Stretch exponent ( $\alpha$ ) and spin-lattice relaxation time ( $T_1$ ) for Fluorinert and Teflon. Red curve is a fit to the temperature dependent  $T_1$  given by Eq. C.2

$^{13}\text{C}$  NMR probe is of prime importance for  $A_3\text{C}_{60}$  systems since it measures carbon on the  $\text{C}_{60}$  molecules and thus provides a direct, on-site, observation of the electronic properties originating from the  $\text{C}_{60}$   $t_{1u}$  orbitals. In this way the spin-lattice relaxation rate measurements provide unfiltered dynamic spin susceptibility since their structural factor  $A(\vec{q})$  in Eq. 3.53 is  $\vec{q}$  independent. For examples, the structural factors for alkali nuclei in the tetrahedral or octahedral sites are due to the transferred hyperfine interaction  $\vec{q}$  dependent and can even become zero at certain  $\vec{q}$  vectors (Sec. 3.3.2).

Despite important information that  $^{13}\text{C}$  NMR can provide its signal is rather difficult to obtain due to low  $^{13}\text{C}$  natural abundance of 1.1%. In addition, the carbon nuclei are also present in many materials, normally used for NMR experiments, which can give an additional signal that interfere with the one from the sample. For this reason, when measuring  $^{13}\text{C}$  NMR, materials of the NMR experiments are carefully chosen not to contain carbon. However, in high-pressure experiments materials like pressure-transmitting medium and non-conducting soft sample holder can not be substituted with the carbon-free alternatives.

In our high-pressure NMR experiments we used solid polymer Teflon  $-(\text{CF}_2-\text{CF}_2)_n-$  for the sample holder and liquid Fluorinert ( $\text{C}_{15}\text{F}_{33}\text{N}$ ) as a pressure transmitting medium. Both materials are made from carbon atoms and are thus expected to give an additional contribution to our  $^{13}\text{C}$  NMR measurements. The  $^{13}\text{C}$  spectrum of  $\text{Cs}_3\text{C}_{60}$  does not notably differ from the previous  $^{13}\text{C}$  NMR on  $A_3\text{C}_{60}$  spectra [7], however, during the spin-lattice relaxation time measurements we can observe, mostly above 200 K, an additional

two order of magnitude longer relaxation component with a relative intensity of 10-20%. Such a long spin-lattice relaxation time could in principle be attributed to *bco* Cs<sub>x</sub>C<sub>60</sub> impurity phase, however, its small intensity of 7% is not enough to account for the long  $T_1$  relaxation component. The only remaining contributions can come from Teflon and Fluorinert materials. The long relaxation component of several tens of seconds is practically impossible to measure accurately especially for <sup>13</sup>C probe where long data acquisition is required to obtain appreciable signal. The inaccurate determination of long relaxation component is reflected in the poor accuracy of the short component which we are interested in. For this reason we separately measured larger quantities of Teflon and Fluorinert materials and measure their spin-lattice relaxation times which we later used when fitting the <sup>13</sup>C magnetization recovery curve, and thus we reduced the number of fitting parameters (Fig. C.2).

Temperature dependent spin-lattice relaxation time  $T_1$  of the Teflon and Fluorinert sample was fitted with

$$T_1^{\text{TF}}(T) = T_1(0) + \gamma \exp\left(-\frac{T - T_0}{\theta}\right), \quad (\text{C.2})$$

with  $T_1(0) = 1.6$  s,  $\gamma = 100$  s,  $T_0 = 125$  K, and  $\theta = 13.3$  K. The magnetization recovery curve was for every temperature and pressure fitted with

$$M_z(t) = A + B_1 [1 - \exp(-t^\alpha/T_1)] + B_2 \left(1 - \exp[-t^{\alpha^{\text{TF}}}/T_1^{\text{TF}}(T)]\right) \quad (\text{C.3})$$

with  $\alpha^{\text{TF}} = 0.65$  and  $T_1^{\text{TF}}(T)$  given by Eq. C.2. In this way the number of free fitting parameters was reduced to  $A$ ,  $B_1$ ,  $B_2$ ,  $T_1$ , and  $\alpha$ , and thus the spin-lattice relaxation time was determined more precisely.

## C.2 $^{133}\text{Cs}$ NMR spectra decomposition

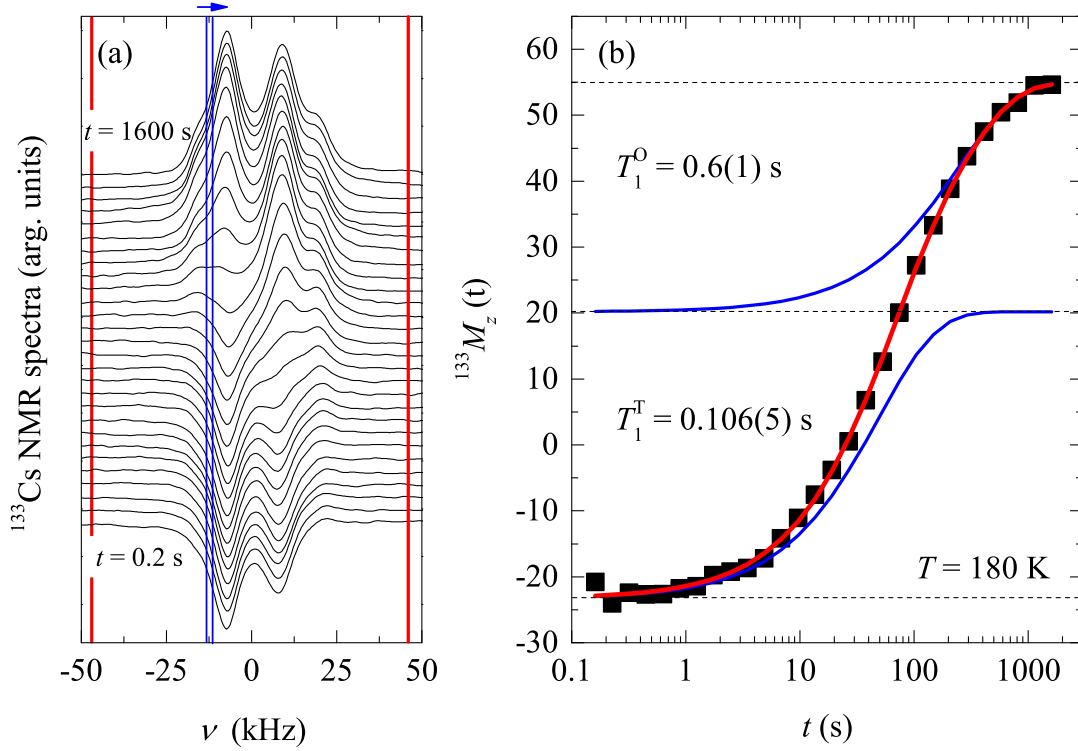


Figure C.3: (a)  $^{133}\text{Cs}$  NMR inversion recovery spectra for  $\text{Rb}_x\text{Cs}_{3-x}\text{C}_{60}$   $x = 0.75$  compound at  $T = 180$  K. (b) Integral between two red lines of each spectra is fitted with two exponential function Eq. C.4. For linescan analysis fitting of Eq. C.4 with fixed spin-lattice relaxation rates is repeated in the narrow interval, between two blue lines, over the whole spectrum.

$^{133}\text{Cs}$  NMR spectra at room temperature show two clearly resolvable lines corresponding to O and T interstitial sites (Fig. 7.6a). However, at low temperatures these two lines merge which makes it impossible to extract their lineshifts based on the spectra alone. Fortunately, their spin-lattice relaxation times are different enough so we can use this information to decompose individual lines using the magnetization recovery data (Fig. C.3a). First we determine both T- and O-site spin-lattice relaxation times by integrating the entire spectrum (within red lines in Fig. C.3a). The obtained magnetization data is fitted with two component exponential model (Fig. C.3b),

$$M_z(t) = A + B^{\text{T}} [1 - \exp(-t/T_1^{\text{T}})] + B^{\text{O}} [1 - \exp(-t/T_1^{\text{O}})]. \quad (\text{C.4})$$

In the next step narrower spectral interval is selected (within blue lines in Fig. C.3a) and after integration the obtained magnetization data is fitted with Eq. C.4 where  $T_1^{\text{T}}$  and  $T_1^{\text{O}}$  are kept fixed with values obtained in the initial step. After fitting, new  $B^{\text{T}}$  and  $B^{\text{O}}$  parameters correspond to the amount of T- and O-site spectral intensity at this narrow interval. In order to extract the individual components this step is repeated along the whole spectrum. Decomposed red and blue spectra in Fig. 7.6a are  $B^{\text{T}}$  and  $B^{\text{O}}$  calculated at each frequency in the narrow interval of  $\Delta\nu = 3$  kHz.

# (Extended Abstract in Slovene)

## Razširjeni povzetek v slovenščini

### Uvod

Fulereni, dopirani z alkalnimi kovinami ( $A_3C_{60}$ ,  $A$  = alkalne kovine), so molekularni superprevodniki z rekordno visoko temperaturo prehoda v superprevodno fazo ( $T_c = 38$  K) [13, 14]. Do pred nedavnim so fulerenski superprevodniki veljali za običajne superprevodnike, ki se jih da razložiti s standardno teorijo superprevodnosti, znano kot teorija Berdena, Cooperja in Shriefferja (BCS) [10]. Vendar je z odkritjem zadnjega in največjega predstavnika te družine,  $Cs_3C_{60}$ , postala ta razlaga vprašljiva. Namreč,  $Cs_3C_{60}$  ni tako kot ostali člani družine prevoden, temveč je izolator pri visokih temperaturah ter antiferomagnetni izolator pri nizkih temperaturah. Šele pod tlakom (cca. 2 kbar)  $Cs_3C_{60}$  postane prevoden in superprevoden pri nizkih temperaturah. Pod visokimi tlaki, kjer je volumen primerljiv z volumnom ostalih članov te družine, njegova temperatura prehoda sovпада s temperaturami prehodov teh članov. S spreminjanjem tlaka ali volumna lahko torej pomerimo celoten fazni diagram. Če vključimo v fazni diagram meritve na  $Cs_3C_{60}$  vidimo, da ima superprevodna faza nemonoton potek v obliki kupole in meji na antiferomagnetno izolatorsko fazo [13, 14]. Takšen diagram je zelo podoben faznim diagramom neobičajnih superprevodnikov, kot so kuprati, železovi pniktidi, težki fermioni in drugi [49]. S tem odkritjem se ponovno postavlja pomembno vprašanje: ali je mogoče fulerenske superprevodnike še vedno opisati s standardno BCS teorijo superprevodnosti ali pa  $A_3C_{60}$  predstavljajo povsem novo družino neobičajnih superprevodnikov.

Fulereni so okrogle  $C_{60}$  molekule v obliki prisekanega ikozaedra, ki so podobne nometnim žogam. Odkrili so jih Kroto, *et al.* [1] med poskusom reprodukcije medzvezdnega materiala v laboratoriju leta 1985. Visoka ikozaedrična simetrija molekule  $C_{60}$  je sprva vzbudila veliko zanimanja med teoretiki, a šele z odkritjem boljšega sinteznega postopka raziskovalcev Kräthmer *et al.*, s katerim lahko danes pridelamo večje količine materiala, so fulereni postali praktično uporabni in so se hitro razširili na različna področja uporabe. Danes so fulereni nepogrešljivi na področjih, kot so kemija fulerenov, tehnologija lubrikantov, razvoj novih sončnih celic ter na področju superprevodnikov. Fulereni so sestavljeni iz 60 ogljikovih atomov, postavljenih v ogliščih prisekanega ikozaedra (Slika 1.1a), ki so med seboj povezani s krajšimi enojnimi (1.391 Å) ter daljšimi dvojnimi vezmi (1.455 Å). Premer molekule  $C_{60}$  je 7.1 Å. Povezani ogljiki na molekuli  $C_{60}$  tvorijo 12 petkotnikov in 20 šestkotnikov. Petkotniki so sestavljeni iz samih enojnih vezi medtem, ko so šestkotniki sestavljeni iz alternirajočih enojnih in dvojnih vezi (Slika 1.1a). Molekula  $C_{60}$  ima visoko ikozaedrično simetrijo ( $I_h$ ) z 15 dvoštevimi rotacijskimi osmi,

20 trištevni osmi, 24 petštevni osmi, simetrijsko operacijo identitete in inverzijo. Kot bomo videli je visoka simetrija molekule ključna za njene specialne lastnosti, saj ikozaedrična simetrija povzroči visoko degeneracijo elektronskih in fononskih molekularnih stanj kar je pomembno za elektronske in superprevodne lastnosti. Na sliki 1.1b so prikazana elektronska stanja proste molekule  $C_{60}$ . Najvišja nezasedena molekularna orbitala  $h_u$  je petkrat degenerirana in polno zasedena, najnižja nezasedena molekularna orbitala  $t_{1u}$  pa je trikrat degenerirana in ne vsebuje nobenega elektrona. Molekule  $C_{60}$  tvorijo kristale, kjer so, podobno kot atomi, molekule  $C_{60}$  postavljene v ploskovno centrirano kubično *pck* strukturo. V kristalni strukturi so molekule  $C_{60}$  odmaknjene druga od druge za 3.1 Å, kar je primerljivo z razdaljo med plastmi grafita (3.35 Å [7]). Zaradi relativno šibke interakcije se lahko fulereni pri visokih temperaturah vrtijo na svojem mestu. Poznamo tri različne načine rotacijske dinamike molekul kot funkcijo temperature [28]: pri visokih temperaturah se molekule vrtijo popolnoma naključno – izotropno. Pri nižjih temperaturah (pod okoli 280 K) se pojavi dvojna dinamika, kjer se molekule hitro reorientirajo okoli izbrane osi, ta pa počasi preskakuje med različnimi smermi. Pri še nižjih temperaturah (150 K) počasno preskakovanje osi zamrzne in ostane le uniaksialna reorientacija molekul  $C_{60}$ . Pri zelo nizkih temperaturah (pod okoli 80 K) zamrzne tudi ta dinamika in molekule postanejo statične. Ko zamrzne izotropna rotacija pri okoli 280 K, kristalna struktura ustreza prostorski grupi  $Pm\bar{3}$ . Vse reorientacije molekul pri nižjih temperaturah so podrejene tej prostorski grupi.

Med  $C_{60}$  molekulami v *pck* strukturi sta dve tetraedrični praznini s premerom 1.1 Å in ena oktaedrična praznina s premerom 2.1 Å znotraj ene osnovne celice (Slika 1.2). V te praznine je zaradi njihove velikosti možno interkalirati atome ali molekule, ki so manjše ali primerljive velikosti. Poseben primer je interkalacija alkalnih kovin, saj se po interkalaciji zunanji elektron alkalne kovine prestavi na molekulo  $C_{60}$ , kar lahko privede do prevodnih lastnosti. Z interkalacijo alkalnih kovin se polni najnižja nezasedena molekularna orbitala  $t_{1u}$ , ki ima lahko do 6 elektronov. Pričakovali bi, da bi bile vse spojine  $A_xC_{60}$  z  $0 < x < 6$  kovinske, vendar se izkaže, da imajo kovinske lastnosti le  $A_3C_{60}$ . Spojine z  $x = 1$  nekontrolirano polimerizirajo [25, 29, 30], spojine z  $x = 2$  so neobstoje in razpadejo na  $x = 1$  ter  $x = 3$  spojine z izjemo  $A = Na$  [31, 32]. Spojine z  $x = 4$ , podobno kot  $Na_2C_{60}$ , tvorijo kristale s telesno centrirano ortorombsko strukturo (*tco*) in so izolatorji kljub temu, da imajo le delno zaseden prevodni pas [15, 25, 31, 32], spojine z  $x = 5$  razpadejo na spojine z  $x = 3$  in  $x = 6$ , kadar pa je interkaliranih vseh šest elektronov ( $A_6C_{60}$ ), je material pasovni izolator [33]. Kovinske in superprevodne lastnosti so torej omejene na polovično zaseden pas. Pokazano je bilo, da se temperatura prehoda v superprevodno fazo strmo spusti, kadar je stehiometrija drugačna od  $x = 3$  [30].

Z interkalacijo treh alkalnih kovin v oktaedrične in tetraedrične praznine ne spremenimo *pck* strukturo  $A_3C_{60}$ . Edina izjema je  $Cs_3C_{60}$ , kjer izredna velikost  $Cs^+$  ionov stabilizira tri polimorfe: *pck*, *A15* oz. telesno centrirano kubično strukturo *tck* ter telesno centrirano ortorombsko strukturo *tco* [14]. Interkalacija večjih ionov alkalnih kovin povečuje osnovno celico kar, kot bomo videli, drastično vpliva na navadne in superprevodne lastnosti  $A_3C_{60}$ . Da bi molekule *pck*  $A_3C_{60}$  zmanjšale interakcijo z velikimi alkalnimi kovinami, se le-te orientirajo tako, da se proti alkalnim kovinam v tetraedričnih votlinah postavijo šestkotniki molekule  $C_{60}$ . Na ta način navidezno povečajo velikost tetraedričnih votlin. S takšno postavitvijo se omeji število možnih orientacij molekul  $C_{60}$  na le dve orientacije, ki se razlikujeta z rotacijo za 90° pravokotno na dvojno vez, ki kaže vzdolž katerekoli kristalne osi. Takšno kristalno strukturo opiše prostorska grupa  $Fm\bar{3}m$  [34]. Zaradi dveh možnih orientacij molekul  $C_{60}$  imajo  $A_3C_{60}$  orientacijski nered tudi, ko molekule  $C_{60}$  postanejo statične. V primeru, ko interkaliramo različne alkalne kovine,

vendar ohranimo njihovo skupno število na 3, kot je npr. pri  $\text{Rb}_x\text{Cs}_{3-x}\text{C}_{60}$ , lahko pride tudi do substitucijskega nereda, kjer so npr. tetraedrične praznine delno zapolnjene z  $\text{Cs}^+$  in delno z  $\text{Rb}^+$  ioni. To sta edina dva možna nereda, ki jih najdemo v *pck*  $A_3\text{C}_{60}$ . Naj omenimo še, da ima A15 polimorf molekule  $\text{Cs}_3\text{C}_{60}$  kristalno strukturo poponoma brez nereda [13]. Zaradi relativno velike razdalje med molekulami  $\text{C}_{60}$  je verjetnost za preskok elektrona iz ene na drugo molekulo majhna. To se odraža v ozki širini prevodnega pasu, izpeljanega iz  $t_{1u}$  molekularnih orbital ( $W \sim 0.5$  eV), če jo primerjamo z energijsko režo med prevodnim ( $t_{1u}$ ) in valenčnim ( $h_u$ ) pasom, ki znaša 1.1 eV [7]. Kovinska faza  $A_3\text{C}_{60}$  spojin je presenetljiva, saj je širina pasu in z njo povezana kinetična energija elektronov manjša od ocenjene odbojne Coulombove interakcije med dvema elektronoma na isti molekuli. Z upoštevanjem efektov senčenja je ta energija,  $U \sim 1$  eV, še vedno večja kot  $W$ , kar bi vodilo do močnih elektronskih korelacij in v lokalizacijo prevodnih elektronov, oz. t.i. Mottovo izolatorsko stanje [5]. Takšno stanje je po vsej verjetnosti prisotno v  $\text{Na}_2\text{C}_{60}$  in  $A_4\text{C}_{60}$  spojinah [31]. Prisotnost močnih elektronskih korelacij v  $A_3\text{C}_{60}$  dodatno potrjuje izolatorsko osnovno stanje fullerenov z interkaliranimi alkalnimi kovinami, ki nimajo kubične strukture. V velike oktaedrične praznine je mogoče poleg alkalne kovine interkalirati tudi nevtralne molekule kot so  $\text{NH}_3$  ali  $\text{CH}_3\text{NH}_2$  (MA), ki zaradi svoje anizotropne oblike porušijo kubično simetrijo kristala. Takšni materiali so  $\text{NH}_3\text{K}_{3-x}\text{Rb}_x\text{C}_{60}$  [17, 35] ali pa  $\text{MAK}_3\text{C}_{60}$  s ploskovno centrirano ortorombsko *pco* osnovno celico [36]. Ze majhna distorzija stran od kubične strukture (največa je  $c = 0.888a$  in  $b = 0.9985a$  pri  $\text{MAK}_3\text{C}_{60}$ ) povzroči izolatorsko stanje. Računi elektronske strukture s teorijo gostotnih funkcionalov (ang. density functional theory ali DFT), kjer se močne elektronske interakcije ne upoštevajo, kažejo, da bi ti materiali morali še vedno biti kovinski, kar je v nasprotju z eksperimentom. To pomeni, da so elektronske korelacije izredno močne in povzročijo lokalizacijo prevodnih elektronov oz. Mottovo izolatorsko stanje [44]. Na kakšen način in do kakšne mere struktura vpliva na osnovno stanje, še vedno ni razjasnjeno.

Zaradi velikega števila relativno lahkih ogljikovih atomov v  $\text{C}_{60}$  ter njihove močne sklopitve preko dvojnih in enojnih vezi imajo intermolekularne vibracije zelo visoko energijo,  $\omega_{\text{ph}} \simeq 0.2$  eV, kar je celo primerljivo s kinetično energijo elektronov ter energijo Coulombove interakcije med elektroni. Vsi ostali fononski načini imajo nižjo energijo, npr. libracije ( $\sim 3$  meV) intermolekularne vibracije ( $\sim 5$  meV), optične vibracije, kjer molekule vibrirajo napram alkalnim kovinam (7–12 meV), kot je prikazano na sliki 1.4. Zaradi visoke simetrije, lahko visoko energijske intramolekularne vibracije interagirajo s trojno-degeneriranimi elektronskimi  $t_{1u}$  orbitalami tudi preko t.i. Jahn-Tellerjevega (JT) pojava. Ta pojav sta odkrila H. Jahn in E. Teller, ki sta prva dokazala JT teorem, ki pravi, da za katerikoli molekularni sistem z degeneriranim elektronskim osnovnim stanjem, ki je posledica simetrije molekule, obstaja interakcija, ki deformira molekulo in zlomi to simetrijo ter odpravi degeneracijo elektronskega osnovnega stanja [6]. Pri  $A_3\text{C}_{60}$  je bil ta pojav prvič predstavljen teoretično [41, 42] in šele kasneje so se na podlagi tega pojavile razlage nekaterih eksperimentalnih rezultatov z JT pojavom [8, 15, 43]. Primer JT deformacije, izračunan za  $A_3\text{C}_{60}$ , je prikazan na sliki 1.5. Superprevodnost v  $A_3\text{C}_{60}$  materialih je bila zanimiva in deležna velike pozornosti že na samem začetku tik po odkritju leta 1991 [9]. Visoka temperatura prehoda ( $T_c = 18$  K), ki je takrat bila tik ob meji maksimalne možne temperature prehoda, kot jo je napovedala teorija BCS, se je nato še povečala s povečevanjem osnovne celice in dosegla maksimalno vrednost  $T_c = 33$  K pri  $\text{RbCs}_2\text{C}_{60}$  [12]. Monotono povečevanje  $T_c$  je bilo v skladu z BCS teorijo, kjer je

temperatura prehoda funkcija gostote stanj  $N(E_F)$  (Enačba 2.11) [46]

$$k_B T_c = 1.14 \hbar \omega_D \exp(-1/\lambda),$$

kjer je  $\lambda = N(E_F) \tilde{V}$  in  $\tilde{V}$  je elektronsko-fononska sklopitvena konstanta. S povečevanjem osnovne celice se povečuje med-molekularna razdalja, s čimer se zmanjšuje prekrivanje elektronskih orbital in s tem verjetnost za preskok elektronov med molekulami. To se odraža v zožanju elektronskih pasov, in ker je število stanja neodvisno od volumna, se gostota stanj pri Fermijevi energiji povečuje. Upoštevajoč BCS enačbo 2.11 se s povečevanjem volumna osnovne celice povečuje tudi  $T_c$ .

S teorijo BCS se je ujemale več eksperimentalnih rezultatov, kot so izotopski efekt, prisotnost t.i. Hebel-Slichterjevega (H-S) vrhu v relaksacijskem času zmerjenim z jedrsko magnetno resonanco (JMR) ter mionsko spinsko rotacijo, superprevodnim razmerjem blizu BCS vrednosti  $2\Delta/k_B T_c = 3.53$  in drugi [7]. Kljub mnogim teoretskim pomislekom in nezmožnostjo kvantitativne napovedi mnogih eksperimentalnih meritev, se je BCS formalizem, bolj točno Migdal–Eliashberg teorija, splošno privzel kot pravi mehanizem superprevodnosti v  $A_3C_{60}$  materialih. Takšen pogled se je močno omajal z odkritjem največjega predstavnika te družine,  $Cs_3C_{60}$ , ki je omogočil konstrukcijo celotnega faznega diagrama  $A_3C_{60}$  družine, kjer ima superprevodna faza nemonotono kupolasto obliko in meji na antiferomagnetno izolatorsko fazo. Takšen fazni diagram je precej bolj podoben faznim diagramom neobičajnih superprevodnikov kot pa običajnim BCS superprevodnikom.

Alternativno teorijo superprevodnosti, prilagojeno prav  $A_3C_{60}$ , so izpeljali Capone *et al.* [62] s pomočjo teorije dinamičnega povprečnega polja (ang. dynamical mean field theory ali DMFT). Pri tej teoriji so avtorji reševali triorbitalni Hubbardov model s Heisenbergovim členom s pomočjo DMFT in iskali antiferomagnetne ter superprevodne rešitve. Upoštevali so močne elektronske korelacije, kar je znotraj približkov povprečnega polja (zanemarjene krajevne prostostne stopnje) obravnavano točno, ter JT in Hundov pojav, v obliki Heisenbergovega člena, saj prvi teži k zmanjševanju skupnega spina in drugi k povečevanju le-tega ( $J_{\text{eff}} = J_{\text{Hund}} - J_{\text{JT}}$ ). Takšno obravnavanje elektronko-fononske sklopitve je eksaktno le v bližini prehoda kovina–izolator (PKI), kjer velja t.i. antiadiabatna limita, kjer so kvazidelci primerljivih ali celo nižjih energij kot intramolekularni fononi. Z upoštevanjem teh efektov so avtorji dobili novo superprevodno fazo v bližini PKI kupolaste oblike, ki meji na antiferomagnetno izolatorsko fazo s faznim prehodom prvega reda. To fazo so poimenovali močno korelirana superprevodna faza.

V tej doktorski disertaciji smo želeli razrešiti mnogo odprtih vprašanj v zvezi z normalno in superprevodno fazo v *pek*  $A_3C_{60}$  sistemih, kot so:

- Kako kristalna struktura vpliva na elektronsko stanje?
- Od kod prihaja misteriozna resonančna črta T' v spektru alkalnih kovin izmerjenih z metodo JMR?
- Kako vpliva strukturni nered na normalno in superprevodno fazo?
- Ali je JT pojav dejansko prisoten v izolatorski in pa tudi v kovinski fazi?
- Kakšen je efekt močnih elektronskih korelacij?
- Kakšen je red prehoda med kovino in izolatorjem in, ali obstaja koeksistenca faz?

- Ali so antiferomagnetne fluktuacije prisotne v bližini prehoda med kovino in izolatorjem?
- Ali so  $A_3C_{60}$  običajni (BCS) superprevodniki ali pa so neobičajni superprevodniki?

Da bi odgovorili na vsa ta vprašanja, smo v tej doktorski disertaciji izdelali visokotlačne celice za meritev JMR in elektronske paramagnetne resonance (EPR) pod visokimi hidrostatskimi tlaki, ter s tehnikam JMR in EPR pomerili vzorce *pck*  $Rb_xCs_{3-x}C_{60}$  z  $x = 0, 0.35, 0.5, 0.75, 1, 2, 3$ ) ter *pco*  $MAK_3C_{60}$ . Detajli visokotlačnih celic in meritev z JMR so opisani v dodatku na koncu disertacije. V nadaljevanju bomo predstavili rezultate raziskave različnih efektov, ki vplivajo na normalne in superprevodne lastnosti fulerenov, dopiranih z alkalnimi kovinami.

## $t_{1u}$ degeneracija

Elektronske in magnetne lastnosti fulerenov, dopiranih z alkalnimi kovinami, so izredno občutljive na odstopanje od kubične strukture. Z odstranitvijo kubične simetrije ti materiali takoj postanejo paramagnetni izolatorji in antiferomagnetni izolatorji pri nizkih temperaturah, kljub temu, da imajo podobne volumne kot drugi kubični kovinski  $A_3C_{60}$ . To na primer velja za  $NH_3Rb_xK_{3-x}C_{60}$  [17, 35] in  $MAK_3C_{60}$  [36, 37]. V tem delu smo želeli odgovoriti na dve pomembni vprašanji: zakaj ti materiali izgubijo kovinske in superprevodne lastnosti ter, ali je mogoče pod visokim tlakom te vzorce ponovno spraviti v kovinsko in superprevodno fazo.

Razlog, zakaj so spojine z ne-kubično osnovno celico izolatorji in po drugi strani, zakaj so tiste s kubično osnovno celico kovine kljub temu, da je Coulombski odboj med dvema elektronoma večji kot njihova kinetična energija, tiči v trojni degeneraciji  $t_{1u}$  stanj. Gunnarsson *et al.*, so pokazali da se zaradi treh degeneriranih stanj efektivna enodelčna širina prevodnega pasu poveča za faktor  $W \rightarrow \sqrt{N_d}W$ , kjer je  $N_d$  število degeneracijskih stanj. Ta faktor je nekoliko ojačan še zaradi frustrirane geometrije *pck* kristalne strukture, kar privede do kritičnega razmerja  $U/W \simeq 2.3$ , pri katerem nastopi PKI [5]. Manini *et al.* [39] so z uporabo DMFT pokazali, da lahko stanja, ki so razcepljena, obravnavamo kot degenerirana vse do tedaj, dokler je razcep manjši od širine prevodnega pasu, izpeljanega iz teh orbital. Vendar se s približevanjem PKI oz., k  $(U/W)_c$  znotraj teorije Fermijeve tekočine efektivna masa kvazidelcev in s tem širina prevodnega pasu renormalizira (zmanjša), kar privede do večje občutljivosti osnovnega stanja na razcep elektronskih stanj. To, da pride do izolatorske faze pri razcepu v točki  $\Gamma$  z  $\Delta = 0.2-0.4W$ , kaže na to, da je renormalizacijski faktor majhen in da je sistem zelo blizu PKI. S pomočjo DMFT so avtorji pokazali, da za fulerene z anizotropno osnovno celico velja t.i. MSDT fazni diagram [39], kjer so različne faze predstavljene kot funkcija  $(U/W)$  in  $(\Delta/W)$  (Slika 4.4). Na tem faznem diagramu je triorbitalna kovinska faza prisotna pri manjših vrednostih  $\Delta/W$  in v limiti, ko je  $\Delta/W = 0$ , sega vse do  $U/W = (U/W)_c$ . Za končne vrednosti  $\Delta/W$  pa kritični  $(U/W)_c$  pada skoraj linearno kot funkcija  $\Delta/W$ .

Da bi preučili obnašanje ortorombskih fulerenov, dopiranih z alkalnimi kovinami, v bližini PKI, smo pomerili  $MAK_3C_{60}$  z EPR pri visokih tlakih (do 7 kbar pri  $\sim 10$  K) in s pomočjo teorije gostotnih funkcijonalov (ang. density functional theory) izračunali nekorelirano elektronsko strukturo. Žal v tem območju  $MAK_3C_{60}$  še ni prešel meje med izolatorjem in kovino, temveč je vseskozi kazal antiferomagnetni prehod, s temperaturo prehoda ( $T_N$ ), ki se je povečevala z zmanjševanjem volumna. Takšno obnašanje je pričakovati, saj zmanjšanje volumna povzroči povečanje prekrivanja molekularnih orbital

in s tem preskakovalnih integralov ( $t$ ). V limiti močnih korelacij se Hubbardov model preslika na Heisnebergov model z  $J = 4t^2/U$ , izmenjalna konstanta pa je sorazmerna z Néelovo temperaturo ( $T_N$ ). Kljub temu, da nismo dosegli PKI, lahko postavimo zgornjo mejo za prehod med kovino in izolatorjem v MSDT faznem diagramu vpeto med točkama  $\Delta/W = 0$ ,  $(U/W)/(U/W)_c = 1$  in  $\Delta/W = 0.2(1)$ ,  $(U/W)/(U/W)_c = 0.93$ . Temu ustreza renormalizacijski faktor v teoriji Fermijeve tekočine  $z = 0.2(1)$  (Slika 4.4).

## Molekulske deformacije

Posebne lastnosti fullerenskih sistemov v veliki meri prihajajo od visoke ikozaedrične simetrije molekul  $C_{60}$ . Visoka stabilnost in togost molekul  $C_{60}$  ohranja to visoko simetrijo tudi v trdni snovi. Zaradi tega je bil efekt deformacije molekul  $C_{60}$  manj raziskan, je pa nedvoumno pomemben za lastnosti fullerenskih sistemov. V tej doktorski disertaciji smo študirali dva tipa deformacij molekul  $C_{60}$ : deformacije zaradi JT pojava in sterične deformacije.

JT pojav, kjer pride do spontane zlomitve simetrije molekule in odstranitve degeneracije osnovnega stanja, je bil pri dopiranih fulerenih najprej opažen pri spojinah  $A_4C_{60}$ . Na teh materialih so z JMR opazili energijsko režo velikosti  $\sim 100$  meV, ki so jo pripisali JT efektu [15, 31], in nekoliko kasneje so na enakih spojinah opazili zlomljeno simetrijo molekule  $C_{60}$  z nevtronskim sipanjem, z meritvami difrakcije X-žarkov ter z infrardečo spektroskopijo [43]. Na kubičnih  $A_3C_{60}$  vzorcih takšnega direktnega dokaza za JT pojav ni bilo, so pa po drugi strani ortorombski fulereni s tremi alkalnimi kovinami v izolatorskem stanju kazali paramagnetne lastnosti, ki ustrezajo stanju z nizkim spinom,  $S = 1/2$ , [16, 18] namesto z visokim spinom,  $S = 3/2$ , kot bi bilo pričakovati za tri dodatne elektrone na molekuli  $C_{60}$ . Nizko spinsko stanje je mogoče realizirati le ob zlomitvi simetrije molekule in odpravitvi degeneracije osnovnega stanja, kar lahko povzroči JT pojav (Slika 5.2). Z odkritjem *pck*  $Cs_3C_{60}$  je bilo opaženo tudi nizko spinsko stanje v paramagnetni in antiferomagnetni izolatorski fazi [13, 14] kar je prvi indirektni dokaz za JT pojav v *pck*  $A_3C_{60}$ .

Prvi direktni dokaz za obstoj JT pojava smo dobili z meritvijo visokoločljivostne JMR, oz. tehnike rotacije vzorca pod magičnim kotom (ang. magic angle spinning, MAS) na  $Cs_3C_{60}$  z merjenem  $^{13}C$  jeder. Molekula  $C_{60}$  ima v  $A_3C_{60}$  kristalni strukturi tri neekvivalentne ogljikove atome (Slika 1.1), ki se v MAS JMR spektru vidijo kot tri ločene črte (vstavljeno v sliki 5.3a). Njihove širine so napram običajnemu JMR spektru močno zožane, saj MAS tehnika navidezno odstrani anizotropno dipolarno interakcijo, ki širi črte. Tukaj moramo poudariti, da se frekvenca vrtenja vzorca med ohlajanjem ni bistveno spreminjala. Preostala širina prihaja iz orientacijskega nereda in od temperaturnih efektov. Z nižanjem temperature se te tri črte opazno širijo in postanejo celo nerazločljive pod  $\sim 150$  K (Slika 5.3b). Edini mehanizem, ki še lahko širi črte ob prisotnosti MAS, je povečevanje števila neekvivalentnih ogljikov, kar pa je v *pck*  $Cs_3C_{60}$  mogoče le če so molekule deformirane zaradi JT pojava. Podobno so ugotovili pred kratkim z infrardečo spektroskopijo na *pck*  $Cs_3C_{60}$  [113]. Z JMR lahko dodatno povemo, da se dinamičen JT pojav upočasnjuje pri nižjih temperaturah in da v tem temperaturnem območju preskakuje med različnimi ekvivalentnimi konfiguracijami na JMR časovni skali ( $\sim 100$  MHz). JT pojav se pri zelo nizkih temperaturah verjetno ustavi v naključnih konfiguracijah, saj difrakcijski eksperimenti z X-žarki ne kažejo odstopanja od ikozaedrične simetrije tudi pri nizkih temperaturah [14].

Visokoresolucijske MAS  $^{13}C$  JMR meritve smo naredili tudi na  $Rb_{0.5}Cs_{2.5}C_{60}$ , ki je

tako blizu PKI, da pod  $T_{\text{MIT}} \sim 110$  K preide iz izolatorskega v kovinsko stanje. Tudi pri tem materialu vidimo podobno obnašanje širine  $^{13}\text{C}$  spektrov tudi pri  $T = 60$  K, ko je vzorec v kovinski fazi (Slika 5.3b). Ti rezultati nedvoumno kažejo na to, da je JT pojav prisoten ne samo v izolatorski, temveč tudi v kovinski fazi blizu PKI. To je pomemben rezultat, ki nakazuje, da je nizko spinsko stanje prisotno tudi v kovinski fazi. Zaradi  $t_{1u}$  simetrije je elektronsko stanje z  $S = 1/2$  invariatno na sferne rotacije in zato lahko nosi tudi orbitalno vrtilno količino. Takšno kovinsko stanje posebno, saj ga ne moremo opisati s teorijo Fermijeve tekočine [149]. Zanimivo je to, da podobno "čudno" kovinsko fazo najdemo tudi pri ostalih neobičajnih superprevodnikih.

Kointerkalacija molekul v oktaedrične votline *per*  $A_3C_{60}$ , kot je npr. pri  $\text{NH}_3\text{K}_3\text{C}_{60}$ ,  $\text{MAK}_3\text{C}_{60}$  ( $\text{MA} = \text{CH}_3\text{NH}_2$ ) ali  $(\text{NH}_3)_3\text{Li}_3\text{C}_{60}$ , lahko privede do zelo kratkih razdalj med molekularnimi protoni in  $\text{C}_{60}^{3-}$ . Na primer, v  $\text{NH}_3\text{K}_3\text{C}_{60}$  je najbližja razdalja N-H...C enaka 2.56 Å [35] in v  $\text{MAK}_3\text{C}_{60}$  je ta razdalja 2.25 – 2.32 Å [36]. Pri  $\text{MAK}_3\text{C}_{60}$  je ta razdalja že dovolj majhna, da pade v območje tipičnih razdalj značilnih za vodikove vezi. Predlagano je bilo, da lahko tako kratke razdalje med protoni in  $\text{C}_{60}$  molekulami močno vplivajo na elektronske in superprevodne lastnosti. Ena takšnih posebnih lastnosti je presenetljivo nizka Néelova temperatura ( $T_N = 11$  K), ki je za red velikosti nižja od Néelovih temperatur ostalih ortorombskih spojin s podobno velikostjo osnovne celice.

Da bi raziskali efekt zmanjševanja osnovne celice na  $\text{C}_{60}$  molekulo v  $\text{MAK}_3\text{C}_{60}$ , smo pomerili EPR pod visokimi pritiski, do 1 GPa pri sobni temperaturi. Opazili smo, da se širina EPR črte s povečevanjem tlaka povečuje bolj kot bi pričakovali za dipolarno razširitev na podlagi izmerjene stisljivosti (Slika 5.4). EPR širina je v sistemih z znatno izmenjalno interakcijo odvisna od dipolarnega faktorja ter obratno sorazmerna z izmenjalno sklopitveno konstanto (Enačba 3.24). Dodatno širitev lahko razložimo le, če se efektivna izmenjalna sklopitvena konstanta zmanjšuje s povečevanjem tlaka, kar je v enostavnih sistemih nemogoče, saj je odvisna od prekrivalnih integralov, ki pa se s tlakom kvečjemu povečujejo. Pri  $\text{MAK}_3\text{C}_{60}$  je zmanjšanje prekrivalnih integralov lahko posledica določenega orbitalnega reda, ki ga povzroči kooperativen JT pojav, kjer se večja elektronska gostota odmakne od dela z večjo elektronsko gostoto sosednjih molekul. Po drugi strani pa je lahko to tudi posledica močnih steričnih efektov, kjer protoni MA molekule lokalno deformirajo molekulo  $\text{C}_{60}$  in na ta način drastično vplivajo na prekrivalne integrale.

Da bi raziskali dogajanje na molekularni ravni v  $\text{MAK}_3\text{C}_{60}$ , smo uporabili DFT v aproksimaciji lokalne gostote (ang. local density approximation, LDA). Kot prvo, naši izračuni kažejo, da bi morala imeti  $\text{MAK}_3\text{C}_{60}$  kovinsko osnovno stanje in ne izolatorsko, kot kaže eksperiment. To pomeni, da so ti materiali dejansko blizu PKI, kjer so močne korelacije pomembne, ki jih pa znotraj DFT ne upoštevamo. JT pojav smo najprej opazili v umetno napihnjeni osnovni celici, kjer smo parametre celice  $\text{MAK}_3\text{C}_{60}$  pomnožili s faktorjem 1.5, v osnovni celici pa pustili le nabito ikozaedrično  $\text{C}_{60}^{3-}$  molekulo. Za kompenzacijo naboja v ozadju je bilo ustrezno poskrbljeno. Po iskanju optimalnih pozicij atomov ogljika, kjer ima sistem najnižjo energijo (relaksacija strukture), smo dobili strukturo z deformirano molekulo  $\text{C}_{60}$ , ki ima  $D_{2h}$  simetrijo, razcepljena stanja v točki  $\Gamma$ , maksimalni odmik od ravnovesne lege za 2 pm ter znižanje energije za 57 meV<sup>1</sup> kar ustreza JT pojavu (Slika 5.5a). Pri umetni strukturi na podlagi  $\text{MAK}_3\text{C}_{60}$ , vendar brez molekul MA, relaksacija ogljikovih atomov ohrani  $D_{2h}$  simetrijo ter podobno energijo JT pojava, čeprav se deformacija nekoliko spremeni (Slika 5.5b). Kadar pa smo

<sup>1</sup>Dejansko znižanje energije po strukturalni relaksaciji je bilo večje zaradi kristalnega polja in popravkov zaradi dolžine vezi znotraj LDA aproksimacije. To energijo smo dobili s primerjavo omenjene relaksacije in takšne, kjer je bilo število elektronov na vsako  $t_{1u}$  orbitalo fiksno, s čimer smo uničili JT pojav.

relaksirali pozicije ogljikovih atomov v realni kristalni strukturi  $\text{MAK}_3\text{C}_{60}$ , deformacija  $\text{C}_{60}$  izgubi  $D_{2h}$  simetrijo, maksimalen odmik od ikozaedrične oblike je 3.4 pm, energija pa je po relaksaciji precej večja kot v primeru JT pojava (Slika 5.5c). S spreminjanjem pozicije MA molekule je lahko opaziti, da se večje deformacije proti središču molekule ujemajo z pozicijo protonov MA molekul, ki so najbližje molekuli  $\text{C}_{60}$  (Slika 5.5d). S tem smo pokazali, da v primeru  $\text{MAK}_3\text{C}_{60}$  sterične deformacije molekule  $\text{C}_{60}$  nadvladajo nad Jahn-Tellerjevimi deformacijami in zato slednje po vsej verjetnosti niso prisotne v  $\text{MAK}_3\text{C}_{60}$ .

## Strukturni nered

Strukturni nered je pomemben efekt, ki ga je potrebno upoštevati med študijem superprevodnih materialov. Efekt nereda na superprevodno stanje je še vedno raziskano področje in še danes se objavljajo novi članki na to temo [202]. Na začetku, ko so bili poznani le običajni BCS superprevodniki, se je nered obravnaval izključno kot efekt, ki uničuje superprevodno stanje in nižja temperaturo prehoda [115]. Vendar pri visokotemperaturnih superprevodnikih na osnovi bakrovih oksidov, superprevodnost nastopi le po dopiranju, ki med drugim povzroči veliko strukturnega nereda. Nered se danes razume kot intrinzična lastnost visokotemperaturnih superprevodnikov – kupratov, kjer elektronske in superprevodne lastnosti lahko variirajo na nano-skali [117].

Pri fullerenskih superprevodnikih je efekt nereda prav tako še precej neraziskan. Ker je za premikanje po faznem diagramu dovolj spreminjanje volumna in zato dopiranje ni potrebno, je nered v fulerenih precej manjši kot npr. pri kupratih. Še več,  $\text{A}_{15}$  polimorf  $\text{Cs}_3\text{C}_{60}$  je celo popolnoma brez strukturnega nereda tudi pod tlakom, kjer kaže superprevodne lastnosti [13]. Ostali fullerenski superprevodniki z *pck* strukturo imajo zaradi prostorske grupe  $Fm\bar{3}m$  orientacijski oz. orientacijski nered molekul  $\text{C}_{60}$ , lahko pa tudi substitucijski nered, kjer oktaedrične ali tetraedrične praznine zasedajo različno veliki alkalijski ioni, npr. v  $\text{Rb}_x\text{Cs}_{3-x}\text{C}_{60}$  za  $x = 1$ . Kljub temu, da je nered prisoten pri *pck*  $\text{A}_3\text{C}_{60}$ , se v splošnem verjame, da je njegov efekt majhen. Vendar bi po drugi strani naj bil ravno orientacijski nered tisti, ki povzroči misteriozno črto T' poleg tetraedrične (T) in oktaedrične (O) črte v JMR spektru, pomerjenem na jadrnih alkalnih kovin [118].

Da bi raziskali efekt orientacijskega in substitucijskega nereda na lastnosti  $\text{A}_3\text{C}_{60}$ , smo pomerili visokoločljivostni MAS  $^{133}\text{Cs}$  JMR na  $\text{Cs}_3\text{C}_{60}$  in  $\text{Rb}_{0.5}\text{Cs}_{2.5}\text{C}_{60}$  vzorcih pri sobni temperaturi. Ker do sedaj še ni bilo pomerjenih spektrov alkalnih kovin pri tako visoki ločljivosti, smo prvič videli ne le tri (O, T in T'), temveč sedem različnih spektralnih črt. Štiri pripadajo oktaedričnem okolju in tri tetraedričnem okolju (Slika 6.1). Pokazali smo, da se vseh sedem črt lahko razloži z dvema orientacijama molekul  $\text{C}_{60}$ , ki obdajata oktaedrične in tetraedrične praznine ter smo s precejšnjo natančnostjo napovedali tudi razmerje intenzitet (Slika 6.2 in 6.3). Zanimivo, T' ustreza najbolj simetrični orientaciji sosednjih molekul  $\text{C}_{60}$  (Slika 6.2a). Poleg tega je zanimivo tudi, zakaj imajo te črte tako velike razmike med seboj. Npr. T' je odmaknjena od glavne T črte za  $\sim 130$  ppm, kar je primerljivo z razmikom med srednjo T in O črto, ki imata popolnoma drugačno okolico, pri čemer imata T in T' enako okolico le z nekoliko zavrtenimi sosednjimi molekulami  $\text{C}_{60}$ . Ena od možnih razlag je prisotnost močnih tokov po površini molekule  $\text{C}_{60}$ . Ta študija je sicer bila že teoretično narejena na izolirani ikozaedrični molekuli  $\text{C}_{60}$ , kjer so opazili le majhne tokove in posledično majhen prispevek k premiku črt alkalnih kovin v bližini molekul  $\text{C}_{60}$  (5–10 ppm) [123], ki pa ni v skladu z našim predlogom. Vendar trdimo, da bi se v primeru pol zapolnjenih  $t_{1u}$  orbital in deformirane  $\text{C}_{60}$  molekule zaradi JT pojava

razmere drastično spremenile, kar bi lahko vodilo do večjih tokov na molekuli.

Na drugi strani substitucijski nered, ki je prisoten pri  $\text{Rb}_{0.5}\text{Cs}_{2.5}\text{C}_{60}$  vpliva na MAS  $^{133}\text{Cs}$  JMR spekter na dva načina. Prvi je generalno širše črte za cca. 50%, in pojavitev dveh dodatnih širokih črt ena pod črtami, ki ustrezajo tetraedričnem mestom ter druga pod črtami, ki ustrezajo oktaedričnem mestom. Drugi pojav je najverjetneje zaradi lokalne zlomitve simetrije, kadar sta vsaj dva alkalna soseda drugega tipa. Poleg oblike spektra je precej bolj očitna razlika v spinsko-mrežnem relaksacijskem času, izmerjenem na teh mestih, kar nakazuje, da je zamenjava Cs atomov z Rb atomi v večji meri spremenila elektronske lastnosti, kar je povezano z manjšim volumnom osnovne celice. Primerjava med *pck* in A15 kristalno strukturo, kaže na to, da makroskopske lastnosti niso močno odvisne, ne od Bravaisove mreže, kot tudi ne od nereda, ki je prisoten v *pck*  $\text{A}_3\text{C}_{60}$ . Efekt nereda lahko ocenimo s primerjavo Néelove ( $T_N = 2.2$  K) in Weissove temperature ( $\theta = -105(2)$  K) [14] pri močno frustriranem *pck*  $\text{Cs}_3\text{C}_{60}$ . Končna Néelova temperatura, kljub frustraciji, je posledica neekvivalentnih prekrivalnih integralov med najbližjimi sosedi, na katere lahko vpliva orientacijski nered. Če je orientacijski nered edini, ki vpliva na prekrivalne integrale, je njegov prispevek največ nekaj procentov. V splošnem to ni nujno res, saj lahko na izmenjalne poti vpliva tudi JT pojav ter ikozaedrična oblika molekul. To pomeni, da je vpliv strukturnega nereda na makroskopske lastnosti kvečjemu za nekaj procentov.

Ugotovili smo, da orientacijski ali substitucijski nered ne vpliva drastično na makroskopske lastnosti, v največji meri za nekaj procentov. Večji vpliv ima na lokalne lastnosti, ki jih lahko izmerimo z JMR. Naše meritve tudi kažejo na močnejše tokove po molekulah  $\text{C}_{60}$ , kot je bilo razumljeno do sedaj.

## Elektronske korelacije

Prisotnost močnih elektronskih korelacij v fullerenskih superprevodnikih je bila pričakovana že od samega začetka raziskovanja teh materialov [7]. Razlog za to je velika Coulonska odbojna interakcija med dvema elektronoma v primerjavi s širino prevodnega pasu  $t_{1u}$ , ki je povezana z elektronsko kinetično energijo. Kljub temu, je bilo splošno sprejeto, da je Coulombska odbojna interakcija močno zasenčena in zato ne vpliva drastično na elektronske in superprevodne lastnosti  $\text{A}_3\text{C}_{60}$ .

Nedavna dognanja, ki so povezana z odkritjem največjega predstavnika fullerenske družine superprevodnikov,  $\text{Cs}_3\text{C}_{60}$ , [13, 14, 124, 125], kjer so močne elektronske korelacije očitno prisotne, kličejo po ponovni evalvaciji prejšnjih argumentov. Med drugim tudi superprevodno stanje v tem območju močno spominja na ostale neobičajne superprevodnike, za katere so značilne močne elektronske korelacije ter bližina s PKI. Močne korelacije imajo torej osrednjo vlogo pri fullerenuh, ki so dopirani z alkalnimi kovinami. Da bi njihove efekte natančneje raziskali, smo z JMR merili  $\text{Cs}_3\text{C}_{60}$  pod visokimi hidrostatskimi tlaki ter  $\text{Rb}_x\text{Cs}_{3-x}\text{C}_{60}$  pri ambientnem tlaku, s čimer smo uspeli prečesati celoten fazni diagram *pck*  $\text{A}_3\text{C}_{60}$ .

Najprej naj omenimo, da ima temperaturna odvisnost inverznega spinsko-mrežnega relaksacijskega časa, deljenega s temperaturo ( $1/T_1T$ ), ki je po Moryinem izrazu sorazmeren dinamični lokalni spinski susceptibilnosti (Enačba 3.53), podobno obnašanje, ne glede na to, na katerem jedru (mestu) merimo ( $^{13}\text{C}$ ,  $^{133}\text{Cs}$  ali  $^{87}\text{Rb}$ ) in ne glede na tehniko merjenja, ali z visokotlačnimi meritvami na  $\text{Cs}_3\text{C}_{60}$  ali pa z meritvami na  $\text{Rb}_x\text{Cs}_{3-x}\text{C}_{60}$  (Slika 7.2). Kot zanimivost naj omenimo, da enako temperaturno obnašanje kaže tudi uniformna spinska susceptibilnost, pomerjena s SQUID magnetometrom (Dodatek B.2.2). Temper-

aturna odvisnost spinske susceptibilnosti ima tri različna območja: visokotemperaturno območje, kjer susceptibilnost sledi Curie-Weissovem zakonu,  $\chi(T) = C/(T - \theta)$ , tipično za izolatorsko stanje, izrazit maksimum pri  $T_{\text{MIT}}$  ter padec susceptibilnosti z zmanjševanjem temperature in ponoven padec pod  $T_c$ , ki je odraz odprtja superprevodne energijske reže. Z zmanjševanjem volumna, bodisi preko povečevanja tlaka ali pa z interkalacijo manjših alkalnih kovin, se  $T_{\text{MIT}}$  prestavlja k višjim temperaturam, padec susceptibilnost pod  $T_{\text{MIT}}$  pa postaja vedno manj izrazit. V limiti zelo majhnih volumnov ( $x > 2$ ) je temperaturna odvisnost spinske susceptibilnosti skoraj konstantna, kar je značilno za kovinsko fazo. Oba skrajna primera sta dobro razumljiva: visoke temperature pri vzorcih z velikim volumnom kažejo izolatorsko obnašanje, nizke temperature pri vzorcih z majhnim volumnom pa kovinsko obnašanje. Vmesna faza, kjer spinska susceptibilnost pada z zmanjševanjem temperature, pa po drugi strani še ni znana.

Medtem, ko je spinsko-mrežni relaksacijski čas pomerjen na različnih jedrih podoben, se premiki spektralnih črt precej bolj razlikujejo med različnimi jedri. Na primer, premik  $^{13}\text{C}$  spektrov je neopazen zaradi velike širine in anizotropije  $^{13}\text{C}$  črt. Podobno obnašanje, kot smo ga pomerili z spinsko-mrežnim relaksacijskim časom, je prisotno le v drugem momentu ali širini  $^{13}\text{C}$  spektra. Premiki črt  $^{133}\text{Cs}$  ali  $^{87}\text{Rb}$  se močno razlikujejo tudi med oktaedričnimi in tetraedričnimi mesti (Slika 7.7). Kljub temu, da premiki prav tako kažejo tri različna območja, je njihov potek skoraj nemogoče direktno primerjati s spinsko susceptibilnostjo, kot smo jo pomerili s spinsko-mrežnim relaksacijskim časom.

Na premike spektralnih črt vplivata dva efekta: kemijski premik, ki je odvisen od lokalnih tokov elektronov v atomskih ali molekularnih orbitalah, ter Knightov premik, ki je sorazmeren lokalni spinski susceptibilnosti (Enačba 7.11),

$$\alpha\delta_{\text{iso}} = \alpha\sigma_{\text{iso}} + \alpha K_{\text{iso}} = \alpha\sigma_{\text{iso}} + \alpha A\chi_s.$$

V zgornji enačbi  $\alpha$  predstavlja ustrezno črto (O, T, ali T'),  $\sigma$  predstavlja kemijski premik,  $A$  pa hiperfine konstanto. Da bi razložili premike črt z enačbo 7.11, smo najprej preverili standarden Jaccarino-Cligston plot, kjer premike črt rišemo kot funkcijo uniformne spinske susceptibilnosti. Ta analiza privzame, da sta tako kemijski premik kot hiperfina konstanta temperaturno neodvisna, kot je pogosto primer. Vendar takšna analiza ne daje realnih rezultatov (Slika 7.8). To pomeni, da sta kemijski premik ali pa hiperfina interakcija temperaturno odvisni. Da bi poenostavili analizo, smo testirali dva enostavna primera. V prvem primeru je kemijski premik temperaturno neodvisen, s temperaturo pa se lahko spreminja hiperfina konstanta, v drugem primeru pa sta vlogi kemijskega premika in hiperfine konstante zamenjani. Pokazali smo, da je bolj verjeten drugi primer, kjer je kemijski premik temperaturno močno odvisen, hiperfina konstanta pa je temperaturno neodvisna. Tak pojav je precej redek, saj je kemijski premik običajno temperaturno neodvisen, v našem primeru pa se lahko spremeni tudi za nekaj sto ppm (Slika 7.10). Vendar, kot smo opazili pri vplivu orientacijskega nereda, bi lahko prisotnost tokov na molekuli  $\text{C}_{60}$  povzročilo tudi dobljene kemijske premike, ki so enakega reda velikosti kot razmik med T in T' črto pri sobni temperaturi. To je še en pokazatelj, da so tokovi na molekuli lahko veliki, kar je med drugim lahko tudi povezano z JT deformacijami molekul  $\text{C}_{60}$ . Moramo pa se zavedati, da je to le poenostavljen model in da bi v realnosti lahko bila temperaturno odvisna oba, tako kemijski premik, kot tudi hiperfina konstanta.

Prisotnost antiferomagnetnih fluktuacij je v bližini PKI znan pojav pri neobičajnih superprevodnikih, kot so kuprati, železovi pniktidi ali organski superprevodniki BEDT-TTF. Pri fullerenskih superprevodnikih direktnega dokaza za antiferomagnetne fluktuacije nimamo. Te se izražajo kot opazen porast inverznega spinsko-mrežnega relaksacijskega časa, deljenega s temperaturo, ki je opazen le na določenih jedrih, kjer se zaradi simetrije

okolice prispevki antiferomagnetnih fluktuacij ne odštejejo. V primeru *pck*  $A_3C_{60}$  bi se antiferomagnetne fluktuacije morale opaziti na tetraedričnih mestih, ne pa na oktaedričnih mestih, kjer se magnetna polja sosedov odštejejo. Efekt antiferomagnetnih fluktuacij bi moral biti viden samo v spinsko-mrežnem relaksacijskem času in ne v Knightovem premiku ali uniformni spinski susceptibilnosti, pomeren s SQUID magnetometrom. Ker noben od naštetih primerov ne velja za *pck*  $A_3C_{60}$  sklepamo, da antiferomagnetne fluktuacije niso prisotne, ali pa so močno zadušene zaradi močno frustrirane *pck* geometrije. Indirektni dokaz za njih je mogoče dobiti iz fenomenološkega Korringinega faktorja  $\beta$  (Eq. 3.83)

$$(T_1T) K^2 = \frac{\hbar}{4\pi k_B} \frac{\gamma_e^2}{\gamma_n^2} \beta.$$

ki je manjši od ena v prisotnosti antiferomagnetnih fluktuacij in večji od ena kadar so prisotne feromagnetne fluktuacije. V primeru  $Rb_xCs_{3-x}C_{60}$  je ta koeficient med 0.2 in 0.5, kar nakazuje na prisotnost antiferomagnetnih fluktuacij. Vendar je potrebno poudariti, da smo za izračun faktorja  $\beta$  uporabili Knightov premik, dobljen iz drugega poenostavljenega modela, ki ni nujno točen.

Temperaturna odvisnost spinske susceptibilnosti pod  $T_{MIT}$  spominja na pseudogap fazo, ki je bila opažena pri kupratih. Takšno fazo napoveduje tudi DMFT v bližini PKI [62]. Vendar je takšno obnašanje spinske susceptibilnosti mogoče razložiti tudi na druge načine. Eden takšnih načinov bi lahko bila koeksistenca kovinske in izolatorske faze. Ta model lahko ovržemo, saj z eksperimentom nismo opazili histereznega obnašanja, ko smo prešli mejo med kovino in izolatorjem med počasnim segrevanjem in ohlajanjem na večjih vzorcih. Drugi možen model je postopno preskakovanje elektronov, ki so najprej bili lokalizirani s spinom  $S = 1/2$ , nato pa zaradi dvojne zasedenosti po preskoku tvorijo spin-singlete, s čimer ne prispevajo več k spinski susceptibilnosti [146].

Temperature prehodov v superprevodno stanje in tiste, ki ustrezajo maksimumu spinske susceptibilnosti, smo postavili na  $(V, T)$  fazni diagram, kjer predstavljajo meje med kovino in superprevodnikom ter med kovino in izolatorjem (Slika 7.15). Točke na superprevodni kupoli se zadovoljivo ujemajo s predhodnimi meritvami na  $A_3C_{60}$ . Meja med kovino in izolatorjem je poševna črta v faznem diagramu, nagnjena proti manjšim volumnom pri višjih temperaturah. Nagnjena črta nakazuje, da imata kovinska in izolatorska faza različni entropiji. Detajlna analiza s Clausius-Clapyronovo enačbo (Enačba 7.13) pokaže, da entropijo paramagnetnega izolatorskega stanja ni le  $S_i = k_B \log 2$ , kot bi bilo pričakovati za enostaven paramagnetni izolator, temveč potrebuje še dodaten prispevek. Najverjetnejši kandidat je JT pojav.

Zanimivo je tudi obnašanje  $1/T_1T$  kot funkcija volumna pri temperaturah tik nad temperaturo prehoda v superprevodno fazo. V kovinski fazi, je namreč  $1/T_1T$  sorazmeren Paulijevi spinski susceptibilnosti, ki pa je sorazmerna z gostoto stanj pri Fermijevi energiji. Na ta način lahko v grobem približku testiramo kaj se dogaja z gostoto stanj, oz. spinsko susceptibilnostjo v bližini PKI. Zbrane meritve  $1/T_1T$  tik na  $T_c$  so prikazane na sliki 7.16. Najprej opazimo, da se spinska susceptibilnost monotono povečuje s povečevanjem volumna. V neposredni bližini PKI susceptibilnost močno naraste. Takšno obnašanje ne moremo pripisati povečevanju gostote stanj pri Fermijevi energiji, kot jo dobimo iz DFT računov, kjer elektronske korelacije niso upoštevane. Precej boljše ujemanje je z rezultati DMFT, ki upoštevajo elektronske korelacije, vendar zanemarijo krajevne prostostne stopnje. Ta približek je najbrž razlog, da ujemanje v neposredni bližini PKI odpove. S to analizo smo pokazali, da so elektronske korelacije prisotne tudi v kovinski fazi in verjetno prav tako v superprevodni fazi.

# Superprevodnost

Fulereni, dopirani z alkalnimi kovinami, so molekularni superprevodniki z rekordno visoko temperaturo prehoda v superprevodno stanje ( $T_c = 38$  K) [13]. Zaradi visoke temperature prehoda so bili fulereni deležni velike pozornosti že kmalu po odkritju superprevodne faze, kar pa se je še okrepilo z odkritjem, da se  $T_c$  še nadaljno povečuje s povečevanjem velikosti osnovne celice. Meritve, ki so bile opravljene na prvih spojinah z manjšimi osnovnimi celicami, so bile v skladu s standardno BCS teorijo superprevodnosti. S časoma se je pojavilo več teoretičnih in tudi eksperimentalnih argumentov, ki so nasprotovali razlagi z BCS teorijo. Najmočnejši dokazi pa so prišli z odkritjem največjega predstavnika,  $Cs_3C_{60}$ , ki ima Mottovo izolatorsko stanje pri ambientnem tlaku [13, 14]. Meritve pod višjimi tlaki, kjer se pojavita kovinska in superprevodna faza, so pokazale, da ima  $Cs_3C_{60}$  nemonoton potek  $T_c$  kot funkcije volumna, kar močno spominja na neobičajne superprevodnike, kot so kuprati, železovi pniktidi in drugi [49].

Ta opažanja postavljajo pomembno vprašanje: ali so  $A_3C_{60}$  še vedno standardni superprevodniki, ki jih je mogoče razložiti znotraj BCS formalizma tudi v bližini PKI, ali pa so to nova družina neobičajnih superprevodnikov, za katere so pomembni efekti, ki jih BCS formalizem ne vključuje. Da bi odgovorili na to vprašanje, smo opravili široko raziskavo superprevodne faze  $A_3C_{60}$  preko celotnega faznega diagrama z uporabo visokotlačnih JMR meritev na *pck*  $Cs_3C_{60}$  in JMR meritev pri ambientnem tlaku na  $Rb_xCs_{3-x}C_{60}$ .

Nemonoton potek  $T_c$ -ja kot funkcije volumna osnovne celice znotraj standardne BCS teorije ni mogoče razumeti, saj je  $T_c$  enolična funkcija gostote stanj pri Fermijevi energiji, ta pa, kot smo pokazali, monoton narašča s povečevanjem osnovne celice. Kvalitativen opis  $T_c$  je v principu mogoč z razširjeno BCS teorijo – Migdal-Eliashberg teorijo, ki vključuje celotno informacijo o fononskem spektru ter Coulombovo odbojno interakcijo v obliki efektivnega renormaliziranega parametra. Nemonoton potek bi lahko dobili, če bi se v bližini PKI ta efektivni parameter močno povečal, kar bi pomenilo, da bi se sklopitev s fononi, ki povzročajo njegovo renormalizacijo, drastično zmanjšati, kar pomeni, da bi drugi fononi postali pomembni za superprevodnost. Še več, če želimo kvantitativno izračunati vrednost  $T_c$  ob ocenjenih vrednostih za Coulombov parameter, gostoto stanje in šibko sklopitveno konstanto, potrebujemo optične fonone kot mediatorje privlačne interakcije med elektroni, ki tvorijo Cooperjeve pare. Naslednji pojav, ki smo ga merili z JMR, je Hebel-Slichterjev koherentni vrh, ki je opazen v spinsko-mrežnem relaksacijskem času tik pod  $T_c$ . Prisotnost H-S vrha je standardni indikator za običajno BCS superprevodnost in je med drugim služila tudi kot ena prvih potrditev BCS teorije. V fullerenskih superprevodnikih je H-S vrh sicer prisoten, vendar je močno potlačen, med drugim tudi zaradi velikega magnetnega polja, ki se uporablja pri JMR eksperimentu. Pri naših eksperimentih na  $Cs_3C_{60}$  in  $Rb_xCs_{3-x}C_{60}$  opazimo le ostanek H-S koherentnega vrha opazen le kot zamaknjen padec spinsko-mrežnega relaksacijskega časa pri temperaturi  $\Delta T_c \sim 4$  K nižje od  $T_c$  pri vzorcih z majhnim volumnom (Slika 8.2). S približevanjem PKI, se  $\Delta T_c$  zmanjšuje in povsem izgine tik ob PKI. Zbirka vseh izmerjenih  $\Delta T_c$  kot funkcija volumna (Slika 8.3) kaže, da je H-S vrh skoraj neodvisen od volumna, dokler pri  $V \simeq 760 \text{ \AA}^3 / C_{60}$  ne začne občutno izginjati. Obstaja več mehanizmov, ki zadušijo in uničijo H-S vrh, kot so magnetno polje, končni življenjski čas Cooperjevih parov, močna elektronsko-fononska sklopitev ter močna elektron-elektronska interakcija. V primeru, ko spreminjamo le velikost osnovne celice, je edina mogoča razlaga za opaženo zadušenje H-S vrha prisotnost močnih elektronske korelacij.

Naslednji parameter, ki smo ga določili iz spinsko-mrežnega relaksacijskega časa v superprevodni fazi, je superprevodno razmerje  $2\Delta/k_B T_c$ . Opaženo eksponentno zmanjšanje

vanje  $1/T_1$  potrjuje, da ima superprevodna reža izotropno obliko in  $s$ -valovno simetrijo (Slika 8.5). To je v nasprotju npr. z kuprati ali organskimi superprevodniki BEDT-TTF, kjer  $1/T_1$  pada proti nič s potenčno odvisnostjo, ki je tipična za močno anizotropni superprevodni ureditveni parameter z  $d$ -valovno simetrijo [7]. Naše meritve kažejo, da je imajo vzorci pri majhnih volumnih ali visokih tlakih vrednost superprevodnega razmerja enako, kot je BCS vrednost  $2\Delta/k_B T_c = 3.53$ . S povečevanjem volumna ali približevanjem PKI se začne superprevodno razmerje povečevati (najbolj pri  $V \simeq 760 \text{ \AA}^3 / C_{60}$ ) in doseže vrednost  $2\Delta/k_B T_c \simeq 5.5$  tik ob PKI (Slika 8.7). Ojačenje superprevodnega razmerja pomeni, da je se ojačila sklopitev med elektroni in fononi. Razširjena BCS teorija za močnejše sklopitve pokaže, da bi za  $2\Delta/k_B T_c \simeq 5.5$  bilo potrebno upoštevati optične fonone kot mediatorje med elektroni v Cooperjevih parih. Ponovno pa se pojavi vprašanje, zakaj bi se pri  $V \simeq 760 \text{ \AA}^3 / C_{60}$  kar tako spremenili relevantni fononi.

BCS formalizem bi še vedno lahko do neke mere razložil eksperimentalne rezultate, v kolikor so optični fononi res prisotni in relevantni za superprevodnost pri  $A_3C_{60}$ . Vendar, ali so optični fononi res prisotni? Obstajajo trije pomembni argumenti proti optičnim fononom: (1) izotopski efekt na alkalnih kovinah je bil znotraj eksperimentalne napake neizmerljiv, (2)  $T_c$  je enolična funkcija volumna in ni odvisna od tipa interkalirane alkalne kovine. To dodatno potrjuje enakovrednost naših meritev pod visokim tlakom na  $Cs_3C_{60}$  vzorcu ter pri ambientnem tlaku na  $Rb_xCs_{3-x}C_{60}$  vzorcih. (3) Znotraj BCS formalizma ni nobenega mehanizma, ki bi izbral ene fonone namesto drugih le na podlagi gostote stanje pri Fermijevi energiji, ki je edini parameter odvisen od volumna osnovne celice. Odsotnost optičnih fononov ter močne elektronske korelacije v superprevodni fazi, kot smo pokazali z analizo H-S vrha, strogo nasprotujejo BCS formalizmu. Zato lahko zaključimo, da  $A_3C_{60}$  niso standardni BCS superprevodniki, temveč so nova družina neobičajnih superprevodnikov, kjer so močne elektronske korelacije osrednjega pomena.

Trenutno se najbolj ujema z eksperimentalnimi rezultati teorija DMFT. Ta napove prisotnost močnih elektronskih korelacij, nemonotono obliko superprevodne faze, ki se dotika antiferomagnetne izolatorske faze, boljše ujemanje spinske susceptibilnosti tik nad  $T_c$  ter odlično ujemanje poteka  $2\Delta/k_B T_c$  z našimi visoko tlačnimi meritvami na  $Cs_3C_{60}$  (Slika 8.7). DMFT je torej trenutno najboljši kandidat za teorijo superprevodnosti na  $A_3C_{60}$ , vendar je potrebno opraviti še več testov, da bi se ta teorija uveljavila. Eden takšnih testov bi lahko bil nadaljno stiskanje  $MAK_3C_{60}$  do tako nizkih volumnov, da bi material postal kovinski. Ključno vprašanje bi bilo, ali bi pri nizkih temperaturah stisnjen  $MAK_3C_{60}$  postal superprevoden ali ne. Če je JT pojav ključen, na čemer temelji DMFT, potem superprevodne faze ne bi bilo moč najti, saj, kot smo pokazali, sterični efekti velike MA molekule prevladajo nad JT pojavom. V nasprotnem primeru, če bi superprevodnost lahko opazili pri relativno visokih temperaturah, potem DMFT ni pravilna teorija superprevodnosti družine  $A_3C_{60}$ .

## Zaključki

V tej doktorski disertaciji smo opravili obsežno študijo normalnih in superprevodnih lastnosti fulerenov, dopiranih z alkalnimi kovinami, po celotnem faznem diagramu. V ta namen smo razvili visokotlačni celici za elektronsko paramagnetno resonančno ter jedrsko magnetno resonančno tehniko, ki nam omogoča meritve pod visokimi tlaki in s tem meritve po celotnem faznem diagramu. Raziskali smo več vplivov na lastnosti dopiranih fulerenov od vloge trojne degeneracije stanj, ki tvorijo prevodni pas, deformacije ikosaedrične molekule  $C_{60}$ , vpliv strukturnega nereda, pomembnost močnih elektronskih

korelacij ter lastnosti superprevodne faze.

Pokazali smo, da zaradi močnih elektronskih korelacij že majhno odstopanje od kubične simetrije, ki dvignejo degeneracijo elektronskih stanj v prevodnem pasu, vodi do Mottovega izolatorskega stanja. Na podlagi visokotlačnih eksperimentov in računov elektronske strukture smo ocenili, da je zgornja meja za renormalizacijski faktor  $z = 0.2 - 0.3$ . S pomočjo visokoločljivostne jedrske magnetne resonance s tehniko vrtenja vzorca pod magičnim kotom ter kriostatom, ki omogoča vrtenje pri kriogenih temperaturah, smo prvič direktno opazili JT pojav pri  $\text{Cs}_3\text{C}_{60}$  v izolatorski fazi ter pri  $\text{Rb}_{0.5}\text{Cs}_{2.5}\text{C}_{60}$  v kovinski fazi v bližini PKI. Ta eksperimentalni rezultat je zelo pomemben, saj kaže na to, da kovinsko fazo v bližini prehoda ni mogoče opisati s teorijo Fermijeve tekočine. Pokazali smo tudi, da pri ortorombski spojini  $\text{MAK}_3\text{C}_{60}$  kratka razdalja med protoni molekule MA in molekulo  $\text{C}_{60}$  povzroči močne sterične efekte, ki deformirajo molekulo in prevladajo nad JT pojavom. To ima drastičen vpliv na elektronsko strukturo in magnetne lastnosti spojine  $\text{MAK}_3\text{C}_{60}$ .

Strukturni nered, ki v ploskovno centriranih kubičnih  $A_3\text{C}_{60}$  spojinah nastopi kot orientacijski oz. orientacijski nered molekul  $\text{C}_{60}$  ali pa kot substitucijski nered, kadar so med molekularnimi prazninami različno veliki alkani atomi, zanemarljivo vpliva na makroskopske lastnosti. Vendar je po drugi strani na lokalni skali njihov vpliv precej bolj izrazit. Z orientacijskim neredom nam je uspelo razložiti prvič opaženih sedem različnih spektralnih črt v jedrsko magnetno resonančnem spektru na jedru  $^{133}\text{Cs}$ . S tem smo dokončno rešili misteriozen izvor dodatne T' črte, ki jo je bilo moč opaziti že s prejšnji eksperimenti na  $A_3\text{C}_{60}$ . Opazili smo tudi, da so molekularni tokovi na  $\text{C}_{60}$  zelo verjetno precej močnejši, kot je bilo razumljeno do sedaj, tudi za faktor 10. Če se bo izkazalo za pravilno ima to pomembne posledice pri analizi premikov spektralnih črt in celo potencialno aplikativno vrednost.

Pokazali smo, da so močne elektronske korelacije prisotne tako v izolatorski kot tudi v kovinski fazi v bližini PKI. Spinska susceptibilnost ima običajno obnašanje v izolatorski ter v kovinski fazi. Po drugi strani pa v vmesnem območju kaže precej nenavadno obnašanje, kjer po izrazitem maksimumu, ki ustreza PKI, spinska susceptibilnost pade z zmanjševanjem temperature. Takšno obnašanje je podobno pseudogap obnašanju, kot je značilno za kuprate. Lahko pa je to tudi posledica povečanega preskakovanja elektronov, ki ob dvojni zasedenosti tvorijo spinske singlete in s tem ne prispevajo več k spinski susceptibilnosti. V bližini PKI kažejo nenavadno kompleksno obnašanje tudi premiki spektralnih črt. Te lahko razlagamo z močno temperaturno odvisnostjo kemijskega premika, kar je v skladu s hipotezo o močnih tokovih na molekulah  $\text{C}_{60}$ , vendar je v praksi to redko opaženo. V vsakem primeru je takšno obnašanje zelo nenavadno in je najbrž specifično za fullerenske sisteme. Rezultati JMR ne ponujajo direktnega dokaza o prisotnosti antiferomagnetnih fluktuacij, tako kot pri ostalih neobičajnih superprevodnikih. Imamo le indirekten dokaz preko Korringinega fenomenološkega faktorja, ki je manjši od ena. Z obširnimi meritvami jedrske magnetne resonance smo prvič detajlno določili meje na celotnem faznem diagramu. Pokazali smo, da se superprevodna kupola odlično ujema s preteklimi meritvami ter, da je meja med kovino in izolatorjem poševna linija. Naklon te linije dodatno potrjuje prisotnost JT pojava v izolatorski fazi.

Z meritvijo superprevodnih lastnosti, kot so temperatura prehoda, Hebel-Slichterjev koherentni vrh ter superprevodno razmerje  $2\Delta/k_B T_c$ , smo dokazali, da  $A_3\text{C}_{60}$  niso običajni BCS superprevodniki, temveč predstavljajo novo družino neobičajnih superprevodnikov. To je morda najpomembnejša ugotovitev te doktorske disertacije. Izmerjene superprevodne lastnosti trenutno najbolje opiše DMFT, ki je bila razvita za  $A_3\text{C}_{60}$ .

# List of publications

## Directly related to this doctoral dissertation

1. POTOČNIK, Anton, MANINI, Nicola, KOMELJ, Matej, TOSATTI, Erio, ARČON, Denis. Orthorhombic fulleride  $(\text{CH}_3\text{NH}_2)\text{K}_3\text{C}_{60}$  close to Mott-Hubbard instability: *ab initio* study. Phys. rev. B, 2012, vol. 86, no. 8, p. 085109-1-085109-7.
2. GANIN, Alexey Yu., JEGLIČ, Peter, ARČON, Denis, POTOČNIK, Anton. Polymorphism control of superconductivity and magnetism in  $\text{Cs}_3\text{C}_{60}$  close to the Mott transition. Nature (Lond.), 2010, vol. 466, no. 7303, p. 221-225.
3. JEGLIČ, Peter, ARČON, Denis, POTOČNIK, Anton, GANIN, Alexey Yu., TAKABAYASHI, Yasuhiro, ROSSEINSKY, Matthew, PRASSIDES, Kosmas. Low-moment antiferromagnetic ordering in triply charged cubic fullerenes close to the metal-insulator transition. Phys. rev. B, 2009, vol. 80, no. 19, p. 195424-1-195424-5.

## Other publications from the field of magnetism and superconductivity

1. HERAK, Mirta, ZORKO, Andrej, PREGELJ, Matej, ZAHARKO, Oksana, POSNJAK, Gregor, JAGLIČIĆ, Zvonko, POTOČNIK, Anton, LUETKENS, H., TOL, J. van, OZAROWSKI, Andrzej, BERGER, Helmuth, ARČON, Denis. Magnetic order and low-energy excitations in the quasi-one-dimensional antiferromagnet  $\text{CuSe}_2\text{O}_5$  with staggered fields. Phys. rev. B, 2013, vol. 87, no. 10, p. 104413-1-104413-12.
2. ZORKO, Andrej, JEGLIČ, Peter, POTOČNIK, Anton, ARČON, Denis, BALČYTIS, A., JAGLIČIĆ, Zvonko, LIU, X., TCHOUGRÉEFF, A. L., DRONSKOWSKI, Richard. Unconventional magnetism in a nitrogen-containing analog of cupric oxide. Phys. rev. lett., 2011, vol. 107, no. 4, p. 047208-1-047208-4.
3. ZORKO, Andrej, PREGELJ, Matej, POTOČNIK, Anton, TOL, J. van, OZAROWSKI, Andrzej, SIMONET, Virginie, LEJAY, P., PETIT, S., BALLOU, Rafik. Role of antisymmetric exchange in selecting magnetic chirality in  $\text{Ba}_3\text{NbFe}_3\text{Si}_2\text{O}_{14}$ . Phys. rev. lett., 2011, vol. 107, no. 25, p. 257203-1-257203-5.
4. HERAK, Mirta, ZORKO, Andrej, ARČON, Denis, POTOČNIK, Anton, KLANJŠEK, Martin, TOL, J. van, OZAROWSKI, Andrzej, BERGER, Helmuth. Symmetric and antisymmetric exchange anisotropies in quasi-one-dimensional  $\text{CuSe}_2\text{O}_5$  as revealed by ESR. Phys. rev., B, 2011, vol. 84, no. 18, p. 184436-1-184436-8.
5. BLINC, Robert, CEVC, Pavel, POTOČNIK, Anton, ŽEMVA, Boris, GORESHNIK, Evgeny A., HANŽEL, Darko, GREGOROVIC, Alan, TRONTELJ, Zvonko, JAGLIČIĆ, Zvonko, LAGUTA, Valentin V., PEROVIĆ, Mara, DALAL, Naresh S.,

- SCOTT, James Floyd. Magnetic properties of multiferroic  $K_3Cr_2Fe_3F_{15}$ . *J. appl. phys.*, 2010, vol. 107, no. 4, p. 043511-1-043511-5.
6. OMERZU, Aleš, ANŽELAK, Bernarda, TUREL, Iztok, ŠTRANČAR, Janez, POTOČNIK, Anton, ARČON, Denis, ARČON, Iztok, MIHAILOVIĆ, Dragan, MATSUI, Hiroshi. Strong correlations in highly electron-doped Zn(II)-DNA complexes. *Phys. rev. lett.*, 2010, vol. 104, no. 15, p. 156804-1-156804-4.
  7. JEGLIČ, Peter, POTOČNIK, Anton, KLANJŠEK, Martin, BOBNAR, Matej, JAGODIČ, Marko, KOCH, Klaus, ROSNER, Helge, MARGADONNA, Serena, LV, B., GULOY, A. M., ARČON, Denis.  $^{75}As$  nuclear magnetic resonance study of antiferromagnetic fluctuations in the normal state of LiFeAs. *Phys. rev. B*, 2010, vol. 81, no. 14, p. 140511-1-140511-4.
  8. POTOČNIK, Anton, ZORKO, Andrej, ARČON, Denis, GORESHNIK, Evgeny A., ŽEMVA, Boris, BLINC, Robert, CEVC, Pavel, TRONTELJ, Zvonko, JAGLIČIĆ, Zvonko, SCOTT, James Floyd. Muon spin relaxation in some multiferroic fluorides. *Phys. rev. B*, 2010, vol. 81, no. 21, p. 214420-1-24420-6.
  9. ARČON, Denis, JEGLIČ, Peter, ZORKO, Andrej, POTOČNIK, Anton, GANIN, Alexey Yu., TAKABAYASHI, Yasuhiro, ROSSEINSKY, Matthew, PRASSIDES, Kosmas. Coexistence of localized and itinerant electronic states in the multiband iron-based superconductor  $FeSe_{0.42}Te_{0.58}$ . *Phys. rev. B*, 2010, vol. 82, no. 14, p. 140508-1-140508-4.
  10. VILFAN, Mojca, POTOČNIK, Anton, KAVČIČ, Blaž, OSTERMAN, Natan, POBERAJ, Igor, VILFAN, Andrej, BABIČ, Dušan. Self-assembled artificial cilia. *Proc. Natl. Acad. Sci. U. S. A.*, 2010, vol. 107, no. 5, p. 1844-1847.
  11. DJERDJ, Igor, CAO, Minhua, ROCQUFELTE, Xavier, ČERNÝ, Radovan, JAGLIČIĆ, Zvonko, ARČON, Denis, POTOČNIK, Anton, GOZZO, Fabia, NIEDERBERGER, Markus. Structural characterization of a nanocrystalline inorganic-organic hybrid with fiberlike morphology and one-dimensional antiferromagnetic properties. *Chem. mater.*, 2009, vol. 21, no. 14, p. 3356-3369.
  12. BLINC, Robert, TAVČAR, Gašper, ŽEMVA, Boris, GORESHNIK, Evgeny A., HANŽEL, Darko, CEVC, Pavel, POTOČNIK, Anton, LAGUTA, Valentin V., TRONTELJ, Zvonko, JAGLIČIĆ, Zvonko, SCOTT, James Floyd. Electron paramagnetic resonance and Mössbauer study of antiferromagnetic  $K_3Cu_3Fe_2F_{15}$ . *J. appl. phys.*, 2009, vol. 106, no. 2, p. 023924-1-023924-4.
  13. UMEK, Polona, GLOTER, Alexandre, PREGELJ, Matej, DOMINKO, Robert, JAGODIČ, Marko, JAGLIČIĆ, Zvonko, ZIMINA, Anna, BRZHEZINSKAYA, Mery, POTOČNIK, Anton, FILIPIČ, Cene, LEVSTIK, Adrijan, ARČON, Denis. Synthesis of 3D hierarchical self-assembled microstructures formed from  $\alpha$ - $MnO_2$  nanotubes and their conducting and magnetic properties. *The journal of physical chemistry C*, 2009, vol. 113, no. 33, p. 14798-14803.
  14. LEVSTIK, Adrijan, FILIPIČ, Cene, BOBNAR, Vid, POTOČNIK, Anton, ARČON, Denis, DRNOVŠEK, Silvo, HOLC, Janez, JAGLIČIĆ, Zvonko. Ordering of polarons in the charge-disordered phase of  $Pr_{0.7}Ca_{0.3}MnO_3$ . *Phys. rev. B*, 2009, vol. 79, no. 15, p. 153110-1-153110-4.

# Bibliography

- [1] H. W. Kroto, J. R. Heath, S. C. O'Brien, R. F. Curl, and R. E. Smalley. C<sub>60</sub>: Buckminsterfullerene. *Nature*, 318(6042):162–163, 1985. URL <http://www.nature.com/nature/journal/v318/n6042/abs/318162a0.html>.
- [2] Maurizio Prato. [60]fullerene chemistry for materials science applications. *J. Mater. Chem.*, 7:1097–1109, 1997. URL <http://dx.doi.org/10.1039/A700080D>.
- [3] Carsten Deibel and Vladimir Dyakonov. Polymer–fullerene bulk heterojunction solar cells. *Reports on Progress in Physics*, 73(9):096401, 2010. URL <http://stacks.iop.org/0034-4885/73/i=9/a=096401>.
- [4] N. Sano, H. Wang, M. Chhowalla, I. Alexandrou, and G. a. J. Amaratunga. Nanotechnology: Synthesis of carbon 'onions' in water. *Nature*, 414(6863):506–507, 2001. URL <http://www.nature.com/nature/journal/v414/n6863/full/414506b.html>.
- [5] Gunnarsson Olle. *Alkali-Doped Fullerenes; Narrow-Band Solids with Unusual Properties*. World Scientific, 1 edition, 2004.
- [6] C. C. Chancey and M.C.M. O'Brian. *The Jahn-Teller Effect in C<sub>60</sub> and Other Icosahedral Complexes*. Princeton University Press, Princeton, New Jersey, 1997.
- [7] Charles H. Pennington and Victor A. Stenger. Nuclear magnetic resonance of C<sub>60</sub> and fulleride superconductors. *Rev. Mod. Phys.*, 68:855–910, Jul 1996. doi: 10.1103/RevModPhys.68.855. URL <http://link.aps.org/doi/10.1103/RevModPhys.68.855>.
- [8] Robert Blinc, Peter Jeglič, Tomaž Apih, Janez Seliger, Denis Arčon, and Aleš Omerzu. Beltlike C<sub>60</sub><sup>-</sup> Electron Spin Density Distribution in the Organic Ferromagnet TDAE-C<sub>60</sub>. *Phys. Rev. Lett.*, 88:086402, 2002. URL <http://link.aps.org/doi/10.1103/PhysRevLett.88.086402>.
- [9] A. F. Hebard, M. J. Rosseinsky, R. C. Haddon, D. W. Murphy, S. H. Glarum, T. T. M. Palstra, A. P. Ramirez, and A. R. Kortan. Superconductivity at 18 K in potassium-doped C<sub>60</sub>. *Nature*, 350(6319):600–601, 1991. URL <http://www.nature.com/nature/journal/v350/n6319/pdf/350600a0.pdf>.
- [10] J. Bardeen, L. N. Cooper, and J. R. Schrieffer. Theory of superconductivity. *Phys. Rev.*, 108:1175–1204, 1957. URL <http://link.aps.org/doi/10.1103/PhysRev.108.1175>.

- [11] M. J. Rosseinsky, A. P. Ramirez, S. H. Glarum, D. W. Murphy, R. C. Haddon, A. F. Hebard, T. T. M. Palstra, A. R. Kortan, S. M. Zahurak, and A. V. Makhija. Superconductivity at 28 K in  $\text{Rb}_x\text{C}_{60}$ . *Phys. Rev. Lett.*, 66(21):2830–2832, 1991. URL <http://link.aps.org/doi/10.1103/PhysRevLett.66.2830>.
- [12] K. Tanigaki, T. W. Ebbesen, S. Saito, J. Mizuki, J. S. Tsai, Y. Kubo, and S. Kuroshima. Superconductivity at 33 K in  $\text{Cs}_x\text{Rb}_y\text{C}_{60}$ . *Nature*, 352(6332):222–223, 1991. URL <http://www.nature.com/nature/journal/v352/n6332/pdf/352222a0.pdf>.
- [13] Y. Takabayashi, A. Y. Ganin, P. Jeglic, D. Arcon, T. Takano, Y. Iwasa, Y. Ohishi, M. Takata, N. Takeshita, K. Prassides, and M. J. Rosseinsky. The Disorder-Free Non-BCS Superconductor  $\text{Cs}_3\text{C}_{60}$  Emerges from an Antiferromagnetic Insulator Parent State. *Science*, 323(5921):1585–1590, 2009. URL <http://www.sciencemag.org/cgi/doi/10.1126/science.1169163>.
- [14] Alexey Y. Ganin, Yasuhiro Takabayashi, Peter Jeglic, Denis Arçon, Anton Potočnik, Peter J. Baker, Yasuo Ohishi, Martin T. McDonald, Manolis D. Tzirakis, Alec McLennan, George R. Darling, Masaki Takata, Matthew J. Rosseinsky, and Kosmas Prassides. Polymorphism control of superconductivity and magnetism in  $\text{Cs}_3\text{C}_{60}$  close to the Mott transition. *Nature*, 466:221–225, 2010. URL <http://www.nature.com/nature/journal/v466/n7303/full/nature09120.html>.
- [15] V. Brouet, H. Alloul, S. Garaj, and L. Forró. Gaps and excitations in fullerides with partially filled bands: NMR study of  $\text{Na}_2\text{C}_{60}$  and  $\text{K}_4\text{C}_{60}$ . *Phys. Rev. B*, 66:155122, 2002. URL <http://link.aps.org/doi/10.1103/PhysRevB.66.155122>.
- [16] Ferenc Simon, András Jánossy, Ferenc Murányi, Titusz Fehér, Hideo Shimoda, Yoshihiro Iwasa, and László Forró. Magnetic resonance in the antiferromagnetic and normal state of  $\text{NH}_3\text{K}_3\text{C}_{60}$ . *Phys. Rev. B*, 61:R3826–R3829, 2000. URL <http://link.aps.org/doi/10.1103/PhysRevB.61.R3826>.
- [17] J. Arvanitidis, K. Papagelis, Y. Takabayashi, T. Takenobu, Y. Iwasa, M. J. Rosseinsky, and K. Prassides. Magnetic ordering in the ammoniated alkali fullerides  $(\text{NH}_3)\text{K}_{3-x}\text{Rb}_x\text{C}_{60}$  ( $x = 2, 3$ ). *Journal of Physics: Condensed Matter*, 19(38):386235, 2007. URL <http://stacks.iop.org/0953-8984/19/i=38/a=386235>.
- [18] Alexey Yu. Ganin, Yasuhiro Takabayashi, Matej Pregelj, Andrej Zorko, Denis Arçon, Matthew J. Rosseinsky, and Kosmas Prassides. EPR Analysis of Spin Susceptibility and Line Width in the Hyperexpanded Fulleride  $(\text{CH}_3\text{NH}_2)\text{K}_3\text{C}_{60}$ . *Chemistry of Materials*, 19(13):3177–3182, 2007. URL <http://pubs.acs.org/doi/abs/10.1021/cm070016p>.
- [19] Jun Nagamatsu, Norimasa Nakagawa, Takahiro Muranaka, Yuji Zenitani, and Jun Akimitsu. Superconductivity at 39 K in magnesium diboride. *Nature*, 410(6824):63–64, 2001. URL <http://www.nature.com/nature/journal/v410/n6824/full/410063a0.html>.
- [20] Cao Wang, Linjun Li, Shun Chi, Zengwei Zhu, Zhi Ren, Yuke Li, Yuetao Wang, Xiao Lin, Yongkang Luo, Shuai Jiang, Xiangfan Xu, Guanghan Cao, and Zhu'an Xu. Thorium-doping-induced superconductivity up to 56 K in  $\text{Gd}_{1-x}\text{Th}_x\text{FeAsO}$ . *EPL (Europhysics Letters)*, 83(6):67006, 2008. URL <http://stacks.iop.org/0295-5075/83/i=6/a=67006>.

- [21] A. Schilling, M. Cantoni, J. D. Guo, and H. R. Ott. Superconductivity above 130 K in the Hg-Ba-Ca-Cu-O system. *Nature*, 363(6424):56–58, 1993. URL <http://www.nature.com/nature/journal/v363/n6424/abs/363056a0.html>.
- [22] H. W. Kroto. Symmetry, Space, Stars and C<sub>60</sub>. Nobel Lecture, December 1996.
- [23] Zhongfang Chen, Judy I. Wu, Clémence Corminboeuf, Jonathan Bohmann, Xin Lu, Andreas Hirsch, and Paul von Ragué Schleyer. Is C<sub>60</sub> buckminsterfullerene aromatic? *Physical Chemistry Chemical Physics*, 14(43):14886, 2012. URL <http://xlink.rsc.org/?DOI=c2cp42146a>.
- [24] R. C. Haddon. Electronic structure, conductivity and superconductivity of alkali metal doped C<sub>60</sub>. *Accounts of Chemical Research*, 25(3):127–133, 1992. URL <http://pubs.acs.org/doi/abs/10.1021/ar00015a005>.
- [25] O. Gunnarsson. Superconductivity in fullerides. *Rev. Mod. Phys.*, 69:575–606, Apr 1997. doi: 10.1103/RevModPhys.69.575. URL <http://link.aps.org/doi/10.1103/RevModPhys.69.575>.
- [26] W. Krätschmer, Lowell D. Lamb, K. Fostiropoulos, and Donald R. Huffman. Solid C<sub>60</sub>: a new form of carbon. *Nature*, 347(6291):354–358, 1990. URL <http://www.nature.com/nature/journal/v347/n6291/abs/347354a0.html>.
- [27] M. J. Rosseinsky. Recent developments in the chemistry and physics of metal fullerides. *Chemistry of materials*, 10(10):2665–2685, 1998. URL <http://pubs.acs.org/doi/abs/10.1021/cm980226p>.
- [28] R. Blinc, J. Seliger, J. Dolinšek, and D. Arčon. Two-dimensional <sup>13</sup>C NMR study of orientational ordering in solid C<sub>60</sub>. *Phys. Rev. B*, 49:4993–5002, 1994. URL <http://link.aps.org/doi/10.1103/PhysRevB.49.4993>.
- [29] R. Tycko, G. Dabbagh, D. W. Murphy, Q. Zhu, and J. E. Fischer. Electronic properties and phase transitions of RbC<sub>60</sub> and CsC<sub>60</sub>: Investigation by nmr spectroscopy. *Phys. Rev. B*, 48:9097–9105, Sep 1993. URL <http://link.aps.org/doi/10.1103/PhysRevB.48.9097>.
- [30] Kosmas Prassides. Fullerenes. *Current Opinion in Solid State and Materials Science*, 2(4):433–439, 1997. URL <http://www.sciencedirect.com/science/article/pii/S135902869780085X>.
- [31] V. Brouet, H. Alloul, F. Quéré, G. Baumgartner, and L. Forró. Detection by NMR of a “Local Spin Gap” in Quenched CsC<sub>60</sub>. *Phys. Rev. Lett.*, 82:2131–2134, 1999. URL <http://link.aps.org/doi/10.1103/PhysRevLett.82.2131>.
- [32] H. Alloul. Electronic Correlations, Jahn-Teller Distortions and Mott Transition to Superconductivity in Alkali-C<sub>60</sub> Compounds. *EPJ Web of Conferences*, 23:00015, 2012. URL [http://epjwoc.epj.org/articles/epjconf/abs/2012/05/epjconf\\_eura2011\\_00015/epjconf\\_eura2011\\_00015.html](http://epjwoc.epj.org/articles/epjconf/abs/2012/05/epjconf_eura2011_00015/epjconf_eura2011_00015.html).
- [33] Matteo Belli. *Magnetic and Transport Properties of Intercalated Fullerides*. PhD thesis, University of Parma, Department of Physics, 2006. URL [http://www.fis.unipr.it/nanocarbon/pdf/theses/PhDthesis\\_belli.pdf](http://www.fis.unipr.it/nanocarbon/pdf/theses/PhDthesis_belli.pdf).

- [34] Peter W. Stephens, Laszlo Mihaly, Peter L. Lee, Robert L. Whetten, Shiou-Mei Huang, Richard Kaner, François Deiderich, and Karoly Holczer. Structure of single-phase superconducting  $K_3C_{60}$ . *Nature*, 351(6328):632–634, 1991.
- [35] M. J. Rosseinsky, D. W. Murphy, R. M. Fleming, and O. Zhou. Intercalation of ammonia into  $K_3C_{60}$ . *Nature*, 364(6436):425–427, 1993. URL <http://www.nature.com/nature/journal/v364/n6436/pdf/364425a0.pdf>.
- [36] Alexey Yu. Ganin, Yasuhiro Takabayashi, Craig A. Bridges, Yaroslav Z. Khimyak, Serena Margadonna, Kosmas Prassides, and Matthew J. Rosseinsky. Methylaminated potassium fulleride,  $(CH_3NH_2)K_3C_{60}$ : Towards hyperexpanded fulleride lattices. *Journal of the American Chemical Society*, 128(46):14784–14785, 2006. URL <http://pubs.acs.org/doi/abs/10.1021/ja066295j>.
- [37] Yasuhiro Takabayashi, Alexey Yu. Ganin, Matthew J. Rosseinsky, and Kosmas Prassides. Direct observation of magnetic ordering in the  $(CH_3NH_2)K_3C_{60}$  fulleride. *Chem. Commun.*, 0:870–872, 2007. URL <http://dx.doi.org/10.1039/B614596E>.
- [38] Serena Margadonna, Kosmas Prassides, Hideo Shimoda, Taishi Takenobu, and Yoshihiro Iwasa. Orientational ordering of  $C_{60}$  in the antiferromagnetic  $(NH_3)K_3C_{60}$  phase. *Phys. Rev. B*, 64:132414, 2001. URL <http://link.aps.org/doi/10.1103/PhysRevB.64.132414>.
- [39] Nicola Manini, Giuseppe E. Santoro, Andrea Dal Corso, and Erio Tosatti. Sensitivity of the mott transition to noncubic splitting of the orbital degeneracy: Application to  $NH_3K_3C_{60}$ . *Phys. Rev. B*, 66:115107, 2002. URL <http://link.aps.org/doi/10.1103/PhysRevB.66.115107>.
- [40] Arthur F. Hebard. Superconductivity in Doped Fullerenes. *Physics Today*, 45(11):26–32, 1992. URL <http://link.aip.org/link/?PTO/45/26/1>.
- [41] Assa Auerbach, Nicola Manini, and Erio Tosatti. Electron-vibron interactions in charged fullerenes. I. Berry phases. *Phys. Rev. B*, 49:12998–13007, 1994. URL <http://link.aps.org/doi/10.1103/PhysRevB.49.12998>.
- [42] Nicola Manini, Erio Tosatti, and Assa Auerbach. Electron-vibron interactions in charged fullerenes. II. Pair energies and spectra. *Phys. Rev. B*, 49:13008–13016, 1994. URL <http://link.aps.org/doi/10.1103/PhysRevB.49.13008>.
- [43] G. Klupp, K. Kamarás, N. M. Nemes, C. M. Brown, and J. Leão. Static and dynamic Jahn-Teller effect in the alkali metal fulleride salts  $A_4C_{60}$  ( $A = K, Rb, Cs$ ). *Phys. Rev. B*, 73:085415, 2006. URL <http://link.aps.org/doi/10.1103/PhysRevB.73.085415>.
- [44] A. Potočnik, N. Manini, M. Komelj, E. Tosatti, and D. Arčon. Orthorhombic fulleride  $(CH_3NH_2)K_3C_{60}$  close to Mott-Hubbard instability: *Ab initio* study. *Phys. Rev. B*, 86:085109, 2012. URL <http://link.aps.org/doi/10.1103/PhysRevB.86.085109>.
- [45] P. Durand, G. R. Darling, Y. Dubitsky, A. Zaopo, and M. J. Rosseinsky. The Mott-Hubbard insulating state and orbital degeneracy in the superconducting  $C_{60}^{3-}$  fulleride family. *Nat. Mater.*, 2:605–610, 2003. URL <http://dx.doi.org/10.1038/nmat953>.

- [46] Michael Tinkham. *Introduction to Superconductivity*. McGraw-Hill Inc., New York, 2 edition, 1996.
- [47] V. A. Stenger, C. H. Pennington, D. R. Buffinger, and R. P. Ziebarth. Nuclear Magnetic Resonance of  $A_3C_{60}$  Superconductors. *Phys. Rev. Lett.*, 74:1649–1652, 1995. URL <http://link.aps.org/doi/10.1103/PhysRevLett.74.1649>.
- [48] Zhe Zhang, Chia-Chun Chen, Stephen P. Kelty, Hongjie Dai, and Charles M. Lieber. The superconducting energy gap of  $Rb_3C_{60}$ . *Nature*, 353(6342):333–335, 1991. URL <http://www.nature.com/nature/journal/v353/n6342/pdf/353333a0.pdf>.
- [49] C. W. Chu. High-temperature superconductivity: Alive and kicking. *Nature Phys.*, 5(11):787–789, 2009. URL <http://www.nature.com/nphys/journal/v5/n11/full/nphys1449.html>.
- [50] Steven C. Erwin and Warren E. Pickett. Theoretical Fermi-Surface Properties and Superconducting Parameters for  $K_3C_{60}$ . *Science*, 254(5033):842–845, 1991. URL <http://www.sciencemag.org/content/254/5033/842.abstract>.
- [51] S. Satpathy, V. P. Antropov, O. K. Andersen, O. Jepsen, O. Gunnarsson, and A. I. Liechtenstein. Conduction-band structure of alkali-metal-doped  $C_{60}$ . *Physical Review B*, 46(3):1773–1793, 1992. URL <http://link.aps.org/doi/10.1103/PhysRevB.46.1773>.
- [52] W. Kohn. Nobel lecture: Electronic structure of matter-wave functions and density functionals. *Rev. Mod. Phys.*, 71:1253–1266, 1999. URL <http://link.aps.org/doi/10.1103/RevModPhys.71.1253>.
- [53] Masatoshi Imada and Takashi Miyake. Electronic Structure Calculation by First Principles for Strongly Correlated Electron Systems. *Journal of the Physical Society of Japan*, 79(11):112001, 2010. URL <http://jpsj.ipap.jp/link?JPSJ/79/112001/>.
- [54] G. R. Darling, A. Y. Ganin, M. J. Rosseinsky, Y. Takabayashi, and K. Prassides. Intermolecular overlap geometry gives two classes of fulleride superconductor: Electronic structure of 38 K  $T_c$   $Cs_3C_{60}$ . *Phys. Rev. Lett.*, 101:136404, 2008. URL <http://link.aps.org/doi/10.1103/PhysRevLett.101.136404>.
- [55] P. Hohenberg and W. Kohn. Inhomogeneous electron gas. *Phys. Rev.*, 136:B864–B871, 1964. URL <http://link.aps.org/doi/10.1103/PhysRev.136.B864>.
- [56] W. Kohn and L. J. Sham. Self-consistent equations including exchange and correlation effects. *Phys. Rev.*, 140:A1133–A1138, 1965. URL <http://link.aps.org/doi/10.1103/PhysRev.140.A1133>.
- [57] J. G. Bednorz and K. A. Müller. Possible high- $T_c$  superconductivity in the Ba-La-Cu-O system. *Zeitschrift für Physik B Condensed Matter*, 64(2):189–193, 1986. URL <http://dx.doi.org/10.1007/BF01303701>.
- [58] V. V. Schmidt. *The Physics of Superconductors: Introduction to Fundamentals and Applications*. Springer-Verlag, Berlin, Heidelberg, 1997.
- [59] J. Bardeen. Theory of the Meissner Effect in Superconductors. *Phys. Rev.*, 97:1724–1725, 1955. URL <http://link.aps.org/doi/10.1103/PhysRev.97.1724>.

- [60] Charles P. Slichter. Magnetic Resonance and Superconductivity: Some History, Ancient and in the Making. *Journal of Superconductivity and Novel Magnetism*, 19(3-5):159–166, 2006. URL <http://link.springer.com/article/10.1007/s10948-006-0151-1>.
- [61] J. P. Carbotte. Properties of boson-exchange superconductors. *Rev. Mod. Phys.*, 62:1027–1157, 1990. URL <http://link.aps.org/doi/10.1103/RevModPhys.62.1027>.
- [62] Massimo Capone, Michele Fabrizio, Claudio Castellani, and Erio Tosatti. *Colloquium: Modeling the unconventional superconducting properties of expanded A<sub>3</sub>C<sub>60</sub> fullerides*. *Rev. Mod. Phys.*, 81:943–958, Jun 2009. doi: 10.1103/RevModPhys.81.943. URL <http://link.aps.org/doi/10.1103/RevModPhys.81.943>.
- [63] Antoine Georges, Gabriel Kotliar, Werner Krauth, and Marcelo J. Rozenberg. Dynamical mean-field theory of strongly correlated fermion systems and the limit of infinite dimensions. *Rev. Mod. Phys.*, 68:13–125, 1996. URL <http://link.aps.org/doi/10.1103/RevModPhys.68.13>.
- [64] Antoine Georges, Luca de’ Medici, and Jernej Mravlje. Strong electronic correlations from Hund’s coupling. *arXiv:1207.3033*, July 2012. URL <http://arxiv.org/abs/1207.3033>.
- [65] Ryogo Kubo and Kazuhisa Tomita. A general theory of magnetic resonance absorption. *Journal of the Physical Society of Japan*, 9(6):888–919, 1954. URL <http://jpsj.ipap.jp/link?JPSJ/9/888/>.
- [66] Plischke Michael and Bergersen Birger. *Equilibrium Statistical Physics*. World Scientific, 3 edition, 2006.
- [67] Charles P. Slichter. *Principles of Magnetic Resonance*. Springer-verlag, 3 edition, 1996.
- [68] G. P. Pake. *Paramagnetic Resonance*. W. A. Benjamin Inc., 2465 Broadway, New York 25, N.Y., 1962.
- [69] Neil W. Ashcroft and David N. Mermin. *Solid State Physics*. Thomson Learning, Toronto, 1 edition, January 1976.
- [70] Charles Kittel. *Introduction to Solid State Physics*. John Wiley and Sons., New York, 8 edition, 2005.
- [71] Tôru Moriya. Anisotropic superexchange interaction and weak ferromagnetism. *Phys. Rev.*, 120:91–98, Oct 1960. URL <http://link.aps.org/doi/10.1103/PhysRev.120.91>.
- [72] T. G. Castner and Mohindar S. Seehra. Antisymmetric exchange and exchange-narrowed electron-paramagnetic-resonance linewidths. *Phys. Rev. B*, 4:38–45, Jul 1971. URL <http://link.aps.org/doi/10.1103/PhysRevB.4.38>.
- [73] J. H. Van Vleck. The dipolar broadening of magnetic resonance lines in crystals. *Phys. Rev.*, 74:1168–1183, Nov 1948. URL <http://link.aps.org/doi/10.1103/PhysRev.74.1168>.

- [74] M. H. Levitt. *Spin Dynamics: Basics of Nuclear Magnetic Resonance*. John Wiley & Sons Ltd., Southern Gate, Chichester, 2 edition, 2008.
- [75] Anatole Abragam. *Principles of Nuclear Magnetism*. Oxford University Press, 1986.
- [76] Pascal P. Man. *Quadrupole Coupling in Nuclear Magnetic Resonance, General, in Encyclopedia of Analytical Chemistry*. John Wiley & Sons, 2000. URL <http://www.pascal-man.com/EACself.pdf>.
- [77] Andrew Smerald and Nic Shannon. Angle-resolved nmr: Quantitative theory of  $^{75}\text{As}$   $T_1$  relaxation rate in  $\text{BaFe}_2\text{As}_2$ . *Phys. Rev. B*, 84:184437, 2011. URL <http://link.aps.org/doi/10.1103/PhysRevB.84.184437>.
- [78] Tôru Moriya. The effect of electron-electron interaction on the nuclear spin relaxation in metals. *J. Phys. Soc. Jpn.*, 18:516–520, 1963. URL <http://jpsj.ipap.jp/link?JPSJ/18/516/>.
- [79] R. Blinc, G. Tavčar, B. Žemva, E. Goreshnik, D. Hanzel, P. Cevc, A. Potočnik, V. Laguta, Z. Trontelj, Z. Jagličič, and J. F. Scott. Electron paramagnetic resonance and mössbauer study of antiferromagnetic  $\text{K}_3\text{Cu}_3\text{Fe}_2\text{F}_{15}$ . *J. Appl. Phys.*, 106(2):023924, 2009. URL <http://link.aip.org/link/?JAP/106/023924/1>.
- [80] A. Zorko, F. Bert, P. Mendels, P. Bordet, P. Lejay, and J. Robert. Easy-axis kagome antiferromagnet: Local-probe study of  $\text{Nd}_3\text{Ga}_5\text{SiO}_{14}$ . *Phys. Rev. Lett.*, 100:147201, 2008. URL <http://link.aps.org/doi/10.1103/PhysRevLett.100.147201>.
- [81] Jürgen Winterlik, Gerhard H. Fecher, Catherine A. Jenkins, Claudia Felser, Claus Mühle, Klaus Doll, Martin Jansen, Leonid M. Sandratskii, and Jürgen Kübler. Challenge of Magnetism in Strongly Correlated Open-Shell  $2p$  Systems. *Phys. Rev. Lett.*, 102:016401, 2009. URL <http://link.aps.org/doi/10.1103/PhysRevLett.102.016401>.
- [82] Volnianska o. and Boguslawski P. Magnetism of solids resulting from spin polarization of  $p$  orbitals. *J. Phys.: Condens. Matter*, 22(7):073202, 2010. URL <http://stacks.iop.org/0953-8984/22/i=7/a=073202>.
- [83] Carrington Alan and McLachlan Andrew D. *Introduction to Magnetic Resonance*. Horper & Row, 1967.
- [84] Tôru Moriya. Nuclear magnetic relaxation in antiferromagnetics. *Progress of Theoretical Physics*, 16(1):23–44, 1956. URL <http://ptp.ipap.jp/link?PTP/16/23/>.
- [85] J. J. van der Klink and H. B. Brom. NMR in metals, metal particles and metal cluster compounds. *Progress in Nuclear Magnetic Resonance Spectroscopy*, 36(2):89–201, 2000. URL <http://www.sciencedirect.com/science/article/pii/S0079656599000205>.
- [86] L. C. Hebel and C. P. Slichter. Nuclear spin relaxation in normal and superconducting aluminum. *Phys. Rev.*, 113:1504–1519, Mar 1959. URL <http://link.aps.org/doi/10.1103/PhysRev.113.1504>.
- [87] Kei Yosida. Paramagnetic susceptibility in superconductors. *Phys. Rev.*, 110:769–770, May 1958. URL <http://link.aps.org/doi/10.1103/PhysRev.110.769>.

- [88] Douglas E. MacLaughlin. Magnetic resonance in the superconducting state. *Solid State Physics*, 31:1 – 69, 1976. URL <http://www.sciencedirect.com/science/article/pii/S008119470860541X>.
- [89] John R. Schrieffer. *Theory of superconductivity*. W. A. Benjamin, New York, 1 edition, 1964.
- [90] Han-Yong Choi. Coulomb Suppression of NMR Coherence Peak in Fullerene Superconductors. *Phys. Rev. Lett.*, 81:441–444, 1998. doi: 10.1103/PhysRevLett.81.441.
- [91] W. A. MacFarlane, R. F. Kiefl, S. Dunsiger, J. E. Sonier, J. Chakhalian, J. E. Fischer, T. Yildirim, and K. H. Chow. Muon-spin-relaxation studies of the alkali-fulleride superconductors. *Phys. Rev. B*, 58:1004–1024, Jul 1998. URL <http://link.aps.org/doi/10.1103/PhysRevB.58.1004>.
- [92] Todd M. Alam and Gary P. Drobny. Solid-state nmr studies of dna structure and dynamics. *Chemical Reviews*, 91(7):1545–1590, 1991. URL <http://pubs.acs.org/doi/abs/10.1021/cr00007a014>.
- [93] Jr. W. M. Walsh and Jr. L. W. Rupp. Enhanced ESR sensitivity using a dielectric resonator. *Review of Scientific Instruments*, 57(9):2278–2279, 1986. URL <http://link.aip.org/link/?RSI/57/2278/1>.
- [94] S. Del Monaco, J. Brivati, G. Gualtieri, and A. Sotgiu. Dielectric resonators in a TE<sub>102</sub> X-band rectangular cavity. *Review of Scientific Instruments*, 66(10):5104–5105, 1995. URL <http://link.aip.org/link/?RSI/66/5104/1>.
- [95] Marek Jaworski, Andrzej Sienkiewicz, and Charles P. Scholes. Double-stacked dielectric resonator for sensitive EPR measurements. *Journal of Magnetic Resonance*, 124(1):87 – 96, 1997. URL <http://www.sciencedirect.com/science/article/pii/S109078079691006X>.
- [96] Andrzej Sienkiewicz, Bertrand Vilenó, Slaven Garaj, Marek Jaworski, and László Forró. Dielectric resonator-based resonant structure for sensitive ESR measurements at high-hydrostatic pressures. *Journal of Magnetic Resonance*, 177(2): 261 – 273, 2005. URL <http://www.sciencedirect.com/science/article/pii/S1090780705002752>.
- [97] Motoyuki Nomura, Yoshiaki Yamamoto, Yukinori Ochiai, and Hiroshi Fujiwara. The measurement of the resistance of manganin wire with the cubic-anvil type pressure apparatus. *Japanese Journal of Applied Physics*, 18(2):363–366, 1979. URL <http://jjap.jsap.jp/link?JJAP/18/363/>.
- [98] J. D. Thompson. Low-temperature pressure variations in a self-clamping pressure cell. *Review of Scientific Instruments*, 55(2):231–234, 1984. URL <http://link.aip.org/link/?RSI/55/231/1>.
- [99] Yoshiya Uwatoko, Sakae Todo, Kazuhiro Ueda, Ahimusa Uchida, Masashi Kosaka, Nobuo Mori, and Takehiko Matsumoto. Material properties of Ni-Cr-Al alloy and design of a 4 GPa class non-magnetic high-pressure cell. *Journal of Physics: Condensed Matter*, 14(44):11291, 2002. URL <http://stacks.iop.org/0953-8984/14/i=44/a=469>.

- [100] S Klotz, J-C Chervin, P Munsch, and G Le Marchand. Hydrostatic limits of 11 pressure transmitting media. *Journal of Physics D: Applied Physics*, 42(7):075413, 2009. URL <http://stacks.iop.org/0022-3727/42/i=7/a=075413>.
- [101] V. A. Sidorov and R. A. Sadykov. Hydrostatic limits of fluorinert liquids used for neutron and transport studies at high pressure. *Journal of Physics: Condensed Matter*, 17(40):S3005, 2005. URL <http://stacks.iop.org/0953-8984/17/i=40/a=002>.
- [102] L. D. Merkle, I. L. Spain, and R. C. Powell. Effects of pressure on the spectra and lifetimes of  $\text{Nd}_x\text{Y}_{1-x}\text{P}_5\text{O}_{14}$  and ruby. *Journal of Physics C: Solid State Physics*, 14(14):2027, 1981. URL <http://stacks.iop.org/0022-3719/14/i=14/a=013>.
- [103] Jon H. Eggert, Kenneth A. Goettel, and Isaac F. Silvera. Ruby at high pressure. I. Optical line shifts to 156 GPa. *Phys. Rev. B*, 40:5724–5732, 1989. URL <http://link.aps.org/doi/10.1103/PhysRevB.40.5724>.
- [104] Kazuko Koyama-Nakazawa, Masahito Koeda, Masato Hedo, and Yoshiya Uwatoko. In situ pressure calibration for piston cylinder cells via ruby fluorescence with fiber optics. *Review of Scientific Instruments*, 78(6):066109, 2007. URL <http://link.aip.org/link/?RSI/78/066109/1>.
- [105] Deirdre D. Ragan, R. Gustavsen, and David Schiferl. Calibration of the ruby  $R_1$  and  $R_2$  fluorescence shifts as a function of temperature from 0 to 600 k. *Journal of Applied Physics*, 72:5539–5544, 1992. URL <http://link.aip.org/link/?JAP/72/5539/1>.
- [106] Olle Gunnarsson, Erik Koch, and Richard M. Martin. Mott-Hubbard insulators for systems with orbital degeneracy. *Physical Review B*, 56(3):1146–1152, 1997. URL <http://link.aps.org/doi/10.1103/PhysRevB.56.1146>.
- [107] Denis Arčon, Alexey Y. Ganin, Yasuhiro Takabayashi, Matthew J. Rosseinsky, and Kosmas Prassides. Magnetic Properties and Phase Transitions in  $(\text{CH}_3\text{NH}_2)\text{K}_3\text{C}_{60}$  Fulleride: An  $^1\text{H}$  and  $^2\text{H}$  NMR Spectroscopic Study. *Chemistry of Materials*, 20(13):4391–4397, 2008. URL <http://pubs.acs.org/doi/abs/10.1021/cm800578e>.
- [108] Denis Arčon, Matej Pregelj, Andrej Zorko, Alexey Yu. Ganin, Matthew J. Rosseinsky, Yasuhiro Takabayashi, Kosmas Prassides, Hans van Tol, and L.-C. Brunel. Antiferromagnetic resonance in methylaminated potassium fulleride  $\text{CH}_3\text{NH}_2\text{K}_3\text{C}_{60}$ . *Phys. Rev. B*, 77:035104, 2008. URL <http://link.aps.org/doi/10.1103/PhysRevB.77.035104>.
- [109] Roberto Macovez, Michael R. C. Hunt, Andrea Goldoni, Maddalena Pedio, and Petra Rudol. Surface Hubbard U of alkali fullerenes. *Journal of Electron Spectroscopy and Related Phenomena*, 183(1-3):94–100, 2011. URL <http://www.sciencedirect.com/science/article/pii/S0368204810001696>.
- [110] P. Jeglič, D. Arčon, A. Potočnik, A. Y. Ganin, Y. Takabayashi, M. J. Rosseinsky, and K. Prassides. Low-moment antiferromagnetic ordering in triply charged cubic fullerenes close to the metal-insulator transition. *Phys. Rev. B*, 80:195424, 2009. URL <http://link.aps.org/doi/10.1103/PhysRevB.80.195424>.

- [111] C. Goze, F. Rachdi, and M. Mehring. High-resolution  $^{13}\text{C}$  NMR investigation in  $\text{Cs}_4\text{C}_{60}$ . *Phys. Rev. B*, 54:5164–5167, 1996. URL <http://link.aps.org/doi/10.1103/PhysRevB.54.5164>.
- [112] N. Sato, H. Tou, Y. Maniwa, K. Kikuchi, S. Suzuki, Y. Achiba, M. Kosaka, and K. Tanigaki. Analysis of  $^{13}\text{C}$  – NMR spectra in  $\text{C}_{60}$  superconductors: Hyperfine coupling constants, electronic correlation effect, and magnetic penetration depth. *Phys. Rev. B*, 58:12433–12440, 1998. URL <http://link.aps.org/doi/10.1103/PhysRevB.58.12433>.
- [113] Gyöngyi Klupp, Péter Matus, Katalin Kamarás, Alexey Y. Ganin, Alec McLennan, Matthew J. Rosseinsky, Yasuhiro Takabayashi, Martin T. McDonald, and Kosmas Prassides. Dynamic Jahn-Teller effect in the parent insulating state of the molecular superconductor  $\text{Cs}_3\text{C}_{60}$ . *Nature Communications*, 3:912, 2012. URL <http://www.nature.com/ncomms/journal/v3/n6/full/ncomms1910.html>.
- [114] P. Dahlke and M. J. Rosseinsky. Molecular Structure, Orientational Order, and Jahn-Teller Distortion of the  $\text{C}_{60}^{4-}$  Anion in  $\text{Cs}_4\text{C}_{60}$ . *Chemistry of Materials*, 14(3):1285–1291, 2002. URL <http://dx.doi.org/10.1021/cm010386s>.
- [115] T. R. Kirkpatrick and D. Belitz. Suppression of superconductivity by disorder. *Phys. Rev. Lett.*, 68:3232–3235, 1992. URL <http://link.aps.org/doi/10.1103/PhysRevLett.68.3232>.
- [116] M. Kraus, H. Sindlinger, H. Werner, R. Schlögl, V. Thommen, H.P. Lang, H.-J. Güntherodt, and K. Lüders. DC-magnetization studies on superconducting fullerenes. *Journal of Physics and Chemistry of Solids*, 57(6-8):999–1003, 1996. URL <http://www.sciencedirect.com/science/article/pii/S0022369795003878>.
- [117] S. H. Pan, J. P. O’Neal, R. L. Badzey, C. Chamon, H. Ding, J. R. Engelbrecht, Z. Wang, H. Eisaki, S. Uchida, A. K. Gupta, K.-W. Ng, E. W. Hudson, K. M. Lang, and J. C. Davis. Microscopic electronic inhomogeneity in the high-Tc superconductor  $\text{Bi}_2\text{Sr}_2\text{CaCu}_2\text{O}_{8+x}$ . *Nature*, 413(6853):282–285, 2001. URL <http://www.nature.com/nature/journal/v413/n6853/full/413282a0.html>.
- [118] M. Kraus, O. Klein, G. Buntkowsky, and K. Lüders. New aspects in the interpretation of the T’ and T  $^{87}\text{Rb}$  NMR lines in  $\text{Rb}_3\text{C}_{60}$ . *Physica B: Condensed Matter*, 271(1-4):7–14, 1999. URL <http://www.sciencedirect.com/science/article/pii/S0921452699002392>.
- [119] Martin P. Gelfand and Jian Ping Lu. Orientational Disorder and Electronic States in  $\text{C}_{60}$  and  $\text{A}_3\text{C}_{60}$ , where A is an Alkali Metal. *Phys. Rev. Lett.*, 68:1050–1053, 1992. URL <http://link.aps.org/doi/10.1103/PhysRevLett.68.1050>.
- [120] G. Zimmer, K. F. Thier, M. Mehring, F. Rachdi, and J. E. Fischer.  $^{87}\text{Rb}$  NMR and the T’ problem in  $\text{Rb}_3\text{C}_{60}$ . *Physical Review B*, 53(9):5620, 1996. URL [http://prb.aps.org/abstract/PRB/v53/i9/p5620\\_1](http://prb.aps.org/abstract/PRB/v53/i9/p5620_1).
- [121] K. Gorny, C. Hahm, J. A. Martindale, S. Yu, C. H. Pennington, D. R. Buffinger, and R. P. Ziebarth. Is  $\text{Rb}_3\text{C}_{60}$  Really  $\text{Rb}_3\text{C}_{60}$ ?. The NMR T, T’ Problem. *Physical review letters*, 79(25):5118–5121, 1997. URL <http://link.aps.org/doi/10.1103/PhysRevLett.79.5118>.

- [122] C. H. Pennington, C. Hahm, V. A. Stenger, K. Gorny, C. H. Recchia, J. A. Martindale, D. R. Buffinger, and R. P. Ziebarth. Double-resonance NMR probes of structural distortions in alkali-metal-fulleride superconductors. *Phys. Rev. B*, 54:R6853–R6856, 1996. URL <http://link.aps.org/doi/10.1103/PhysRevB.54.R6853>.
- [123] Alfredo Pasquarello, Michael Schlüter, and R. C. Haddon. Ring Currents in Icosahedral  $C_{60}$ . *Science*, 257(5077):1660–1661, September 1992. URL <http://www.sciencemag.org/content/257/5077/1660>.
- [124] Y. Ihara, H. Alloul, P. Wzietek, D. Pontiroli, M. Mazzani, and M. Riccò. NMR Study of the Mott Transitions to Superconductivity in the Two  $Cs_3C_{60}$  Phases. *Phys. Rev. Lett.*, 104:256402, 2010. URL <http://link.aps.org/doi/10.1103/PhysRevLett.104.256402>.
- [125] Y. Ihara, H. Alloul, P. Wzietek, D. Pontiroli, M. Mazzani, and M. Riccò. Spin dynamics at the Mott transition and in the metallic state of the  $Cs_3C_{60}$  superconducting phases. *EPL (Europhysics Letters)*, 94(3):37007, 2011. URL <http://stacks.iop.org/0295-5075/94/i=3/a=37007>.
- [126] José Luís Martins and N. Troullier. Structural and electronic properties of  $K_nC_{60}$ . *Phys. Rev. B*, 46:1766–1772, 1992. URL <http://link.aps.org/doi/10.1103/PhysRevB.46.1766>.
- [127] R. C. Haddon, L. E. Brus, and Krishnan Raghavachari. Electronic structure and bonding in icosahedral  $C_{60}$ . *Chemical Physics Letters*, 125(5-6):459–464, 1986. URL <http://www.sciencedirect.com/science/article/pii/0009261486870798>.
- [128] Y. Nomura, K. Nakamura, and R. Arita. *Ab initio* derivation of electronic low-energy models for  $C_{60}$  and aromatic compounds. *Physical Review B*, 85(15):155452, 2012. URL <http://prb.aps.org/abstract/PRB/v85/i15/e155452>.
- [129] M. Z. Huang, Y. N. Xu, and W. Y. Ching. Electronic structures of  $K_3C_{60}$ ,  $RbK_2C_{60}$ ,  $Rb_2KC_{60}$ ,  $Rb_3C_{60}$ ,  $Rb_2CsC_{60}$ , and  $Cs_3C_{60}$  crystals. *Physical Review B*, 46(10):6572, 1992. URL [http://prb.aps.org/abstract/PRB/v46/i10/p6572\\_1](http://prb.aps.org/abstract/PRB/v46/i10/p6572_1).
- [130] W. L. Yang, V. Brouet, X. J. Zhou, Hyoungh J. Choi, Steven G. Louie, Marvin L. Cohen, S. A. Kellar, P. V. Bogdanov, A. Lanzara, A. Goldoni, F. Parmigiani, Z. Husain, and Z.-X. Shen. Band Structure and Fermi Surface of Electron-Doped  $C_{60}$  Monolayers. *Science*, 300(5617):303–307, 2003. URL <http://www.sciencemag.org/content/300/5617/303>.
- [131] R. W. Lof, M. A. van Veenendaal, B. Koopmans, H. T. Jonkman, and G. A. Sawatzky. Band gap, excitons, and Coulomb interaction in solid  $C_{60}$ . *Physical Review Letters*, 68(26):3924–3927, 1992. URL <http://link.aps.org/doi/10.1103/PhysRevLett.68.3924>.
- [132] V. P. Antropov, O. Gunnarsson, and O. Jepsen. Coulomb integrals and model Hamiltonians for  $C_{60}$ . *Phys. Rev. B*, 46:13647–13650, 1992. URL <http://link.aps.org/doi/10.1103/PhysRevB.46.13647>.
- [133] M. B. J. Meinders, L. H. Tjeng, and G. A. Sawatzky. Comment on "C 1s Autoionization Study of Electron Hopping Rates in Solid  $C_{60}$ ". *Phys. Rev. Lett.*, 73:2937–2937, 1994. URL <http://link.aps.org/doi/10.1103/PhysRevLett.73.2937>.

- [134] J. E. Han, E. Koch, and O. Gunnarsson. Metal-insulator transitions: Influence of lattice structure, Jahn-Teller effect, and Hund's rule coupling. *Physical review letters*, 84(6):1276–1279, 2000. URL <http://link.aps.org/doi/10.1103/PhysRevLett.84.1276>.
- [135] R. Tycko, G. Dabbagh, M. J. Rosseinsky, D. W. Murphy, A. P. Ramirez, and R. M. Fleming. Electronic properties of normal and superconducting alkali fullerenes probed by  $^{13}\text{C}$  nuclear magnetic resonance. *Phys. Rev. Lett.*, 68:1912–1915, 1992. URL <http://link.aps.org/doi/10.1103/PhysRevLett.68.1912>.
- [136] W. H. Wong, M. E. Hanson, W. G. Clark, G. Grüner, J. D. Thompson, R. L. Whetten, S.-M. Huang, R. B. Kaner, F. Diederich, P. Petit, J.-J. André, and K. Holczer. Normal-State Magnetic Properties of  $\text{K}_3\text{C}_{60}$ . *EPL (Europhysics Letters)*, 18(1):79, 1992. URL <http://stacks.iop.org/0295-5075/18/i=1/a=015>.
- [137] Michael R. Norman. The Challenge of Unconventional Superconductivity. *Science*, 332(6026):196–200, 2011. URL <http://www.sciencemag.org/content/332/6026/196.abstract>.
- [138] K. Miyagawa, A. Kawamoto, and K. Kanoda. Proximity of Pseudogapped Superconductor and Commensurate Antiferromagnet in a Quasi-Two-Dimensional Organic System. *Phys. Rev. Lett.*, 89:017003, 2002. URL <http://link.aps.org/doi/10.1103/PhysRevLett.89.017003>.
- [139] M. Takigawa.  $^{63}\text{Cu}$  and  $^{17}\text{O}$  NMR studies on the magnetic and superconducting properties of  $\text{YBa}_2\text{Cu}_3\text{O}_{7-y}$ . *Appl. Magn. Reson.*, 3(3-4):495–508, 1992. URL <http://link.springer.com/article/10.1007/BF03166280>.
- [140] A. M. Clogston and V. Jaccarino. Susceptibilities and Negative Knight Shifts of Intermetallic Compounds. *Phys. Rev.*, 121:1357–1362, 1961. URL <http://link.aps.org/doi/10.1103/PhysRev.121.1357>.
- [141] N. J. Curro, B.-L. Young, J. Schmalian, and D. Pines. Scaling in the emergent behavior of heavy-electron materials. *Phys. Rev. B*, 70:235117, 2004. URL <http://link.aps.org/doi/10.1103/PhysRevB.70.235117>.
- [142] H. Alloul, K. Holczer, Y. Yoshinari, and O. Klein.  $^{39}\text{K}$  NMR study of phase transitions and electronic properties in  $\text{K}_3\text{C}_{60}$ . *Physica C: Superconductivity*, 235-240(0):2509 – 2510, 1994. URL <http://www.sciencedirect.com/science/article/pii/0921453494924759>.
- [143] G. Zimmer, K. F. Thier, M. Mehring, and F. Rachdi. NMR on alkali fullerenes. *Applied Magnetic Resonance*, 11(2):263–283, 1996. URL <http://www.springerlink.com/index/VG48651N58G4J568.pdf>.
- [144] V. A. Stenger, C. Recchia, J. Vance, C. H. Pennington, D. R. Buffinger, and R. P. Ziebarth. NMR measurement of superconducting-state spin susceptibility in alkali fullerenes. *Physical Review B*, 48(13):9942–9944, 1993. URL <http://link.aps.org/doi/10.1103/PhysRevB.48.9942>.
- [145] R. R. Walstedt. *The NMR Probe of High- $T_c$  Materials*. Springer, Berlin, Heidelberg, 2008.

- [146] Kazushi Kanoda and Reizo Kato. Mott Physics in Organic Conductors with Triangular Lattices. *Annual Review of Condensed Matter Physics*, 2(1):167–188, 2011. URL <http://www.annualreviews.org/doi/abs/10.1146/annurev-conmatphys-062910-140521>.
- [147] Eddy Yusuf, B. J. Powell, and Ross H. McKenzie. Antiferromagnetic spin fluctuations in the metallic phase of quasi-two-dimensional organic superconductors. *Phys. Rev. B*, 75:214515, 2007. URL <http://link.aps.org/doi/10.1103/PhysRevB.75.214515>.
- [148] M. Mehring, F. Rachdi, and G. Zimmer. Analysis of the  $^{13}\text{C}$  Knight shift and spin-lattice relaxation  $A_3\text{C}_{60}$  ( $A = \text{Rb}$  or  $\text{K}$ ). *Philos. Mag. B*, 70(3):787–794, 1994. URL <http://www.tandfonline.com/doi/abs/10.1080/01418639408240251>.
- [149] Lorenzo De Leo and Michele Fabrizio. Surprises in the Phase Diagram of an Anderson Impurity Model for a Single  $\text{C}_{60}^{n-}$  Molecule. *Phys. Rev. Lett.*, 94(23):236401, 2005. URL <http://link.aps.org/doi/10.1103/PhysRevLett.94.236401>.
- [150] Massimo Capone, Luca de’ Medici, and Antoine Georges. Solving the dynamical mean-field theory at very low temperatures using the Lanczos exact diagonalization. *Phys. Rev. B*, 76:245116, 2007. URL <http://link.aps.org/doi/10.1103/PhysRevB.76.245116>.
- [151] Ivan Kuščer and Slobotan Žumer. *Toplota*. DMFA, Ljubljana, 1987.
- [152] A. P. Ramirez, M. J. Rosseinsky, D. W. Murphy, and R. C. Haddon. Specific-heat jump at  $T_c$  and normal-state magnetic susceptibility of  $A_3\text{C}_{60}$ . *Phys. Rev. Lett.*, 69:1687–1690, 1992. URL <http://link.aps.org/doi/10.1103/PhysRevLett.69.1687>.
- [153] Yutaka Maniwa, Takahito Saito, Atushi Ohi, Kenji Mizoguchi, Kiyoshi Kume, Koichi Kikuchi, Isao Ikemoto, Shinzo Suzuki, Yohji Achiba, Mayumi Kosaka, Katsumi Tanigaki, and Thomas W. Ebbesen. Electronic States and Superconductivity in Alkali-Intercalated Fullerenes:  $^{13}\text{C}$ -NMR Study in  $\text{Na}_2\text{RbC}_{60}$ ,  $\text{Na}_2\text{CsC}_{60}$ ,  $\text{K}_3\text{C}_{60}$ ,  $\text{K}_2\text{RbC}_{60}$ ,  $\text{K}_2\text{CsC}_{60}$ ,  $\text{KRbCsC}_{60}$ ,  $\text{Rb}_2\text{CsC}_{60}$  and  $\text{RbCs}_2\text{C}_{60}$ . *Journal of the Physical Society of Japan*, 63(3):1139–1148, 1994. URL <http://jpsj.ipap.jp/link?JPSJ/63/1139/>.
- [154] G. Quirion, C. Bourbonnais, E. Barthel, P. Auban, D. Jérôme, J. M. Lambert, A. Zahab, P. Bernier, C. Fabre, and A. Rassat.  $^{13}\text{C}$  Nuclear Relaxation and Normal-State Properties of  $\text{K}_3\text{C}_{60}$  under Pressure. *Euro Phys. Lett.*, 21(2):233, 1993. URL <http://iopscience.iop.org/0295-5075/21/2/019>.
- [155] F. Aryasetiawan, O. Gunnarsson, E. Koch, and R. M. Martin. Pauli susceptibility of  $A_3\text{C}_{60}$  ( $A=\text{K},\text{Rb}$ ). *Phys. Rev. B*, 55:R10165–R10168, 1997. URL <http://link.aps.org/doi/10.1103/PhysRevB.55.R10165>.
- [156] D. B. McWhan, J. P. Remeika, T. M. Rice, W. F. Brinkman, J. P. Maita, and A. Menth. Electronic Specific Heat of Metallic Ti-Doped  $\text{V}_2\text{O}_3$ . *Phys. Rev. Lett.*, 27:941–943, 1971. URL <http://link.aps.org/doi/10.1103/PhysRevLett.27.941>.

- [157] W. F. Brinkman and T. M. Rice. Application of Gutzwiller's Variational Method to the Metal-Insulator Transition. *Phys. Rev. B*, 2:4302–4304, 1970. URL <http://link.aps.org/doi/10.1103/PhysRevB.2.4302>.
- [158] A. M. Finkel'stein. Weak localization and coulomb interaction in disordered systems. *Zeitschrift für Physik B Condensed Matter*, 56(3):189–196, 1984. URL <http://dx.doi.org/10.1007/BF01304171>.
- [159] V. Buntar and H. W. Weber. Magnetic properties of fullerene superconductors. *Superconductor Science and Technology*, 9(8):599–616, 1996. URL <http://sprg.ssl.berkeley.edu/~cepheid/240b/u608r1.pdf>.
- [160] R. Akis, C. Jiang, and J.P. Carbotte. Quasiparticle damping, anisotropy and Fermi liquid corrections to NMR in superconductors. *Physica C: Superconductivity*, 176(4–6):485–495, 1991. URL <http://www.sciencedirect.com/science/article/pii/0921453491900532>.
- [161] R. F. Kiefl, W. A. MacFarlane, K. H. Chow, S. Dunsiger, T. L. Duty, T. M. S. Johnston, J. W. Schneider, J. Sonier, L. Brard, R. M. Strongin, J. E. Fischer, and A. B. Smith. Coherence peak and superconducting energy gap in  $\text{Rb}_3\text{C}_{60}$  observed by muon spin relaxation. *Phys. Rev. Lett.*, 70:3987–3990, 1993. doi: 10.1103/PhysRevLett.70.3987.
- [162] Takashi Imai, Tadashi Shimizu, Hiroshi Yasuoka, Yutaka Ueda, and Koji Kosuge. Anomalous Temperature Dependence of Cu Nuclear Spin-Lattice Relaxation in  $\text{YBa}_2\text{Cu}_3\text{O}_{6.91}$ . *Journal of the Physical Society of Japan*, 57(7):2280–2283, 1988. URL <http://jpsj.ipap.jp/link?JPSJ/57/2280/>.
- [163] Y. Kohori, Y. Yamato, Y. Iwamoto, T. Kohara, E. D. Bauer, M. B. Maple, and J. L. Sarrao. NMR and NQR studies of the heavy fermion superconductors  $\text{CeTIn}_5$  ( $T = \text{Co}$  and  $\text{Ir}$ ). *Phys. Rev. B*, 64:134526, Sep 2001. doi: 10.1103/PhysRevB.64.134526.
- [164] Yusuke Nakai, Kenji Ishida, Yoichi Kamihara, Masahiro Hirano, and Hideo Hosono. Evolution from Itinerant Antiferromagnet to Unconventional Superconductor with Fluorine Doping in  $\text{LaFeAs}(\text{O}_{1-x}\text{F}_x)$  Revealed by  $^{75}\text{As}$  and  $^{139}\text{La}$  Nuclear Magnetic Resonance. *Journal of the Physical Society of Japan*, 77(7):073701, 2008. URL <http://jpsj.ipap.jp/link?JPSJ/77/073701/>.
- [165] Prassides, K. *et al.* to be published, 2013.
- [166] Susumu Sasaki, Azusa Matsuda, and C. W. Chu. Fermi-Liquid Behavior and BCS  $s$ -Wave Pairing of  $\text{K}_3\text{C}_{60}$  Observed by  $^{13}\text{C}$ -NMR. *Journal of the Physical Society of Japan*, 63(5):1670–1673, 1994. URL <http://jpsj.ipap.jp/link?JPSJ/63/1670/>.
- [167] P. Jess, U. Hübner, S. Behler, V. Thommen-Geiser, H.P. Lang, and H.-J. Güntherodt. Spatially resolved electron tunneling spectroscopy on single crystalline  $\text{Rb}_3\text{C}_{60}$ . *Synthetic Metal*, 77(1-3):201–203, 1996. URL <http://www.sciencedirect.com/science/article/pii/0379677996800877>.
- [168] L. Degiorgi, G. Briceno, M. S. Fuhrer, A. Zettl, and P. Wachter. Optical measurements of the superconducting gap in single-crystal  $\text{K}_3\text{C}_{60}$  and  $\text{Rb}_3\text{C}_{60}$ . *Nature*, 369(6481):541–543, 1994. URL <http://www.nature.com/nature/journal/v369/n6481/pdf/369541a0.pdf>.

- [169] Daniel Koller, Michael C. Martin, László Mihály, György Mihály, Gábor Oszlányi, Gabriel Baumgartner, and László Forró. Energy Gap in Superconducting Fullerides: Optical and Tunneling Studies. *Phys. Rev. Lett.*, 77:4082–4085, 1996. URL <http://link.aps.org/doi/10.1103/PhysRevLett.77.4082>.
- [170] Philip B. Allen and Dierk Rainer. Phonon suppression of coherence peak in nuclear spin relaxation rate of superconductors. *Nature*, 349(6308):396–398, 1991. URL <http://www.nature.com/nature/journal/v349/n6308/abs/349396a0.html>.
- [171] T. W. Ebbesen, J. S. Tsai, K. Tanigaki, H. Hiura, Y. Shimakawa, Y. Kubo, I. Hiro-sawa, and J. Mizuki. Dopant isotope effect on superconductivity in  $\text{Rb}_3\text{C}_{60}$ . *Physica C: Superconductivity*, 203(1-2):163–166, 1992. URL <http://www.sciencedirect.com/science/article/pii/092145349290523F>.
- [172] B. Burk, Vincent H. Crespi, A. Zettl, and Marvin L. Cohen. Rubidium isotope effect in superconducting  $\text{Rb}_3\text{C}_{60}$ . *Phys. Rev. Lett.*, 72:3706–3709, 1994. URL <http://link.aps.org/doi/10.1103/PhysRevLett.72.3706>.
- [173] M. R. Norman and C. Pépin. The electronic nature of high temperature cuprate superconductors. *Reports on Progress in Physics*, 66(10):1547, 2003. URL <http://stacks.iop.org/0034-4885/66/i=10/a=R01>.
- [174] Fusayoshi J. Ohkawa. Strong-Coupling Superconductivity in the Cuprate Oxide. *Journal of the Physical Society of Japan*, 78(8):084712, 2009. URL <http://jpsj.ipap.jp/link?JPSJ/78/084712/>.
- [175] Hugo Keller, Annette Bussmann-Holder, and K. Alex Müller. Jahn-Teller physics and high-T<sub>c</sub> superconductivity. *Materials Today*, 11(9):38–46, 2008. URL <http://www.sciencedirect.com/science/article/pii/S1369702108701780>.
- [176] S. E. Barrett, D. J. Durand, C. H. Pennington, C. P. Slichter, T. A. Friedmann, J. P. Rice, and D. M. Ginsberg. <sup>63</sup>Cu Knight shifts in the superconducting state of  $\text{YBa}_2\text{Cu}_3\text{O}_{7-\delta}$  ( $T_c=90$  K). *Phys. Rev. B*, 41:6283–6296, 1990. URL <http://link.aps.org/doi/10.1103/PhysRevB.41.6283>.
- [177] Subir Sachdev and Bernhard Keimer. Quantum criticality. *Physics Today*, 64(2): 29–35, 2011. URL <http://link.aip.org/link/?PTO/64/29/1>.
- [178] A. J. Drew, Ch Niedermayer, P. J. Baker, F. L. Pratt, S. J. Blundell, T. Lancaster, R. H. Liu, G. Wu, X. H. Chen, I. Watanabe, V. K. Malik, A. Dubroka, M. Rössle, K. W. Kim, C. Baines, and C. Bernhard. Coexistence of static magnetism and superconductivity in  $\text{SmFeAsO}_{1-x}\text{F}_x$  as revealed by muon spin rotation. *Nature Materials*, 8(4):310–314, 2009. URL <http://www.nature.com/nmat/journal/v8/n4/abs/nmat2396.html>.
- [179] Michael R. Norman. High-temperature superconductivity in the iron pnictides. *Physics*, 1:21, 2008. URL <http://link.aps.org/doi/10.1103/Physics.1.21>.
- [180] Hiroshi Kontani, Tetsuro Saito, and Seiichiro Onari. Origin of orthorhombic transition, magnetic transition, and shear-modulus softening in iron pnictide superconductors: Analysis based on the orbital fluctuations theory. *Phys. Rev. B*, 84:024528, 2011. URL <http://link.aps.org/doi/10.1103/PhysRevB.84.024528>.

- [181] T. Shibauchi, A. Carrington, and Y. Matsuda. Quantum critical point lying beneath the superconducting dome in iron-pnictides. *arXiv:1304.6387*, 2013. URL <http://arxiv.org/abs/1304.6387>.
- [182] Satoshi Yamazaki and Yoshio Kuramoto. Repulsive interaction helps superconductivity in fullerides. *arXiv:1211.0096*, 2012. URL <http://arxiv.org/abs/1211.0096>.
- [183] M. M. Qazilbash, J. J. Hamlin, R. E. Baumbach, Lijun Zhang, D. J. Singh, M. B. Maple, and D. N. Basov. Electronic correlations in the iron pnictides. *Nature Physics*, 5(9):647–650, 2009. URL <http://www.nature.com/nphys/journal/v5/n9/abs/nphys1343.html>.
- [184] S.-H. Baek, H.-J. Grafe, L. Harnagea, S. Singh, S. Wurmehl, and B. Büchner. Pseudogap-like phase in  $\text{Ca}(\text{Fe}_{1-x}\text{Co}_x)_2\text{As}_2$  revealed by  $^{75}\text{As}$  NQR. *Phys. Rev. B*, 84:094510, 2011. URL <http://link.aps.org/doi/10.1103/PhysRevB.84.094510>.
- [185] Tuson Park and J D Thompson. Magnetism and superconductivity in strongly correlated  $\text{CeRhIn}_5$ . *New Journal of Physics*, 11(5):055062, 2009. URL <http://stacks.iop.org/1367-2630/11/i=5/a=055062>.
- [186] Tuson Park, V. A. Sidorov, H. Lee, F. Ronning, E. D. Bauer, J. L. Sarrao, and J. D. Thompson. Unconventional quantum criticality in the pressure-induced heavy-fermion superconductor  $\text{CeRhIn}_5$ . *Journal of Physics: Condensed Matter*, 23(9):094218, 2011. URL <http://iopscience.iop.org/0953-8984/23/9/094218>.
- [187] G. R. Stewart. Superconductivity in iron compounds. *Rev. Mod. Phys.*, 83:1589–1652, 2011. URL <http://link.aps.org/doi/10.1103/RevModPhys.83.1589>.
- [188] Antoine Georges, Luca de’ Medici, and Jernej Mravlje. Strong Correlations from Hund’s Coupling. *Annual Review of Condensed Matter Physics*, 4(1):137–178, 2013. URL <http://www.annualreviews.org/doi/abs/10.1146/annurev-conmatphys-020911-125045>.
- [189] Kazushi Kanoda. Metal–Insulator Transition in  $\kappa$ -( $\text{ET}$ ) $_2$ X and ( $\text{DCNQI}$ ) $_2$ M: Two Contrasting Manifestation of Electron Correlation. *Journal of the Physical Society of Japan*, 75(5):051007, 2006. URL <http://jpsj.ipap.jp/link?JPSJ/75/051007/>.
- [190] X. X. Xi. Two-band superconductor magnesium diboride. *Reports on Progress in Physics*, 71(11):116501, 2008. URL <http://stacks.iop.org/0034-4885/71/i=11/a=116501>.
- [191] Guo meng Zhao. Unconventional phonon-mediated superconductivity in  $\text{MgB}_2$ . *New Journal of Physics*, 4(1):3, 2002. URL <http://stacks.iop.org/1367-2630/4/i=1/a=303>.
- [192] Peter Beckett, Mark S. Denning, Ivo Heinmaa, Mukesh C. Dimri, Edward A. Young, Raivo Stern, and Marina Carravetta. High resolution  $^{11}\text{B}$  NMR of magnesium diboride using cryogenic magic angle spinning. *The Journal of Chemical Physics*, 137(11):114201, 2012. URL <http://link.aip.org/link/?JCP/137/114201/1>.

- [193] H. Kotegawa, K. Ishida, Y. Kitaoka, T. Muranaka, and J. Akimitsu. Evidence for Strong-Coupling  $s$ -Wave Superconductivity in  $\text{MgB}_2$ :  $^{11}\text{B}$  NMR Study. *Phys. Rev. Lett.*, 87:127001, 2001. URL <http://link.aps.org/doi/10.1103/PhysRevLett.87.127001>.
- [194] M. I. Eremets. *High Pressure Experimental Methods*. Oxford University Press Inc., New York, 1996.
- [195] F. Sayetat, P. Fertey, and M. Kessler. An Easy Method for the Determination of Debye Temperature from Thermal Expansion Analyses. *Journal of Applied Crystallography*, 31(2):121–127, 1998. URL <http://dx.doi.org/10.1107/S0021889897006936>.
- [196] Otto Zhou, Qing Zhu, John E. Fischer, Nicole Coustel, Gavin B. M. Vaughan, Paul A. Heiney, John P. Mccauley, and Amos B. Smith. Compressibility of  $\text{M}_3\text{C}_{60}$  Fullerene Superconductors: Relation Between  $T_c$  and Lattice Parameter. *Science*, 255:833–835, 1992. URL <http://www.sciencemag.org/content/255/5046/833.abstract>.
- [197] J. Diederichs, J.S. Schilling, K.W. Herwig, and W.B. Yelon. Dependence of the superconducting transition temperature and lattice parameter on hydrostatic pressure for  $\text{Rb}_3\text{C}_{60}$ . *Journal of Physics and Chemistry of Solids*, 58(1):123 – 132, 1997. URL <http://www.sciencedirect.com/science/article/pii/S002236979600087X>.
- [198] S. Margadonna, K. Prassides, H. Simoda, Y. Iwasa, and M. Mézouar. Pressure evolution of the structure of  $(\text{NH}_3)\text{K}_3\text{C}_{60}$ . *Europhysics Letters*, 56(1):61, 2001. URL <http://stacks.iop.org/0295-5075/56/i=1/a=061>.
- [199] Kenji Ishii, Tetsu Watanuki, Akihiko Fujiwara, Hiroyoshi Suematsu, Yoshihiro Iwasa, Hideo Shimoda, Tadaoki Mitani, Hironori Nakao, Yasuhiko Fujii, Youichi Murakami, and Hajime Kawada. Structural phase transition in the ammoniated alkali  $\text{C}_{60}$  compound  $(\text{NH}_3)\text{K}_3\text{C}_{60}$ . *Phys. Rev. B*, 59:3956–3960, 1999. URL <http://link.aps.org/doi/10.1103/PhysRevB.59.3956>.
- [200] Paolo Giannozzi, Stefano Baroni, Nicola Bonini, Matteo Calandra, Roberto Car, Carlo Cavazzoni, Davide Ceresoli, Guido L Chiarotti, Matteo Cococcioni, Ismaila Dabo, Andrea Dal Corso, Stefano de Gironcoli, Stefano Fabris, Guido Fratesi, Ralph Gebauer, Uwe Gerstmann, Christos Gougoussis, Anton Kokalj, Michele Lazzeri, Layla Martin-Samos, Nicola Marzari, Francesco Mauri, Riccardo Mazzarello, Stefano Paolini, Alfredo Pasquarello, Lorenzo Paulatto, Carlo Sbraccia, Sandro Scandolo, Gabriele Sclauzero, Ari P Seitsonen, Alexander Smogunov, Paolo Umari, and Renata M Wentzcovitch. QUANTUM ESPRESSO: a modular and open-source software project for quantum simulations of materials. *Journal of Physics: Condensed Matter*, 21(39):395502, 2009. URL <http://stacks.iop.org/0953-8984/21/i=39/a=395502>.
- [201] Arash A. Mostofi, Jonathan R. Yates, Young-Su Lee, Ivo Souza, David Vanderbilt, and Nicola Marzari. wannier90: A tool for obtaining maximally-localised Wannier functions. *Computer Physics Communications*, 178(9):685 – 699, 2008. URL <http://www.sciencedirect.com/science/article/pii/S0010465507004936>.

- [202] Yonatan Dubi, Yigal Meir, and Yshai Avishai. Nature of the superconductor-insulator transition in disordered superconductors. *Nature*, 449(7164):876–880, 2007. URL <http://www.nature.com/nature/journal/v449/n7164/full/nature06180.html>.

# Izjava

Izjavljam, da je ta disertacija plod lastnega znanstveno-raziskovalnega dela.

Ljubljana, 23. julij 2013

Anton Potočnik